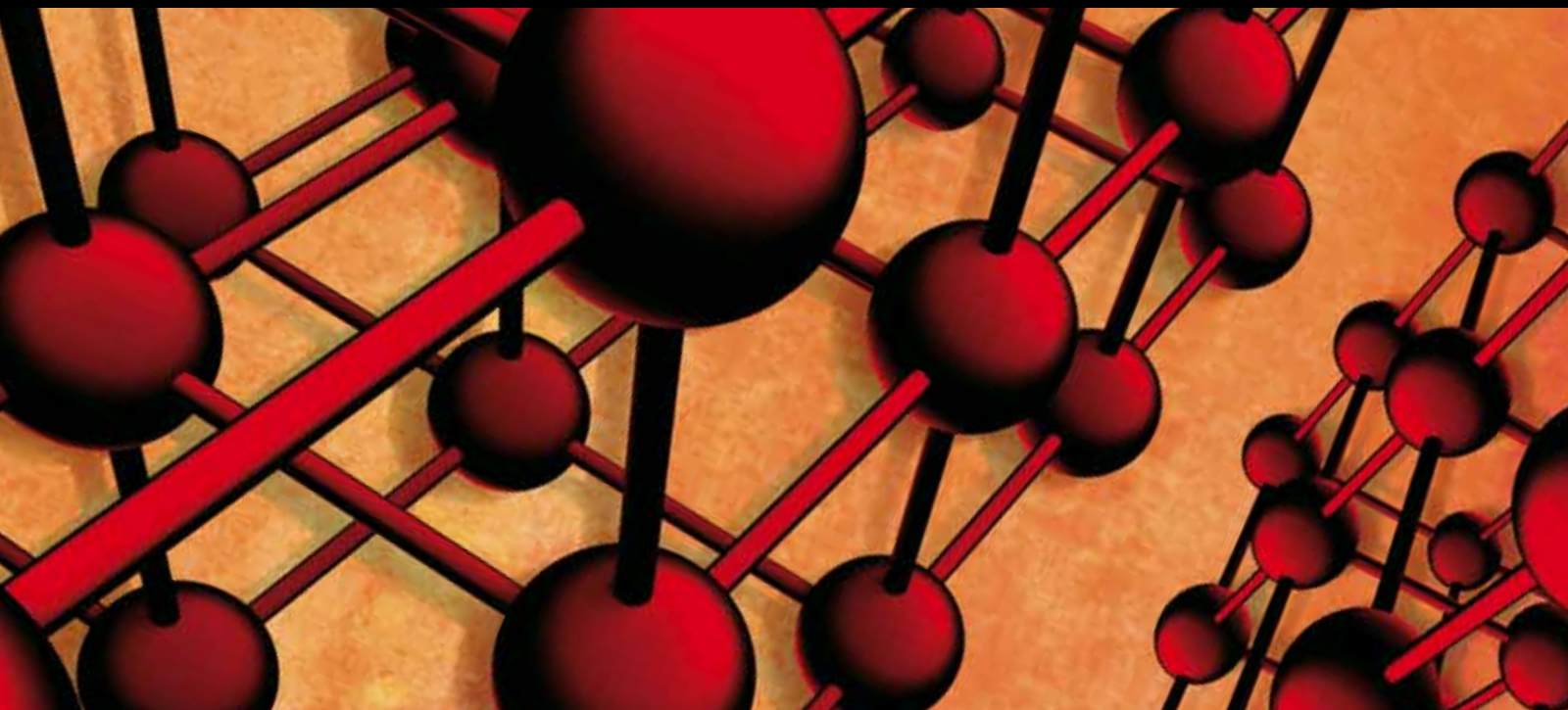


Brittle or Quasi-Brittle Fracture of Engineering Materials: Recent Developments and New Challenges

Guest Editors: F. Berto, M. Elices, M. R. Ayatollahi, S. V. Panin, and K. Tserpes





Brittle or Quasi-Brittle Fracture of Engineering Materials: Recent Developments and New Challenges

Advances in Materials Science and Engineering

**Brittle or Quasi-Brittle Fracture of Engineering
Materials: Recent Developments and
New Challenges**

Guest Editors: F. Berto, M. Elices, M. R. Ayatollahi,
S. V. Panin, and K. Tserpes



Copyright © 2014 Hindawi Publishing Corporation. All rights reserved.

This is a special issue published in “Advances in Materials Science and Engineering.” All articles are open access articles distributed under the Creative Commons Attribution License, which permits unrestricted use, distribution, and reproduction in any medium, provided the original work is properly cited.

Editorial Board

K. G. Anthymidis, Greece
Robert S. Averbach, USA
Amit Bandyopadhyay, USA
Zoe Barber, UK
Yucel Birol, Turkey
Susmita Bose, USA
Steve Bull, UK
Peter Chang, Canada
Daolun Chen, Canada
Manish U. Chhowalla, USA
S. Chinnappanadar, India
Jie Dai, Singapore
Chapal K. Das, India
J. Paulo Davim, Portugal
Seshu B. Desu, USA
Yong Ding, USA
Wei Feng, China
Sergi Gallego, Spain
Lian Gao, China
Hiroki Habazaki, Japan
Richard Hennig, USA
Dachamir Hotza, Brazil
Chun-Hway Hsueh, Taiwan
Shyh-Chin Huang, Taiwan
Rui Huang, USA
Wei Huang, China
Baibiao Huang, China
Jacques Huot, Canada
Jae-Ho Kim, Korea
Jaehwan Kim, Korea
Sridhar Komarneni, USA
Hongchao Kou, China
Prashant Kumta, USA
Jui-Yang Lai, Taiwan

Pavel Lejcek, Czech Republic
Markku Leskela, Finland
Bin Li, China
Feng Li, China
Ying Li, USA
Hai Lin, China
Yuanhua Lin, China
Zhimin Liu, China
Ying Liu, USA
Yuan Liu, China
Gang Liu, China
Tao Liu, China
Jun Liu, China
Meilin Liu, Georgia
Wei Liu, France
Yunqi Liu, China
Maria A. Loi, The Netherlands
Hai Lu, China
Peter Majewski, Australia
Shuichi Miyazaki, Japan
Paul Munroe, Australia
Ali Nazari, Iran
Luigi Nicolais, Italy
Tsutomu Ohzuku, Japan
Xiaoqing Pan, USA
Ganapathiraman Ramanath, USA
Raju V. Ramanujan, Singapore
Manijeh Razeghi, USA
Mohd Sapuan Salit, Malaysia
Jainagesh A. Sekhar, USA
Jiangbo Sha, China
Liyuan Sheng, China
You Song, China
Aloysius Soon, Korea

Charles C. Sorrell, Australia
Steven L. Suib, USA
Sam-Shajing Sun, USA
Weihua Tang, China
Somchai Thongtem, Thailand
Achim Trampert, Germany
Vladimir Tsukruk, USA
Krystyn Van Vliet, USA
Rui Vilar, Portugal
Min Wang, China
Hao Wang, China
Qiang Wang, China
Rui Wang, China
Rong Wang, USA
Lu Wei, China
Jörg Wiezorek, USA
Wei Wu, USA
Gongnan Xie, China
Aiguo Xu, China
Hemmige S. Yathirajan, India
Jianqiao Ye, UK
Wenbin Yi, China
Jinghuai Zhang, China
Jing Zhang, China
Li Zhang, China
Tao Zhang, China
Bin Zhang, China
Jian Zhang, Singapore
Jun Zhang, China
Yufeng Zhang, China
Kai Zhang, China
Rui Zhang, China
Ming-Xing Zhang, Australia
Wei Zhou, China

Contents

Brittle or Quasi-Brittle Fracture of Engineering Materials: Recent Developments and New Challenges,

F. Berto, M. Elices, M. R. Ayatollahi, S. V. Panin, and K. Tserpes

Volume 2014, Article ID 347485, 2 pages

Fatigue Properties of Layered Double Hydroxides Modified Asphalt and Its Mixture, Xing Liu,

Shaopeng Wu, Ling Pang, Yue Xiao, and Pan Pan

Volume 2014, Article ID 868404, 6 pages

Computational and Simulation Analysis of Pull-Out Fiber Reinforced Concrete, Xia Zhao,

Xiong-Jun He, Sheng Yan, and Nguyen Phan Anh

Volume 2014, Article ID 576052, 7 pages

Simulation of Hydraulic Fracture in Unsaturated Soils with High Degree of Saturation, Tielin Chen,

Liangyi Zhang, and Dingli Zhang

Volume 2014, Article ID 981056, 10 pages

Application of T_{33} -Stress to Predict the Lower Bound Fracture Toughness for Increasing the Test Specimen Thickness in the Transition Temperature Region, Kai Lu and Toshiyuki Meshii

Volume 2014, Article ID 269137, 8 pages

Strain Rate Dependent Ductile-to-Brittle Transition of Graphite Platelet Reinforced Vinyl Ester Nanocomposites, Brahmananda Pramanik and P. Raju Mantena

Volume 2014, Article ID 765698, 8 pages

A Brief Review of Some Local Approaches for the Failure Assessment of Brittle and Quasi-Brittle Materials, F. Berto

Volume 2014, Article ID 930679, 10 pages

Toughness Calculation of Postfire Normal Concrete, Qingyang Chen, Anjing Tang, and Zhoudao Lu

Volume 2014, Article ID 452763, 8 pages

An Analytical Model for Predicting the Stress Distributions within Single-Lap Adhesively Bonded Beams, Xiaocong He and Yuqi Wang

Volume 2014, Article ID 346379, 5 pages

Study on Strength and Ultrasonic Velocity of Air-Entrained Concrete and Plain Concrete in Cold Environment, Huai-shuai Shang, Ting-hua Yi, and Xing-xing Guo

Volume 2014, Article ID 706986, 7 pages

Preparation, Microstructure, and Mechanical Properties of Spinel-Corundum-Sialon Composite Materials from Waste Fly Ash and Aluminum Dross, Juntong Huang, Minghao Fang, Zhaohui Huang, Yan'gai Liu, Jingzhou Yang, Saifang Huang, Youguo Xu, Kai Chen, Shuai Yi, and Shaowei Zhang

Volume 2014, Article ID 789867, 10 pages

Effect of Silicon Addition on High-Temperature Solid Particle Erosion-Wear Behaviour of Mullite-SiC Composite Refractories Prepared by Nitrating Reactive, Xiaochao Li, Shusen Chen, Zhaohui Huang,

Minghao Fang, Yan'gai Liu, Xiaowen Wu, Juntong Huang, and Baolin Liu

Volume 2014, Article ID 943542, 8 pages



Average Fracture Energy for Crack Propagation in Postfire Concrete, Kequan Yu, Jiangtao Yu,
and Zhoudao Lu
Volume 2013, Article ID 143208, 13 pages

Al and Si Influences on Hydrogen Embrittlement of Carbide-Free Bainitic Steel, Yanguo Li, Cheng Chen,
and Fucheng Zhang
Volume 2013, Article ID 382060, 7 pages

Editorial

Brittle or Quasi-Brittle Fracture of Engineering Materials: Recent Developments and New Challenges

F. Berto,¹ M. Elices,² M. R. Ayatollahi,³ S. V. Panin,⁴ and K. Tserpes⁵

¹ Department of Management and Engineering, University of Padova, Stradella San Nicola 3, 36100 Vicenza, Italy

² Departamento de Ciencia de Materiales, Universidad Politécnica de Madrid, E. T. S. de Ingenieros de Caminos Canales y Puertos C/ Profesor Aranguren s/n, 28040 Madrid, Spain

³ Fatigue and Fracture Research Laboratory, Center of Excellence in Experimental Solid Mechanics and Dynamics, School of Mechanical Engineering, Iran University of Science and Technology, Narmak, Tehran 16846, Iran

⁴ Department of Mechanical Engineering & Aeronautics, Institute of Strength Physics and Material Science, Siberian Branch of Russian Academy of Sciences, Tomsk 634021, Russia

⁵ Laboratory of Technology & Strength of Materials (LTSM), Department of Mechanical Engineering & Aeronautics, University of Patras, 26500 Patras, Greece

Correspondence should be addressed to F. Berto; berto@gest.unipd.it

Received 17 March 2014; Accepted 17 March 2014; Published 28 April 2014

Copyright © 2014 F. Berto et al. This is an open access article distributed under the Creative Commons Attribution License, which permits unrestricted use, distribution, and reproduction in any medium, provided the original work is properly cited.

Brittle or quasi-brittle fracture of engineering materials is a wide field of research, which involves many researchers devoted to investigating different aspects of the mechanics and physics of fracture. Materials usually treated include metal alloys, polymers, composites, rocks, and ceramics.

Brittle failure is not a phenomenon limited only to static loadings. It may also be related to the fatigue and failure under repeated loading cycles (mechanical or thermal). The material damage process is usually very complex because it involves the combined effects of loading, size and geometry, temperature, and environment. The understanding of the phenomena tied to the dissipation of energy in various forms and the identification of microscopic properties and their interactions with macroscopic variables are the actual challenging topics. The fracture mechanics science emphasizes material characterization techniques and translation of specimen data to design.

The present special issue contains original research and review articles that seek to define possible criteria against brittle and quasi-brittle failure and to present or discuss new sets of experimental data in combination with fracture assessment. Among the areas emphasized in the SI are case histories, material selection and structure design, sample

calculations of practical design problems, material characterization procedures, fatigue crack growth and corrosion, nondestructive testing and inspection, structural failure and ageing, failure prevention methodologies, and maintenance and repair.

The papers submitted by the authors have been subjected to the normal journal peer-review process. Altogether the special issue contains 13 papers.

In the paper entitled “*Effect of silicon addition on high-temperature solid particle erosion-wear behaviour of mullite-SiC composite refractories prepared by nitriding reactive*,” the effects of silicon powder addition and erosion temperature on the erosion-wear resistance of mullite-SiC composite refractories are studied. The work provides the theoretical basis for the development of wear-resistant refractory materials.

In the paper entitled “*Average fracture energy for crack propagation in postfire concrete*” Wedge-splitting tests of postfire concrete specimens are summarised considering ten temperatures varying from room temperature to 600°C. The accurate calculation of the fracture energy at different temperatures is carried out in the paper.

In the paper entitled “*Al and Si influences on hydrogen embrittlement of carbide-free bainitic steel*,” a method based

on the density functional theory is applied to investigate the Al and Si influences on the hydrogen embrittlement of carbide-free bainitic steel. The paper shows that hydrogen embrittlement can be reduced by the presence of Al rather than Si.

In the paper entitled “*Preparation, microstructure, and mechanical properties of spinel-corundum-Sialon composite materials from waste fly ash and aluminum dross*,” a new method is provided to reduce environmental pollution and manufacture low cost high performance refractory materials using the abundant waste materials fly ash and aluminum dross.

The paper entitled “*Study on strength and ultrasonic velocity of air-entrained concrete and plain concrete in cold environment*” deals with the behavior of ultrasonic velocity and mechanical properties of plain concrete and air-entrained concrete subjected to freeze-thaw cycles. In particular the influences of F-T cycles on ultrasonic velocity and mechanical properties of C30 air-entrained concrete and plain concrete have been investigated. The experimental results can be useful for the design of new concrete structure, maintenance, and life prediction of existing concrete structure such as offshore platform and concrete dock wall.

In the paper entitled “*An analytical model for predicting the stress distributions within single-lap adhesively bonded beams*,” an analytical model for assessing the stress field within single-lap adhesively bonded beams under tension has been developed. By combining the governing equations of each adherent with the joint kinematics, the overall system of governing equations can be obtained assuming plane strain conditions. With suitable boundary conditions, the stress distribution of the adhesive in the longitudinal direction is determined.

The paper entitled “*Toughness calculation of postfire normal concrete*” deals with fracture tests of postfire normal concrete tested at ten temperatures up to 600°C. Residual fracture toughness using analytical method is determined at different temperatures.

The paper entitled “*A brief review of some local approaches for the failure assessment of brittle and quasi-brittle materials*” summarizes some local criteria applicable in presence of cracks and sharp/blunt notches.

The paper entitled “*Strain rate dependent ductile-to-brittle transition of graphite platelet reinforced vinyl ester nanocomposites*” is aimed at studying the strain rate dependent ductile-to-brittle transition of vinyl ester based nanocomposites. In more detail, the fracture behavior of xGnP (exfoliated graphite nanoplatelets) reinforced with additional CTBN (carboxyl terminated butadiene nitrile) toughened vinyl ester based nanocomposites is extensively studied.

The paper entitled “*Simulation of hydraulic fracture in unsaturated soils with high degree of saturation*” studies the hydraulic fracture process, considering the couplings of the stress distribution, the fluid flow of the water-air mixture, the compression and dissolution of air, and the element damage evolution. A large number of numerical analyses on hydraulic fracturing in clay with incipient injection slot have been carried out in the paper.

The paper entitled “*Computational and simulation analysis of pull-out fiber reinforced concrete*” investigates by means of complex numerical analyses the behavior of the reinforced concrete in its three constituents: the concrete matrix, the placed fiber reinforcement polymers (FRP), and resin layer.

The paper entitled “*Fatigue properties of layered double hydroxides modified asphalt and its mixture*” is devoted to the study of the influence of layered double hydroxides (LDHs) on the fatigue properties of asphalt mixture. A large bulk of experimental data from fatigue tests are summarized in the paper.

The paper entitled “*Application of T_{33} -stress to predict the lower bound fracture toughness for increasing the test specimen thickness in the transition temperature region*” faces the influence of out-of-plane crack tip constraint on the J calculation showing the capability of the elastic T-stress to accurately capture this behavior.

In doing so, a set of papers united by general direction of studies and giving a wide outlook onto fracture processes to take place in various heterogeneous materials and loading conditions are presented. They describe the peculiarities of fracture process in correlation with structure and provide adequate numerical calculation data to estimate stress-strain state evolution and characterize deformation behavior. We hope that the book will be of substantial interest for specialists in fracture mechanics and provide additional insight onto numerous aspects of brittle and quasi-brittle fracture.

Acknowledgment

We thank the many anonymous reviewers who assisted us in the review process providing useful comments and proposing constructive improvements to the authors. Without their continuous and valuable support also our efforts could have been useless.

F. Berto
M. Elices
M. R. Ayatollahi
S. V. Panin
K. Tserpes

Research Article

Fatigue Properties of Layered Double Hydroxides Modified Asphalt and Its Mixture

Xing Liu, Shaopeng Wu, Ling Pang, Yue Xiao, and Pan Pan

State Key Laboratory of Silicate Materials for Architectures, Wuhan University of Technology, Wuhan 430070, China

Correspondence should be addressed to Ling Pang; lingpang@whut.edu.cn

Received 16 December 2013; Revised 10 March 2014; Accepted 11 March 2014; Published 7 April 2014

Academic Editor: Majid R. Ayatollahi

Copyright © 2014 Xing Liu et al. This is an open access article distributed under the Creative Commons Attribution License, which permits unrestricted use, distribution, and reproduction in any medium, provided the original work is properly cited.

This study investigated the influence of layered double hydroxides (LDHs) on the fatigue properties of asphalt mixture. In this paper, different aging levels (thin film oven test (TFOT) and ultraviolet radiation aging (UV aging for short)) of bitumen modified with various mass ratios of the LDHs were investigated. The TFOT and UV aging process were used to simulate short-term field thermal-oxidative aging and long-term field light UV aging of bitumen, respectively. The influences of LDHs on the fatigue properties of LDHs were evaluated by dynamic shear rheometer (DSR) and indirect tensile fatigue test. Results indicated that the introduction of LDHs could change the fatigue properties of bitumen under a stress control mode. The mixture with modified bitumen showed better fatigue resistance than the mixture with base bitumen. The results illustrated that the LDHs would be alternative modifiers used in the bitumen to improve the lifetime of asphalt pavements.

1. Introduction

Bitumen has been widely used in pavement construction as a binder to bond aggregates [1]. Due to its viscoelastic properties, bitumen binder makes the asphalt pavement more flexible and comfortable for driving compared with cement concrete pavement. As a complex mixture of aliphatic, aromatic, and naphthenic hydrocarbons, the properties of bitumen often change gradually during service life due to the vehicle loads and environmental factors [2, 3].

Thermal oxygen ageing and ultraviolet radiation (UV) ageing, which are considered as an inevitable process in the practical application of asphalt pavement, have great effect on the fatigue properties of asphalt [4–6]. These two ageing types will decrease the physical properties, particularly fatigue properties at room temperature which will cause many problems in the field [7, 8].

In many countries all over the world, traffic loads are increasing not only in number, but also in magnitude. As a result, these increasing vehicle loads accelerate the deterioration of asphalt pavement and lead to fatigue cracking. The cracking can result in moisture penetration which could weaken the soil foundation. The combined effect of aging, cracks, weakened foundation, and so forth will lead to rapid failure of pavement structures. Therefore, it is meaningful

to investigate the fatigue properties in order to extend the fatigue life of asphalt pavement.

Layered double hydroxides (LDHs) have attracted considerable attention as an ultraviolet light resistant material in recent years. These layered materials have multi nestification layered structures. The inorganic layer sheets have the effect of physical shield UV light. Some metal elements of layer sheets and negative ions between layer sheets will chemically absorb UV light. This kind of multichemical absorbability and physical shield effect make the organic material as a material with excellent UV resistant behavior [9–13]. Due to the fundamental structure of LDHs, LDHs has the potential to improve the aging and fatigue resistance of bitumen. As a result, the effect of introducing LDHs into bitumen has received wide attention. Fatigue properties of road materials cannot be ignored due to their important indication of the pavement performance level during the service life of pavement. This study exactly aims at investigating the influence of the LDHs on the fatigue properties of bitumen and mixtures.

2. Experiments

2.1. Materials. SK-90[#] paving bitumen, provided by SK Corp., Korea, was used as the base material. Its physical properties are given in Table 1.

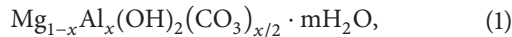
TABLE 1: Physical properties of the base bitumen.

Characteristic	Unit	Value
Penetration [25°C]	0.1 mm	89
Softening point [R and B]	°C	45.5
Ductility [10°C]	cm	20.3
Performance grade	°C	64–28
Dynamic viscosity [60°C]	Pa·s	158
Dynamic viscosity [135°C] [10 ⁻³]	Pa·s	430

TABLE 2: Basic properties of basalt aggregate.

Characteristic	Unit	Value
Specific gravity	g/cm ³	2.719
Water absorption ratio	%	0.98
Abrasion loss	%	18.6
Crushing value	%	14.4

LDHs which appeared white, with bulk density of 0.45 g/cm³, were provided by Rui Fa Chemical Company Limited, Jiangyin, Jiangsu, China. LDHs are a super molecular compound which contains Mg-Al layered double hydroxides complex metallic material. The composition of LDHs is as follows:



where x is the content variation of metallic elements, $0.2 \leq x \leq 0.33$; m is the amount of crystal water, $0 \leq m \leq 2$.

Basalt aggregate used in this study was obtained from Tongliao, Inner Mongolia, China. Table 2 gives the basic physical properties of basalt aggregate.

2.2. Preparation of LDHs Modified Bitumen and Mixture. The modified bitumen was prepared by using a laboratory high shear mixer. Bitumen was first heated to a well fluid at around 140°C in the mixer. Then a certain amount of LDHs was added to bitumen and blended at 4000 r/min rotation speed for about 60 min to ensure homogeneous dispersion. The unmodified bitumen was also processed under these same mix conditions to ensure that the comparison is reasonable.

AC-16C mixture type, designed by Marshall methods, was adopted. The basalt aggregates gradation is shown in Figure 1. Based on the primary design procedure, the optimum bitumen content was concluded at 5.0% by weight of aggregates. In this study, all the asphalt mixture samples used for following research were prepared by Marshall samples and were cut into specimens with thickness of 40 mm.

2.3. Aging Procedures. All bitumen samples were separately aged by oven ageing at 135°C for 5 hours and UV ageing for 8 days. The TFOT ageing procedure was conducted according to ASTM D 1754 [14], while the UV ageing experiment conditions are showed in Table 3.

The uncompacted asphalt mixtures were separately aged by oven ageing at 135°C for 5 hours and UV ageing for 8 days. The same UV strength as used for bitumen binder was used. But the UV radiation can just age asphalt mixture within certain depth [15]. Therefore, during the UV ageing,

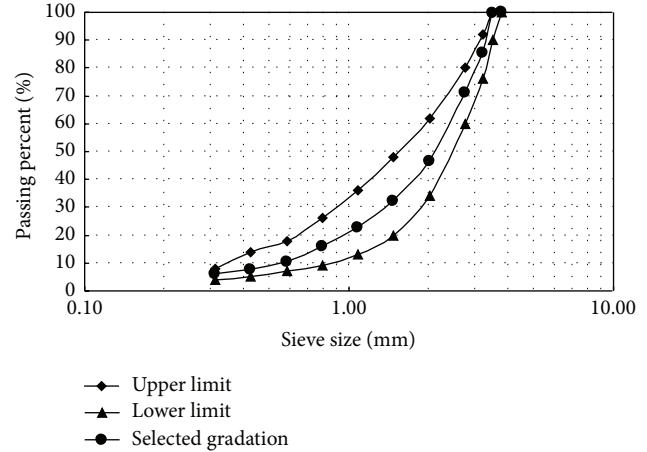


FIGURE 1: Aggregates gradation curves for asphalt mixture.

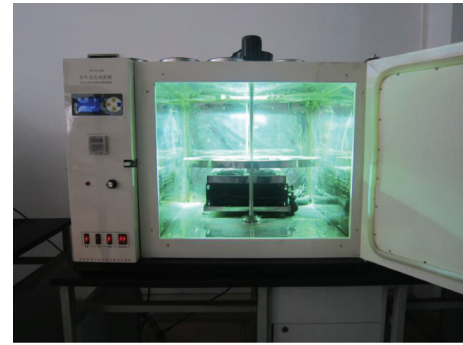


FIGURE 2: UV simulation machine with asphalt mixture in it.

TABLE 3: UV aging test conditions for bitumen binder.

Temperature	UV strength	Film thickness	Aging time
50°C	10,000 $\mu\text{W}/\text{cm}^2$	1250 μm	8 days

the uncompacted asphalt mixtures were turned over every 12 hours. The UV ageing was completed in the UV simulation machine as Figure 2 shows.

2.4. Test Methods. The physical properties of SK-90[#] bitumen and LDHs modified bitumen, including penetration (25°C), softening point (ring and ball method), and ductility (10°C), were investigated according to the standard ASTM D5 [16], ASTM D36 [17], and ASTM D113 [18], respectively.

Dynamic shear rheometer (DSR) MCR101 from Austria Anton Paar Company was used in this study to test the fatigue properties of bitumen binder [19]. The shear geometry of 8 mm diameter with 2 mm gap of bitumen binder was used. The testing frequency was fixed at 10 Hz, while the stress control mode of 0.5 and 0.8 MPa was applied.

Universal testing machine (UTM-25) was used in the mixture fatigue test [20] according to AASHTO T322-03. Figure 3 shows the specimen loading apparatus and deformation sensor mounting system in the UTM-25. The load with a resolution of 1 N was applied over the specimen through the upper strip with a width of 12.5 mm. The lower strip with the

TABLE 4: Detailed parameters used in the mixture fatigue test.

Temperature [°C]	5
Frequency [Hz]	2
Stress ratio* [5°C]	0.4, 0.5, 0.6, 0.65
Waveform	A haversine plus a rest period
Pulse width [ms]	63

*Stress ratio is the ratio of the loading stress and cleavage strength.



FIGURE 3: Indirect tensile testing device for the fatigue test and indirect tensile modulus test.

same width was fixed firmly to the base plate. Two horizontal sensors were recording horizontal deformations within the range of $\pm 0.5 \mu\text{m}$. The vertical sensor was capable of recording the vertical deformation within a range of $\pm 1.0 \mu\text{m}$. The test was performed in a temperature-controlled cabinet which can control the temperature within $\pm 0.1^\circ\text{C}$. Detailed testing conditions are given in Table 4. The cleavage strength of the mixture is the strength of the material damage.

The uniform tensile stress over most of the height of specimen mainly contributed to the fatigue damage of the specimen. Testing temperature of 5°C was chosen for the fatigue tests, and the applied tensile stress was taken lower than the tensile strength.

3. Results and Discussions

3.1. Basic Physical Properties. The softening point and penetration of SK-90[#] bitumen, 3% LDHs, and 5% LDHs modified bitumen before and after aging were shown in Figures 4 and 5. Firstly, when the LDHs were added to bitumen binder, it is obvious to see that the softening point increased slightly and the penetration reduced in a certain degree. Secondly, the more the ratio of LDHs in the bitumen binder, the higher the increment or reduction. The change of these basic physical properties demonstrated that adding small amount of LDHs to bitumen will let the bitumen get harder. It might improve the high temperature property and worsen the low temperature property. The retained penetration ratio of LDHs modified bitumen was higher, while the softening point increment of LDHs modified bitumen was lower after UV aging, compared to base bitumen. In general, the changes of softening point and penetration of LDHs modified bitumen

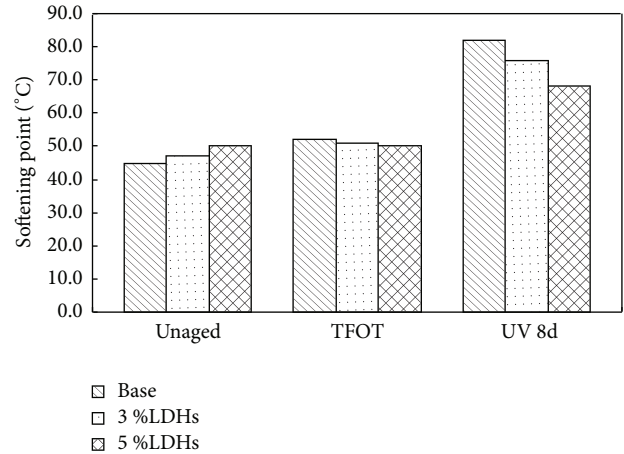


FIGURE 4: Softening point of bitumen.

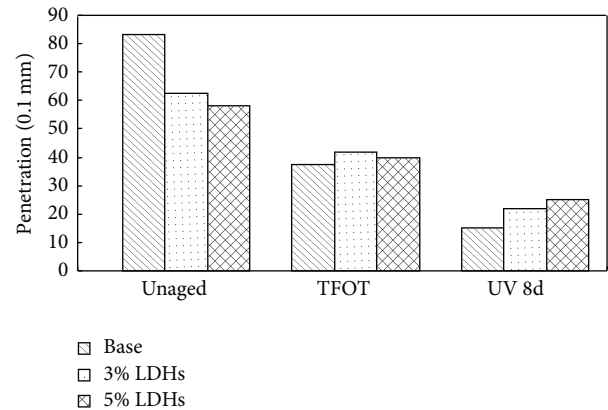


FIGURE 5: Penetration of bitumen.

after TFOT aging and UV 8d aging were much smaller than the changes of SK-90[#] bitumen. This illustrated that the modified bitumen had much better performances than the base bitumen such as temperature sensibility, oxidation ageing resistance, and UV aging resistance. Bitumen modified with 5% of LDHs slightly behaved better than 3% LDHs modified bitumen.

3.2. Fatigue Behavior of Bitumen. The fatigue life of bitumen after UV aging was evaluated by DSR at 10°C . Figures 6 and 7 present the fatigue curves as the function of stress level 0.5 MPa and 0.8 MPa for bitumen after UV 8d aging, respectively. The fatigue life of LDHs modified bitumen is much longer than that of base bitumen. Particularly at lower stress level, these differences are much more remarkable. The fatigue life of 3% LDHs modified bitumen is about 60% longer and 5% LDHs modified bitumen is nearly 2.5 times longer compared to the base bitumen at the lower stress level. At higher stress level, all bitumen becomes worse to resist fatigue crack propagation. The contribution to the fatigue life from LDHs at higher stress level is not as obvious as at low stress level. But the fatigue lives of 3% LDHs modified bitumen and 5% LDHs modified bitumen were slightly longer than the fatigue life of base bitumen.

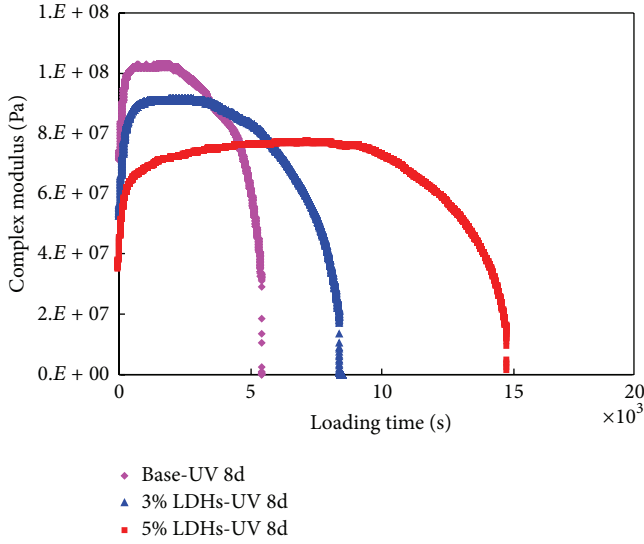


FIGURE 6: Fatigue life as the function of stress level 0.5 MPa after UV 8d aging.

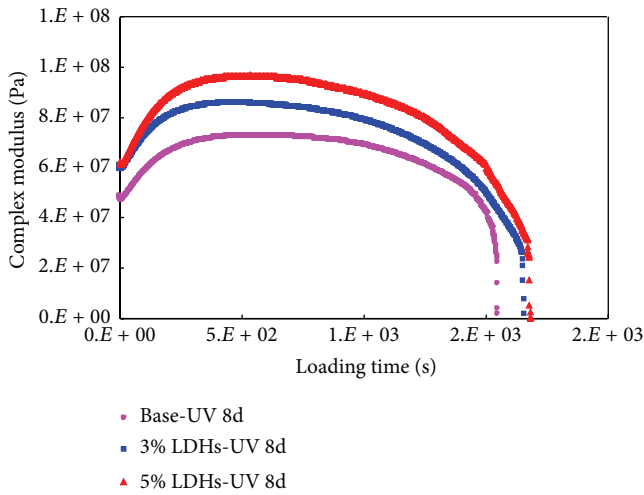


FIGURE 7: Fatigue life as the function of stress level 0.8 MPa after UV 8d aging.

The dispersing structures of LDHs in bitumen have contribution to the UV aging resistance of LDHs modified bitumen. The dispersion of structures corresponds to well-ordered multilayered structures where the bitumen chains are protected by the layer sheets and ions between the layers. The infiltration of oxygen and UV light could be obstructed by the layers in modified bitumen and the energy of UV light that gets into bitumen is therefore reduced. The dispersion and penetration process of oxygen and UV light in modified bitumen was more difficult. So the aging effect was reduced. Therefore, the fatigue life of bitumen can be extended by modifying with LDHs.

3.3. Fatigue Behavior of Asphalt Mixture. Compared with the bitumen, the fatigue behaviour of the mixture was more complicated. Asphalt mixture is a complicated system with

aggregates, binder, and voids as the three main functional sections. The fatigue life of mix is not just a combined contribution from all of the composites in the mixture, but also the interlock structure of the skeleton. The property of bitumen binder dominates viscoelastic property of mix. As a result, the fatigue life of mixture is also highly dependent on the binder behavior. The contribution of bitumen to the mixture's fatigue resistance was related to the load level [21]. Therefore, fatigue tests were conducted at several stress levels in this research.

3.3.1. Indirect Tensile Modulus of Asphalt Mixture. The indirect tensile modulus of asphalt mixture is calculated as follows:

$$M_R = \frac{P(\nu + 0.27)}{t\Delta H}, \quad (2)$$

$$\Delta H = \frac{(\nu + 0.27)}{3.59 \times \Delta V},$$

where M_R is the initial resilience modulus, MPa; P is the load, N; ν is Poisson's ratio; t is the thickness of specimen, mm; ΔH is the transverse resilience deformation, mm; ΔV is the longitudinal resilience deformation, mm.

Temperature has a great influence on Poisson's ratio of mixture. The higher the temperature, the higher the Poisson ratio. Conversely, the lower the temperature, the lower the Poisson ratio. Based on the technical experiences, the Poisson ratio of 0.25 at 5°C was used for asphalt mixture.

Figure 8 shows the indirect tensile modulus of mixture specimens under different stress level at 5°C. With the loading stress increasing, the indirect tensile modulus of asphalt mixture will increase at 5°C. Figure 8 indicates that the introduction of LDHs can decrease the indirect tensile modulus of mixture at 5°C. Lower indirect tensile modulus of asphalt mixture gives better resistance to deformation and internal stresses. Moreover, UV aging can increase the indirect tensile modulus of the asphalt mixture. There are no obvious differences of the increased percentage from unaged binder to UV aged binder between base bitumen and LDHs modified bitumen.

3.3.2. Fatigue Life of Asphalt Mixture. The fatigue life of asphalt mixture is calculated by the following classical fatigue equation [22]:

$$N_f = K \left(\frac{1}{\sigma_0} \right)^n, \quad (3)$$

where N_f is the fatigue life; σ_0 is the load stress, MPa; K and n are regression coefficients which are solved by the test results.

Table 5 presents the indirect tensile fatigue life of all asphalt mixture specimens at 5°C. Figure 9 shows the fatigue life and loading stress double logarithmic diagram. A good linear relationship between the stress level and fatigue life with logarithm transformation can be reached at 5°C.

Under the increasing stress level, the fatigue life decreases with different extent for different asphalt mixture. Under the same conditions, the LDHs modified asphalt mixture has

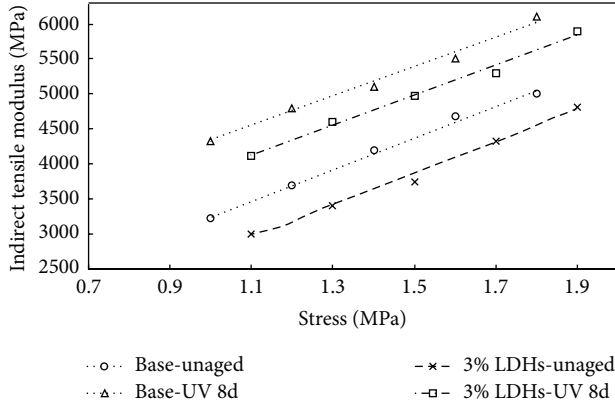


FIGURE 8: Indirect tensile modulus of mixture specimens under different stress level at 5°C.

TABLE 5: Indirect tensile fatigue life of asphalt mixture specimens at 5°C.

Material types	Stress ratio	Stress [MPa]	Fatigue life
Base-unaged	0.4	1.040	89627
	0.5	1.300	37076
	0.6	1.560	14571
	0.65	1.690	8596
Base-UV 8d	0.4	1.204	9746
	0.5	1.505	4587
	0.6	1.806	1471
	0.65	1.957	872
3% LDHs-unaged	0.4	1.052	159127
	0.5	1.315	45186
	0.6	1.578	16317
	0.65	1.710	10102
3% LDHs-UV 8d	0.4	1.200	18541
	0.5	1.500	5540
	0.6	1.800	1845
	0.65	1.950	1078

longer fatigue life than that of base asphalt mixture. After the same period of UV aging, the fatigue life of LDHs modified asphalt mixture is still longer than that of base asphalt mixture. Therefore, it can be concluded that the introduction of LDHs can improve the fatigue life of asphalt mixture.

According to Figure 9, the fatigue equations are regressed and the regression coefficients of K and n are also obtained. Table 6 presents the regression coefficients of fatigue equation at 5°C. The parameter K represents the durability of asphalt mixture. The higher the value of K , the better the durability of asphalt mixture. The parameter n represents the sensitivity of the influence of stress ratio on the fatigue life. The higher the value of n , the more sensitive the influence of stress ratio on the fatigue life.

Firstly, after UV 8d aging, the value of K decreases and the value of n increases. It indicates that UV aging will worsen the durability of the asphalt mixture and increase the sensitivity of the influence of stress ratio on the fatigue life. Secondly, before and after UV aging, the LDHs modified asphalt

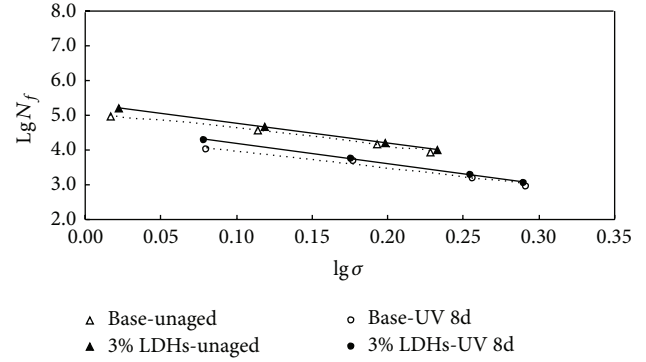


FIGURE 9: Double logarithmic diagram of fatigue life and loading stress at 5°C.

mixture has a higher K and n than base asphalt mixture. On the one hand, it demonstrates that the introduction of LDHs can enhance the durability of the asphalt mixture. On the other hand, it also illustrates that the introduction will let fatigue life of the mixture become more sensitive to the stress ratio on the fatigue life.

4. Conclusions

This paper investigated the fatigue properties of LDHs modified bitumen and asphalt mixture. Fatigue tests on bitumen binder and asphalt mixture were conducted by means of repeated shear test and indirect tensile fatigue test. The following conclusions can be drawn based on the results that are discussed above.

- (1) The changes of softening point and penetration of LDHs modified bitumen after TFOT aging and UV 8d aging were much smaller than the changes of SK-90[#] bitumen. This illustrated that the modified bitumen had much better resistance to oxidation and UV than the base bitumen.
- (2) Repeated shear test on bitumen binder illustrates that adding LDHs to bitumen binder can improve its fatigue properties under a stress control mode. LDHs can increase the fatigue resistance of bitumen, the fatigue life of 3% LDHs modified bitumen is more than 60% longer, and 5% LDHs modified bitumen is nearly 2.5 times longer than the fatigue life of base bitumen at the lower stress level.
- (3) The introduction of LDHs can decrease the indirect tensile modulus of mixture after UV aging. This means that LDHs might enhance the crack resistance at lower temperature conditions.
- (4) Fatigue results of bitumen and mixture with the addition of LDHs imply an improvement in the fatigue behavior of asphalt pavement. The introduction of LDHs into asphalt mixture can enhance its durability but will also increase the stress ratio sensitivity.

About all, the LDHs would be alternative modifiers used for the bitumen to improve the lifetime of asphalt pavements.

TABLE 6: Regression coefficients of fatigue equation at 5°C.

Material types	Fatigue equation	Regression coefficient		R^2
		K	n	
Base-unaged	$\lg N_f = 5.0641 - 4.7775 \lg \sigma$	$1.16E + 05$	4.7775	0.9909
Base-UV 8d	$\lg N_f = 4.4474 - 4.9993 \lg \sigma$	$2.80E + 04$	4.9993	0.9764
3% LDHs-unaged	$\lg N_f = 5.3276 - 5.6591 \lg \sigma$	$2.13E + 05$	5.6591	0.9999
3% LDHs-UV 8d	$\lg N_f = 4.7458 - 5.8369 \lg \sigma$	$5.57E + 04$	5.8369	0.9984

However, the test results listed in this research are limited on two kinds of fatigue test; further research is recommended to prove the conclusions.

Conflict of Interests

The authors declare that there is no conflict of interests.

Acknowledgments

This work is supported by National Project of Scientific and Technical Supporting Programs funded by Ministry of Science & Technology of China (no. 2011BAE28B03) and National Natural Science Foundation of China (no. 51278392). The authors gratefully acknowledge their financial support.

References

- [1] C. Ouyang, S. Wang, Y. Zhang, and Y. Zhang, "Preparation and properties of styrene-butadiene-styrene copolymer/ kaolinite clay compound and asphalt modified with the compound," *Polymer Degradation and Stability*, vol. 87, no. 2, pp. 309–317, 2005.
- [2] J. C. Petersen, "Chemical composition of asphalt as related to asphalt durability. State of the art," *Transportation Research Record*, no. 999, pp. 13–30, 1984.
- [3] W. J. Halstead, "Relation of asphalt chemistry to physical properties and specification," *Association of Asphalt Paving Technologists*, vol. 54, pp. 91–117, 1985.
- [4] C. Ouyang, S. Wang, Y. Zhang, and Y. Zhang, "Improving the aging resistance of asphalt by addition of zinc dialkyldithiophosphate," *Fuel*, vol. 85, no. 7-8, pp. 1060–1066, 2006.
- [5] G. D. Airey and B. Rahimzadeh, "Combined bituminous binder and mixture linear rheological properties," *Construction and Building Materials*, vol. 18, no. 7, pp. 535–548, 2004.
- [6] J. Yu, X. Zeng, S. Wu, L. Wang, and G. Liu, "Preparation and properties of montmorillonite modified asphalts," *Materials Science and Engineering A*, vol. 447, no. 1-2, pp. 233–238, 2007.
- [7] X. Lu and U. Isacsson, "Effect of ageing on bitumen chemistry and rheology," *Construction and Building Materials*, vol. 16, no. 1, pp. 15–22, 2002.
- [8] F. Durrieu, F. Farcas, and V. Mouillet, "The influence of UV aging of a Styrene/Butadiene/Styrene modified bitumen: comparison between laboratory and on site aging," *Fuel*, vol. 86, no. 10-11, pp. 1446–1451, 2007.
- [9] H. Chai, X. Xu, Y. Lin, D. G. Evans, and D. Li, "Synthesis and UV absorption properties of 2,3-dihydroxynaphthalene-6-sulfonate anion-intercalated Zn-Al layered double hydroxides," *Polymer Degradation and Stability*, vol. 94, no. 4, pp. 744–749, 2009.
- [10] Y. Feng, D. Li, Y. Wang, D. G. Evans, and X. Duan, "Synthesis and characterization of a UV absorbent-intercalated Zn-Al layered double hydroxide," *Polymer Degradation and Stability*, vol. 91, no. 4, pp. 789–794, 2006.
- [11] L. Zhang, Y. Lin, Z. Tuo, D. G. Evans, and D. Li, "Synthesis and UV absorption properties of 5-sulfosalicylate-intercalated Zn-Al layered double hydroxides," *Journal of Solid State Chemistry*, vol. 180, no. 4, pp. 1230–1235, 2007.
- [12] B. Wang, H. Zhang, D. G. Evans, and X. Duan, "Surface modification of layered double hydroxides and incorporation of hydrophobic organic compounds," *Materials Chemistry and Physics*, vol. 92, no. 1, pp. 190–196, 2005.
- [13] A. N. Ay, B. Zümreoglu-Karan, A. Temel, and L. Mafra, "Layered double hydroxides with interlayer borate anions: a critical evaluation of synthesis methodology and pH-independent orientations in nano-galleries," *Applied Clay Science*, vol. 51, no. 3, pp. 308–316, 2011.
- [14] ASTM D 1754/D1754M-09. Standard test method for Thin Film Oven Test of bituminous materials.
- [15] Z. Feng, *Study of anti-ultraviolet aging performance of asphalt and aggregate [Ph.D. dissertation]*, Harbin Institute of Technology, Harbin, China, 2004.
- [16] ASTM D5-06. Standard test method for penetration of bituminous materials.
- [17] ASTM D36-09. Standard test method for softening point of bitumen (ring-and-ball apparatus).
- [18] ASTM D113-07. Standard test method for ductility of bituminous materials.
- [19] D. A. Anderson, Y. M. Le Hir, M. O. Marasteanu, J.-P. Planche, D. Martin, and G. Gauthier, "Evaluation of fatigue criteria for asphalt binders," *Transportation Research Record*, no. 1766, pp. 48–55, 2001.
- [20] K. A. Ghuzlan and S. H. Carpenter, "Energy-derived, damage-based failure criterion for fatigue testing," *Transportation Research Record*, no. 1723, pp. 141–149, 2000.
- [21] G. Liu, *Characterization and identification of bitumen with the modification of montmorillonite nanoclay [Ph.D. thesis]*, Delft University of Technology, 2012.
- [22] A. S. Adedimila and T. W. Kennedy, "Repeated-load indirect tensile fatigue characteristics of asphalt mixtures," *Transportation Research Record*, no. 595, pp. 25–33, 1976.

Research Article

Computational and Simulation Analysis of Pull-Out Fiber Reinforced Concrete

Xia Zhao,^{1,2} Xiong-Jun He,¹ Sheng Yan,¹ and Nguyen Phan Anh¹

¹ School of Transportation, Wuhan University of Technology, Wuhan 430070, China

² Binzhou Polytechnic, Binzhou 256603, China

Correspondence should be addressed to Xia Zhao; yxzhaoxia@sina.com

Received 26 November 2013; Revised 15 January 2014; Accepted 16 January 2014 Published 3 April 2014

Academic Editor: Konstantinos I. Tserpes

Copyright © 2014 Xia Zhao et al. This is an open access article distributed under the Creative Commons Attribution License, which permits unrestricted use, distribution, and reproduction in any medium, provided the original work is properly cited.

The computational and simulation analysis of pull-out fiber reinforced concrete was investigated. The finite element analysis was used to make this modeling and analysis on this reinforced system and three parts (concrete matrix, the placed fiber reinforcement polymers (FRP), and resin layer) were studied. A constant load was directly applied on the free end of placed FRP and the deformation, von Mises stress, displacement, and strain of these three analyzed parts were obtained. Meanwhile, the specimen system of bonding strength and strain was calculated by the method of ABAQUS. The results showed that, with the constant load, the von Mises stress, deformation, and strain appeared in these three parts, and the maximum values in both FRP and resin layer were shown at the free end side, which provides an accurate description of the rupture mode.

1. Introduction

Concrete is the most widely used construction material in large quantities for its low cost and wide availability [1, 2]. However, it suffers from low tensile strength and limited strain capacity, which gives rise to formation of microcracks in a loading state. Microcracks have an enormous influence on the durability and the formed cracks accelerate the deterioration by increasing the permeability of the matrix through freezing-and-thawing damage, alkali silica reaction, chloride penetration, and other mechanisms [3, 4]. Nowadays, the researchers find that the fiber reinforcement polymers (FRP) have created an extensive field to control the matrix cracks. The structures achieve a good strengthening effect with FRP in mechanical and durability properties. Their high stiffness, chemical resistance, tensile strength, and fire resistance make them attractive for the next generation high performance reinforced composites materials of the 21st century [5–10].

Prior works on FRP reinforced concrete have focused on the finite element analysis modeling and simulation in the literature [11–30]. Wu et al. [31] studied the cracking behavior and interfacial debonding fracture in FRP-strengthened concrete beams and a finite element analysis was performed

to obtain the different types of debonding propagation along FRP-concrete interface and crack distribution in matrix. Benzarti et al. [32] presented a coupled damage model to predict the durability of concrete elements strengthened by external bonding of FRP plates and their numerical results and experimental tests showed that the model captures well the debonding fracture initiation. An experimental investigation of the fatigue behavior of FRP-concrete was investigated by Carloni et al. [33] and they found that the length of stress transfer zone during fatigue loading was smaller than the stress transfer zone associated with the cohesive crack under quasistatic loading; also the postfatigue results suggested the possibility of a different debonding mechanism during fatigue loading.

In this paper, the finite element analysis [34, 35] was used to make this modeling and analysis on this pull-out FRP/concrete system. Each specimen of bonding strength and strain was calculated by ABAQUS method. The concrete matrix, the strengthening FRP, and resin layer were modeled individually as damageable materials with a constant loading. The von Mises stress, strain, deformation, and displacement were all given to analyze this rupture mode of selected composites.

TABLE 1: Young's modulus and Poisson's ratio of three analyzed parts.

Materials	Young's modulus/GPa	Poisson's ratio
Concrete matrix	3.152×10^4	0.3
FRP	1.618×10^5	0.2
Resin layer	5.21×10^3	0.39

TABLE 2: Summary of testing results.

Specimen	L (mm)	b_b (mm)	t_p (mm)	f_c (MPa)	E_c (MPa)	P_{exp} (kN)	Failure
30 MPa-250-10	250	10.29	1.22	30	31,520	26.6	D

TABLE 3: The detailed dimensions of each three parts.

Sample	L_c (mm)	b_c (mm)	t_c (mm)	L_f (mm)	b_f (mm)	t_f (mm)	L_r (mm)	b_r (mm)	t_r (mm)	P (N)
30 MPa-250-10	350	300	180	350	1.22	10.29	250	1	10.29	26600

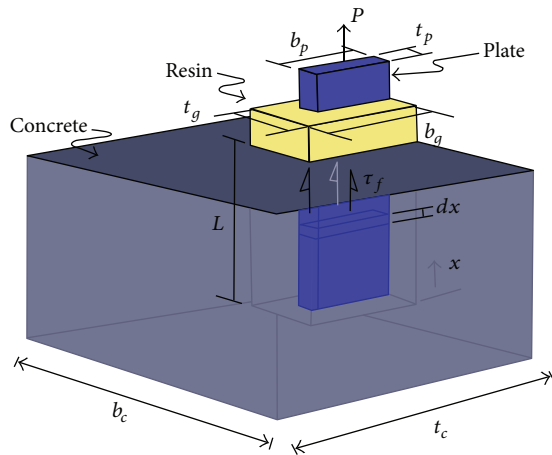


FIGURE 1: Simplified model of FRP-concrete.

2. Computational and Simulation Modes

2.1. Model Design. In order to confirm the analysis of the simulation program and the further studying about the relationship between bonding and slip, a finite element analysis was performed by using ABAQUS 6.8-1 to calculate and simulate the pull-out FRP/concrete system. In the pull-out FRP/concrete model, the main component includes four parts: concrete, FRP, resin, and the bond interface between concrete and FRP. All components were modeled by using 8-node linear brick, which reduced integration and hourglass control (C3D8R).

As a simplified model of pull-out FRP/concrete system, which was shown in Figure 1, it included the concrete matrix, FRP, and the resin. Young's modulus and the Poisson's ratio of these three parts were shown in Table 1.

2.2. Modeling Procedure. Before the model procedures, we assume that the bending effect of FRP is ignored. Meanwhile, only the shear force appears in adhesive layer and the size of each part still stays in a constant value and no deformation occurred.

For each component of this modeled system, the stress-strain curve of concrete follows the mathematical model investigated by Todeschini et al. [36]. The size of the concrete block was $350 \times 300 \times 180$ mm, which was shown in Figure 2. Concrete cylinders were used to define material properties including the compress strength and Young's modulus in Table 2. FRP is assumed as behaving a linear-elastically condition which showed the failure stress and strain in longitudinal tension. At the failure point, FRP loses its tensile strength. The type of constitutive behavior of resin is simulated by an elastic-plastic model with strain hardening for quasistatic response during pull-out testing. In order to define this behavior, the properties of resin were given below, such as Young's modulus of 5210 MPa, the tensile strength of 16 MPa, and Poisson's ratio of 0.39. All components were followed the American Standard ASTM D638. A finite element analysis is used to make this modeling and analysis on this reinforced system. The details of this modeling procedure are as follows.

- (1) Define a 3D concrete block with a sized groove placed in the middle of the matrix. The size of groove is $(1 + 1.22 + 1) \times 10.29$ mm.
- (2) Define a 3D deformable FRP plate ($1.22 \times 10.29 \times L_{FRP}$ mm) which lays in the groove. A constant load is applied at the free size of FRP: $L_{FRP} > L = 250$, where L_{FRP} is length of FRP strip and L stands for bond length of FRP as experimental test.
- (3) Define two layers of the deformable coated resin ($1 \times 10.29 \times 250$ mm). Resin layer is coated between the matrix and FRP. The detailed dimensions of concrete matrix, FRP plate and resin layer are shown in Table 3, where b_c , t_c , b_g , t_g , b_p , and t_p are the width and length of concrete matrix, the placed grooves, and FRP, respectively. τ_f represents the maximum value of interfacial shear stress and L shows the placed length of FRP in matrix. A constant load (26600 N) was applied on the free end of placed FRP.
- (4) Define interfacial bond between FRP plate and concrete and FRP plate and resin layer by tying constraint

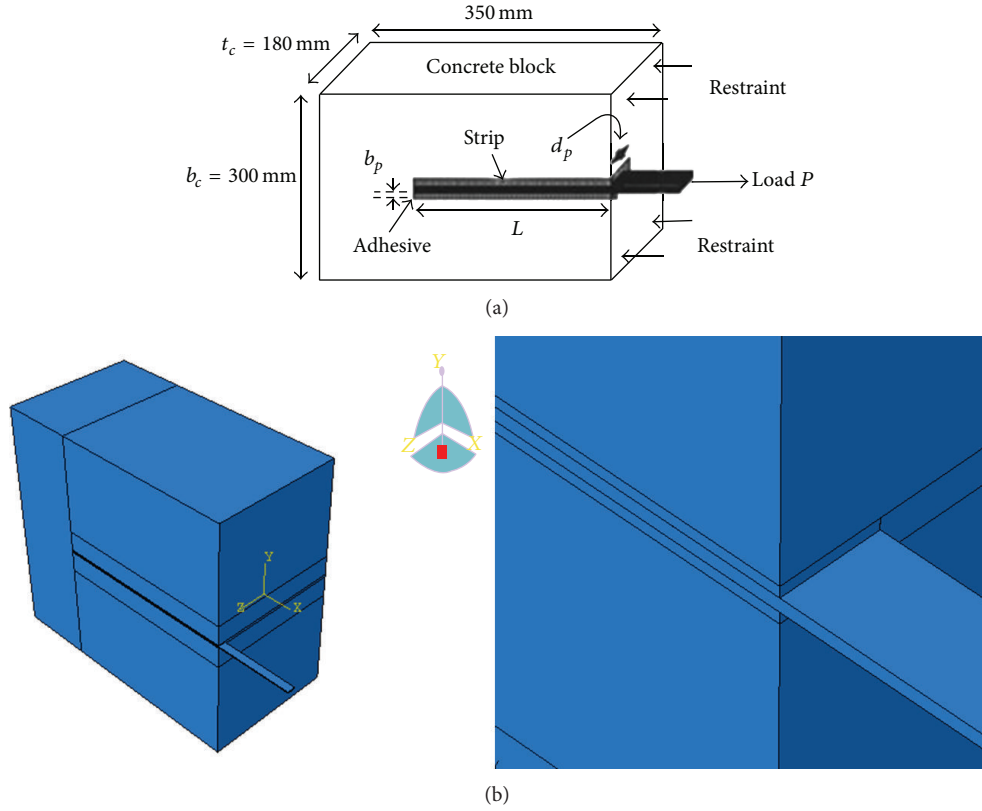


FIGURE 2: The detailed reinforced system model.

of two adjacent surfaces. In this modeling, the tie constraint surfaces include concrete-first resin layer, first resin layer-FRP, FRP-second resin layer, and second resin layer-concrete. The defined model is shown in Figure 2.

2.3. Mesh, Loading, and Boundary Condition. As one important step in this modeling, a detailed meshing [37] can ensure a relatively accurate modeling result. Structural mesh generation technique was applied in this modeling. Mesh of concrete matrix, FRP plate, and resin layer are all shown in Figure 3. A constant load (26600 N) is applied at the free end of FRP plate and the corresponding boundary condition was followed as the experimental test, which was done by Seracino et al. [38]. The loading and boundary condition were shown in Figure 4.

2.4. Analysis Algorithm and Control Solutions. In this simulation, a directly nonlinear analysis technique was employed and this technique followed the method of Newton-Rapson. In the modeling procedures, the system stayed in a static loading condition. Automatic time step was applied with set 1. The maximum number was 100 and the increment size included the initial value 1, the minimum value 1E-05, and the maximum value 1.

3. Analysis

3.1. Calculation. In order to satisfy the accuracy of the model, the bond interface characteristics of the analytical model were calculated by using the method of finite element analysis. In the Seracino et al. [39] model, the predicted IC debonding failures of FPR strengthening system with a constant loading can be calculated by

$$P_{IC} = \alpha_p 0.85 \varphi_f^{0.25} f_c^{0.3} \sqrt{L_{per} E_p A_p} < f_{rupt} A_p. \quad (1)$$

As calculated in (1) and previous design, results of each specimen are shown in Table 4. This thesis uses ABAQUS software to simulate finite element analysis method. All specimen systems were broken down finally.

3.2. Deformation. With the constant loading, a deformation was obtained in FRP plate. No deformation appeared in the area of XY plane and YZ plane; but a remarkable deformation occurred in XZ plane and it was bended inwards. According to the symmetric principle, the deformation was cancelled in XY plane and YZ plane. However, a bending moment was obtained for the constant load in XZ plane. The deformation of this modeling was shown in Figure 5 and an evident deformation occurred at the edge between matrix and FRP plate.

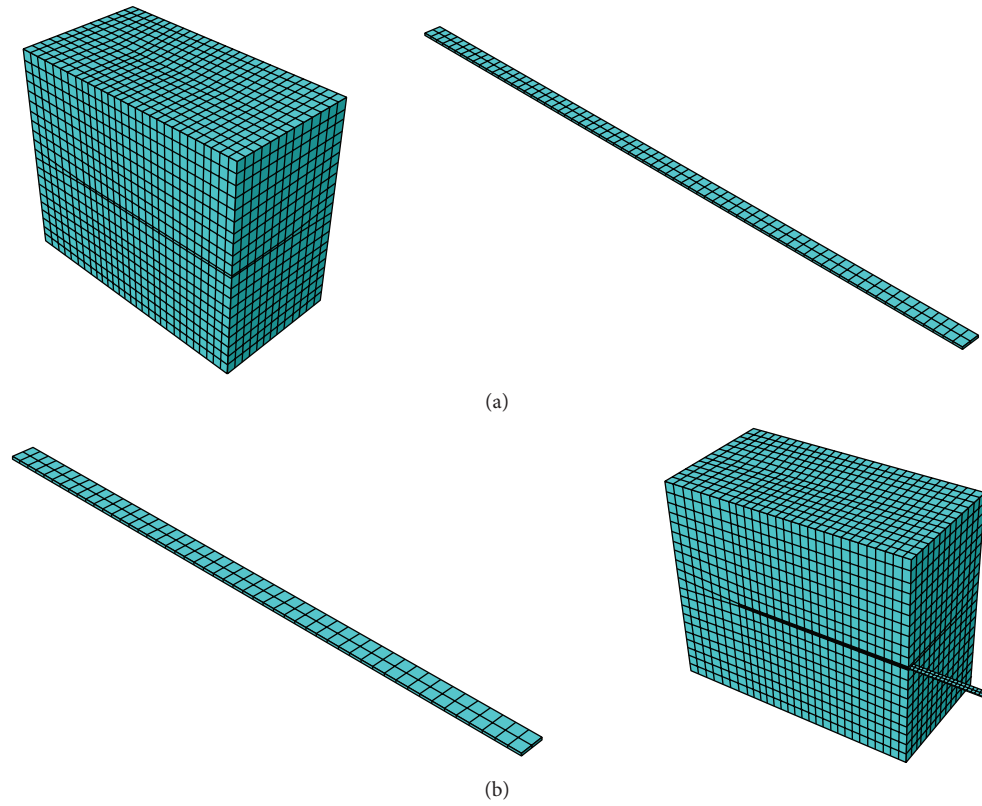


FIGURE 3: Mesh of concrete matrix, FRP plate, resin layer, and the reinforced concrete system.

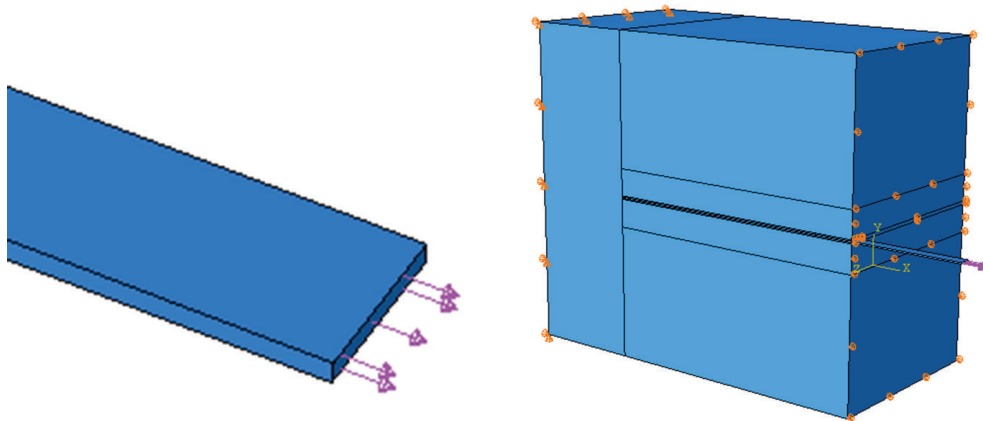


FIGURE 4: The loading and boundary condition of reinforced concrete system.

TABLE 4: Calculation for each specimen test by Abaqus software.

Specimen	Bond strength (kN)	ϵ_{\max} (mm)
30 MPa-100-10	20.4	0.009133
30 MPa-150-10	23.2	0.010213
30 MPa-200-10	27.9	0.012238
30 MPa-250-10	26.6	0.0118
30 MPa-300-10	26.0	0.011452
30 MPa-350-10	23.0	0.010106

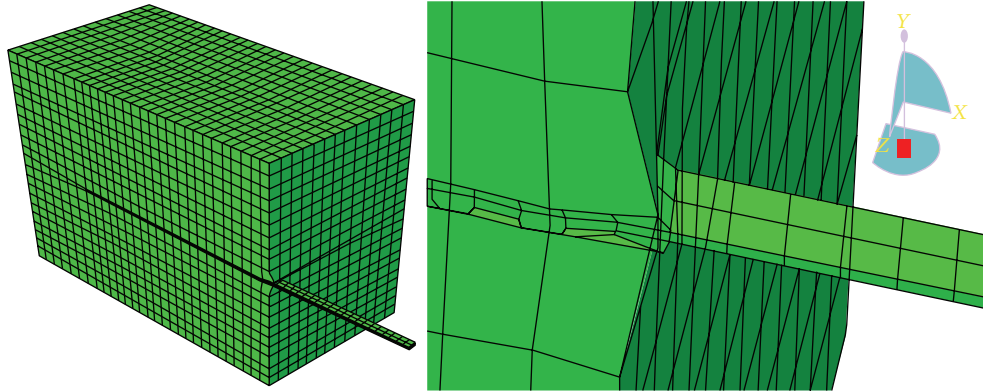


FIGURE 5: Deformation of FRP in this modeling.

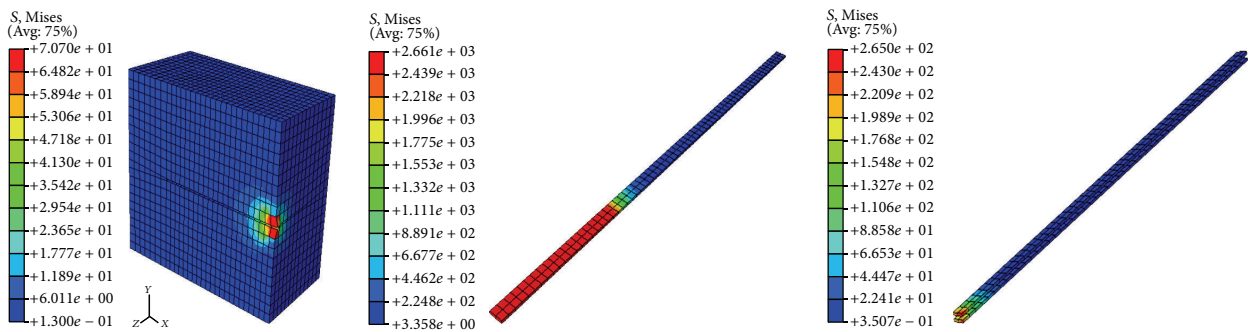


FIGURE 6: von Mises stress of concrete, FRP plate, and resin layer.

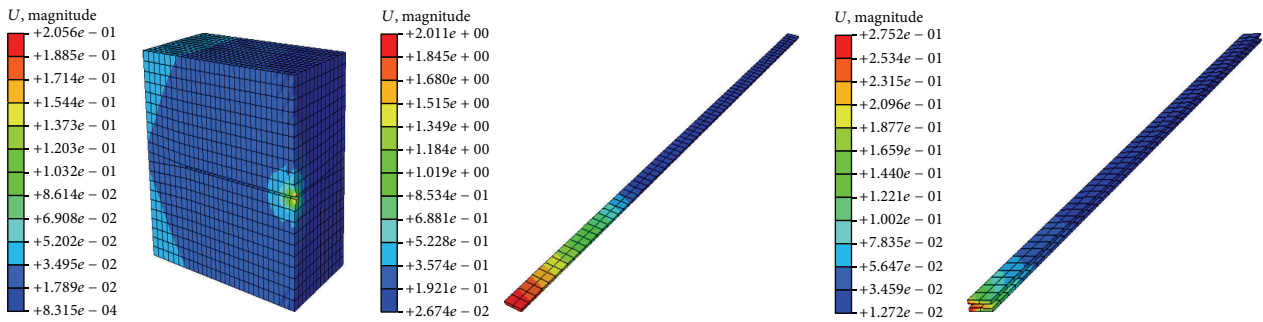


FIGURE 7: Displacement of concrete, FRP plate, and resin layer.

3.3. *von Mises Stress.* von Mises stress [40, 41] was always used to describe the distribution of stress, and the color in each mesh showed the stress value. The stress means to be increased when the color turns from blue to red, and the von Mises stress values can be obtained. The von Mises stress of concrete matrix, FRP plate, and resin layer were all shown in Figure 6. The maximum von Mises stress (2.661×10^3 MPa) value was obtained at the edge between matrix and FRP plate. Meanwhile, the maximum von Mises stress of FRP plate 2.661×10^3 MPa and resin layer 2.661×10^2 MPa appeared at the board edge of FRP plate.

3.4. *Displacement.* The displacement showed the degree of deformation of concrete matrix, FRP plate, and resin layer,

which indirectly reflected the bonding strength. The maximum displacement of tested three parts (Figure 7) appeared at the edge of contact point, and the maximum values were 0.2056 mm, 2.011 mm, and 0.2752 mm, respectively. The displacement decreased with the deeper groove of concrete, which showed that the bonding strength was much higher and a greater durability property was obtained.

3.5. *Strain.* The simulated strain showed the deformation resistance ability, which indirectly reflected the displacement and bonding strength. The same distribution trends were obtained in Figure 8, and the maximum value all occurred at the contact place. All the maximum strain was 2.188×10^{-3} , 1.644×10^{-2} , and 4.637×10^{-2} , respectively.



FIGURE 8: Strain of concrete, FRP plate, and resin layer.

4. Conclusions

In this paper, the computational and modeling analysis of the pull-out FRP/concrete system was studied systematically. A finite element analysis was used in this modeling procedure. Each specimen system of bonding strength and strain was calculated by the method of ABAQUS. All the three parts, concrete matrix, FRP, and resin layer, were studied in this analysis individually. A constant load (26600 N) was applied on the free side of the placed FRP. Deformation, von Mises stress, displacement, and strain of each individual part were obtained and the maximum values all occurred at the edge of the contact point. Meanwhile, the values decreased with the deeper groove of concrete, which showed that the higher bonding strength was gained in the deeper groove, and the contact point was the weakest zone in this pull-out FRP/concrete system.

Further researches are needed to obtain a deeper analysis of pull-out FRP reinforced concrete. Also, the detailed pulling-out process (elastic stage, elastic softening stage, debonding stage, and softening-debonding stage) and slip and shear stress at the interfacial bond shall be explored. We believe that our results at least in the trend are helpful for the research of FRP reinforced concrete system.

Conflict of Interests

The authors declare that there is no conflict of interests regarding the publication of this paper.

Acknowledgment

The authors would like to express appreciation for the financial support by the Natural Science Foundation of China (51178361).

References

- [1] F. M. Lea, *The Chemistry of Cement and Concrete*, Edward Arnold, London, UK, 3rd edition, 1976.
- [2] H. F. W. Taylor, *Cement Chemistry*, Thomas Telford, London, UK, 2nd edition, 1998.
- [3] B. M. Wang, Y. Zhang, and S. Liu, "Influence of carbon nanofibers on the mechanical performance and microstructure

of cement-based materials," *Nanoscience and Nanotechnology Letters*, vol. 5, no. 10, pp. 1112–1118, 2013.

- [4] Z. S. Metaxa, M. S. Konsta-Gdoutos, and S. P. Shah, "Carbon nanofiber cementitious composites: effect of debulking procedure on dispersion and reinforcing efficiency," *Cement and Concrete Composites*, vol. 36, pp. 25–32, 2013.
- [5] T. C. Triantafillou, "Shear strengthening of reinforced concrete beams using epoxy-bonded FRP composites," *ACI Structural Journal*, vol. 95, no. 2, pp. 107–115, 1998.
- [6] R. El-Hacha and S. H. Rizkalla, "Near-surface-mounted fiber-reinforced polymer reinforcements for flexural strengthening of concrete structures," *ACI Structural Journal*, vol. 101, no. 5, pp. 717–726, 2004.
- [7] L. Lam and J. G. Teng, "Strength models for fiber-reinforced plastic-confined concrete," *Journal of Structural Engineering*, vol. 128, no. 5, pp. 612–623, 2002.
- [8] L. Koutas and T. C. Triantafillou, "Use of anchors in shear strengthening of reinforced concrete T-beams with FRP," *Journal of Composites for Construction*, vol. 17, no. 1, pp. 101–107, 2013.
- [9] H. Wang and A. Belarbi, "Ductility characteristics of fiber-reinforced-concrete beams reinforced with FRP rebars," *Construction and Building Materials*, vol. 25, no. 5, pp. 2391–2401, 2011.
- [10] G. Ma, H. Li, and Z. Duan, "Repair effects and acoustic emission technique-based fracture evaluation for predamaged concrete columns confined with fiber-reinforced polymers," *Journal of Composites for Construction*, vol. 16, no. 6, pp. 626–639, 2012.
- [11] H.-T. Hu, F.-M. Lin, and Y.-Y. Jan, "Nonlinear finite element analysis of reinforced concrete beams strengthened by fiber-reinforced plastics," *Composite Structures*, vol. 63, no. 3-4, pp. 271–281, 2004.
- [12] A. M. Malek and H. Saadatmanesh, "Analytical study of reinforced concrete beams strengthened with web-bonded fiber reinforced plastic plates or fabrics," *ACI Structural Journal*, vol. 95, no. 3, pp. 343–352, 1998.
- [13] J. W. Tedesco, J. M. Stallings, and M. El-Mihilmly, "Finite element method analysis of a concrete bridge repaired with fiber reinforced plastic laminates," *Computers and Structures*, vol. 72, no. 1, pp. 379–407, 1999.
- [14] E. Cosenza, G. Manfredi, and R. Realforzo, "Behavior and modeling of bond of FRP rebars to concrete," *Journal of Composites for Construction*, vol. 1, no. 2, pp. 40–51, 1997.
- [15] C. Na and H.-G. Kwak, "A numerical tension-stiffening model for ultra high strength fiber-reinforced concrete beams," *Computers and Concrete*, vol. 8, no. 1, pp. 1–22, 2011.

- [16] H. Hu and W. C. Schnobrich, "Constitutive modeling of concrete by using nonassociated plasticity," *Journal of Materials in Civil Engineering*, vol. 1, no. 4, pp. 199–216, 1989.
- [17] B. Ferracuti, M. Savoia, and C. Mazzotti, "A numerical model for FRP-concrete delamination," *Composites B: Engineering*, vol. 37, no. 4-5, pp. 356–364, 2006.
- [18] S. K. Padmarajaiah and A. Ramaswamy, "A finite element assessment of flexural strength of prestressed concrete beams with fiber reinforcement," *Cement and Concrete Composites*, vol. 24, no. 2, pp. 229–241, 2002.
- [19] M. Samaan, A. Mirmiran, and M. Shahawy, "Model of concrete confined by fiber composites," *Journal of Structural Engineering*, vol. 124, no. 9, pp. 1025–1031, 1998.
- [20] X. Z. Lu, L. P. Ye, J. G. Teng, and J. J. Jiang, "Meso-scale finite element model for FRP sheets/plates bonded to concrete," *Engineering Structures*, vol. 27, no. 4, pp. 564–575, 2005.
- [21] J. F. Chen and J. G. Teng, "Anchorage strength models for FRP and steel plates bonded to concrete," *Journal of Structural Engineering*, vol. 127, no. 7, pp. 784–791, 2001.
- [22] J. G. Teng, J. W. Zhang, and S. T. Smith, "Interfacial stresses in reinforced concrete beams bonded with a soffit plate: a finite element study," *Construction and Building Materials*, vol. 16, no. 1, pp. 1–14, 2002.
- [23] R. S. Y. Wong and F. J. Vecchio, "Towards modeling of reinforced concrete members with externally bonded fiber-reinforced polymer composites," *ACI Structural Journal*, vol. 100, no. 1, pp. 47–55, 2003.
- [24] X. Z. Lu and J. J. Jiang, "A concrete constitutive relationship with various damage models," *China Civil Engineering Journal*, vol. 36, no. 11, pp. 70–74, 2003.
- [25] L. Skarzynski and J. Tejchman, "Determination of representative volume element in concrete under tensile deformation," *Computers and Concrete*, vol. 9, no. 1, pp. 35–50, 2012.
- [26] X. Z. Lu, J. G. Teng, L. P. Ye, and J. J. Jiang, "Bond-slip models for FRP sheets/plates bonded to concrete," *Engineering Structures*, vol. 27, no. 6, pp. 920–937, 2005.
- [27] L. Lam and J. G. Teng, "Strength models for fiber-reinforced plastic-confined concrete," *Journal of Structural Engineering*, vol. 128, no. 5, pp. 612–623, 2002.
- [28] M. N. Youssef, M. Q. Feng, and A. S. Mosallam, "Stress-strain model for concrete confined by FRP composites," *Composites B: Engineering*, vol. 38, no. 5-6, pp. 614–628, 2007.
- [29] T. Jiang and J. G. Teng, "Analysis-oriented stress-strain models for FRP-confined concrete," *Engineering Structures*, vol. 29, no. 11, pp. 2968–2986, 2007.
- [30] M. R. Spoelstra and G. Monti, "FRP-confined concrete model," *Journal of Composites for Construction*, vol. 3, no. 3, pp. 143–150, 1999.
- [31] Z. M. Wu, J. J. Zheng, and X. Wu, "Modeling of debonding and fracture process of FRP-strengthened concrete beams via fracture mechanics approach," *Journal of Reinforced Plastics and Composites*, vol. 32, no. 28, pp. 1–13, 2013.
- [32] K. Benzarti, F. Freddi, and M. Frémond, "A damage model to predict the durability of bonded assemblies. Part I: debonding behavior of FRP strengthened concrete structures," *Construction and Building Materials*, vol. 25, no. 2, pp. 547–555, 2011.
- [33] C. Carloni, K. V. Subramaniam, M. Savoia, and C. Mazzotti, "Experimental determination of FRP-concrete cohesive interface properties under fatigue loading," *Composite Structures*, vol. 94, no. 4, pp. 1288–1296, 2012.
- [34] X. Zhang, H. Li, X. Feng et al., "Mechanical behavior of steel-encased concrete filled prefabricated FRP tubes short column under axial compression based on ABAQUS," *Applied Mechanics and Materials*, vol. 256–259, no. 12, pp. 749–753, 2012.
- [35] J. Song, H. Yan, Z. Guo et al., "Nonlinear finite element analysis and simulation of nacelle-cover of MW-class wind turbine based on ABAQUS," *Machine Building & Automation*, vol. 39, no. 6, pp. 122–125, 2010.
- [36] C. E. Todeschini, A. C. Bianchini, and C. E. Kesler, "Behavior of concrete columns reinforced with high strength steels," *ACI Materials Journal*, vol. 61, pp. 701–716, 1964.
- [37] J. F. Chen and Y. Tao, *Finite Element Modeling of FRP-to-Concrete Bond Behavior Using the Concrete Damage Plasticity Theory Combined with a plastic degradation Model*, Springer, Beijing, China, 5th edition, 2010.
- [38] R. Seracino, N. M. Jones, M. S. M. Ali, M. W. Page, and D. J. Oehlers, "Bond strength of near-surface mounted FRP strip-to-concrete joints," *Journal of Composites for Construction*, vol. 11, no. 4, pp. 401–409, 2007.
- [39] R. Seracino, D. J. Oehlers, and S. Raizal, "Towards a generic model of the intermediate crack debonding resistance of plates adhesively bonded to concrete," in *Proceedings of the International Symposium on bond behavior of FRP in Structures, International Institute of FRP in Construction*, 2005.
- [40] G. V. G. Rao, P. Mahajan, and N. Bhatnagar, "Micro-mechanical modeling of machining of FRP composites-cutting force analysis," *Composites Science and Technology*, vol. 67, no. 3-4, pp. 579–593, 2007.
- [41] M. Lesani, M. R. Bahaari, and M. M. Shokrieh, "Numerical investigation of FRP-strengthened tubular T-joints under axial compressive loads," *Composite Structures*, vol. 100, pp. 71–78, 2013.

Research Article

Simulation of Hydraulic Fracture in Unsaturated Soils with High Degree of Saturation

Tielin Chen, Liangyi Zhang, and Dingli Zhang

School of Civil Engineering, Beijing Jiaotong University, Beijing 100044, China

Correspondence should be addressed to Tielin Chen; chentielin@tsinghua.org.cn

Received 27 November 2013; Accepted 13 February 2014; Published 20 March 2014

Academic Editor: Konstantinos I. Tserpes

Copyright © 2014 Tielin Chen et al. This is an open access article distributed under the Creative Commons Attribution License, which permits unrestricted use, distribution, and reproduction in any medium, provided the original work is properly cited.

A numerical simulation approach of hydraulic fracture process, considering the couplings of the stress distribution, the fluid flow of the water-air mixture, the compression and dissolution of air, and the element damage evolution, has been developed to investigate the mechanisms of crack initiation and propagation in porous media during hydraulic fracturing. The concept of homogenized pore fluid has been adopted to represent the water air mixture. A large number of numerical analysis on hydraulic fracturing in clay with incipient injection slot have been carried out to study the mechanism of hydraulic fracturing in unsaturated soil with the characteristic of critical model I type of crack loading using stress intensity factor K_{Ic} . The results provide a numerical picture depicting the mechanisms of crack initiation and propagation during hydraulic fracturing. The numerical results are in good agreement with the experimental results, which confirms the adequacy and the power of the numerical approach.

1. Introduction

Hydraulic fracturing may be defined as the process of creating a fracture or fracture system in a porous medium by injecting a fluid under pressure through a well bore in order to overcome native stresses. Hydraulic fracturing has been used for more than 50 years to enhance the yield of wells recovering oil at great depth. In the recent past, hydraulic fracturing methods have been developed for creating fractures in soils and making existing fractures larger to enhance the mass transfer of contaminants. The fractures created increase the effective permeability and change paths of fluid flow, thus making in situ remediation more effective and economical. Hydraulic fracturing appears to have useful environmental, agricultural and geotechnical applications.

Hydraulic fracturing techniques are equally applicable to both saturated soils and unsaturated soils to improve the flow of water and air, respectively. Earth's land is mostly located in the unsaturated vadose zone above the water table, so the hydraulic fracturing of unsaturated soil has important significance. An unsaturated soil is commonly referred to as a 3-phase system composed of solids (soil particles), water,

and air. The air-water interface (i.e., the contractile skin) warrants inclusion as an additional phase due to its unique and specific properties. The contractile skin interacts with the soil particles in an independent manner and can significantly change the mechanical behavior of an unsaturated soil. The hydraulic fracturing in unsaturated soil is coupling process of stress distribution, water flow, air flow, water-air interact, and damage evolution, which is arguably one of the most challenging problems.

Especially, the propagation processes of hydraulic fractures enveloped in soil layers are difficult to directly observe, and the details of fracture growth inside soil have generally been inferred from indirect measurements. During the past few years, with the rapid development of computing power, numerical tools have become a good option for gaining some insight into the fracturing process. The main numerical methods coupled with fracture models have been used to simulate fracturing process by many researchers, such as the finite element method (FEM) [1], the mesh-free Galerkin method (EFGM) [2], the extended finite element method (XFEM) [3], the boundary element method (BEM) [4], the discrete element method (DEM) [5], and the displacement

discontinuity method (DDM) [6]. The former four are based on the continuum mechanics, the latter two are based on the noncontinuum mechanics.

Hydraulic fracturing is a more complicated process to simulate, as it involves the coupling of four processes [7, 8]: (i) the mechanical deformation induced by the fluid pressure on the fracture surfaces; (ii) the flow of fluid within the fracture; (iii) the fracture propagation; and (iv) the coupling of seepage and stress in the computational domain around the fracture. The simulation of hydraulic fracturing in rock and soil mass, arguably one of the most challenging computational problems in geoen지니어ing, has been the subject of numerous investigations since the pioneering work of Khristianovic and Zheltov [9]. Many numerical methods have been developed for the simulation of hydraulic fracturing [10–14]. Among these methods, FEM method is the most robust one in comparison with BEM, DEM, and DDM which cannot efficiently solve the elasticity-plasticity equation relating the fluid pressure to the fracture opening [15].

Two approaches, namely, the discrete crack model and the smeared crack model were introduced to FEM by Ngo and Scordelis [16] and Rashid [17], respectively. The discrete crack model is aimed at simulating the initiation and propagation of dominant cracks. In contrast, the smeared crack model is based on the idea that many small cracks nucleate which only in a later stage of the loading process link up to form one or more dominant cracks.

The discrete crack approach in its original form has several disadvantages [18]. In the approach, the cracks are forced to propagate along the element boundaries, so that a mesh bias is introduced. Automatic remeshing with sophisticated computer codes allows the mesh bias to be reduced, nevertheless, a computational difficulty, namely, the continuous change in topology, is inherent in the discrete crack approach and is to a certain extent even aggravated by remeshing procedures.

Since each individual crack is not numerically resolved, the smeared crack model captures the deterioration process through a constitutive relation, thus smearing out the cracks over the continuum. It describes a cracked solid by an equivalent anisotropic continuum with degraded material properties in the direction that is normal to the crack orientation and no remeshing is needed. Although the discrete crack approach is sometimes preferred for being based on a mature theory, the smeared crack analysis seems to be more often applicable for usual FEM analyses from engineering practice.

However, many assumptions and simplifications are made in existing numerical studies; for example, fissures need to be placed inside the analyzed domain prior to analysis [19, 20] or the hardening of grout in soil cannot be described [21]. A numerical model for coupled analysis of flow, stress, and damage was proposed to overcome the shortcoming of the placing of preset of fractures [22]. The approach is similar to smeared crack method. The simulated domain is discretized into large numbers of tiny elements to take into account the small local variations of the material properties. At each loading step, the stress and strain in the elements are calculated and examined against the predefined soil strength. Those elements with the stresses above the material's strength

were considered to be isotropically damaged. The material properties of the damaged element are reduced and the width of the fracture in the damaged element can be calculated. This approach can effectively simulate hydraulic fracturing [22–24] in rocks. In this paper, the extension of the approach for rocks to unsaturated soil is attempted so that hydraulic fracturing in unsaturated soil can be numerically simulated.

In this paper, the Biot's consolidation theory is used as a framework that governs the interactions between the soil skeleton and the pore fluid. The concept of homogenized pore fluid is used to describe water-air mixture fluid. The nonlinear constitutive relationship developed by Duncan and Chang is used to describe the soil deformation for its simplicity. The finite element method (FEM) [25] is employed to discretize the Biot equation. The FEM is chosen because it can readily obtain the solutions of boundary value problems on nonconformal domains.

2. The Concept of an Homogenized Pore Fluid

The effective stress equation for saturated soil

$$\sigma = \sigma' + u_w \quad (1)$$

has been shown to be theoretically valid and practically useful for saturated soils.

For unsaturated soil, Bishop (1959) [26] suggested the following rational equation:

$$\sigma' = (\sigma - u_a) + \chi(u_a - u_w), \quad (2)$$

in which σ' = effective stress, σ = total stress, u_a = pore air pressure, u_w = pore water pressure, and χ = factor whose value ranges from 0 to 1 as degree of saturation varies, and is evaluated experimentally.

However, Sparks [27] has shown that χ can assume values greater than unity, and that it can also be negative. Coleman [28], Blight [29], and Matyas and Radharkrishna [30] have shown that the value of χ applicable to volume change behaviour is different from the value of χ applicable to the strength behaviour of the same soil at the same degree of saturation. This fact indicates that (2) is not fundamentally valid and is not likely to be applicable except under limited ranges of conditions and for limited purposes. Sparks [27] employed a model composed of uniform spheres to develop the following effective stress equation for unsaturated soils:

$$\sigma' = \sigma - \xi_1 u_a - \xi_2 u_w + \xi_3 T_c, \quad (3)$$

in which ξ_1, ξ_2, ξ_3 = parameters, whose values depend on the degree of saturation, and T_c = surface tension of water.

Both of the preceding effective stress equations involve difficulties for practical application. The concept of a "homogenized pore fluid" presented by [31] offers a simple alternative to these equations which is applicable for a limited but useful range of conditions.

The pores of an unsaturated soil are filled partly with gas (air) and partly with liquid (water), and the air phase might be present in an unsaturated soil either in a continuous or an occluded (bubbles) form. An important and frequently

encountered special case is that in which the degree of saturation is sufficiently high so that the air bubbles are occluded. This condition prevails at degrees of saturation greater than about 0.85, which is common in many practical cases.

The concept of a ‘‘homogenized pore fluid’’ is that this mixture of gas and liquid can be considered to be an equivalent homogeneous pore fluid which completely fills the pores of the soil. As the proportions of air and water vary (due to flow of water and air, or due to compression of air and dissolution of air), the mechanical properties of the homogenized pore fluid vary. The compressibility of the pore fluid and changes in the degree of saturation due to changes in pore fluid pressure may be calculated using Boyle’s Law and Henry’s Law [32]. The equation of effective stress may be expressed as

$$\sigma' = \sigma - u_m, \quad (4)$$

in which u_m = effective average pore pressure in the homogenized pore fluid.

Sparks [27] and Barden [33] have found that when the air bubbles are occluded, the pore air pressures and the pore water pressures are very nearly equal. There will inevitably be some small differences between these two pressures as a result of surface tension effects, but these small differences become negligible as the magnitude of the pore pressure increases. Sparks has indicated that for occluded bubbles, the assumption that $u_m = u_w$ introduces very small error. Thus, for this condition, the effective stress equation may be written as follows:

$$\sigma' = \sigma - u_w, \quad (5)$$

in which u_w = pore water pressure. Equation (5) has the same form with (1), but the fluid in (5) is water-air mixture fluid which can be compressed, while (1)’s is incompressible water. Equation (5) is used throughout the following developments, and the results are thus applicable to soils containing water and occluded air bubbles.

3. The Compressibility and Permeability of Pore Fluid

The compressibility (β_m) of pore fluid containing air and water is defined as

$$\beta_m = -\frac{d\varepsilon_v}{du_w}, \quad (6)$$

in which $d\varepsilon_v$ = volumetric strain in pore fluid due to change (du_w) in the fluid pressure. By employing Boyle’s Law and Henry’s Law, the compressibility of an air-water mixture can be expressed in a form suggested by [34]

$$\beta_m = s_r \cdot \beta_w + B_{aw} \cdot \frac{(1 - s_r)}{u_a} + B_{aw} \cdot s_r \cdot \frac{h}{u_a}. \quad (7)$$

The first term in the equation accounts for the compressibility of the water; the second term accounts for Boyle’s Law being applied to the free air; and the third term accounts

for the air driven into solution in accordance with Henry’s Law. The B_{aw} pore pressure parameter is equal to 1 as the air bubbles become occluded, where β_m = compressibility of the air-water mixture, h = volumetric coefficient of air solubility (at 20°C, $h = 0.02$), β_w = compressibility of the water, which can be ignored because it is a slight amount, and s_r = degree of saturation.

With the increase in pore pressure pore air dissolved in the water phase, the saturation variation can be calculated as [35]

$$s_r = s_{r0} \frac{u_w + p_a}{p_a + (1 - h) s_{r0} u_w}, \quad (8)$$

where s_{r0} = initial degree of saturation and p_a = atmospheric pressure.

The permeability of unsaturated clays (k'_w) depends on the degree of saturation. The relationship between the permeability of saturated soil (k_w) and its degree of saturation can often be approximated using the following relationship [36, 37]:

$$k'_w = k_w \left(\frac{(s_r - s_{rf})}{(1 - s_{rf})} \right)^\lambda, \quad (9)$$

where s_{rf} is the threshold degree of saturation at which the water in the pores begins to flow freely. For a degree of saturation less than s_{rf} , the water forms a membrane around the particles and does not flow.

4. Field Equation Governing the Consolidation Phenomenon

Chang and Duncan [31] present an extension of Biot’s theory which makes possible finite element analyses of the consolidation of inelastic, unsaturated soil masses. The basic equations governing consolidation may be stated as follows.

(a) Equilibrium equation. Only changes in stresses and body forces are considered. The geostatic body forces are considered as initial stresses. Consider the following:

$$\sigma_{ij,j} + \rho F_i = 0, \quad (10)$$

where σ_{ij} is the total stress tensor, F_i is the body force per unit of mass, and ρ is the density of the mass.

(b) Total stresses are the sum of the effective stress σ'_{ij} and the pore pressure u . Consider the following:

$$\sigma'_{ij} = \sigma_{ij} - u\delta_{ij}. \quad (11)$$

(c) Continuity equation. For a compressible pore fluid, the volume decrease of the soil is the sum of the water expelled plus the decrease in volume of the fluid within. The continuity equation can therefore be written as

$$-v_{i,i} + \dot{w}_{i,i} - \beta_m \dot{u} = 0, \quad (12)$$

where v_i is the superficial velocity vector, w_i is the displacement vector, and β_m is the compressibility of the pore fluid. ‘‘ $\dot{\cdot}$ ’’ indicates partial differentiation with respect to time.

(d) The effective stress-strain relationship may be expressed in a general form as follows:

$$\sigma'_{ij} = C_{ijkl}\varepsilon_{kl}, \quad (13)$$

where ε_{kl} is the strain tensor, which is related to the displacements through

$$\varepsilon_{kl} = \frac{1}{2} (w_{k,l} + w_{l,k}), \quad (14)$$

where C_{ijkl} is the tensor relating stress and strain.

(e) Darcy's Law. It is assumed that the flow of water is governed by Darcy's Law as follows:

$$v_i = k_{ij} (u_{,j} + \rho_f F_j), \quad (15)$$

where k_{ij} is the permeability tensor, F_j is the body force per unit of fluid, and ρ_f is the density of the fluid.

To define the problem, both displacement and flow boundary conditions must be specified. For the displacement boundary conditions, it is assumed that part of the boundary surface S_T is subjected to known applied tractions, \bar{T}_i , while the remainder of the surface S_D is subjected to specified displacements, \bar{W}_i . For the flow boundary condition, it is assumed that part of the boundary surface S_q is subjected to a specified flow velocity, \bar{q} , while the remainder of the surface S_u is subjected to known pore pressures, \bar{u} . The boundary conditions may be written in the following form:

$$\begin{aligned} w_i &= \bar{w}_i & \text{on } S_D \text{ for } t \geq 0, \\ \sigma_{ij}n_j &= \bar{T}_i & \text{on } S_T \text{ for } t \geq 0, \\ u &= \bar{u} & \text{on } S_u \text{ for } t > 0, \\ v_i n_i &= \bar{q} & \text{on } S_q \text{ for } t > 0, \end{aligned} \quad (16)$$

where n_i is the normal vector to the boundary surface and $(-)$ indicates a prescribed quantity.

5. Constitutive Equation

The nonlinear elastic model proposed by Duncan and Chang is used as the constitutive relationship for solids. The main features of the model are summarized here. The tangential Young's modulus can be expressed as

$$E_t = K P_a \left(\frac{\sigma_3}{P_a} \right)^n \left[1 - \frac{R_f (1 - \sin \varphi) (\sigma_1 - \sigma_3)}{2c \cos \varphi + 2\sigma_3 \sin \varphi} \right]^2. \quad (17)$$

The elastic Young's modulus for unloading and reloading is

$$E_{ur} = K_{ur} P_a \left(\frac{\sigma_3}{P_a} \right)^n. \quad (18)$$

The tangential volumetric modulus is described by

$$B = K_b P_a \left(\frac{\sigma_3}{P_a} \right)^n, \quad (19)$$

where c is cohesion, φ is internal friction angle, p_a is atmospheric pressure, K , K_b , K_{ur} are initial modulus values, m and n are parameters, and R_f is a failure ratio that is defined as

$$R_f = \frac{(\sigma_1 - \sigma_3)_f}{(\sigma_1 - \sigma_3)_{ult}}, \quad (20)$$

where $(\sigma_1 - \sigma_3)_f$ is the principal stress difference when the soil is assumed to be in failure and $(\sigma_1 - \sigma_3)_{ult}$ is the asymptotic value of the principal stress difference.

Eight parameters of the constitutive model c , φ , K , K_b , K_{ur} , m , n , and R_f can be determined by conventional triaxial tests.

6. Mechanics of Fracture Initiation and Propagation

The tensile and shear failures are both considered here. An element is considered to be fractured in the tension mode if its minor effective principal stress exceeds the tensile strength of the element as follows:

$$\sigma'_3 \leq -\sigma'_t, \quad (21)$$

where σ'_3 is the minor effective principal stress and σ'_t is the tensile failure strength of the element. Compression is assumed to be positive.

An element is considered to be fractured in the shear mode if the shear stress satisfied the Mohr-Coulomb failure criterion as follows:

$$F = (c' + \sigma' \tan \phi') - \tau, \quad (22)$$

where τ is the shear stress, σ' the effective normal stress, c' the effective stress cohesion intercept, and ϕ' the effective stress angle of friction or shearing resistance.

Once an element is judged to be fractured, that is, mesh element damaged, many smeared cracks occur in this element and the stiffness of the soil is reduced.

The stiffness of the fracture can be described by [38]

$$K' = K e^{-b/\xi}, \quad (23)$$

where K is the initial modulus of the soil just prior to the occurrence of cracks, b is the total width of smeared cracks in an element (m), and ξ is a scaling parameter indicating the amount of deformation needed to change the stiffness by a factor of e . K_b , K_{ur} also follow the formula. The total width of smeared cracks is the difference between the widths of the element after and before cracking. The value of ξ is related to the material types and is 10^{-4} in this investigation.

The permeability is not a constant and is a function of stresses because the fracture aperture is most likely to change as the stress conditions vary. The effect of stresses on permeability can be expressed as [22]

$$k(\sigma, u_w) = \omega_1 k'_w \exp \left(-\omega_3 \left(\frac{\sigma_{ii}}{3} - \omega_2 u_w \right) \right), \quad (24)$$

where ω_1 is the damage factor of permeability reflecting the increase in permeability induced by damage of soil, ω_2 and ω_3 are coupling parameters reflecting the influence of stress on the coefficient of permeability.

7. The Simulation of K_{Ic} of Unsaturated Soil during Hydraulic Fracture

The critical stress at the onset of propagation depended on the length of the initial slot. The strength was characterized by the stress intensity factor K_I [39, 40] as follows:

$$K_I = \sigma_c \sqrt{\pi a} f(b), \quad (25)$$

where σ_c is far-field stress, a is the half-length of the fracture, and $f(b)$ is some function of the geometry of the fracture and enveloping material.

A basic assumption is that propagation under dilation, or mode I, loading occurs when the stress intensity equals a critical value K_{Ic} . The magnitude of K_{Ic} is commonly regarded as a material property characterizing the resistance of a material to mode I fracturing; here it is called fracture toughness.

Fracture toughness has been applied to prediction of the onset of hydraulic fracturing of soil [41–43], but the validity of that application needs to be examined further.

The stress intensity factor of soil can be defined as follows:

$$K_I = P_d \sqrt{\pi a} f(b). \quad (26)$$

Driving pressure P_d is the difference between the fluid pressure p within a fracture and the confining stress σ_n acting normal to the fracture as follows:

$$P_d = p - \sigma_n. \quad (27)$$

The function $f(b)$ in (26) is equal to unity if the fracture is straight, loaded uniformly, and embedded in a homogeneous, isotropic, linearly-elastic material, and it can be taken as a correction factor for practical constraints such as finite sample size or slots intersected by a hole. Singh [37] have given expressions for $f(b)$ for a straight slot containing an axial hole and for a straight slot embedded in a rectangular sample of finite size. These conditions represent corrections of <5% for the geometries and dimensions used in this work, so $f(b)$ will be set to unity. So, fracture toughness will be determined using the critical driving pressure P_{df} and the half-length of the initial slot a_i as

$$K_{Ic} = P_{df} \sqrt{\pi a_i}. \quad (28)$$

The propagation of hydraulic fractures in soil was studied in the laboratory by glycerine injected at a constant rate into rectangular samples of silty clay confined in a triaxial cell [41–43]. In order to examine the validity of the application, a large number of numerical analyses on hydraulic fracturing in clay with incipient injection slot have been carried out to investigate the relation between K_{Ic} and a_i . And the results are compared with experimental results [41–43].

A simulation domain $0.1 \text{ m} \times 0.39 \text{ m}$ with incipient injection slot is the same with the test [41–43]. The soil mass within the simulated area is under the plane strain boundary condition, as shown in Figure 1.

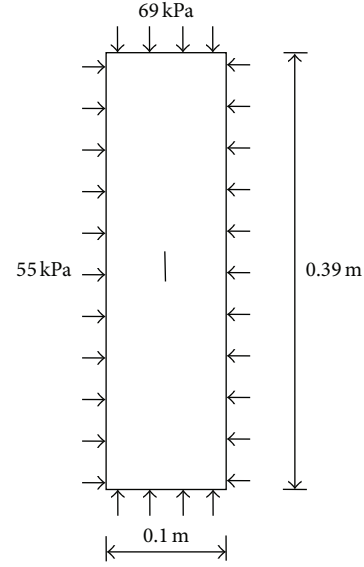


FIGURE 1: The simulation model.

TABLE 1: Input material properties parameters for numerical models.

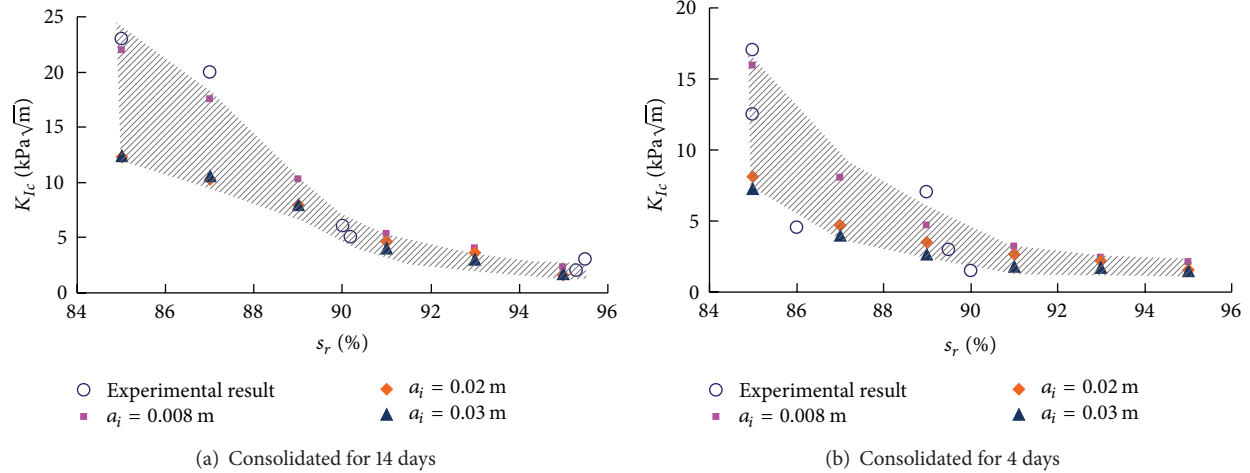
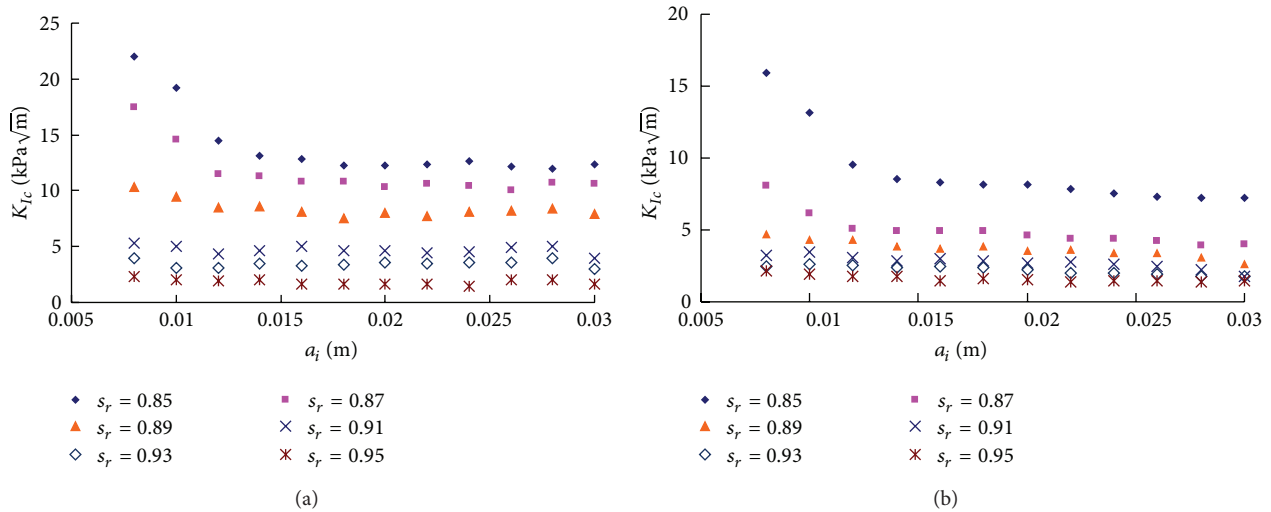
Index	Value
K_0	120
K_{b0}	204
K_{ur0}	240
m	0.5
n	0.6
R_f	0.95
c	15 kPa
φ	25°
ξ	10^{-4}
λ	3
S_{rf}	0.3
k_w	$5e - 6 \text{ cm/s}$
α	3
ω_1	20
ω_2	0.1
ω_3	0.05

The relationship between initial modulus values and saturation can be obtained from the experimental results [41] as follows:

$$\begin{aligned} K &= K_0 - 5K_0 (s_r - 0.85), \\ K_b &= K_{b0} - 5K_{b0} (s_r - 0.85), \\ K_{ur} &= K_{ur0} - 5K_{ur0} (s_r - 0.85). \end{aligned} \quad (29)$$

The input parameters for these simulations are tabulated in Table 1.

Six cases of the initial saturation from 0.85 to 0.95 at interval 0.02, 12 cases of length of the starter slot from 0.008 m to 0.03 m at interval 0.002 m, 2 cases of consolidation durations of 4 days and 14 days are considered. A flow rate of

FIGURE 2: K_{Ic} as a function of s_r .FIGURE 3: K_{Ic} as a function of a_i .

$0.033 \text{ cm}^3/\text{s}$ which was the same with the test was used for all the simulations described below.

The numerical analysis can capture details of the K_{Ic} at various saturation in the range $>85\%$. The result is shown in Figures 2 and 3. The laboratory records [42] and the simulations in Figures 2 and 3 show a remarkable similarity. The simulations can accommodate K_{Ic} changes caused by the saturation and the length of start slot.

Both saturation and duration of consolidation had a marked effect on K_{Ic} . Among samples consolidated for 14 days, for $a_i = 0.008 \text{ m}$, K_{Ic} is greatest ($22 \text{ kPa}\sqrt{\text{m}}$) at $s_r = 0.85$. The fracture toughness decreases abruptly to $2.33 \text{ kPa}\sqrt{\text{m}}$ as s_r increases from 0.85 to 0.95. For $a_i = 0.03 \text{ m}$, the fracture toughness decreases abruptly from $12.4 \text{ kPa}\sqrt{\text{m}}$ to $1.68 \text{ kPa}\sqrt{\text{m}}$. The sharp change in K_{Ic} occurs in the range $0.85 \leq s_r < 0.91$. A slight decrease in K_{Ic} occurs with further increase in s_r , although the decrease is small and K_{Ic} is almost independent of s_r in the range 0.91–0.95.

Consolidation appears to toughen the clay, according to simulation results of samples consolidated for 4 days and 14 days under a static pressure of 69 kPa. The K_{Ic} of the samples consolidated for 14 days is greater by $6.1 \text{ kPa}\sqrt{\text{m}}$ than the K_{Ic} of 4 days consolidated samples at similar $s_r = 0.85$ and $a_i = 0.008 \text{ m}$. With the increase of saturation, the difference of K_{Ic} is reduced, which means that the tough effect of consolidation is weakened.

The forms of the experimental and simulation curves in Figures 2 and 4 are similar; they all show K_{Ic} decreasing markedly over a few percent of s_r .

Fracture toughness appears to be independent of the length of the starter slot in the range $s_r > 0.91$ and to be dependent of the length of the starter slot in the range $0.85 < s_r < 0.91$ under the conditions used here. Increase of the length of the starter slot can decrease this dependence.

As we all know, negative pore pressure can affect the strength of the soil. The area of negative pore pressure zone

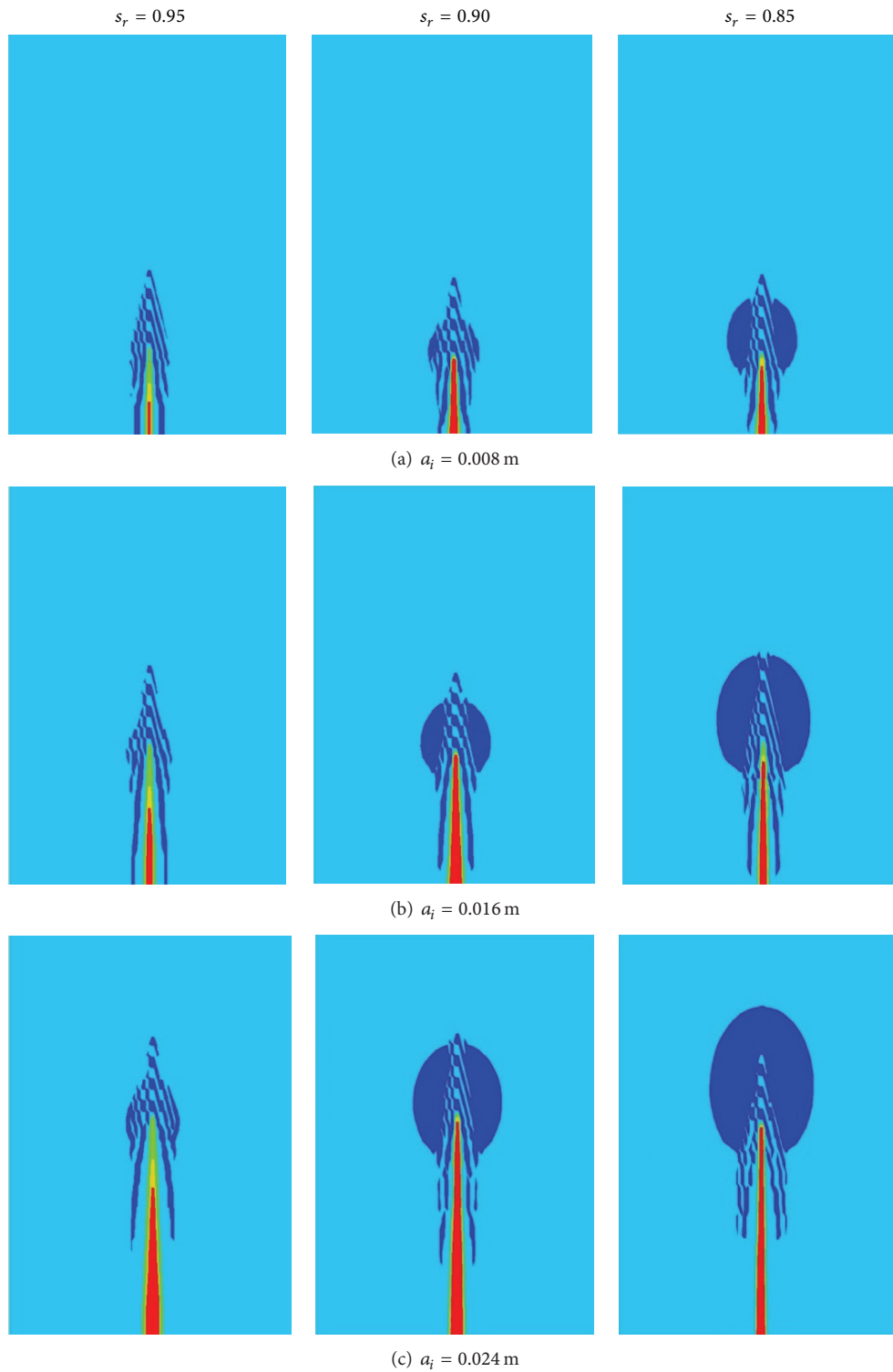


FIGURE 4: Negative pore pressure zone (dark blue color) at different saturations arranged in columns.

(NPZ) may explain the dependence between fracture toughness and saturation and length of starter slot. Figure 4 shows the NPZ before fracture tip. Only half of the simulated domain is displayed because of symmetry. When the saturation is higher (0.95), the area of NPZ and the length of the starter

slot are almost independent of each other (Figure 4). When the saturation is lower (0.85), the length of the starter slot has a greater impact on the area of NPZ (Figure 4).

Fracture toughness has been introduced as a parameter that could possibly be used to indicate the onset of

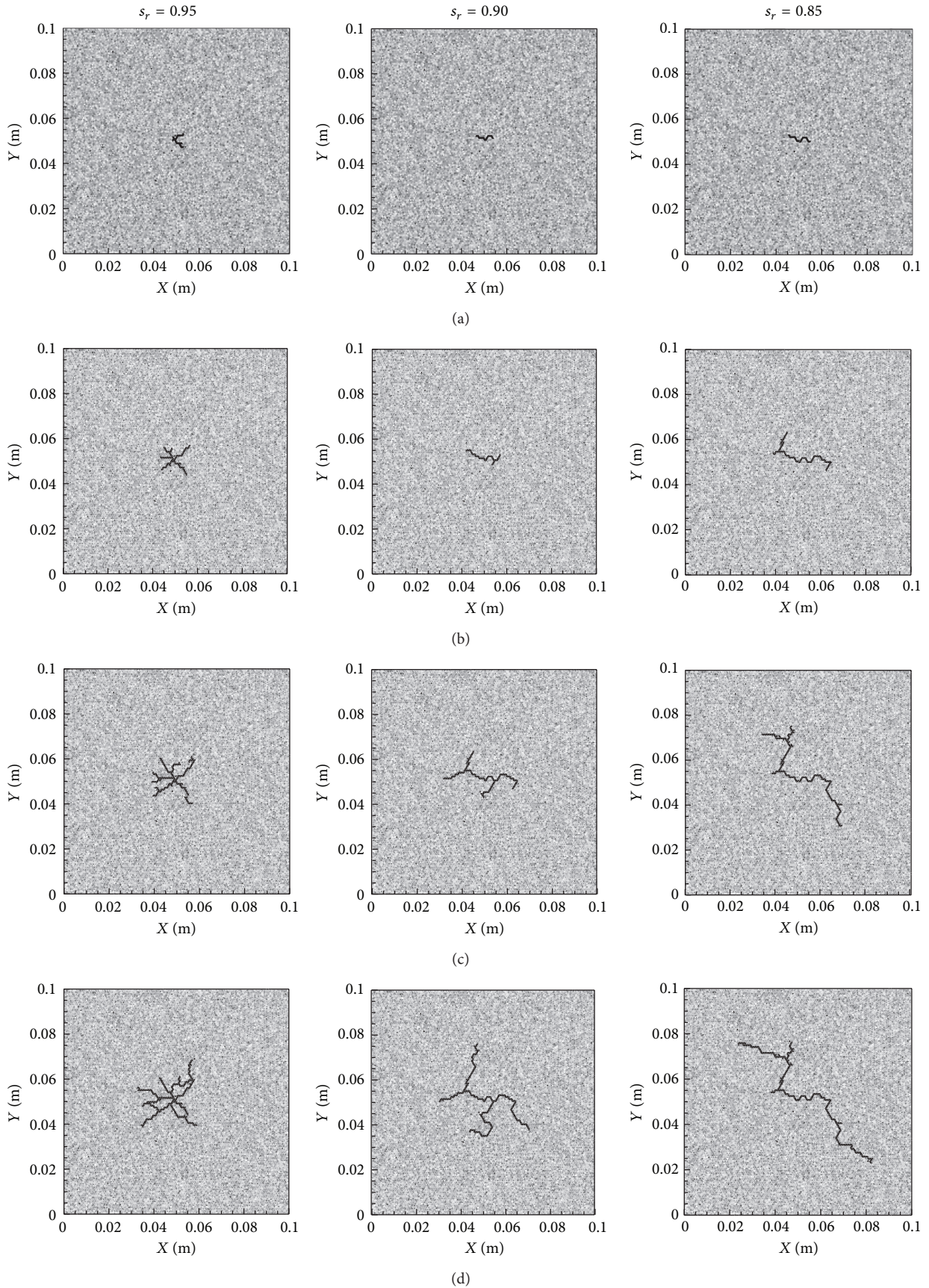


FIGURE 5: The simulated fracture propagation process at different saturations arranged in columns.

propagation. If it is a material property, fracture toughness must be independent of slot length. It can depend on saturation, however, although the dependence is expected to be similar to other properties that also depend on saturation.

From the simulation results, the K_{Ic} depends on the length of the initial slot and the saturation of the soil. It is apparent from Figures 2 and 3 that the value of K_{Ic} varies over more than a factor of ten, so that some methods of anticipating K_{Ic} will be required in order for this to be a useful predictor of the onset of propagation.

8. The Simulation of Hydraulic Fracture in Heterogeneity Unsaturated Soil

Actual soil is often heterogeneous, in order to demonstrate the effectiveness of this approach to simulate hydraulic fracture in heterogeneous unsaturated soil, three simulations are carried out. A simulation domain $0.1\text{ m} \times 0.1\text{ m}$ with initial injection tiny holes in the center is considered here. All boundaries are fixed displacement, undrained boundary. The distribution of heterogeneity remains the same and the saturation varies from one sample to another.

To take the heterogeneity into account, different material properties for different elements are assigned randomly following the Weibull distribution as follows:

$$\psi = \frac{\vartheta}{\eta_0} \left(\frac{\eta}{\eta_0} \right)^{\vartheta-1} \exp \left[- \left(\frac{\eta}{\eta_0} \right)^{\vartheta} \right], \quad (30)$$

where η is the variable representing a certain material property, η_0 is the mean value of the corresponding material property, and ϑ is the homogeneity index. ϑ is a parameter defined by the shape of the distribution function that describes the degree of material heterogeneity. A larger ϑ implies a more homogeneous material and vice versa. Therefore, the parameter ϑ is called the homogeneity index. The higher the value of the homogeneity index ϑ , the greater the number of elements with properties close to η_0 . In the study, K_0 , K_{b0} , K_{ur0} , c , φ are accorded to the Weibull distribution by $\vartheta = 3$.

Figure 5 shows the simulated fracture propagation process. Each column is a simulation result at a saturation. Saturation has a significant impact on fracture propagation and distribution. When saturation is high ($s_r = 0.95$), numerous cracks gathered near the initial hole and cross-cuttings occur between the cracks. The lower the saturation, the farther away the cracks spread from the initial hole and the fewer the number of cracks there is.

Hydraulic fracturing appears to have useful environmental and geotechnical applications, but the details of fracture morphology and propagation in soil are poorly known because the propagation processes of hydraulic fractures enveloped in soil layers are difficult to directly observe. The simulation results may provide some insight.

9. Conclusions

A numerical simulation approach of hydraulic fracture process of unsaturated soil with high saturation has been presented. The approach can consider the coupling of stress

distribution, water-air mixture fluid flow, compression and dissolution of air, and element damage evolution. A key to the approach is the concept of homogenized pore fluid which is that the mixture of gas and liquid can be considered to be an equivalent homogeneous pore fluid which completely fills the pores of the soil. As the proportions of air and water vary (due to flow of water and air, or due to compression of air and dissolution of air), the mechanical properties of the homogenized pore fluid vary correspondingly.

A large number of numerical analyses on hydraulic fracturing in unsaturated soil with incipient injection slot have been carried out to study the characteristics of critical stress intensity factor K_{Ic} of model I type of crack loading. The numerical results were shown to be in good agreement with the experimental results. The propagation of hydraulic fracturing in unsaturated soil has been simulated also. The simulation results have indicated that saturation is a fundamental constraint on the hydraulic fracturing in clay.

Although this study is a preliminary attempt and needs further development, the simulation results may provide some insight of the crack initiation and propagation mechanisms during hydrofracturing of unsaturated soil with high saturation.

Conflict of Interests

The authors declare that there is no conflict of interests regarding the publication of this paper.

Acknowledgments

The authors gratefully acknowledge the financial support of the National Basic Research Program of China under Grant 2010CB732100 and the National Natural Science Foundation of China under Grant 51278041.

References

- [1] R. S. Barsoum, "Further application of quadratic isoparametric finite elements to linear fracture mechanics of plate bending and general shells," *International Journal of Fracture*, vol. 11, no. 1, pp. 167–169, 1975.
- [2] B. N. Rao and S. Rahman, "Efficient meshless method for fracture analysis of cracks," *Computational Mechanics*, vol. 26, no. 4, pp. 398–408, 2000.
- [3] B. Lecampion, "An extended finite element method for hydraulic fracture problems," *Communications in Numerical Methods in Engineering*, vol. 25, no. 2, pp. 121–133, 2009.
- [4] A. Frangi, G. Novati, R. Springhetti, and M. Rovizzi, "3D fracture analysis by the symmetric Galerkin BEM," *Computational Mechanics*, vol. 28, no. 3–4, pp. 220–232, 2002.
- [5] K.-B. Min and L. Jing, "Numerical determination of the equivalent elastic compliance tensor for fractured rock masses using the distinct element method," *International Journal of Rock Mechanics and Mining Sciences*, vol. 40, no. 6, pp. 795–816, 2003.
- [6] X. C. Tan, S. Q. Kou, and P.-A. Lindqvist, "Application of the DDM and fracture mechanics model on the simulation of rock breakage by mechanical tools," *Engineering Geology*, vol. 49, no. 3–4, pp. 277–284, 1998.

- [7] J. Adachi, E. Siebrits, A. Peirce, and J. Desroches, "Computer simulation of hydraulic fractures," *International Journal of Rock Mechanics and Mining Sciences*, vol. 44, no. 5, pp. 739–757, 2007.
- [8] A. P. Bunger, E. Detournay, and D. I. Garagash, "Toughness-dominated hydraulic fracture with leak-off," *International Journal of Fracture*, vol. 134, no. 2, pp. 175–190, 2005.
- [9] S. A. Khristianovic and Y. P. Zheltov, "Formation of vertical fractures by means of highly viscous fluids," in *Proceedings of the 4th World petroleum congress*, vol. 2, pp. 579–586, Rome, Italy, 1955.
- [10] A. P. Peirce and E. Siebrits, "A dual mesh multigrid preconditioner for the efficient solution of hydraulically driven fracture problems," *International Journal for Numerical Methods in Engineering*, vol. 63, no. 13, pp. 1797–1823, 2005.
- [11] B. Lecampion and E. Detournay, "An implicit algorithm for the propagation of a hydraulic fracture with a fluid lag," *Computer Methods in Applied Mechanics and Engineering*, vol. 196, no. 49–52, pp. 4863–4880, 2007.
- [12] L. Jing, Y. Ma, and Z. Fang, "Modeling of fluid flow and solid deformation for fractured rocks with discontinuous deformation analysis (DDA) method," *International Journal of Rock Mechanics and Mining Sciences*, vol. 38, no. 3, pp. 343–355, 2001.
- [13] K. I.-I. Eshiet, *Modelling of hydraulic fracturing and its engineering application [Ph.D. thesis]*, University of Leeds, 2012.
- [14] Z. P. Bazant and H. Ohtsubo, "Geothermal heat extraction by water circulation through a large crack in dry hot rock mass," *International Journal for Numerical and Analytical Methods in Geomechanics*, vol. 2, no. 4, pp. 317–327, 1978.
- [15] M. B. Dusseault and J. McLennan, "Massive multi-stage hydraulic fracturing: where are we?" 2011, ARMA, http://www.arma-rocks.org/documents/newsletters/2011.01_02_winter.pdf.
- [16] D. Ngo and A. C. Scordelis, "Finite element analysis of reinforced concrete beams," *Journal of the American Concrete Institute*, vol. 64, pp. 152–163, 1967.
- [17] Y. R. Rashid, "Analysis of reinforced concrete pressure vessels," *Nuclear Engineering and Design*, vol. 7, pp. 334–344, 1968.
- [18] R. de Borst, J. J. C. Remmers, A. Needleman, and M.-A. Abellan, "Discrete vs smeared crack models for concrete fracture: bridging the gap," *International Journal for Numerical and Analytical Methods in Geomechanics*, vol. 28, no. 7–8, pp. 583–607, 2004.
- [19] B. Carrier and S. Granet, "Numerical modeling of hydraulic fracture problem in permeable medium using cohesive zone model," *Engineering Fracture Mechanics*, vol. 79, pp. 312–328, 2012.
- [20] C. Wisser, C. E. Augarde, and H. J. Burd, "Numerical modelling of compensation grouting above shallow tunnels," *International Journal for Numerical and Analytical Methods in Geomechanics*, vol. 29, no. 5, pp. 443–471, 2005.
- [21] M. J. Yang, Z. Q. Yue, P. K. K. Lee, B. Su, and L. G. Tham, "Prediction of grout penetration in fractured rocks by numerical simulation," *Canadian Geotechnical Journal*, vol. 39, no. 6, pp. 1384–1394, 2002.
- [22] C. A. Tang, L. G. Tham, P. K. K. Lee, T. H. Yang, and L. C. Li, "Coupled analysis of flow, stress and damage (FSD) in rock failure," *International Journal of Rock Mechanics and Mining Sciences*, vol. 39, no. 4, pp. 477–489, 2002.
- [23] S. Y. Wang, L. Sun, A. S. K. Au, T. H. Yang, and C. A. Tang, "2D-numerical analysis of hydraulic fracturing in heterogeneous geo-materials," *Construction and Building Materials*, vol. 23, no. 6, pp. 2196–2206, 2009.
- [24] W. Peng, M. Xian-biao, L. Jin-bin, and D. Chun-zhi, "Study of the borehole hydraulic fracturing and the principle of gas seepage in the coal seam," in *Proceedings of the 6th International Conference on Mining Science and Technology (ICMST '09)*, pp. 1561–1573, October 2009.
- [25] K. J. Bathe, *Finite Element Procedures*, Prentice-Hall, Englewood Cliffs, NJ, USA, 1996.
- [26] A. W. Bishop, "The principle of effective stress," *Teknisk Ukeblad, Norway*, vol. 106, no. 39, pp. 859–863, 1959.
- [27] A. D. W. Sparks, "Theoretical considerations of stress equations for partly saturated soils," in *Proceedings of the 3rd Regular Conference for Africa on Soil Mechanics and Foundation Engineering*, Salisbury, Southern Rhodesia, 1963.
- [28] J. D. Coleman, "Stress/strain relations for partly saturated soil," *Geotechnique*, vol. 12, pp. 348–350, 1962.
- [29] G. E. Blight, "A study of effective stress for volume change," in *Proceedings of the Symposium on Moisture Equilibrium and Moisture Changes in Soils Beneath Covered Areas*, pp. 259–269, Butterworths, Australia, 1965.
- [30] E. L. Matyas and H. Radharkrishna, "Volume change characteristics of partially saturated soils," *Geotechnique*, vol. 18, no. 4, pp. 432–448, 1968.
- [31] C. S. Chang and J. M. Duncan, "Consolidation analysis for partly saturated clay by using an elastic-plastic effective stress-strain model," *International Journal for Numerical & Analytical Methods in Geomechanics*, vol. 7, no. 1, pp. 39–55, 1983.
- [32] A. W. Skempton and A. W. Bishop, "Building materials, their elasticity and inelasticity," in *Soils*, North Holland, Amsterdam, The Netherlands, 1954.
- [33] L. Barden, "Consolidation of compacted and unsaturated clays," *Geotechnique*, vol. 15, no. 3, pp. 267–286, 1965.
- [34] D. G. Fredlund, "Density and compressibility characteristic of air-water mixtures," *Canadian Geotechnical Journal*, vol. 13, no. 4, pp. 386–396, 1976.
- [35] J. W. Hilf, "Estimating construction pore pressure in rolled earth dams," in *Proceedings of the 2nd International Conference on Soil Mechanics and Foundation Engineering*, pp. 234–240, Rotterdam, The Netherlands, 1948.
- [36] C. S. Chang, *Analysis of consolidation of earth and rockfill dams [Ph.D. thesis]*, University of California, Berkeley, Calif, USA, 1976.
- [37] R. Singh, "Unsteady and unsaturated flow in soils in two dimensions," Tech. Rep. 54, Department of Civil Engineering, Stanford University, 1965.
- [38] R. Gothäll and H. Stille, "Fracture-fracture interaction during grouting," *Tunnelling and Underground Space Technology*, vol. 25, no. 3, pp. 199–204, 2010.
- [39] G. R. Irwin, "Analysis of stresses and strains near the end of a crack traversing a plate," *Journal of Applied Mechanics*, vol. 24, pp. 361–364, 1957.
- [40] H. Tada, P. C. Paris, and G. R. Irwin, *The Stress Analysis of Cracks Handbook*, Paris Productions, 2nd edition, 1985.
- [41] L. C. Murdoch, "Hydraulic fracturing of soil during laboratory experiments—1. Methods and observations," *Geotechnique*, vol. 43, no. 2, pp. 255–265, 1993.
- [42] L. C. Murdoch, "Hydraulic fracturing of soil during laboratory experiments—2. Propagation," *Geotechnique*, vol. 43, no. 2, pp. 267–276, 1993.
- [43] L. C. Murdoch, "Hydraulic fracturing of soil during laboratory experiments—3. Theoretical analysis," *Geotechnique*, vol. 43, no. 2, pp. 277–287, 1993.

Research Article

Application of T_{33} -Stress to Predict the Lower Bound Fracture Toughness for Increasing the Test Specimen Thickness in the Transition Temperature Region

Kai Lu¹ and Toshiyuki Meshii²

¹ Graduate School of Engineering, University of Fukui, 3-9-1 Bunkyo, Fukui-shi, Fukui 910-8507, Japan

² Faculty of Engineering, University of Fukui, 3-9-1 Bunkyo, Fukui-shi, Fukui 910-8507, Japan

Correspondence should be addressed to Toshiyuki Meshii; meshii@u-fukui.ac.jp

Received 28 December 2013; Accepted 23 January 2014; Published 13 March 2014

Academic Editor: Filippo Berto

Copyright © 2014 K. Lu and T. Meshii. This is an open access article distributed under the Creative Commons Attribution License, which permits unrestricted use, distribution, and reproduction in any medium, provided the original work is properly cited.

This work was motivated by the fact that although fracture toughness of a material in the ductile-to-brittle transition temperature region J_c exhibits the test specimen thickness (TST) effect on J_c , frequently described as $J_c \propto (\text{TST})^{-1/2}$, experiences a contradiction that is deduced from this empirical formulation; that is, $J_c = 0$ for large TST. On the other hand, our previous works have showed that the TST effect on J_c could be explained as a difference in the out-of-plane constraint and correlated with the out-of-plane T_{33} -stress. Thus, in this work, the TST effect on J_c for the decommissioned Shoreham reactor vessel steel A533B was demonstrated from the standpoint of out-of-plane constraint. The results validated that T_{33} was effective for describing the J_c decreasing tendency. Because the Shoreham data included a lower bound J_c for increasing TST, a new finding was made that T_{33} successfully predicted the lower bound of J_c with increasing TST. This lower bound J_c prediction with T_{33} conquered the contradiction that the empirical $J_c \propto (\text{TST})^{-1/2}$ predicts $J_c = 0$ for large TST.

1. Introduction

The cleavage fracture toughness J_c of a material in the ductile-to-brittle transition (DBT) temperature region, which is important in the assessment of aging steel structures and reactor pressure vessels, has been known to exhibit test specimen size effects, even when tested using a standardized specimen [1–9]. For example, J_c obtained using a shallow cracked specimen exhibits a higher value than that obtained using a deep cracked specimen. Another known size effect is the test specimen thickness (TST) effect on J_c , hereafter abbreviated as the TST effect on J_c , which is described as $J_c \propto B^{(-1/2)}$ ($B \equiv \text{TST}$) [2, 10]. The two most physically logical explanations in general are the statistical weakest link (SWL) size effect and the loss of the crack-tip constraint [2]. Both explanations lead to an increasing toughness with decreasing TST. The difference in J_c obtained with a different planar specimen configuration, including the crack depth [4], has been explained as the differences in the crack-tip constraint or the hydrostatic stress triaxiality, which J fails to describe [3, 5–9].

However, the TST effect has been explained in terms of the SWL size effect being dominant [6, 11–13], even though J_c does not decrease indefinitely with thickness [6], which contradicts the prediction from the SWL size effect [2].

Based on the above, the authors believed that the contribution of the crack-tip constraint to the TST effect on J_c could be demonstrated if the TST effect (especially the bounded nature of J_c with increasing TST) was demonstrated using a series of nonstandard test specimens whose planar configurations are identical but whose thickness-to-width ratios, B/W , are changed to realize different thickness specimens and if the test results were reproduced using finite element analysis (FEA). This use of nonstandard test specimens was prompted by the inability to predict the bounded nature of J_c using the SWL formulation. This prediction was thought to be enabled by these specimens because the out-of-plane crack-tip constraint will increase and saturate with increasing B/W , but the in-plane crack-tip constraint will not change. The fracture toughness tests for a series of nonstandard compact-tension (CT) and three-point-bend (3PB, also named as

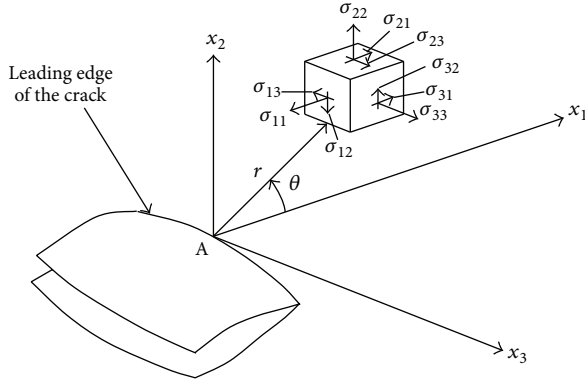


FIGURE 1: Three-dimensional coordinate system for the region along the crack front.

SE(B) specimen) specimens for 0.55% carbon steel S55C [14–16] and 0.40% carbon chromium molybdenum steel SCM440 [17] validated the noticeable contribution of the out-of-plane crack-tip constraint to the TST effects on J_c , and the constraint parameter T_{33} -stress was demonstrated to be effective for correlating this out-of-plane crack-tip constraint with the TST effects on J_c [14–17]. These results indicated a possibility of correlating the fracture toughness of a test specimen and the crack-like flaws in the structure more accurately by considering T_{33} .

This work is an extension of our previous studies regarding the point that the contribution of the out-of-plane crack-tip constraint to the TST effect on J_c was demonstrated for the decommissioned Shoreham reactor vessel steel, ASTM A533 Grade B Class 1 (A533B) [1], which is experimentally formulated as J_c [N/mm] = $2.3 \cdot |T_{33}|^{0.6}$ ($80 \leq |T_{33}| \leq 320$ MPa) to describe the J_c decreasing tendency for increasing TST. Because the Shoreham data included a lower bound of J_c for increasing TST, a new finding was made that T_{33} successfully predicted the lower bound J_c with increasing TST. This lower bound J_c prediction with T_{33} resolves the contradiction that the empirical $J_c \propto (\text{TST})^{-1/2}$ predicts $J_c = 0$ for large TST.

2. TST Effect on J_c Described by the T_{33} -Stress

2.1. T-Stress. In an isotropic linear elastic body containing a crack subjected to symmetric (mode I) loading, the leading two terms in a series expansion of the stress field very near to the crack front are [18]

$$\begin{Bmatrix} \sigma_{11} \\ \sigma_{22} \\ \sigma_{33} \\ \sigma_{12} \\ \sigma_{23} \\ \sigma_{31} \end{Bmatrix} = \frac{K_I}{\sqrt{2\pi r}} \begin{Bmatrix} \cos \frac{\theta}{2} \left(1 - \sin \frac{\theta}{2} \sin \frac{3\theta}{2} \right) \\ \cos \frac{\theta}{2} \left(1 + \sin \frac{\theta}{2} \sin \frac{3\theta}{2} \right) \\ 2\nu \cos \frac{\theta}{2} \\ \sin \frac{\theta}{2} \cos \frac{\theta}{2} \cos \frac{3\theta}{2} \\ 0 \\ 0 \end{Bmatrix} + \begin{Bmatrix} T_{11} \\ 0 \\ T_{33} \\ 0 \\ 0 \\ 0 \end{Bmatrix}, \quad (1)$$

$$T_{33} = E\varepsilon_{33} + \nu T_{11},$$

where r and θ are the in-plane polar coordinates of the plane normal to the crack front, as shown in Figure 1, and K_I is the local mode I stress intensity factor (SIF) at location A. Here x_1 is the direction formed by the intersection of the plane normal to the crack front and the crack plane. The terms T_{11} and T_{33} are the amplitudes of the second-order terms in the three-dimensional series expansion of the crack front stress field in the x_1 and x_3 directions, respectively.

2.2. TST Effect on J_c Described by T_{33} -Stress. In our previous works [14, 15, 17], the following relationships were obtained for 0.55% carbon steel S55C [14, 15] and 0.40% carbon chromium molybdenum steel SCM440 [17] with both CT and 3PB specimens:

$$\begin{cases} J_c \text{ [N/mm]} = 2.6 \text{ [N}^{1/2}\text{]} \cdot |T_{33}|^{1/2} \\ \text{(CT, } 60 \leq |T_{33}| \leq 180 \text{ MPa)} \\ J_c \text{ [N/mm]} = 3.1 \text{ [N}^{1/2}\text{]} \cdot |T_{33}|^{1/2} \\ \text{(3PB, } 80 \leq |T_{33}| \leq 160 \text{ MPa)}, \end{cases} \quad \text{S55C at } 20^\circ\text{C:}$$

$$\begin{cases} J_c \text{ [N/mm]} = 4.6 \text{ [N}^{1/2}\text{]} \cdot |T_{33}|^{1/2} \\ \text{(CT, } 120 \leq |T_{33}| \leq 260 \text{ MPa)} \\ J_c \text{ [N/mm]} = 4.8 \text{ [N}^{1/2}\text{]} \cdot |T_{33}|^{1/2} \\ \text{(3PB, } 100 \leq |T_{33}| \leq 210 \text{ MPa)}. \end{cases} \quad \text{SCM440 at } -50^\circ\text{C:} \quad (2)$$

The object of these works was to demonstrate that the out-of-plane crack-tip constraint has a noticeable contribution to the TST effect on J_c and that the TST effect can be correlated with a mechanical parameter T_{33} (expressing the out-of-plane crack-tip constraint).

Because the bounded nature of J_c with increasing TST could not be realized with the tested specimens of thickness-to-width ratios $B/W = 0.25, 0.4, \text{ and } 0.5$, the tested results with large B/W were searched in the published documents, and the decommissioned Shoreham reactor vessel steel data [1] were found to fulfill our requirement. In the following, Shoreham's J_c data were compiled to validate the relationship $J_c \propto |T_{33}|^\gamma$ (γ : material constant) and, in particular, to correlate the bounded nature of J_c for increasing TST with T_{33} .

3. Compilation of the Decommissioned Shoreham Reactor Vessel Steel Fracture Toughness Test Data from the Standpoint of Out-of-Plane Constraint

3.1. Prediction of a Lower Bound of J_c for Increasing TST with T_{33} . From our recent elastic FEA results for the nonstandard 3PB specimen with various B/W values, as shown in Figure 2(a), the midplane T_{33} normalized in the form of $\beta_{33} = T_{33}(\pi a)^{1/2}/K_I$ exhibited a strong dependence on B/W [17]. β_{33} was negative for $B/W < 1.5$, whereas it was positive and approached $\nu\beta_{11}$ ($\beta_{11} = T_{11}(\pi a)^{1/2}/K_I$) for increasing TST.

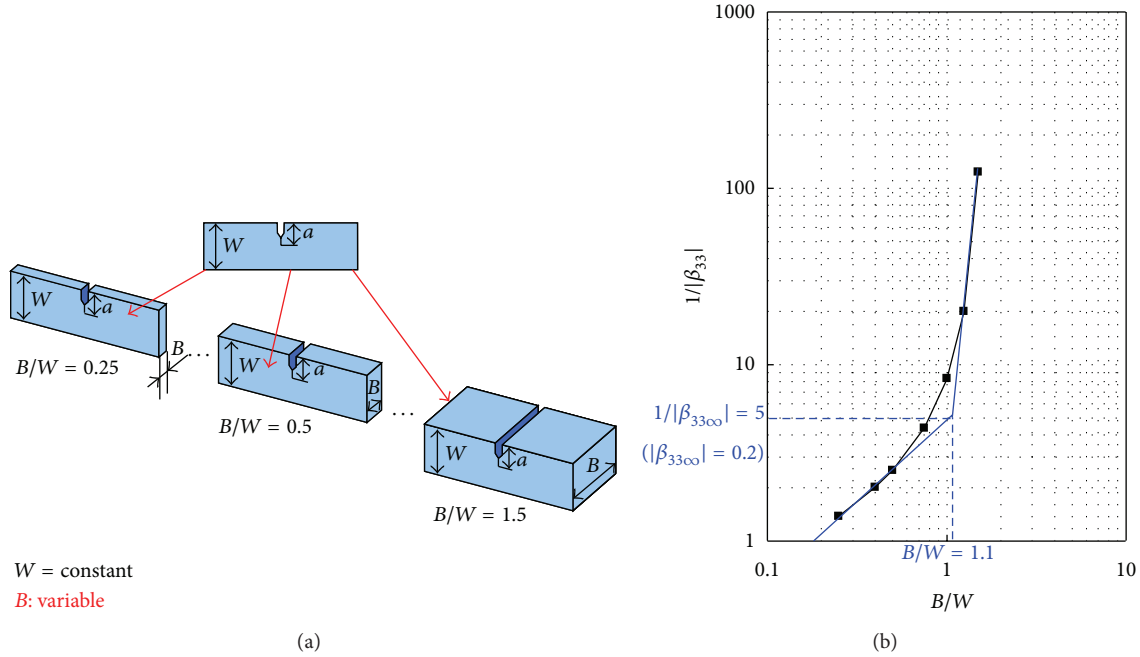


FIGURE 2: The TST effect on the normalized T_{33} of the nonstandard 3PB specimen at the specimen midplane ($W = 25$ mm, $a/W = 0.5$; $\nu = 0.3$) [16] recompiled in the log-log form.

The negative β_{33} recompiled in the log-log form, as shown in Figure 2(b), exhibited $|\beta_{33}| \propto (B/W)^{-1}$ for $B/W \leq 0.5$ and a bounded nature for $B/W \geq 1.1$ in an engineering sense. This engineering onset of the bounded nature of $|\beta_{33}| = 0.2$ was defined as the bounded value $|\beta_{33\infty}|$. Because the SIF corresponding to the fracture load K_c exhibited a small change with TST [14–17], it was thought that the experimental formulation $J_c = C|T_{33}|^\gamma$ (C, γ : material constants) together with $|T_{33\infty}| = |\beta_{33\infty}| \cdot K_c/(\pi a)^{1/2}$ could predict the lower bound value of $J_{c\min}$ with increasing TST as follows:

$$J_{c\min} = C|T_{33\infty}|^\gamma = C \left\{ \frac{|\beta_{33\infty}| K_c}{(\pi a)^{1/2}} \right\}^\gamma. \quad (3)$$

3.2. Compilation of the Decommissioned Shoreham Reactor Vessel Steel Fracture Toughness Test Data from the Standpoint of the Out-of-Plane Constraint. To determine whether the relationship $J_c = C|T_{33}|^\gamma$ is valid for other materials and especially whether the lower bound $J_{c\min}$ can be predicted by T_{33} , the decommissioned Shoreham reactor vessel steel [1] A533B was selected in this work because a large amount of fracture toughness test data for A533B with various thickness 3PB specimens at a common temperature -91°C (located in the DBT temperature region) was published. A more detailed description for the fracture toughness tests can be found in [1].

Here, the fracture toughness test data for 3PB specimens with width $W = 25.4$ and 50.8 mm whose thicknesses $B = 8, 15.9, 31.8,$ and 63.5 mm (thickness-to-width ratio $B/W = 0.157\sim 2.5$) were recompiled from the published results [1] on the standpoint of the out-of-plane crack-tip constraint. Although the eight replicate fracture toughness test results reported in [1] for these 3PB specimens were considered to be

valid overall, some of the individual K_{Jc} datum still appeared to deviate greatly from the remainder in each B/W set. Considering the fact that the K_{Jc} scatter from eight replicate tests always exceeded the guideline value as given in ASTM E1921 [19], we thought it was necessary to recompile these test results because the impact of the apparent deviated K_{Jc} datum for each B/W set was considered non-negligible in studying the TST effect on the cleavage fracture toughness. Therefore, the cases with maximum and minimum K_{Jc} values were excluded, with the test results of the remaining cases summarized in Tables 1 and 2.

The K_c in the tables was obtained as the SIF K corresponding to the fracture load P_c from the following equation in ASTM E1921 [19]:

$$K = \frac{PS}{BW^{3/2}} f\left(\frac{a}{W}\right). \quad (4)$$

Here, $S = 4W$ is the support span, and f is a function of a/W , which is given in the ASTM E1921 [19].

K_{Jc} in the table is the fracture toughness in terms of the SIF. J_c was calculated from K_{Jc} as $J_c = K_{Jc}^2 \cdot (1 - \nu^2)/E$, where the value of Young's modulus of $E = 207.9$ GPa and the value of Poisson's ratio of $\nu = 0.29$ were used, as specified in [20]. T_{33c} , which reflects the fracture load and the actual crack length, was calculated from the β_{33} solutions of elastic FEA, as summarized in the Appendix. μ and Σ are the average and standard deviation of each value, respectively. $2\Sigma/\mu$ is a reference value that was used to represent the magnitude of the data scatter.

It is seen from Tables 1 and 2 that, except for the case of $W = 50.8$ mm with a very thin thickness $B = 8$ mm ($2\Sigma/\mu = 63.8\%$), the reference value $2\Sigma/\mu$ of K_{Jc} was in the range from 33.1% to 45.6% for the selected specimens, which

TABLE 1: Fracture toughness test and FEA results for A533B compiled from the Shoreham reactor pressure vessel data [1] (3PB, $W = 25.4$ mm, -91°C ; μ : average, Σ : standard deviation).

B mm (B/W)	Serial number	1	2	3	4	5	6	μ	Σ	$2\Sigma/\mu$ %
8 (0.315)	a/W^*	0.5	0.49	0.5	0.5	0.5	0.5	0.50	0.0	1.6
	P_c kN*	9.61	9.49	9.02	9.52	9.61	8.99	9.37	0.3	6.2
	K_c MPa m ^{1/2}	80.3	76.8	75.3	79.6	80.3	75.1	77.9	2.4	6.3
	K_{Jc} MPa m ^{1/2} *	149	131	118	124	157	98	129.5	21.4	33.1
	J_c N/mm	97.8	75.6	61.3	67.7	108.6	42.3	75.6	24.3	64.3
	T_{33c} MPa	-234.4	-226.0	-219.9	-232.2	-234.4	-219.1	-227.7	7.0	-6.2
15.9 (0.63)	a/W^*	0.52	0.52	0.52	0.52	0.52	0.52	0.52	0.0	0.0
	P_c kN*	18.2	18.8	17.4	17.3	18.4	17.9	18.0	0.6	6.2
	K_c MPa m ^{1/2}	81.7	84.1	78.2	77.6	82.5	80.3	80.7	2.5	6.2
	K_{Jc} MPa m ^{1/2} *	130	126	92	89	131	100	111.3	19.8	35.5
	J_c N/mm	74.5	69.9	37.3	34.9	75.6	44.1	56.0	19.3	68.8
	T_{33c} MPa	-112.7	-116.0	-107.9	-107.1	-113.8	-110.9	-111.4	3.5	-6.2
31.8 (1.25)	a/W^*	0.52	0.52	0.52	0.52	0.53	0.52	0.52	0.0	1.6
	P_c kN*	35.4	37.5	38.5	32.9	35.1	34.6	35.7	2.0	11.4
	K_c MPa m ^{1/2}	79.3	84.1	86.4	73.8	81.2	77.6	80.4	4.5	11.3
	K_{Jc} MPa m ^{1/2} *	89	126	128	84	96	90	102.2	19.6	38.4
	J_c N/mm	34.9	69.9	72.2	31.1	40.6	35.7	47.4	18.6	78.4
	T_{33c} MPa	-12.5	-13.3	-13.6	-11.6	-9.8	-12.2	-12.2	1.4	-22.4
63.5 (2.5)	a/W^*	0.5	0.49	0.49	0.5	0.49	0.49	0.49	0.0	2.1
	P_c kN*	76.3	57.9	77.0	49.2	60.4	70.4	65.2	11.2	34.2
	K_c MPa m ^{1/2}	80.3	59.0	78.6	51.7	61.6	71.8	67.2	11.5	34.2
	K_{Jc} MPa m ^{1/2} *	94	62	89	52	63	78	73.0	16.6	45.6
	J_c N/mm	38.9	16.9	34.9	11.9	17.5	26.8	24.5	10.8	88.4
	T_{33c} MPa	15.0	9.3	12.4	9.7	9.7	11.3	11.3	2.2	39.0

* Published results in [1].

satisfied the guideline for $2\Sigma/\mu$ given in ASTM E1921 [19] for K_{Jc} . Here the guideline for $2\Sigma/\mu$ is $56(1-20/\mu)\%$ with the range from 40.7% to 47.4% for the data in Tables 1 and 2. As a result, it could be concluded that the scatter in the K_{Jc} data of the selected specimens summarized in the tables was acceptable in an engineering sense.

One interesting fact was that the change in K_c , that is, the SIF for the fracture load P_c , exhibited a relatively small dependence on B/W , although a significant change in the fracture toughness J_c was observed. The average K_c for each B/W was in the range from 67.2 to 80.7 MPa m^{1/2} for $W = 25.4$ mm and 75.8 to 95.7 MPa m^{1/2} for $W = 50.8$ mm. This result was similar to the experience with S55C [14–16] and SCM440 [17], which validated one of the assumptions used to predict the lower bound of J_c for large TST proposed in Section 3.1.

The relationship between J_c and T_{33c} for A533B is shown in Figure 3; note that T_{33c} reflects the fracture load and the actual crack length for each B/W , as summarized in Table 1 and 2. The solid marks represent the average for each B/W . The difference in W was distinguished by the color of the marks. As shown in Figure 3, all the data in Tables 1 and 2 are fitted to the power law expression

$$J_c [\text{N/mm}] = 2.3 \cdot |T_{33}|^{0.6} \quad (5)$$

for A533B tested using 3PB specimens at -91°C . J_c seemed to be bounded for $2|T_{33c}| < 100$ MPa. The bounded value of J_c in Figure 3 for the case of $W = 25.4$ mm was obtained from Table 1 as an average J_c for the specimens of $B/W = 1.25$ and 2.5. For the case of $W = 50.8$ mm, the bounded J_c was obtained from Table 2 as an average for $B/W = 1.25$.

On the other hand, if the method to predict the lower bound $J_{c\min}$ for increasing TST proposed in Section 3.1 is applied, for the case of $W = 25.4$ mm as an example, first $|T_{33\infty}|$ is calculated with $|\beta_{33\infty}| = 0.2$ for the case of $a/W = 0.5$ and $K_c = 79.7$ MPa m^{1/2} (the averaged SIF for $B/W = 0.315\sim 1.25$ was used from Table 1, considering the fact that K_c exhibited a very small dependence on TST) as $|T_{33\infty}| = |\beta_{33\infty}| \cdot K_c / (\pi a)^{1/2} = 0.2 \times 79.7 / (\pi \cdot 0.0127)^{1/2} = 79.8$ MPa. Then, the lower bound $J_{c\min}$ is predicted from (3) as $J_{c\min} = 2.3 \times |79.8|^{0.6} = 31.8$ N/mm, and it was close to experimental average 36.0 N/mm. In case of $W = 50.8$ mm, by the same method, $J_{c\min} = 27.2$ N/mm was obtained and was also very close to the experimental average 27.9 N/mm.

In summary, the TST effect on J_c of A533B could be described by T_{33} , as $J_c = 2.3 \cdot |T_{33}|^{0.6}$ for $80 \leq |T_{33}| \leq 320$ MPa. In addition, the lower bound value of $J_{c\min} = 31.8$ N/mm was obtained for $W = 25.4$ mm and $J_{c\min} = 27.2$ N/mm for $W = 50.8$ mm; both of them were close to

TABLE 2: Fracture toughness test and FEA results for A533B compiled from the Shoreham reactor pressure vessel data [1] (3PB, $W = 50.8$ mm, -91°C ; μ : average, Σ : standard deviation).

B mm (B/W)	Serial number	1	2	3	4	5	6	μ	Σ	$2\Sigma/\mu$ %
8 (0.157)	a/W^*	0.48	0.49	0.48	0.49	0.49	0.48	0.49	0.0	2.3
	P_c kN*	17.4	15.5	16.8	19.4	15.2	17.7	17.0	1.5	18.1
	K_{Ic} MPa m ^{1/2}	96.6	88.7	93.2	110.8	86.8	98.0	95.7	8.6	17.9
	K_{Jc} MPa m ^{1/2} *	122	101	112	205	94	123	126.2	40.3	63.8
	J_c N/mm	65.6	44.9	55.3	185.1	38.9	66.7	76.1	54.5	143.4
	T_{33c} MPa	-327.7	-300.5	-316.0	-375.3	-294.2	-332.3	-324.3	29.0	-17.9
15.9 (0.313)	a/W^*	0.49	0.49	0.49	0.49	0.49	0.49	0.49	0.0	0.0
	P_c kN*	36.7	30.5	35.9	34.9	23.3	35.9	32.9	5.2	31.6
	K_{Ic} MPa m ^{1/2}	105.8	88.0	103.4	100.5	67.1	103.4	94.7	14.9	31.6
	K_{Jc} MPa m ^{1/2} *	129	93	122	121	69	122	109.3	23.4	42.8
	J_c N/mm	73.3	38.1	65.6	64.5	21.0	65.6	54.7	20.5	74.8
	T_{33c} MPa	-225.4	-187.4	-220.3	-214.1	-142.9	-220.2	-201.7	31.8	-31.6
31.8 (0.63)	a/W^*	0.5	0.5	0.5	0.5			0.50	0.0	0.0
	P_c kN*	62.7	56.5	60.6	43.6			55.9	8.5	30.6
	K_{Ic} MPa m ^{1/2}	93.2	83.9	90.0	64.9			83.0	12.7	30.6
	K_{Jc} MPa m ^{1/2} *	99	88	96	66	—	—	87.3	14.9	34.2
	J_c N/mm	43.2	34.1	40.6	19.2			34.3	10.8	62.7
	T_{33c} MPa	-98.4	-88.6	-95.1	-68.5			-87.7	13.4	-30.6
63.5 (1.25)	a/W^*	0.51	0.52	0.52	0.51	0.52		0.52	0.0	2.1
	P_c kN*	119.0	77.3	107.1	96.4	84.6		96.9	16.8	34.7
	K_{Ic} MPa m ^{1/2}	91.5	61.4	85.0	74.0	67.1		75.8	12.4	32.7
	K_{Jc} MPa m ^{1/2} *	99	62	86	76	70	—	78.6	14.4	36.6
	J_c N/mm	43.2	16.9	32.6	25.4	21.6		27.9	10.3	73.5
	T_{33c} MPa	-13.2	-7.2	-10.0	-10.7	-7.9		-9.8	2.4	-48.8

*Published results in [1].

the experimental average value, which indicated that T_{33} can successfully predict the bounded nature of J_c .

4. Discussion

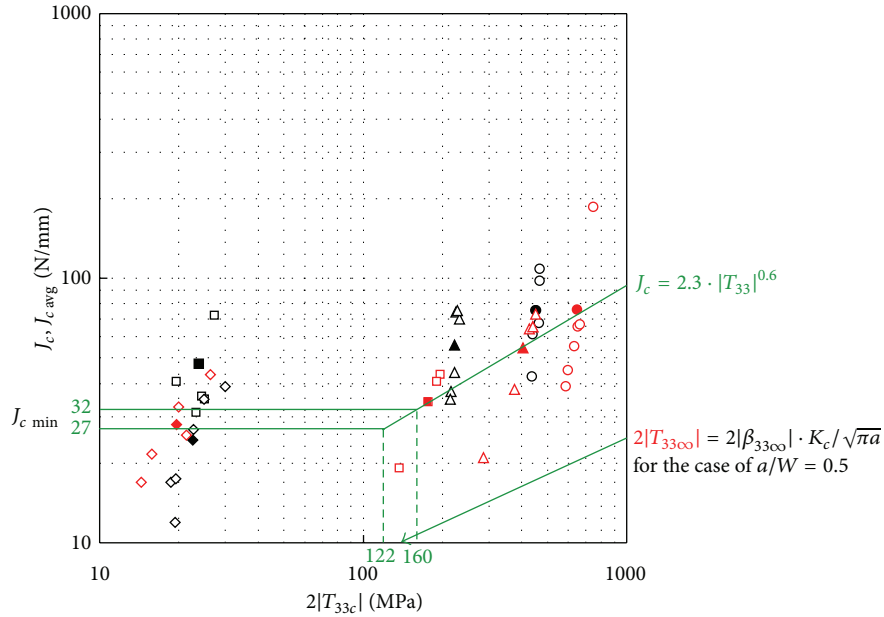
In this work, the TST effect and the bounded nature of J_c observed for the decommissioned Shoreham reactor vessel steel, A533B, at -91°C , which is in the DBT range [1], were compiled by T_{33} -stress in the general form of (5). In (5), the similar power law relationship between J_c and T_{33} was also valid for the combination of S55C [14, 15] and SCM440 [17] tested using both CT and 3PB specimens. In addition, T_{33} , which seemed to be useful for predicting the bounded nature of J_c for S55C [16], has also been proven to be valid for A533B. In these empirical equations, the TST effect and the bounded nature of J_c were described with a single out-of-plane elastic parameter T_{33} taken at the specimen midplane. Although the depicted relationship between the fracture toughness J_c of a material and T_{33} must be validated for other materials and other types of test specimen configurations, using T_{33} as a relevant out-of-plane constraint parameter is definitely worthy of further investigation.

It could be argued that the relationship $J_c \propto B^{(-1/2)} \propto |T_{33}|^{0.6}$ (Figure 3) is similar to the formulation deduced from the SWL model, but no more than what is predicted by the

SWL model ($J_c \propto B^{(-1/2)}$) [2], because $|T_{33}|$ first approaches to 0 for large TST (Note: with increase in TST for 3PB specimen, negative T_{33} first increases, crosses 0 and converges to νT_{11}). As Anderson et al. indicated, as a contradiction of the SWL model, the “fracture toughness does not decrease indefinitely with thickness [6].” On the point that T_{33} exhibits a saturating tendency for large TST, T_{33} has also been proven to be able to predict the bounded behavior of J_c (Figure 3). The advantage of using T_{33} is that T_{33} has the characteristic to not only describe the TST effect on J_c but to also predict the bounded nature of J_c . This advantage of T_{33} successfully avoids the contradiction deduced from the SWL model; that is, $J_c \rightarrow 0$ for $B \rightarrow \infty$.

ASTM E1921 [19] presents a method to adjust J_c for CT’s TST change by considering the empirical relationship $J_c \propto B^{(-1/2)}$, under the assumption that 1-inch (1T) thickness CT toughness data exists. The presented method in this paper for a 3PB specimen can be generally applied to any type of test specimens, if a curve similar to Figure 2 is obtained. The fact that 1T CT test data are not necessary for our method can help practitioners in their works.

When the proposed general formulation of (3) is practically used for determining the lower bound of J_c for a specific material tested with a fracture toughness test specimen, the material constants C and γ should be first determined by conducting measurements on at least two different-sized



W (mm)	25.4		50.8			
B (mm)	B/W	Jc	Jc avg	B/W	Jc	Jc avg
8	0.315	○	●	0.157	○	●
15.9	0.63	△	▲	0.313	△	▲
31.8	1.25	□	■	0.63	□	■
63.5	2.5	◇	◆	1.25	◇	◆

FIGURE 3: Relationship between J_c and T_{33c} (A533B, -91°C , 3PB).

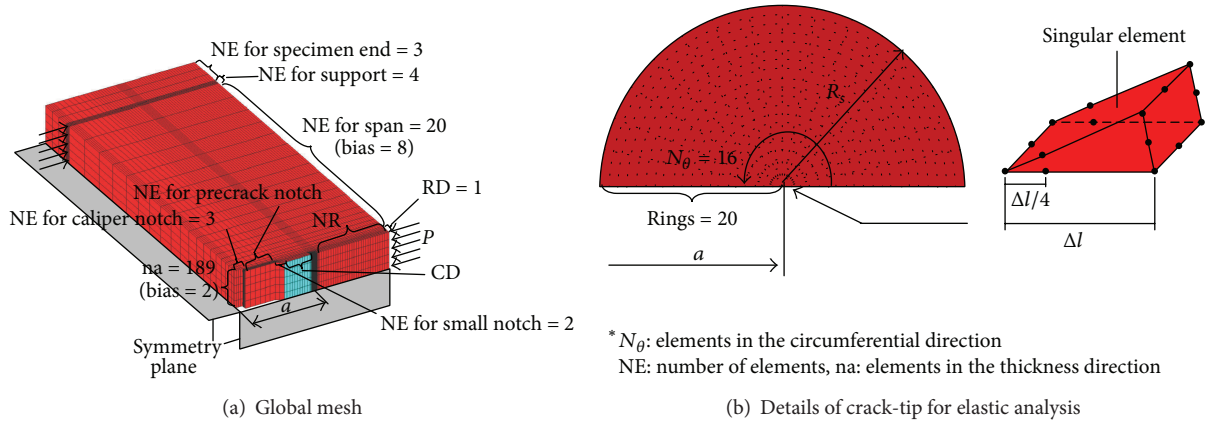


FIGURE 4: Typical finite element model of the 3PB specimen.

specimens. Nevertheless, if measurements on only one size of specimen are conducted, (3) can also be simply but not accurately applied for predicting the lower bound fracture toughness just by assuming $\gamma = 1/2$ in the relationship $J_c \propto |T_{33}|^\gamma$ for that one size of specimen considered, because the material constant $\gamma = 1/2$ has been verified for the materials S55C and SCM440 tested with both CT and 3PB specimens [14, 15, 17]; in addition, this work validated that the approximated $\gamma = 0.6$ which is close to $\gamma = 1/2$ was applicable for the material A533B tested using 3PB specimens.

The normalized T_{33} -stress solutions used in this work were taken at the specimen midplane. It is true that these

values are distributed in the specimen thickness direction [21]. There are many possibilities to treat this 3D effect, but, considering the fact that the fracture tends to initiate at the specimen midplane, the values at the specimen midplane were chosen to represent the characteristic intensity of these values.

5. Conclusions

This paper demonstrated for the decommissioned Shoreham reactor vessel steel A533B [1] that the out-of-plane crack-tip constraint has a noticeable contribution to the TST effect

TABLE 3: Summary of the generated mesh for elastic analysis ($S/W = 4$, $R_s = 0.4$ mm).

W mm	B/W	a/W	$\Delta l/a$	Number of elements (NE) for precrack notch	CD	NR	Nodes	Elements
25.4	0.315	0.49	0.0016	6	10	30	368609	87591
		0.50						
	0.63	0.52	0.0015			28	366579	87143
		0.53						
2.5	0.49	0.0016	30	368609	87591			
	0.50							
50.8	0.157	0.48	0.00082	10	9	30	371654	88263
		0.49	0.00080		10	30	372669	88487
	0.313	0.49	0.00080		10	30	372669	88487
		0.50	0.00079		9	30	371654	88263
	1.25	0.51	0.00077		12	28	372669	88487
		0.52	0.00076		15	25	372669	88487

TABLE 4: Normalized T_{33} -stress solutions (β_{33}) at the specimen midplane for 3PB specimens ($\nu = 0.29$).

$W = 25.4$ mm			$W = 50.8$ mm		
B/W	a/W	β_{33}	B/W	a/W	β_{33}
0.315	0.49	-0.582	0.157	0.48	-0.938
	0.50	-0.583		0.49	-0.947
0.63	0.52	-0.281	0.313	0.49	-0.596
	0.53	-0.032		0.50	-0.298
1.25	0.52	-0.032	0.63	0.50	-0.298
	0.53	-0.025		0.51	-0.041
2.5	0.49	0.031	1.25	0.51	-0.041
	0.50	0.037		0.52	-0.034

on J_c and that the magnitude of this out-of-plane crack-tip constraint can be described by the elastic T_{33} -stress. The experimental expression of the TST effect on J_c using T_{33} -stress, which was proposed for 0.55% carbon steel S55C and 0.40% carbon chromium molybdenum steel SCM440 with both CT and 3PB specimens in our previous work [14, 15, 17], was shown to be a correct description for A533B. In concrete, the experimental relationship for A533B was compiled as J_c [N/mm] = $2.3 \cdot |T_{33}|^{0.6}$ ($80 \leq |T_{33}| \leq 320$ MPa) to describe the J_c decreasing tendency for increasing TST. Because the Shoreham data included a lower bound J_c for increasing TST, a new discovery was that T_{33} successfully predicted the lower bound of J_c with increasing TST. This lower bound of J_c prediction with T_{33} resolved the contradiction that the empirical $J_c \propto (\text{TST})^{-1/2}$ predicts $J_c = 0$ for large TST.

Appendix

The normalized β_{33} solutions used to calculate T_{33c} in Tables 1 and 2 were obtained from the elastic FEA. In the present FEA, all the 3PB specimen dimensions were specified in accordance with those recorded in [1], and the material properties were set to be consistent with those specified in [20] for A533B.

The typical FEA model of the 3PB specimen used in the present elastic analysis is shown in Figure 4, with the details for the generated mesh being summarized in Table 3. The details of the elastic FEA procedure can be found in our recent work [17]. The normalized T_{33} -stress, β_{33} , at the specimen midplane is summarized in Table 4, which is in a good agreement with the interpolated solutions from our previous results [22].

Nomenclature

B :	Specimen thickness
C :	Material constant (see (3))
E :	Young's modulus
J :	J -integral
J_c and $J_{c \text{ avg}}$:	Fracture toughness and its average
$J_{c \text{ min}}$:	Lower bound fracture toughness
K_I :	Local mode I stress intensity factor (SIF)
K_{Jc} :	Fracture toughness ($K_{Jc} = [E \cdot J_c / (1 - \nu^2)]^{1/2}$)
K_c :	SIF corresponding to fracture load
P_c :	Fracture load
R_s :	Crack tube radius
S :	Support span for 3PB specimen
T_{11} and T_{33} :	T -stresses
T_{33c} :	T_{33} -stress corresponding to fracture load
$T_{33\infty}$:	Bounded value of T_{33} -stress
W :	Specimen width
a :	Crack length
r, θ :	In-plane polar coordinates
x_j :	Crack-tip local coordinates ($j = 1, 2, 3$)
Δl :	Singular element size
Σ :	Standard deviation
β_{11}, β_{33} :	Normalized forms of the T -stresses
$\beta_{33\infty}$:	Bounded value of β_{33}
γ :	Material constant (see (3))
μ :	Average value
ν :	Poisson's ratio
σ_{ij} :	Stress components ($i, j = 1, 2, 3$).

Conflict of Interests

The authors declare that there is no conflict of interests regarding the publication of this paper.

Acknowledgments

This work was supported in part by JSPS KAKENHI Grant no. 24561038. Their support is greatly appreciated.

References

- [1] H. J. Rathbun, G. R. Odette, T. Yamamoto, and G. E. Lucas, "Influence of statistical and constraint loss size effects on cleavage fracture toughness in the transition—a single variable experiment and database," *Engineering Fracture Mechanics*, vol. 73, no. 1, pp. 134–158, 2006.
- [2] K. Wallin, "The size effect in K_{IC} results," *Engineering Fracture Mechanics*, vol. 22, no. 1, pp. 149–163, 1985.
- [3] M. Nevalainen and R. H. Dodds Jr., "Numerical investigation of 3-D constraint effects on brittle fracture in SE(B) and C(T) specimens," *International Journal of Fracture*, vol. 74, no. 2, pp. 131–161, 1995.
- [4] R. H. Dodds Jr., T. L. Anderson, and M. T. Kirk, "A framework to correlate a/W ratio effects on elastic-plastic fracture toughness (J_c)," *International Journal of Fracture*, vol. 48, no. 1, pp. 1–22, 1991.
- [5] M. T. Kirk, R. H. Dodds, and T. L. Anderson, "An approximate technique for predicting size effects on cleavage fracture toughness (J_c) using the elastic T stress," in *Fracture Mechanics*, J. D. Landes, D. E. McCabe, and J. A. M. Boulet, Eds., vol. 24, pp. 62–86, American Society for Testing and Materials, Philadelphia, Pa, USA, 1994.
- [6] T. L. Anderson, D. Stienstra, and R. H. Dodds, "A theoretical framework for addressing fracture in the ductile-brittle transition region," in *Fracture Mechanics*, J. D. Landes, D. E. McCabe, and J. A. M. Boulet, Eds., vol. 24, pp. 186–214, American Society for Testing and Materials, Philadelphia, Pa, USA, 1994.
- [7] T. J. Theiss and J. W. Bryson, "Influence of crack depth on the fracture toughness of reactor pressure vessel steel," in *Constraint Effects in Fracture*, E. M. Hackett, Ed., pp. 104–119, American Society for Testing and Materials, Philadelphia, Pa, USA, 1993.
- [8] J. D. G. Sumpter, "An experimental investigation of the T stress approach," in *Constraint Effects in Fracture*, E. M. Hackett, Ed., pp. 495–502, American Society For Testing and Materials, Philadelphia, Pa, USA, 1993.
- [9] M. T. Kirk, K. C. Koppenhoefer, and C. F. Shih, "Effect of constraint on specimen dimensions needed to obtain structurally relevant toughness measures," in *Constraint Effects in Fracture*, E. M. Hackett, Ed., pp. 79–103, American Society for Testing and Materials, Philadelphia, Pa, USA, 1993.
- [10] J. P. Petti and R. H. Dodds Jr., "Coupling of the Weibull stress model and macroscale models to predict cleavage fracture," *Engineering Fracture Mechanics*, vol. 71, no. 13-14, pp. 2079–2103, 2004.
- [11] K. Wallin, T. Saario, and K. Torronen, "Statistical model for carbide induced brittle fracture in steel," *Metal Science*, vol. 18, no. 1, pp. 13–16, 1984.
- [12] T. Lin, A. G. Evans, and R. O. Ritchie, "A statistical model of brittle fracture by transgranular cleavage," *Journal of the Mechanics and Physics of Solids*, vol. 34, no. 5, pp. 477–497, 1986.
- [13] C. Ruggieri, "Probabilistic treatment of fracture using two failure models," *Probabilistic Engineering Mechanics*, vol. 13, no. 4, pp. 309–319, 1998.
- [14] T. Meshii and T. Tanaka, "Experimental T_{33} -stress formulation of test specimen thickness effect on fracture toughness in the transition temperature region," *Engineering Fracture Mechanics*, vol. 77, no. 5, pp. 867–877, 2010.
- [15] T. Tanaka and T. Meshii, "Formulating test specimen thickness effect on fracture toughness with T_{33} -stress: case of 3PB test specimen," in *Proceedings of the ASME Pressure Vessels and Piping Division/K-PVP Conference (PVP '10)*, pp. 1213–1219, Seattle, Wash, USA, July 2010.
- [16] T. Meshii, K. Lu, and R. Takamura, "A failure criterion to explain the test specimen thickness effect on fracture toughness in the transition temperature region," *Engineering Fracture Mechanics*, vol. 104, pp. 184–197, 2013.
- [17] T. Meshii and T. Tanaka, "Framework to correlate test specimen thickness effect on fracture toughness with T_{33} -stress," in *Proceedings of the ASME Pressure Vessels and Piping Conference*, pp. 1109–1117, Baltimore, Md, USA, Baltimore, Md, USA, 2011.
- [18] T. Nakamura and D. M. Parks, "Determination of elastic T -stress along three-dimensional crack fronts using an interaction integral," *International Journal of Solids and Structures*, vol. 29, no. 13, pp. 1597–1611, 1992.
- [19] ASTM, E1921-10 Standard test method for determination of reference temperature, T_0 , for ferritic steels in the transition range. Annual Book of ASTM Standards. American Society for Testing and Materials, Philadelphia, Pa, USA, 2010.
- [20] H. J. Rathbun, G. R. Odette, M. Y. He, and T. Yamamoto, "Influence of statistical and constraint loss size effects on cleavage fracture toughness in the transition—a model based analysis," *Engineering Fracture Mechanics*, vol. 73, no. 18, pp. 2723–2747, 2006.
- [21] J. Qu and X. Wang, "Solutions of T -stresses for quarter-elliptical corner cracks in finite thickness plates subject to tension and bending," *International Journal of Pressure Vessels and Piping*, vol. 83, no. 8, pp. 593–606, 2006.
- [22] K. Lu and T. Meshii, "Three-dimensional T -stresses for three-point-bend specimens with large thickness variation," *Engineering Fracture Mechanics*, pp. 197–203, 2014.

Research Article

Strain Rate Dependent Ductile-to-Brittle Transition of Graphite Platelet Reinforced Vinyl Ester Nanocomposites

Brahmananda Pramanik and P. Raju Mantena

Department of Mechanical Engineering, University of Mississippi, University, MS 38677, USA

Correspondence should be addressed to P. Raju Mantena; meprm@olemiss.edu

Received 28 November 2013; Accepted 6 January 2014; Published 25 February 2014

Academic Editor: Filippo Berto

Copyright © 2014 B. Pramanik and P. R. Mantena. This is an open access article distributed under the Creative Commons Attribution License, which permits unrestricted use, distribution, and reproduction in any medium, provided the original work is properly cited.

In previous research, the fractal dimensions of fractured surfaces of vinyl ester based nanocomposites were estimated applying classical method on 3D digital microscopic images. The fracture energy and fracture toughness were obtained from fractal dimensions. A noteworthy observation, the strain rate dependent ductile-to-brittle transition of vinyl ester based nanocomposites, is reinvestigated in the current study. The candidate materials of xGnP (exfoliated graphite nanoplatelets) reinforced and with additional CTBN (Carboxyl Terminated Butadiene Nitrile) toughened vinyl ester based nanocomposites that are subjected to both quasi-static and high strain rate indirect tensile load using the traditional Brazilian test method. High-strain rate indirect tensile testing is performed with a modified Split-Hopkinson Pressure Bar (SHPB). Pristine vinyl ester shows ductile deformation under quasi-static loading and brittle failure when subjected to high-strain rate loading. This observation reconfirms the previous research findings on strain rate dependent ductile-to-brittle transition of this material system. Investigation of both quasi-static and dynamic indirect tensile test responses show the strain rate effect on the tensile strength and energy absorbing capacity of the candidate materials. Contribution of nanoreinforcement to the tensile properties is reported in this paper.

1. Introduction

Vinyl ester based composites are mostly considered in applications such as pipelines and chemical storage tanks. The ester groups in the molecular structure are susceptible to water degradation by hydrolysis. The vinyl ester molecule features fewer ester groups, hence, exhibits better resistance to water and to some chemicals [1, 2]. The reactive sites in vinyl ester resin are positioned only at the ends of the molecule and hence it helps in improving the length of molecular chain. This long-chain molecular structure masks vinyl ester resin somewhat tough and resilient. Hence, this candidate material is being considered in ship superstructures which may be subjected to shock waves, impact, and high-strain rate loading.

Characterizing material strength and energy absorption response of materials at higher strain rates has gained increasing attention from multiple researchers. Several attempts [1, 3–10] have focused on improving the mechanical properties of vinyl ester composites by providing reinforcement. Graphite nanoplatelet reinforcement and toughening with

CTBN liquid-rubber agent are recently being considered for this composite system. In previous research [11], the authors focused on the roughness of fractured surface. Fractal dimensionality of the fractured failure surface was quantified for predicting the fracture energy and toughness of vinyl ester based nanocomposites. The authors observed [11–15] that the candidate composite systems are high in stiffness, but low in strength, and fail in a brittle fashion. It is observed that the failure of high stiffness and low strength materials is initiated by tensile stress concentrations. Hence, the investigation of the dynamic response of such materials under high-strain rate tensile loading requires serious consideration.

In this paper, previous research on investigation of fractured surface of the candidate materials [11] is revisited and discussed with respect to the strain-rate dependent ductile-to-brittle transition. Indirect tensile characterization of the high stiffness low strength graphite platelet reinforced vinyl ester nanocomposites has been performed in the current study. The strength and energy absorption capacity of the candidate materials in both quasi-static and high-strain rate testing are reported. The focus of this research is to

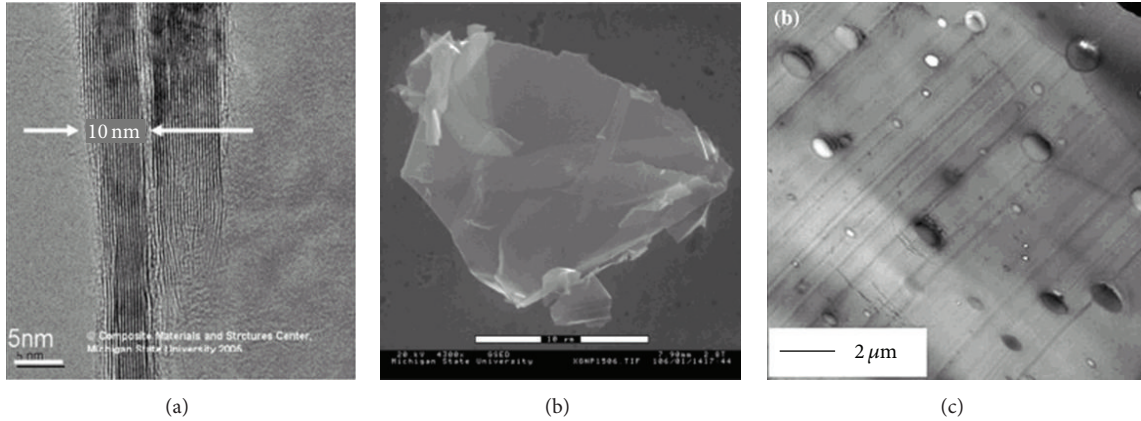


FIGURE 1: Typical SEM and TEM morphology of nanoparticle dispersion. (a) Edge view of xGnP flake [8], (b) lateral view of xGnP flake [8], and (c) globular CTBN particles [10].

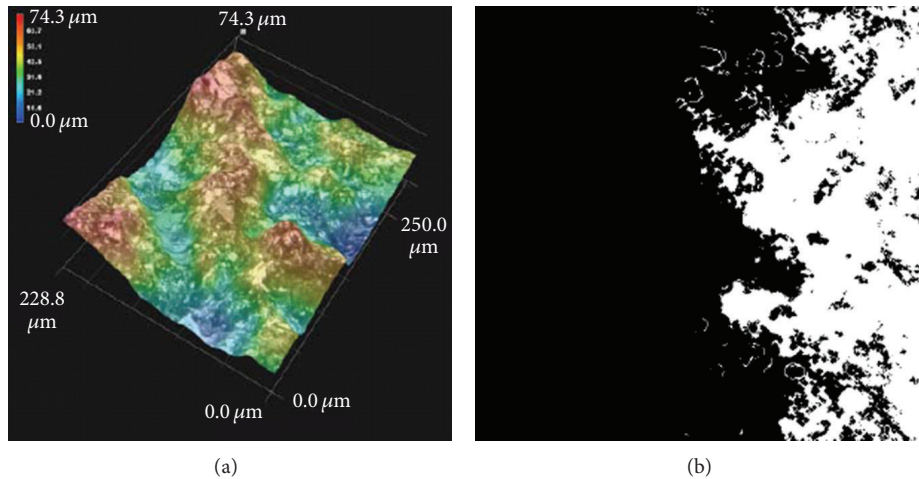


FIGURE 2: (a) 3D image of typical fractured surface at 1000 times magnification and (b) closed-contour at $10\ \mu\text{m}$ depth [11].

demonstrate the indirect tensile strain rate effect on specimen failure mechanism and the contribution of reinforcing and toughening inclusions on improving mechanical properties. This investigation compares the indirect tensile high-strain rate brittle fracture with quasi-static ductile response.

2. Materials and Methods

2.1. Materials. Five different Derakane 510A-40 vinyl ester thermoset nanocomposite panels [2] are considered for the dynamic indirect tensile characterization. The brominated bisphenol-A based vinyl ester consists of 38 weight% styrene, added to Butanone peroxide, N, N-Dimethylaniline, Cobalt Naphthenate, and 2-4-Pentanedione additives to impart maximum fire retardance, chemical resistance, and toughness. Pure brominated vinyl ester polymer (VE) is reinforced with 1.25 weight% and 2.5 weight% exfoliated graphite nanoplatelets (1.25xGnP + VE and 2.5xGnP + VE, resp.) in two different batches. One of the reinforced nanocomposite batches was toughened with 10 weight% almost unreactive liquid carboxyl terminated butadiene nitrile (CTBN) rubber (1.25xGnP + CTBN + VE and 2.5xGnP + CTBN + VE).

2.2. Material Fabrication. The nanoparticles are exfoliated and homogeneously dispersed in polymer matrix by applying sonication technique. The homogeneous exfoliation and dispersion is performed in 1 gal container for 4 hours, followed by 4 passes through a flow cell connected to a 100 W sonicator. The resin solution was mixed for 2 min with FlackTek speed mixer at 3000 rpm. The solution of vinyl ester resin with nanoreinforcement and toughening agent is poured into a mold, kept at room temperature for 30 minutes, and then postcured at 80°C for 3 hours [8]. Typical SEM and TEM morphology of the candidate materials are shown in Figure 1.

2.3. Fracture Energy and Toughness from Fractal Dimension of Fractured Surface. The failed specimens subjected to low velocity impact [15] and quasi-static direct tensile [12] loading were considered in this study. The posttest specimens were as carefully transferred to the observation platform as no further damage may occur to the fractured surface. 3D digital microscopic image (Figure 2(a)) of fractured surface [11] was captured at 1000 times magnification. The contours of the 3D image (Figure 2(b)) at $10\ \mu\text{m}$ incremental depths were

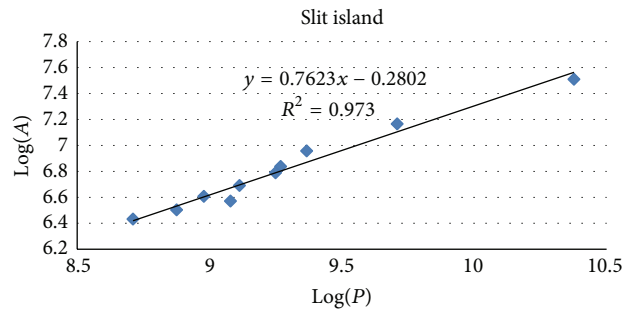


FIGURE 3: Determination of surface fractal dimension from the slope of the regression line on scatter-plot of logarithmic area versus perimeter [11].

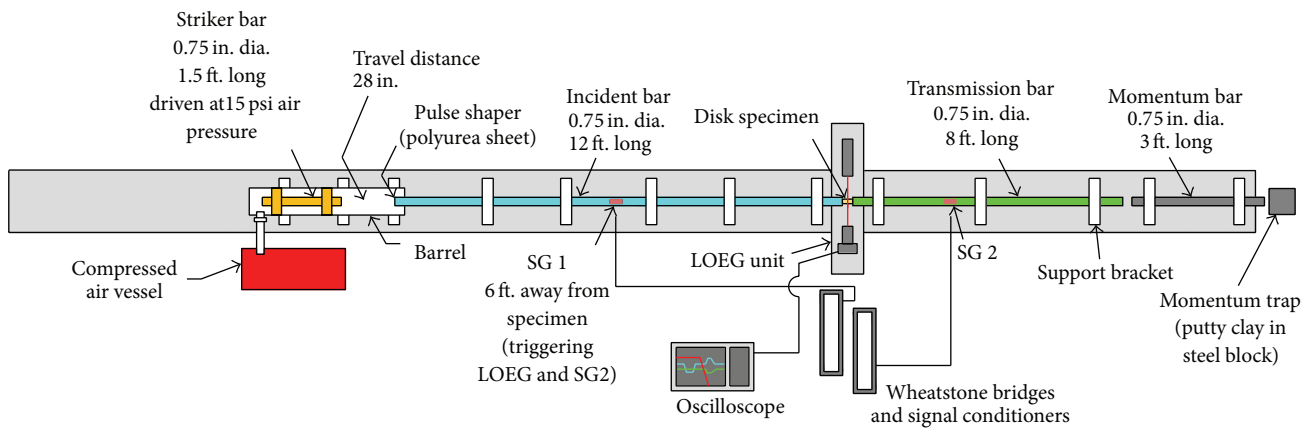


FIGURE 4: SHPB setup for indirect tensile tests including Laser Occluding Expansion Gage (LOEG) system.

extracted using 3D Profile Measurement Software, VHX-H2MK. The area and perimeter of the respective closed-contours were estimated using MATLAB functions. The fractal surface dimensionality is obtained from the slope of the regression line on logarithmic area versus perimeter scatter-plot (Figure 3). The fracture energy (J_{IC}) was estimated using equation $J_{IC} = \pi S_Y^2 L^{(Ds-2)}/E$, where S_Y is yield strength, L is scale of observation, Ds is surface fractal dimension, and E is Young’s modulus. The fracture toughness (K_{IC}) was obtained using equation $K_{IC} = (J_{IC} \cdot E)^{0.5}$.

2.4. High-Strain Rate Indirect Tensile Testing. The molded nanocomposite panels are machined into disk specimens with a diameter of 12.7 mm using carbide tipped tool in CNC machine. Traditional split-Hopkinson Pressure Bar (SHPB) apparatus is modified [18] to adapt conventional Brazilian test method (Figure 4) for obtaining high-strain rate indirect tensile response. The tests are performed approximately at 1000/s strain rate. The disk specimen is held diametrically (Figure 5) by concave end fixtures in between incident bar and transmission bar. The specimen is impacted along the loading axis. The applied compressive forces on the opposite ends (F_1 and F_2) of the specimen are obtained

from SHPB response. The indirect tensile stress experienced by the specimen in transverse direction is obtained using the equation $(F_1 + F_2)/(\pi Db)$, where D is diameter and b is thickness of the specimen. The indirect tensile strain is obtained using Laser Occluding Expansion Gage (LOEG) unit. It detects the tensile strain developed along transverse diameter. The strength of the material is obtained from the maximum stress before failure and the area under the stress (σ) versus strain (ϵ) curve $E = \int_0^{\epsilon_{ut}} \sigma(\epsilon)d\epsilon$ gives the energy (E) absorbing capacity.

Three samples in each candidate material group were selected for evaluation. The average response is reported along with the maximum data-scatter.

2.5. Quasi-Static Indirect Tensile Testing. Quasi-static indirect tensile experiments [18] are conducted on EnduraTec, a pneumatically driven materials test system (Figure 6). An interface load cell is used to measure the axial load. The disk specimen is mounted diametrically within vertically aligned concave end fixtures. LOEG unit is oriented transversely with respect to the loading axis for measuring the induced transverse tensile strain in disk specimen. The crosshead displacement is set at 0.015 mm/s which deforms the specimen approximately at 0.0001/s strain rate.

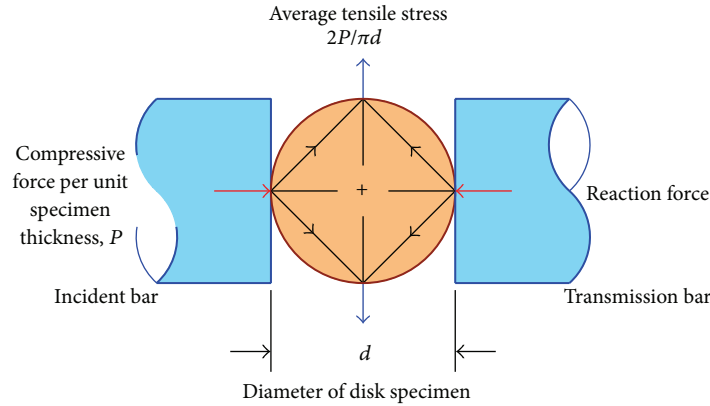


FIGURE 5: Induced tensile stress in circular disk specimen along transverse direction due to applied compressive loading.

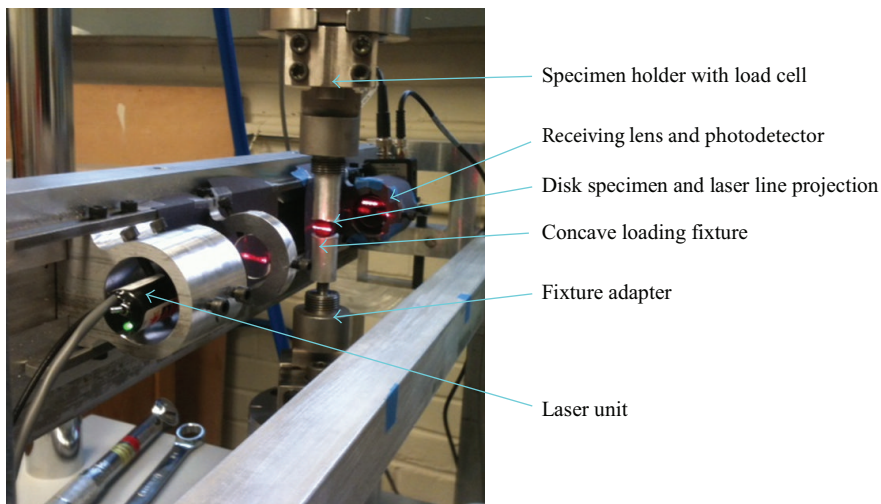


FIGURE 6: Quasi-static indirect tensile test setup with LOEG.

3. Results and Discussion

3.1. Quasi-Static Indirect Tensile Response. The quasi-static indirect tensile response of pure vinyl ester specimens (Figure 7(a)) showed ductile deformation response beyond the load cell limit (10 kN). Hence, the conventional Brazilian disk test method, which is appropriate for brittle materials, could not capture the true behavior of pure vinyl ester under quasi-static loading due to its ductility. However, addition of xGnP and CTBN makes the vinyl ester polymer more brittle (Figure 7(b)) and thus suitable for this indirect experimental method.

The quasi-static indirect tensile stress-strain history for pure vinyl ester, xGnP reinforced, and CTBN toughened samples are shown in Figures 8(a)(i) and 8(b)(i). As mentioned earlier, stress-strain plots for only the pure vinyl ester specimens have been terminated due to load cell capacity before specimen failure occurs, whereas reinforced samples failed within the load cell range. It can be observed in Figures 8(a)(ii) and 8(b)(ii) that tensile strength of pure vinyl ester is reduced by the addition of xGnP reinforcement (Figure 8(a)(ii)) and even with CTBN toughening

(Figure 8(b)(ii)). Energy absorbing capacity (Figures 8(a)(iii) and 8(b)(iii)) is similarly affected by the addition of xGnP (Figure 8(a)(iii)). The addition of CTBN did not improve the energy absorbing capacity (Figure 8(b)(iii)) of pure vinyl ester; however, a marginal enhancement (Figure 8(b)(iii)) can be observed when compared to only xGnP reinforced (i.e., without CTBN, Figure 8(a)(iii)) nanocomposites.

3.2. High-Strain Rate Indirect Tensile Response. Figure 9 summarizes the indirect tensile high-strain rate response of xGnP reinforced and with additional CTBN toughened vinyl ester nanocomposites at strain rate of 1000/s from SHPB tests. All the nanoreinforced specimens including pure vinyl ester failed in a brittle manner under dynamic tensile loading (Figures 9(a)(i) and 9(b)(i)).

It can be observed that the tensile strength of pure vinyl ester remains unchanged with xGnP reinforcement (Figure 9(a)(ii)). Addition of CTBN toughening to the 1.25 weight % xGnP reinforced nanocomposites showed a marginal improvement (Figure 9(b)(ii)). The energy absorbing capacity of pure vinyl ester is improved with xGnP

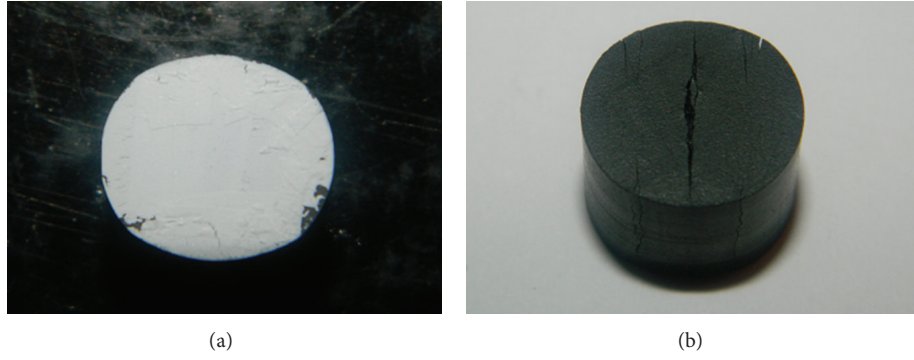


FIGURE 7: Posttest photographs of (a) pure vinyl ester sample elliptically deformed without diametrical splitting and (b) nanoreinforced composite sample with diametrical splitting.

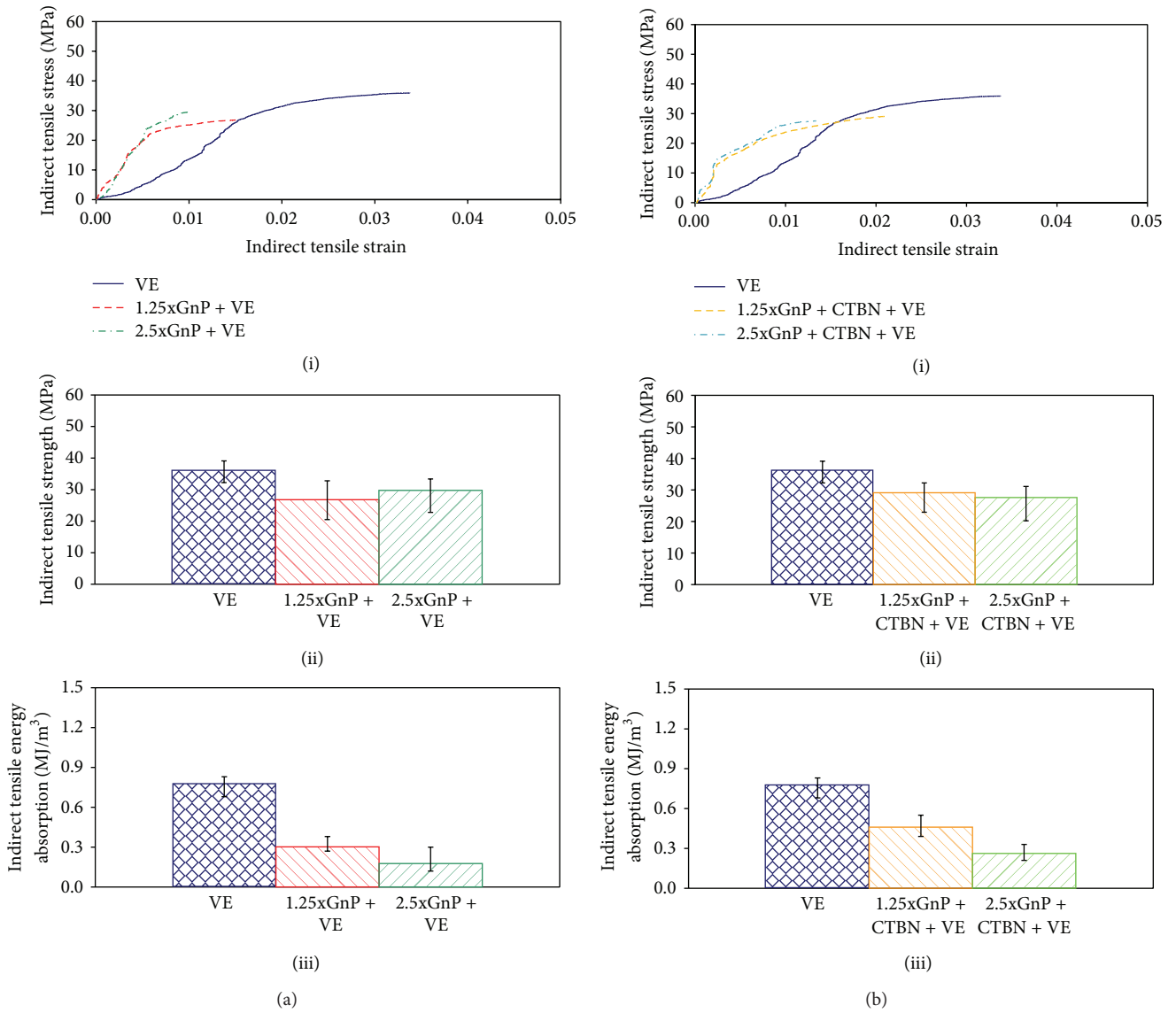


FIGURE 8: Quasi-static indirect tensile response. (i) Typical stress versus strain behavior, (ii) strength, and (iii) energy absorbing capacity of (a) graphite platelet reinforced and (b) with additional CTBN toughened vinyl ester nanocomposites (note: pure vinyl ester specimens did not fail within the 10 kN load cell limit of test equipment used for quasi-static testing).

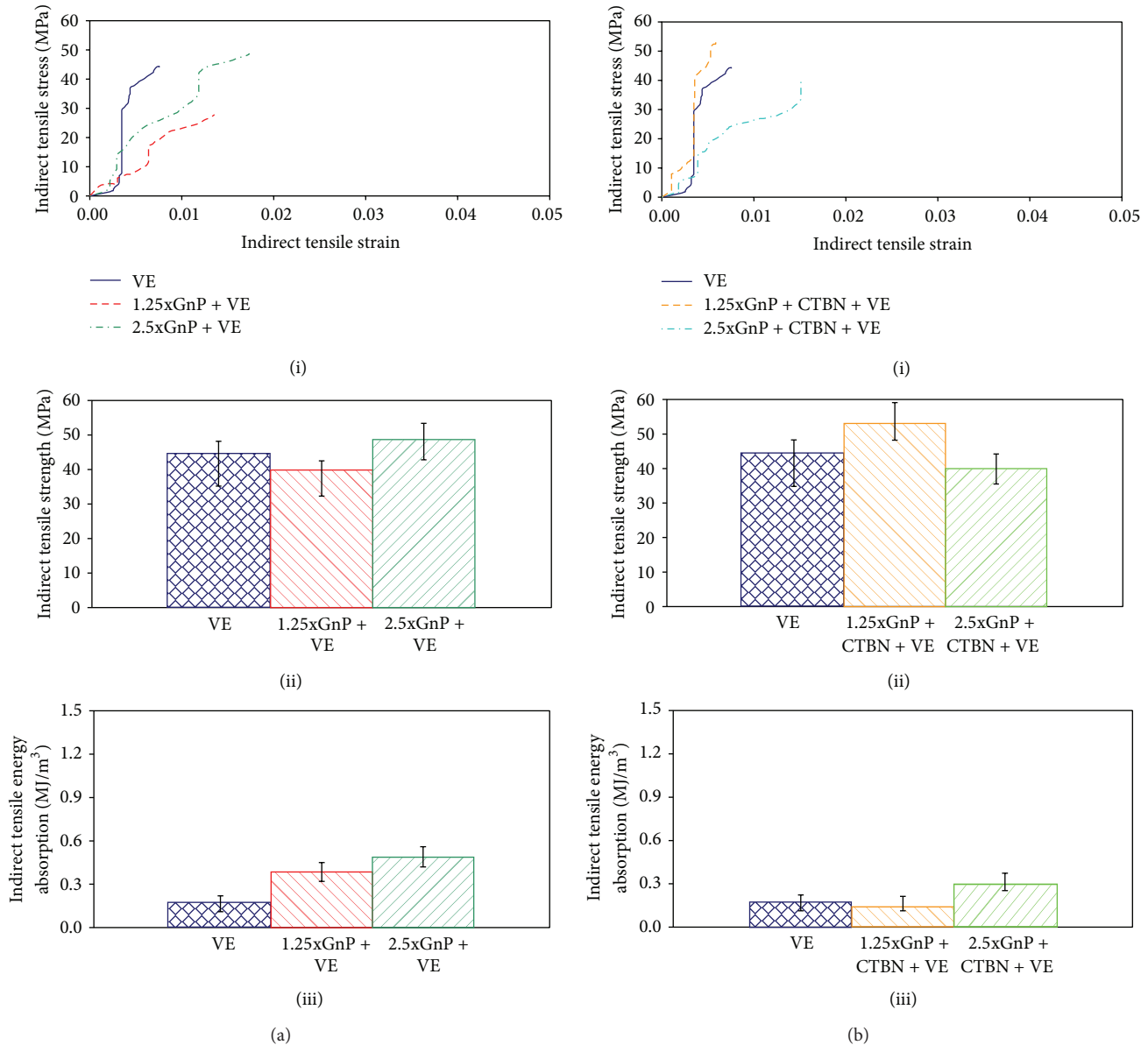


FIGURE 9: High-strain rate indirect tensile response from SHPB tests. (i) Typical stress versus strain behavior, (ii) strength, and (iii) energy absorbing capacity of (a) graphite platelet reinforced and (b) additionally CTBN toughened vinyl ester nanocomposites.

(Figure 9(a)(iii)) reinforcement. However, this improvement is reduced about 50% by further CTBN toughening to the xGnP reinforced nanocomposites (Figure 9(b)(iii)).

3.3. Strain Rate Effect. Previous research on fractal analysis of fractured surface revealed the strain rate dependent ductile-to-brittle transition [11]. The relationship between fractal dimension of the fractured surface and fracture energy of different materials [16, 17] suggests that some composite materials can behave as either ductile or brittle at different strain rates. The authors [11] confirmed that quasi-static direct tensile loading develops ductile fractal surface, whereas low velocity impact creates brittle fractal surface as shown in Figure 10.

In present research, comparative observation of Figures 8 and 9 shows the strain rate dependency of tensile strength and energy absorbing capacity of these candidate materials. As noted earlier, during quasi-static tests pure vinyl ester did not fail within maximum load limit of the load cell used, deforming elliptically in a ductile manner (Figures 7(a), 8(a)(i), and 8(b)(i)). However, it failed in a brittle fashion at much lesser strain (Figures 9(a)(i) and 9(b)(i)) under the high-strain rate SHPB loading. This ductile-to-brittle transition may be due to the significant influence of strain rate effect. These nanocomposites can be considered as thermo-viscoelastic under high-strain rate loading in Hopkinson bar experiments, and the time-temperature superposition principle would be applicable for characterizing their response. A

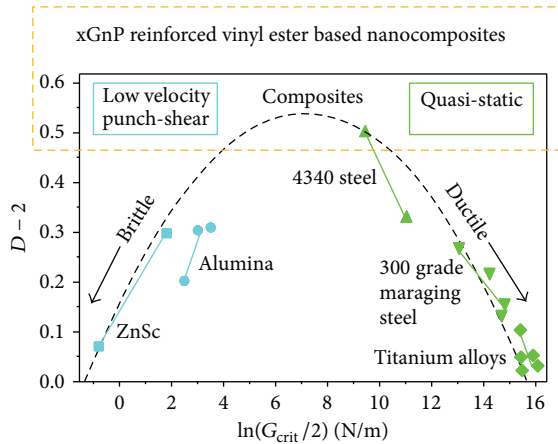


FIGURE 10: Strain rate dependent ductile-to-brittle transition of fracture propagation mechanism investigated by surface fractal analysis [11, 16, 17].

higher strain rate would correspond to a shorter loading time, equivalent to lower temperatures [19] causing the ductile-to-brittle transition of the specimen. Similar phenomenon has been previously observed by the authors while measuring fractal parameters of the fractured surfaces on the same candidate materials generated [11].

About 25% increase in tensile strength is observed at high-strain rate loading (Figures 9(a)(ii) and 9(b)(ii)) with respect to the quasi-static response (Figures 8(a)(ii) and 8(b)(ii)). The energy absorption capacity of pure vinyl ester is adversely affected under high-strain rate loading, whereas it is improved with the addition of xGnP reinforcement (Figures 8(a)(iii) and 9(a)(iii)). However, additional CTBN toughening agent could not contribute towards increasing the energy absorbing capacity (Figures 8(b)(iii) and 9(b)(iii)).

4. Conclusions

Surface fractal analysis, in previous research, depicted the ductile or brittle fracture propagation mechanism, depending upon the rate of loading. In the current research, quasi-static and high-strain rate experimental investigations characterize the effect of strain rate and the contribution of xGnP reinforcement along with CTBN toughening on the indirect tensile properties of vinyl ester based nanocomposites. Tensile strength and energy absorbing capacity of pure vinyl ester are reduced by the addition of xGnP reinforcement and even with CTBN toughening under quasi-static loading. Addition of CTBN marginally improved the energy absorbing capacity of the only xGnP reinforced (without CTBN) nanocomposites under quasi-static loading. Tensile strength of pure vinyl ester remains almost the same with the addition of xGnP reinforcement and even with CTBN toughening under high-strain rate loading. Energy absorbing capacity of pure vinyl ester is improved with addition of xGnP reinforcement under high-strain rate loading. Pure vinyl ester shows ductile-to-brittle transition from quasi-static to high-strain rate loading. Tensile strength observed in quasi-static test is increased at

high-strain rate loading for these candidate nanocomposites. The energy absorption capacity of pure vinyl ester is adversely affected under high-strain rate loading.

Conflict of Interests

The authors declare that there is no conflict of interests regarding the publication of this paper.

Acknowledgments

Partial support for this research was provided by Office of Naval Research, Solid Mechanics Program (Dr. Yapa D. S. Rajapakse, Program Manager) Grant no. N00014-7-1-1010 and US Army Research Office under the DOD-PIRT sub-contract through North Carolina A & T University Grant no. 300223243A. The vinyl ester nanocomposite panels were manufactured by Dr. Larry Drzal's group at Michigan State University.

References

- [1] K. N. Shivakumar, G. Swaminathan, and M. Sharpe, "Carbon/vinyl ester composites for enhanced performance in marine applications," *Journal of Reinforced Plastics and Composites*, vol. 25, no. 10, pp. 1101–1116, 2006.
- [2] Ashland Inc, "DERAKANE 510A-40 epoxy vinyl ester resin," Technical Datasheet Document 1775V2 F2, 2011, (English).
- [3] D. D. L. Chung, "Exfoliation of graphite," *Journal of Materials Science*, vol. 22, no. 12, pp. 4190–4198, 1987.
- [4] M. L. Auad, P. M. Frontini, J. Borrajo, and M. I. Aranguren, "Liquid rubber modified vinyl ester resins: fracture and mechanical behavior," *Polymer*, vol. 42, no. 8, pp. 3723–3730, 2001.
- [5] J. Fröhlich, R. Thomann, and R. Mülhaupt, "Toughened epoxy hybrid nanocomposites containing both an organophilic layered silicate filler and a compatibilized liquid rubber," *Macromolecules*, vol. 36, no. 19, pp. 7205–7211, 2003.
- [6] A. Yasmin and I. M. Daniel, "Mechanical and thermal properties of graphite platelet/epoxy composites," *Polymer*, vol. 45, no. 24, pp. 8211–8219, 2004.
- [7] H. Fukushima and L. T. Drzal, "Graphite nanoplatelets as reinforcement for polymers: structural and electrical properties," in *Proceedings of the 17th International Conference on American Society for Composites*, 2004.
- [8] L. T. Drzal and H. Fukushima, "Exfoliated graphite nanoplatelets (xGnP): a carbon nanotube alternative," in *Proceedings of the NSTI Nanotechnology Conference and Trade Show*, vol. 1, pp. 170–173, Boston, Mass, USA, May 2006.
- [9] J. Lu, I. Do, L. T. Drzal, R. M. Worden, and I. Lee, "Nanomaterial-decorated exfoliated graphite nanoplatelet based glucose biosensors with high sensitivity and fast response," *ACS Nano*, vol. 2, no. 9, pp. 1825–1832, 2008.
- [10] M. Zeng, X. Sun, X. Yao et al., "Free-volume properties and toughening behavior of cyanate ester resin/carboxyl-randomized liquid butadiene-acrylonitrile rubber composites," *Journal of Materials Science*, vol. 44, no. 16, pp. 4270–4278, 2009.
- [11] B. Pramanik, T. Tadealli, and P. R. Mantena, "Surface fractal analysis for estimating the fracture energy absorption of nanoparticle reinforced composites," *Materials*, vol. 5, no. 5, pp. 922–936, 2012.

- [12] A. Magableh, *Viscoelastic and shock response of nanoclay and graphite platelet reinforced vinyl ester nanocomposites*, [PhD dissertation], Department of Mechanical Engineering, University of Mississippi, 2010.
- [13] P. R. Mantena, A. H. D. Cheng, A. Al-Ostaz, and A. M. Rajendran, "Blast and impact resistant composite structures for navy ships," in *Proceedings of Marine Composites and Sandwich Structures*, Office of Naval Research, Solid Mechanics Program Review, Adelphi, Md, USA, September 2010.
- [14] B. Pramanik and P. R. Mantena, "Viscoelastic response of graphite platelet and CTBN reinforced vinyl ester nanocomposites," *Materials Sciences and Applications*, vol. 2, no. 11, pp. 1667–1674, 2011.
- [15] B. Pramanik and P. R. Mantena, "Energy absorption of nano-reinforced and sandwich composites in ballistic and low-velocity punch-shear," *Open Journal of Composite Materials*, vol. 2, no. 3, pp. 87–96, 2012.
- [16] R. E. Williford, "Multifractal fracture," *Scripta Metallurgica*, vol. 22, no. 11, pp. 1749–1754, 1988.
- [17] C. Lu, "Some notes on the study of fractals in fracture," in *Proceedings of 5th Australasian Congress on Applied Mechanics (ACAM '07)*, pp. 234–239, Brisbane, Australia, December 2007.
- [18] B. Pramanik, *High-strain rate tensile characterization of graphite platelet reinforced vinyl ester nanocomposites using split-hopkinson pressure bar*, [PhD dissertation], Department of Mechanical Engineering, The University of Mississippi, 2013.
- [19] W. Chen, F. Lu, and M. Cheng, "Tension and compression tests of two polymers under quasi-static and dynamic loading," *Polymer Testing*, vol. 21, no. 2, pp. 113–121, 2002.

Review Article

A Brief Review of Some Local Approaches for the Failure Assessment of Brittle and Quasi-Brittle Materials

F. Berto

Department of Management and Engineering, University of Padua, Stradella San Nicola 3, 36100 Vicenza, Italy

Correspondence should be addressed to F. Berto; filippo.berto@unipd.it

Received 14 November 2013; Accepted 14 January 2014; Published 25 February 2014

Academic Editor: Manuel Elices

Copyright © 2014 F. Berto. This is an open access article distributed under the Creative Commons Attribution License, which permits unrestricted use, distribution, and reproduction in any medium, provided the original work is properly cited.

Brittle failure of components weakened by cracks and notches is a topic of active and continuous research. It is a key topic for all researchers who face the problem of fracture of materials under different loading conditions and deals with a large number of applications in different engineering fields. This topic is significant in all the cases where intrinsic defects of materials or geometrical discontinuities give rise to localized stress concentration which, in brittle materials, may generate a crack leading to catastrophic failure or to a shortening of the assessed structural life. Whereas cracks are viewed as unpleasant entities in most engineering materials, U- and V-notches of different acuities are sometimes deliberately introduced in design and manufacturing of structural components. The main aim of the present contribution is to present a short review of some local approaches applicable near stress raisers both sharp and blunt allowing the reader to have an update state of the art for the considered criteria.

1. Introduction

Brittle failure of components in particular when weakened by cracks and sharp and blunt V-notches is a relevant topic of active and continuous research. It is attractive for all researchers who face the problem of fracture of materials under different loading conditions and deals with a large number of applications in different engineering fields, not only with the mechanical one. It is no longer uncommon for the scientists and engineers to speak of the same language when dealing with the design and manufacturing of intricate devices and this is particularly true when they are nanometer or smaller in size and large-scale effects take place. In fact, the attempt to strike a common ground on which physical events might be connected is a curiosity that arises naturally in research. By analyzing the topography of the cracking of ice-wedge polygons in Arctic permafrost of mud flats in Death Valley and of craze-cracks (heat-checking) at the bore of a gun tube it is easy to observe that they are all strikingly similar. However, they span five orders of magnitude in scale, with the maximum plate dimensions for ice and mud being, respectively, 22 and 0.25 meters and with the minimum plate size for gun tube craze cracking being about 0.2 millimeters.

Design based on damage tolerance criteria often deals with notched components giving rise to localized stress concentrations which, in brittle materials, may generate a crack leading to catastrophic failure or to a shortening of the assessed structural life.

When the stress concentrators are cracks, or sharp V-notches, the tools derived from linear elastic fracture mechanics are applicable. As soon as the notch is blunted, that is, the notch root radius is not zero, the stress singularity disappears and linear elastic fracture mechanics is no longer applicable. The problem becomes more involved if the loading symmetry is lost, that is, when the notched structural component is subjected to mixed mode loading. Moreover modelling damage around blunted notches has proven very difficult and is strongly dependent on the microstructural aspects of each material. In fact, under mixed mode loading, particularly for notches with a nonnegligible radius, providing a suitable unifying fracture criterion is the current challenge which requires further investigations. The scarcity of experimental results available in the literature dealing with blunt notches under prevalent mode II, mode III, or compression loadings confirms that the problem of brittle or quasi-brittle fracture of blunt notched components is far from being completely solved.

The most important and revolutionary concept for the fracture assessment is that based on the definition of an “elementary” volume and “structural support length” introduced many years ago by Neuber [1–3]. It states that not the theoretical maximum notch stress is the static or fatigue strength-effective parameter in the case of pointed or sharp notches, but rather the notch stress averaged over a short distance normal to the notch edge. The concept can be applied not only to static loadings but also to high cycle fatigue regime. As an extension of Neuber’s concept, more recently Radaj proposed the application of the fictitious notch rounding for the fracture and fatigue assessment of structural materials [4–6].

Fundamentals of critical distance mechanics applied to static brittle failure state that crack propagation occurs when the normal strain or circumferential stress at some critical distance from the crack tip reaches a given critical value. The proposal of mode I dominance for cracked plates which is another key concept was suggested by Erdogan and Sih in their pioneering work dated 1963 [7]. It deals with cracked plates under plane loading and transverse shear and states that the crack grows in the direction almost perpendicular to the maximum tangential stress in radial direction from its tip. Some recent and effective improvements of the maximum tangential stress criterion have been proposed by Ayatollahi and coworkers [8–12] taking into account also the contribution due to the T-stress. Other researchers applied the Point and Line methods to assess the fatigue and fracture behaviour of different materials weakened by sharp and blunt notches [13–17].

Dealing with the strain energy density concept, it is worthwhile contemplating some fundamental contributions by Sih where the concept of “core region” surrounding the crack tip was proposed. The main idea is that the continuum mechanics stops short at a distance from the crack tip, providing the concept of the radius of the core region. The strain energy density factor (S) was defined as the product of the strain energy density by a critical distance from the point of singularity. Sih’s criterion is a point-wise criterion. Failure was thought of as controlled by a critical value of the S -factor, whereas the direction of crack propagation was determined by imposing a minimum condition on S [18–20].

Gillemot, first, measured the deformation energy required for crack initiation in a unit volume of material calling that parameter Absorbed Specific Fracture Energy (ASFE). A simple link between the strain energy density factor (S) and the ASFE was found [21–23]. Considering the fracture energy some interesting developments have been carried out by Elices and coworkers dealing with the cohesive zone model applied to different materials and weakened not only by cracks but also by notches [24–28].

Different from Sih’s criterion, which is a pointwise criterion, the averaged strain energy density criterion has been proposed in [29] and applied combining the concept of elementary volume proposed by Neuber and the local mode I concept proposed by Erdogan and Sih. The new criterion states that brittle failure occurs when the mean value of the strain energy density over a control volume (which becomes an area in two dimensional cases) is equal to a critical energy for the material. The SED approach is based both on a precise

definition of the control volume and the fact that the critical energy does not depend on the notch sharpness. Such a method was formalised and applied first to sharp, zero radius, V-notches and later extended to blunt U- and V-notches under mode I loading [30] and applied to welded joints [31–33]. The control radius of the volume, over which the energy has to be averaged, depends on the ultimate tensile strength, the fracture toughness, and Poisson’s ratio in the case of static loads, whereas it depends on the unnotched specimen’s fatigue limit, the threshold stress intensity factor range, and Poisson’s ratio under high cycle fatigue loads. The approach was successfully used under both static and fatigue loading conditions to assess the strength of notched and welded structures subjected to predominant mode I and also to mixed mode loading. Dealing with both notched and welded components, a final synthesis of more than 2400 experimental data from static and fatigue tests has been carried out. Very different materials have been considered with a control radius, ranging from $0.4 \mu\text{m}$ to $500 \mu\text{m}$ [34, 35].

Dealing with brittle failure of notched components and summarising the most recent experimental results reported in the literature, a complete review of the main local approaches applicable near stress raisers both sharp and blunt has been carried out in [35]. Among the discussed criteria attention is paid to the volume-based SED approach developed in the above mentioned paper and recently applied to assess the brittle failure of a large bulk of materials. After an accurate summary of the analytical frame and the theoretical basis, some recent data from isostatic graphite (see [36] and references therein), largely used atomic reactors for excellent isotropic electrical, thermal, and mechanical properties, under different loading conditions have been discussed in detail together with data from polymethyl methacrylate [37]. A final synthesis summarising all the data available up to now from very different materials is reported in the paper. The application of the SED approach to three-dimensional problems and the advantages of the approach in comparison with other proposed local approaches are discussed in [35] as well.

A short review of some local approaches familiar to the author and applicable near stress raisers both sharp and blunt is reported in the present paper. Recent useful references are provided for authors engaged in such topics giving an update state of the art of each considered criterion.

2. Generalized Maximum Tangential Stress Criterion

One of the fundamental idea in the fracture assessment of brittle fracture is the so-called local mode I concept. The proposal of mode I dominance was suggested in [7] dealing with cracked plates (see Figure 1) under plane loading and transverse shear, where the crack grows in the direction almost perpendicular to the maximum tangential stress (MTS) in radial direction from its tip. This theory is one of the widely used theories for mixed mode crack growth. In more detail the criterion states that the crack propagation starts along the direction on which the tangential stress becomes maximum. Along that line the shear stress is equal to zero

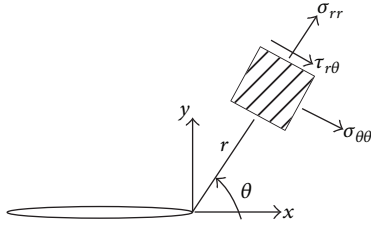


FIGURE 1: Plate with a central crack.

and a principal stress state occurs. The fracture starts when the maximum tangential stress (σ_θ) reaches a critical stress (σ_c) for the material equal to the fracture stress in uniaxial tension. Mathematically the conditions for the crack growth direction can be expressed by the following equations:

$$\frac{\partial \sigma_{\theta\theta}}{\partial \theta} = 0, \quad \frac{\partial^2 \sigma_{\theta\theta}}{\partial \theta^2} < 0, \quad (1a)$$

$$\sigma_{\theta\theta}(\theta_c) = \sigma_c. \quad (1b)$$

The singular stress field in the vicinity of the crack tip is expressed by the following equation:

$$\begin{Bmatrix} \sigma_{\theta\theta} \\ \sigma_{rr} \\ \tau_{r\theta} \end{Bmatrix} = \frac{K_I}{4\sqrt{2\pi r}} \times \left[\begin{pmatrix} 3 \cos\left(\frac{\theta}{2}\right) \\ 5 \cos\left(\frac{\theta}{2}\right) \\ \sin\left(\frac{\theta}{2}\right) \end{pmatrix} + \begin{pmatrix} \cos\left(\frac{3\theta}{2}\right) \\ -\cos\left(\frac{3\theta}{2}\right) \\ \sin\left(\frac{3\theta}{2}\right) \end{pmatrix} \right] + \frac{K_{II}}{4\sqrt{2\pi r}} \times \left[\begin{pmatrix} -3 \sin\left(\frac{\theta}{2}\right) \\ -5 \sin\left(\frac{\theta}{2}\right) \\ \cos\left(\frac{\theta}{2}\right) \end{pmatrix} + 3 \begin{pmatrix} -\sin\left(\frac{3\theta}{2}\right) \\ \sin\left(\frac{3\theta}{2}\right) \\ \cos\left(\frac{3\theta}{2}\right) \end{pmatrix} \right]. \quad (2)$$

In (2) K_I and K_{II} are the stress intensity factors according to the linear elastic fracture mechanics.

By observing that the circumferential stress $\sigma_{\theta\theta}$ at the direction of crack extension is a principal stress the shear stress $\tau_{r\theta}$ along that direction vanishes. It can be easily shown that the above criterion for the crack growth direction is the solution of the following equation:

$$K_I \sin \theta + K_{II} (3 \cos \theta - 1) = 0. \quad (3)$$

For the calculation of the stress $\sigma_{\theta\theta}$ from (2) a critical distance r_0 measured from the crack tip must be introduced. The concept of a core region surrounding the crack tip has been proposed by Sih [18–20]. The idea is that the continuum mechanics solution, as well as experimental measurement, stops at a distance r_0 from the crack tip. The distance r_0 serves as a scale size of analysis at the continuum level. This criterion has been widely used because of its simplicity. Moreover, it has been supported by many experimental observations. The application of this criterion can be found from the works by several authors and in particular by Ayatollahi and coworkers who extended the approach to sharp and blunt V-notches considering not only the singular terms but also the nonsingular ones [8–12].

3. Sih's Criterion

The concept of “core region” surrounding the crack tip was proposed in [18–20]. The main idea is that the continuum mechanics stops short at a distance from the crack tip, providing the concept of the radius of the core region. The strain energy density factor S was defined as the product of the strain energy density by a critical distance from the point of singularity. Failure was thought of as controlled by a critical value S_c , whereas the direction of crack propagation was determined by imposing a minimum condition on S . The theory was extended to employ the total strain energy density near the notch tip, and the point of reference was chosen to be the location on the surface of the notch where the maximum tangential stress occurs. It is worth mentioning that Sih's criterion is a pointwise criterion. The material element is always kept at a finite distance from the crack or the notch tip outside the “core region” where the inhomogeneity of the material due to microcracks, dislocations, and grain boundaries precludes an accurate analytical solution. The theory can account for yielding and fracture and is applicable also to ductile materials. Depending on the local stress state, the radius of the core region may or may not coincide with the critical ligament r_c that corresponds to the onset of unstable crack extension. The ligament r_c depends on the fracture toughness K_{IC} , the yield stress σ_y , Poisson's ratio ν , and, finally, on the ratio between dilatational and distortional components of the strain energy density. The direction of σ_{\max} determines maximum distortion, while σ_{\min} relates to dilatation. Distortion is associated with yielding; dilatation tends to be associated with the creation of free surfaces or fracture and occurs along the line of expected crack extension.

A critical value of strain energy density function $(dW/dV)_c$ has been extensively used since 1965, when first the ratio $(dW/dV)_c$ was determined experimentally for various engineering materials by using plain and notched specimens. The deformation energy required for crack initiation in a unit volume of material is called Absorbed Specific Fracture Energy (ASFE) and its links with the critical value of J_c and the critical factor S_c were widely discussed. This topic was deeply considered in [21–23] where it was shown that $(dW/dV)_c$ is equivalent to S_c/r , with S_c being the critical strain energy density factor and the radius vector r the location of failure. Since distributions of the absorbed

specific energy W in notched specimens are not uniform, it was assumed that the specimen cracks as soon as a precise energy amount has been absorbed by the small plastic zone at the root of the notch. If the notch is sufficiently sharp, specific energy due to the elastic deformation is small enough to be neglected as an initial approximation. While measurements of the energy in an infinitely small element are not possible, they can be approximated with sufficient accuracy by calculating the fracture energy over the entire fractured cross section of an unnotched tensile specimen.

Dealing with pointed V-notches the volume energy density factor S was defined and applied as an extension of the method proposed for the crack case. Potential sites of fracture initiation were assessed and the rate change of volume with surface $\Delta V/\Delta A$ was accurately evaluated by using numerical models showing that the local variation of this parameter should be kept smaller than the global average of $\Delta V/\Delta A$ in the system to assure the reliability of the numerical results. Moreover, the critical strain energy density factor, S_c , was plotted as a function of the notch opening angle both for symmetrical and skew-symmetrical loadings [20].

More precisely Sih wrote S as follows [18–20]:

$$S = a_{11}(\theta) K_I^2 + 2a_{12}(\theta) K_I K_{II} + a_{22}(\theta) K_{II}^2, \quad (4)$$

where K_I and K_{II} are the stress intensity factors of Linear Elastic Fracture Mechanics and a_{11} , a_{12} , a_{22} are the angular functions depending on Poisson's ratio ν and the shear modulus; G is related to Young's modulus E as $E = 2G(1 + \nu)$. These functions are

$$\begin{aligned} a_{11} &= \frac{1}{16G} [(1 + \cos(\theta))(\kappa - \cos(\theta))], \\ a_{12} &= \frac{1}{16G} \sin \theta [2 \cos(\theta) - (\kappa - 1)], \\ a_{22} &= \frac{1}{16G} [(\kappa + 1)(1 - \cos \theta) + (1 + \cos \theta)(3 \cos \theta - 1)]. \end{aligned} \quad (5)$$

Here κ takes the value $(3-4\nu)$ for plane strain and $(3-\nu)/(1+\nu)$ for plane stress conditions.

Sih wrote that “the initial crack growth takes place in the direction along which the strain energy density factor S possesses a stationary (minimum) value”; that is,

$$\frac{\partial S}{\partial \theta} = 0. \quad (6)$$

As stated by Sih himself, the S -criterion requires no calculation on the energy release rate and thus possesses the inherent advantage of being able to treat all mixed mode problems for the first time. Unlike the conventional Griffith's theory which measures only the amplitude of local stresses, the fundamental parameter S is direction-sensitive. The difference between Griffith's parameter and S is analogous to the difference between a scalar and a vector. Sih's criterion has been applied prevalently to cracks and sharp notches. However, worth mentioning is also the application to two particular notches: elliptic holes and hyperbolic notches [19].

The extension to other notch shapes is possible, with S being a unifying parameter. This is the main advantage of the present approach.

4. Neuber's Fictitious Notch Rounding (FNR) Approach

According to Neuber [1–3], the theoretical maximum notch stress is not the effective parameter able to control static or fatigue strength in the case of pointed or sharp notches. The notch stress has to be averaged over a short distance normal to the notch edge. Materials have a specific “elementary” volume, which results in a specific “structural support length.” The support effect can be described by averaging the maximum notch stresses in a small material volume (micro-support length ρ^*) at the notch root (with radius ρ). The averaged stress may be expressed by the maximum stress of a corresponding notch of an enlarged, fictitious radius, with the enlargement being expressed by the material parameter ρ^* modified by the microsupport factor s which expresses the influence of multiaxiality and the strength criterion. The length ρ^* exclusively depends on the microstructural material conditions, for example, expressed by the yield limit σ_Y in the high-cycle fatigue range (Neuber [1–3]) or by the fracture toughness K_{Ic} and the local fracture stress σ_{mc} according to $\rho^* = (2/\pi)(K_{Ic}/\sigma_{mc})^2$ in static loading.

The relation $\rho^* = (1/2\pi)(K_{Ic}/\sigma_Y)^2$ with yield limit σ_Y (approximately equal to the ultimate strength in the case of brittle fracture) given by Neuber [1–3] is conformed with the “critical distance approach.”

The fictitious notch rounding concept and its mathematical foundation originate from a time in which the importance of the notch stresses for strength assessments became clear resulting in a demand to determine these stresses either experimentally or theoretically. In order to fully appreciate Neuber's contribution, it is necessary to consider the micro-support concept within the context of the notch stress theory in general which was an amazing achievement at that time and has remained so up to today.

Following Neuber's concept, Radaj [4–6] proposed to predict the high-cycle fatigue strength of welded joints (toe and root failures) based on fictitious notch rounding. The worst case assessment for low-strength steels introduced $\rho = 0$ mm, $s = 2.5$, and $\rho^* = 0.4$ mm. This procedure was proven to be generally applicable to welded joints in structural steels and aluminium alloys. It has become a standardised procedure within the IIW design recommendations.

With the aim to make clear the main points of the Neuber's approach only mode I loading is considered here. When the notch radius is very small, or tends to zero in the worst case condition, the theoretical stress concentration factor K_t reaches very high values and brittle or fatigue failure of the component can no longer be described by the theoretical peak value of the notch stress. Obviously, not the theoretical peak stress but the stress averaged over a material element of finite size can be assumed as decisive for local failure when considering sharp rounded or pointed notches, that is inclusive of corner notches and cracks.

The microstructural material element at the notch tip is characterised by the material-dependent microstructural support length ρ^* . A rough first approximation from experimental results states that $\rho^* \approx 0.1$ mm for low-strength steels and aluminium alloys in fatigue. Stress averaging is performed over this length solving the notch problem and integrating the theoretical notch stresses σ_{th} over ρ^* :

$$\bar{\sigma} = \frac{1}{\rho^*} \int_{x_0}^{x_0+\rho^*} \sigma_{th} dx. \quad (7)$$

In order to simplify this procedure, Figure 2(a), Neuber [1–3] has introduced the concept of fictitious notch rounding. The averaged notch stress $\bar{\sigma}$ can directly be determined by analysing a notch with fictitiously enlarged notch radius ρ_f , Figure 2(b):

$$\rho_f = \rho + s\rho^*. \quad (8)$$

Here, ρ is the actual notch radius and s is the support factor which depends on the multiaxiality of the stress state and the applied failure criterion, $s = 2.0 - 3.0$ in tension loading and $s = 1.0$ in out-of-plane shear loading according to Neuber [1–3]. The factor s results from performing the averaging process for different loading conditions and equivalent stresses.

The method given by Neuber for determining the fictitious notch radius ρ_f (and therefrom the support factor s) consists of the following steps:

- (i) to describe the relevant (equivalent) stress σ (or τ) in the bisector (that is the assumed crack path) by the closed-form expressions for the sharp rounded V-notch (without microstructural support);
- (ii) to determine the peak stress $\bar{\sigma}$ (or $\bar{\tau}$) averaged over the microstructural support length ρ^* (other closed-form expressions);
- (iii) to equate the expression of $\bar{\sigma}$ (or $\bar{\tau}$) for finite ρ^* with that of $\bar{\sigma}$ (or $\bar{\tau}$) for $\rho^* = 0$, in order to derive the fictitious radius ρ_f dependent on ρ , ρ^* , and 2α by numerical procedures;
- (iv) to derive the factor $s = (\rho_f - \rho)/\rho^*$ which is also dependent on ρ , ρ^* , and 2α in general.

Some lacks and controversies remained in Neuber's approach. In particular it has to be noted that the proposal given in the in-plane shear loading was completely neglected and the values of s were given without any reference to the notch opening angle, while a strong influence of this angle was originally stated by Neuber (at least for sharp notches) considering the normal stress criterion both for tension and torsion loading. Also in the more recent edition of Neuber's book [3], the influence of the notch opening angle has disappeared and a single value of s seems to be proposed to describe fictitious notch rounding for any notch opening angle. The values of s given by Neuber for tension (and bending) loading are referring to the plane stress conditions of flat specimens and to (approximately) plane strain condition of axis-symmetric specimens with a circumferential notch. Another missing point was to provide the blunt

notch solution taking into account the influence of other notch geometrical parameters besides the notch radius. In conclusion, some intriguing doubts remain with respect to the application of the approach, in particular when dealing with sharp notches with arbitrary notch opening angles. It has to be also underlined that although Neuber always spoke of "elementary volume" his method is based on an integration on a line and the contribution of the notch flanks is not fully considered in the computation.

With the aim to address the main open points of Neuber's work, the FNR approach was applied to V-notches (see Figure 2) subjected to pure mode I taking advantage of some analytical solutions reported in the literature. The factor s , which quantifies the multiaxiality effect, was found to be highly dependent on the notch opening angle 2α . Table 1 summarizes the values of s under mode I loading and different failure criteria as summarized in a recent review (see [38] and references therein).

Only taking into account the variability of the opening angle, a sound correspondence was found between the theoretical stress concentration factors $K_t(\rho_f)$ (evaluated at the fictitiously rounded notch) and the effective stress concentration factors \bar{K}_t (obtained by integrating the relevant stress over the distance ρ^* in the bisector line of the pointed V-notch).

5. Cohesive Zone Model Applied to Notches

The cohesive model was first proposed in the 1960s by Dugdale [39] and Barenblatt [40] from a theoretical point of view to eliminate the stress singularity at the tip of the crack. In the 1970s, Hillerborg [41] generalised the cohesive zone (CZM) model to explain fracture process where no initial macroscopic crack existed. This last generalization is the starting point for applying this model to notches. A review of this model, together with some improvements, was made in a recent paper by Elices and coworkers [24].

The criterion states that a cohesive crack initiates at the point where the maximum principal stress σ_{11} first reaches a critical value, being termed the cohesive strength f_t . This cohesive crack initiates in the direction perpendicular to the maximum principal stress. After its formation, the cohesive crack opens while transferring stress from one face to the other one. The transferred stress strictly depends on the crack opening displacement. For a monotonic load and local mode I, the stress transferred σ is normal to the crack faces and is a unique function of the crack opening displacement w . The material function linking σ and w is termed the softening function (see Figure 3).

The material behaviour is usually characterised by the constitutive equations of the bulk material and the softening function. As shown in [25–28] the bulk material behaviour can, in many cases, be assumed linearly elastic and the softening function a rectangular law (see Figure 4).

The rectangular softening function has been successfully employed for PMMA at -60°C where fracture assessment of notches in mode I was the prime concern [28]. This softening curve is the simplest one and depends only on two parameters: the cohesive stress f_t and the fracture energy

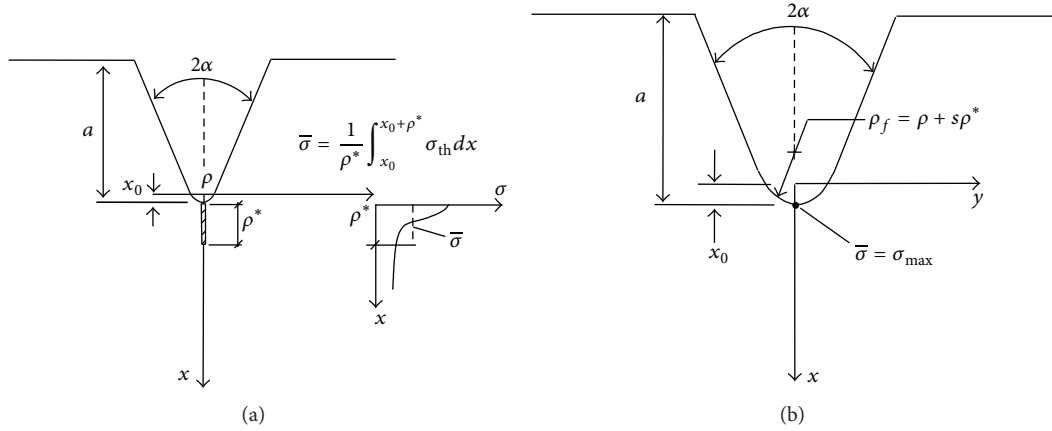


FIGURE 2: Application of the notch rounding approach to mode I loading.

TABLE 1: Microstructural support factor s (plateau values) of tension-loaded V-notches for different failure criteria under plane stress and plane strain conditions.

2α	Normal stress	von Mises plane stress	von Mises plane strain	Beltrami plane stress	Beltrami plane strain
0°	2.00	2.50	2.90	2.30	2.42
90°	2.81	3.37	3.80	3.14	3.28
120°	3.67	4.32	4.84	4.06	4.24
135°	4.56	5.33	5.94	5.02	5.22
150°	6.38	7.41	8.20	6.99	7.25

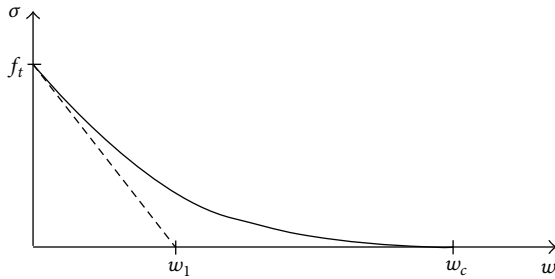


FIGURE 3: Cohesive softening function and initial linear approximation.

G_F . There, the cohesive strength f_t was assumed as equal to the tensile strength measured at -60°C from unnotched specimens, while the fracture energy was calculated from the knowledge of the fracture toughness and

$$G_F = \frac{K_{IC}^2}{E'}, \quad (9)$$

where $E' = E/(1 - \nu^2)$.

In mode I loading, the geometry and loading are symmetrical to the symmetry plane of the notch. This has the advantage of knowing, *a priori*, the crack path as well as the plane on which the cohesive process zone develops and allows us to model only half of the geometry. The cohesive process zone can be modelled on this plane as a mixed boundary condition by stipulating a relationship between stresses and displacements given by the softening function.

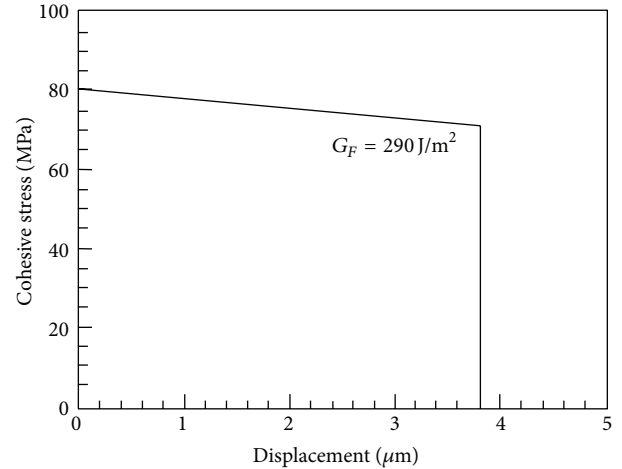


FIGURE 4: Typical softening function for PMMA.

In mixed mode loading the problem is more complex, given that the fracture path is initially unknown. This problem could be overcome by using the local mode I approach, with the hypothesis that the cohesive crack initiates ahead of the notch in the point where the principal stress reaches its maximum value. It could then be analysed by placing close to this point, perpendicular to the notch edge, a band of cohesive elements, where the behaviour is defined by the softening function in a similar manner to mode I. To improve slightly this procedure, a triangle of special elements can be placed

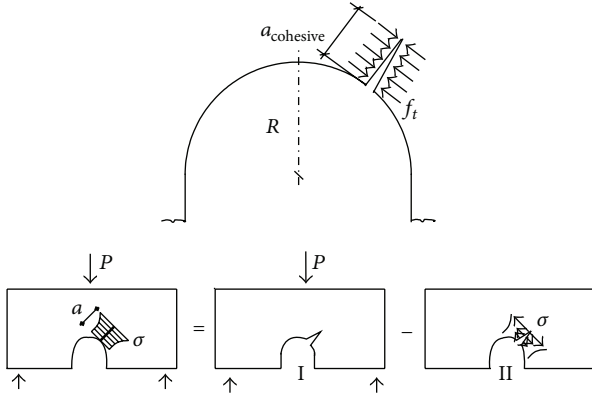


FIGURE 5: Cohesive crack and superposition diagram.

near the critical point, allowing a possible curvature in the initial path of the cohesive crack.

A freeware finite element code (COFE) has been developed at the Department of Materials Science at the Universidad Politécnica de Madrid by Planas and Sancho [42]. The local mode I hypothesis is employed to determine the initial position of the cohesive crack: the point at the notch boundary where the main elastic principal stress is at a maximum. After a first linear elastic calculation to reach such a point, an isosceles triangle is commonly placed over it with the height of the triangle perpendicular to the notch to simulate the cohesive crack. The size of the element decreases near the critical point on the notch up to $4 \mu\text{m}$. Special cohesive elements are placed into the triangular area, using the embedded crack technique. Bulk elements are conventional linear triangular plane strain elements. Calculations are usually performed controlling the displacement of the node at the cohesive crack initial point.

The procedure predicts the maximum load when the maximum displacement between the lips of the cohesive crack reaches the critical value, w_c , equal to the fracture energy divided by the cohesive stress f_t . When the problem is formulated analytically and an actual crack is considered, two equations govern fracture: the maximum displacement among the cohesive crack lips and the fact that the stresses are finite near the cohesive crack. Thus, the stress intensity factor must be equal to zero; that is,

$$w_c = \frac{G_F}{f_t}, \quad (10)$$

$$K_I = 0. \quad (11)$$

Using the superposition principle, the initial state can be analysed as a combination of two auxiliary states, shown in Figure 5: a loaded notched sample, having a crack without transferring stresses and a notched sample without external loads and with a crack loaded by cohesive forces. By introducing this concept into ((10), (11)) one reaches at the analytical formulation that permits to solve the problem. A general description of these two equations and the detailed procedure can be found in [43].

6. The Averaged Strain Energy Density Criterion

Different from Sih's criterion, which is a pointwise criterion, the averaged Strain Energy Density (SED) method as formalized for sharp [29] and blunt notches [30] is reminiscent of Neuber's concept of elementary volume as well as of the local mode I concept proposed by Erdogan and Sih [7]. The averaged SED method condenses together the advantages to be an energy-based criterion with those tied to the definition to a material-dependent structural volume.

With the aim of clarifying the bases of the syntheses presented in this paper both in relation to static failure of brittle or quasi-brittle materials and the fatigue strength of notched components and welded joints, the framework of the SED approach will be presented in detail in the next sections.

The SED approach is based on the idea that under prevailing tensile stresses failure occurs when the strain energy density averaged over a given control volume reaches a critical value, $\bar{W} = W_c$, where W_c depends on the material. If the material behaviour is ideally brittle, then W_c can be evaluated by using simply the conventional ultimate tensile strength σ_t , so that $W_c = \sigma_t^2/2E$. In principle W_c as determined from uniaxial tests cannot be considered independent of the loading mode. Under compression, for example, the critical value of W_c is surely different from the critical value under tension.

Often unnotched specimens exhibit a nonlinear behaviour, whereas the behaviour of notched specimens remains linear. Under these circumstances the stress σ_t should be substituted by the maximum normal stress existing at the edge at the moment preceding the cracking.

In plane problems, the control volume becomes a circle or a circular sector with a radius R_0 in the case of cracks or pointed V-notches in mode I or mixed, I + II, mode loading (Figures 6(a), and 6(b)). A useful expression for the radius R_0 surrounding the control volume has been provided for the crack case under plane strain and plane stress conditions [34, 35]:

$$R_0 = \frac{(1 + \nu)(5 - 8\nu)}{4\pi} \left(\frac{K_{IC}}{\sigma_t} \right)^2 \quad \text{plane strain}, \quad (12a)$$

$$R_0 = \frac{(5 - 3\nu)}{4\pi} \left(\frac{K_C}{\sigma_t} \right)^2 \quad \text{plane stress}. \quad (12b)$$

In the presence of a notch root radius equal to zero it is possible to determine the total strain energy over the area of radius R_0 and then the mean value of the elastic SED referred to the area Ω . The final relationship under pure mode I loading and sharp notches is

$$\bar{W}_1 = \frac{I_1}{4E\lambda_1(\pi - \alpha)} \left(\frac{K_1}{R_0^{1-\lambda_1}} \right)^2, \quad (13)$$

where λ_1 is Williams' mode I eigenvalue and K_1 is the corresponding notch stress intensity factor. The parameter I_1 is different under plane stress and plane strain conditions and is provided in previous references as a function of the notch opening angle and Poisson's ratio [34, 35].

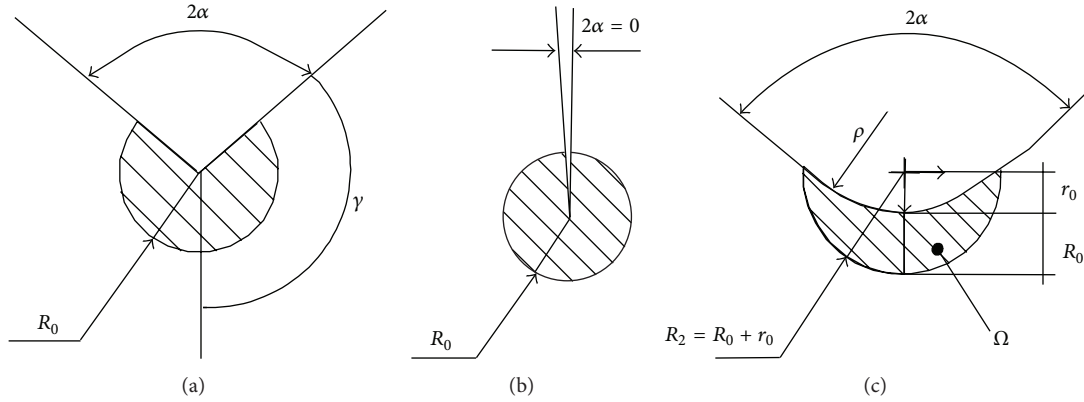


FIGURE 6: Critical volume (area) for sharp V-notch (a), crack (b), and blunt V-notch (c) under mode I loading. Distance $r_0 = \rho \times (\pi - 2\alpha) / (2\pi - 2\alpha)$.

Equation (13) can be extended to pointed V-notches under a different combination of mode I + II + III loadings [29, 32] as a function of the corresponding notch stress intensity factors K_1 , K_2 , and K_3 and of the angular functions e_1 , e_2 , and e_3 [34, 35]. Consider

$$\bar{W} = \frac{e_1}{E} \left[\frac{K_1}{R_0^{1-\lambda_1}} \right]^2 + \frac{e_2}{E} \left[\frac{K_2}{R_0^{1-\lambda_2}} \right]^2 + \frac{e_3}{E} \left[\frac{K_3}{R_0^{1-\lambda_3}} \right]^2. \quad (14)$$

In the presence of rounded V-notches it is possible to link the SED to the maximum principal stress at the notch tip. When the area embraces the semicircular edge of the notch (and not its rectilinear flanks), the mean value of SED can be expressed in the following form [30]:

$$\bar{W}_1 = F(2\alpha) \times H\left(2\alpha, \frac{R_0}{\rho}\right) \times \frac{\sigma_{\text{tip}}^2}{E}, \quad (15)$$

where $F(2\alpha)$ depends on the notch opening angle. H is summarised in [30] as a function of opening angles and the Poisson's ratio.

The proposal of mode I dominance was suggested first by Erdogan and Sih [7] when dealing with cracked plates under plane loading and transverse shear, where the crack grows in the direction almost perpendicular to the maximum tangential stress in radial direction from its tip. By testing plexiglass plates weakened by a crack under pure shear loading, Erdogan and Sih showed that the fracture angle varied around 70 degrees with very small scatter. That angle was in agreement with the theoretical value (70.5 degrees) obtained in the skew-symmetric case.

In the case of sharp V-notches two different eigenvalues characterize the in-plane stress field under mode I and under mode II loading and this fact does not allow determining an equivalent NSIF governing the scale effect. The mode I dominance can be directly taken into account by using Sih's parameter S (which the product of the strain energy density and a convenient distance from the point of singularity) or the SED concept over a material-dependent control volume.

In the case of blunt notches under mixed mode loading the maximum elastic stress is out of the notch bisector line

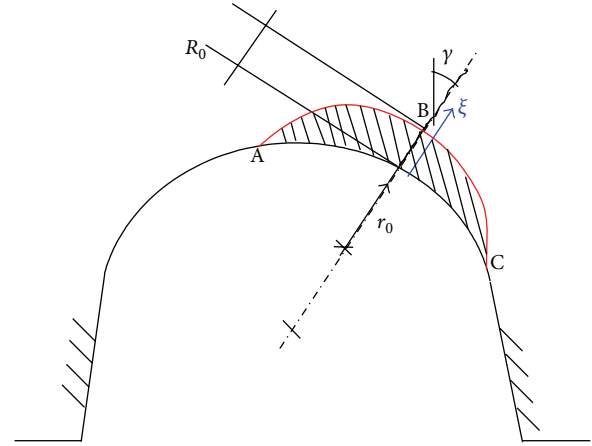


FIGURE 7: V-notch under mixed mode loading.

and its position varies along the notch edge as a function of mode I to mode II stress distributions. This makes the problem of brittle fracture from blunt V-notches more complex than under mode I. In parallel the number of experimental data reported in the literature is quite limited, in particular with reference to prevalent mode II loading conditions, and this makes it difficult to accurately check the different theoretical formulations.

Dealing with blunt U- and V-notches the concept of equivalent local mode I, although not exact in principle, can be seen as an accurate engineering approximation [44, 45]. In particular the SED was generalised from mode I to mixed mode (I + II), under the hypothesis of an equivalent local mode I along the normal line to the notch edge, at a point where the principal stress reaches its maximum value. The approach was used to assess rupture loads of U-notched components made of PMMA and tested at -60°C under mixed mode loading [44, 45].

According to the coordinate system shown in Figure 7, the stress component $\sigma_{\theta\theta}$ normalised to its maximum value occurring along the notch edge is plotted in Figure 8 as a function of the normalised distance ξ/ρ . The inclined path

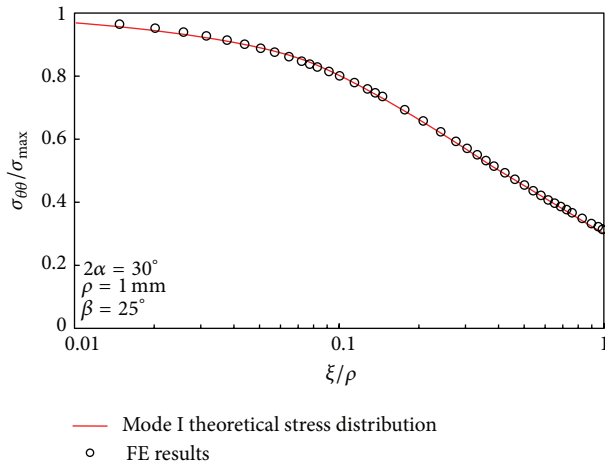


FIGURE 8: Proof of equivalent local mode I.

is perpendicular to the notch edge and starts from the point of the maximum of $\sigma_{\theta\theta}$ stress component along the notch profile. The finite element results are compared with the mode I theoretical solution. The agreement is satisfactory under prevalent mode II, independent of the notch radius. In parallel, the shear stress component has been verified to be zero, as it happens along the notch bisector under mode I loading. This observation leads to the conclusion that under mixed mode loading the line normal to the notch edge and starting from the point of maximum principal stress behaves as a virtual bisector line under pure mode I, confirming the applicability of the equivalent local mode I concept.

The SED can be also easily determined, once defined the control volume, by using a commercial finite element program. In fact, as opposed to the direct evaluation of the stress-based parameters, which needs very refined meshes, the mean value of the elastic SED on the control volume can be determined with high accuracy by using coarse meshes [46]. Very refined meshes are necessary to directly determine the NSIFs from the local stress distributions. Refined meshes are not necessary when the aim of the finite element analysis is to determine the mean value of the local strain energy density on a control volume surrounding the points of stress singularity. The SED in fact can be derived directly from nodal displacements, so that also coarse meshes are able to give sufficiently accurate values for it. As widely described in [35] the SED approach has been recently applied for the fracture assessment of different materials showing the capability of the approach to predict the fracture and fatigue assessments of different kind of materials as well as a large variety of geometries.

7. Conclusions

Brittle failure of components weakened by cracks or sharp and blunt V-notches is a topic of active research. It is attractive for all researchers who face the problem of brittle and quasi-brittle fracture of materials under different loading

conditions. It involves a large number of applications in different engineering fields.

In this paper some criteria for fracture assessment are reviewed, briefly discussing their assumptions. Several representative criteria are included in the review quoting some recent references where the reader can find more details for the direct application of each considered criterion. However, the list of approaches discussed in this paper is not complete and limited to those criteria more familiar to the author's background and research activity.

Conflict of Interests

The author declares that there is no conflict of interests regarding the publication of this paper.

References

- [1] H. Neuber, *Kerbspannungslehre*, Springer, Berlin, Germany, 2nd edition, 1958.
- [2] H. Neuber, "Über die berücksichtigung der spannungskonzentration bei festigkeitsberechnungen," *Konstruktion*, vol. 20, no. 7, pp. 245–251, 1968.
- [3] H. Neuber, *Kerbspannungslehre*, Springer, Berlin, Germany, 3rd edition, 1985.
- [4] D. Radaj, *Design and Analysis of Fatigue Resistant Welded Structures*, Abington, Cambridge, UK, 1990.
- [5] D. Radaj, C. M. Sonsino, and W. Fricke, *Fatigue Assessment of Welded Joints by Local Approaches*, Woodhead Publishing, Cambridge, UK, 2006.
- [6] D. Radaj and M. Vormwald, *Advanced Methods of Fatigue Assessment*, Springer, Heidelberg, Germany, 2013.
- [7] F. Erdogan and C. G. Sih, "On the crack extension in plates under plane loading and transverse shear," *Journal of Basic Engineering*, vol. 85, no. 4, pp. 519–525, 1963.
- [8] D. J. Smith, M. R. Ayatollahi, and M. J. Pavier, "The role of T-stress in brittle fracture for linear elastic materials under mixed-mode loading," *Fatigue & Fracture of Engineering Materials and Structures*, vol. 24, no. 2, pp. 137–150, 2001.
- [9] M. R. Ayatollahi and M. R. M. Aliha, "Cracked Brazilian disc specimen subjected to mode II deformation," *Engineering Fracture Mechanics*, vol. 72, no. 4, pp. 493–503, 2005.
- [10] M. R. Ayatollahi, M. R. M. Aliha, and H. Saghafi, "An improved semi-circular bend specimen for investigating mixed mode brittle fracture," *Engineering Fracture Mechanics*, vol. 78, no. 1, pp. 110–123, 2011.
- [11] M. R. Ayatollahi and A. R. Torabi, "Tensile fracture in notched polycrystalline graphite specimens," *Carbon*, vol. 48, no. 8, pp. 2255–2265, 2010.
- [12] M. R. Ayatollahi and A. R. Torabi, "Failure assessment of notched polycrystalline graphite under tensile-shear loading," *Materials Science and Engineering A*, vol. 528, no. 18, pp. 5685–5695, 2011.
- [13] L. Susmel and D. Taylor, "A simplified approach to apply the theory of critical distances to notched components under torsional fatigue loading," *International Journal of Fatigue*, vol. 28, no. 4, pp. 417–430, 2006.
- [14] L. Susmel and D. Taylor, "On the use of the theory of critical distances to predict static failures in ductile metallic materials

- containing different geometrical features," *Engineering Fracture Mechanics*, vol. 75, no. 15, pp. 4410–4421, 2008.
- [15] L. Susmel and D. Taylor, "The theory of critical distances to predict static strength of notched brittle components subjected to mixed-mode loading," *Engineering Fracture Mechanics*, vol. 75, no. 3-4, pp. 534–550, 2008.
- [16] L. Susmel, "The theory of critical distances: a review of its applications in fatigue," *Engineering Fracture Mechanics*, vol. 75, no. 7, pp. 1706–1724, 2008.
- [17] L. Susmel and D. Taylor, "The theory of critical distances to estimate finite lifetime of notched components subjected to constant and variable amplitude torsional loading," *Engineering Fracture Mechanics*, vol. 98, pp. 64–79, 2013.
- [18] G. C. Sih, "Strain-energy-density factor applied to mixed mode crack problems," *International Journal of Fracture*, vol. 10, no. 3, pp. 305–321, 1974.
- [19] G. C. Sih, *Mechanics of Fracture Initiation and Propagation: Surface and Volume Energy Density Applied as Failure Criterion*, Kluwer Academic, Dodrecht, The Netherlands, 1991.
- [20] G. C. Sih and J. W. Ho, "Sharp notch fracture strength characterized by critical energy density," *Theoretical and Applied Fracture Mechanics*, vol. 16, no. 3, pp. 179–214, 1991.
- [21] L. F. Gillemot, "Brittle fracture of welded materials," in *Proceedings of the 2nd Commonwealth Welding Conference*, pp. 353–358, London, UK, 1965.
- [22] L. F. Gillemot, "Criterion of crack initiation and spreading," *Engineering Fracture Mechanics*, vol. 8, no. 1, pp. 239–253, 1976.
- [23] L. F. Gillemot, E. Czoboly, and I. Havas, "Fracture mechanics applications of absorbed specific fracture energy: notch and unnotched specimens," *Theoretical and Applied Fracture Mechanics*, vol. 4, no. 1, pp. 39–45, 1985.
- [24] M. Elices, G. V. Guinea, F. J. Gómez, and J. Planas, "The cohesive zone model: advantages, limitations and challenges," *Engineering Fracture Mechanics*, vol. 69, no. 2, pp. 137–163, 2002.
- [25] F. J. Gómez and M. Elices, "Fracture of components with V-shaped notches," *Engineering Fracture Mechanics*, vol. 70, no. 14, pp. 1913–1927, 2003.
- [26] F. J. Gómez and M. Elices, "A fracture criterion for sharp V-notched samples," *International Journal of Fracture*, vol. 123, no. 3-4, pp. 163–175, 2003.
- [27] F. J. Gómez and M. Elices, "A fracture criterion for blunted V-notched samples," *International Journal of Fracture*, vol. 127, no. 3, pp. 239–264, 2004.
- [28] F. J. Gómez, M. Elices, and J. Planas, "The cohesive crack concept: application to PMMA at -60°C ," *Engineering Fracture Mechanics*, vol. 72, no. 8, pp. 1268–1285, 2005.
- [29] P. Lazzarin and R. Zambardi, "A finite-volume-energy based approach to predict the static and fatigue behavior of components with sharp V-shaped notches," *International Journal of Fracture*, vol. 112, no. 3, pp. 275–298, 2001.
- [30] P. Lazzarin and F. Berto, "Some expressions for the strain energy in a finite volume surrounding the root of blunt V-notches," *International Journal of Fracture*, vol. 135, no. 1-4, pp. 161–185, 2005.
- [31] P. Lazzarin, T. Lassen, and P. Livieri, "A notch stress intensity approach applied to fatigue life predictions of welded joints with different local toe geometry," *Fatigue & Fracture of Engineering Materials and Structures*, vol. 26, no. 1, pp. 49–58, 2003.
- [32] P. Lazzarin, C. M. Sonsino, and R. Zambardi, "A notch stress intensity approach to assess the multiaxial fatigue strength of welded tube-to-flange joints subjected to combined loadings," *Fatigue & Fracture of Engineering Materials and Structures*, vol. 27, no. 2, pp. 127–140, 2004.
- [33] P. Livieri and P. Lazzarin, "Fatigue strength of steel and aluminium welded joints based on generalised stress intensity factors and local strain energy values," *International Journal of Fracture*, vol. 133, no. 3, pp. 247–278, 2005.
- [34] F. Berto and P. Lazzarin, "A review of the volume-based strain energy density approach applied to V-notches and welded structures," *Theoretical and Applied Fracture Mechanics*, vol. 52, no. 3, pp. 183–194, 2009.
- [35] F. Berto and P. Lazzarin, "Recent developments in brittle and quasi-brittle failure assessment of engineering materials by means of local approaches," *Materials Science and Engineering: R*, vol. 75, pp. 1–48, 2014.
- [36] F. Berto, P. Lazzarin, and M. R. Ayatollahi, "Brittle fracture of sharp and blunt V-notches in isostatic graphite under torsion loading," *Carbon*, vol. 63, pp. 101–116, 2013.
- [37] F. Berto, D. Cendon, P. Lazzarin, and M. Elices, "Fracture behaviour of notched round bars made of PMMA subjected to torsion at -60°C ," *Engineering Fracture Mechanics*, vol. 102, pp. 271–287, 2013.
- [38] D. Radaj, P. Lazzarin, and F. Berto, "Generalised Neuber concept of fictitious notch rounding," *International Journal of Fatigue*, vol. 51, pp. 105–115, 2013.
- [39] D. S. Dugdale, "Yielding of steel sheets containing slits," *Journal of the Mechanics and Physics of Solids*, vol. 8, no. 2, pp. 100–104, 1960.
- [40] G. I. Barenblatt, "The mathematical theory of equilibrium of cracks in brittle fracture," *Advances in Applied Mechanics*, vol. 7, pp. 55–129, 1962.
- [41] A. Hillerborg, M. Modéer, and P. E. Petersson, "Analysis of crack formation and crack growth in concrete by means of fracture mechanics and finite elements," *Cement and Concrete Research*, vol. 6, no. 6, pp. 773–781, 1976.
- [42] J. Planas and J. M. Sancho, "Computational Orientated Finite Elements, COFE," Tech. Rep. JP0501, Departamento de Ciencia de los Materiales, Universidad Politécnica de Madrid, Madrid, Spain, 2007.
- [43] Z. P. Bažant and J. Planas, *Fracture and Size Effect in Concrete and Other Quasibrittle Materials*, CRC Press, Boca Raton, Fla, USA, 1998.
- [44] F. J. Gómez, M. Elices, F. Berto, and P. Lazzarin, "Local strain energy to assess the static failure of U-notches in plates under mixed mode loading," *International Journal of Fracture*, vol. 145, no. 1, pp. 29–45, 2007.
- [45] F. Berto, P. Lazzarin, F. J. Gómez, and M. Elices, "Fracture assessment of U-notches under mixed mode loading: two procedures based on the "equivalent local mode I" concept," *International Journal of Fracture*, vol. 148, no. 4, pp. 415–433, 2007.
- [46] P. Lazzarin, F. Berto, and M. Zappalorto, "Rapid calculations of notch stress intensity factors based on averaged strain energy density from coarse meshes: theoretical bases and applications," *International Journal of Fatigue*, vol. 32, no. 10, pp. 1559–1567, 2010.

Research Article

Toughness Calculation of Postfire Normal Concrete

Qingyang Chen,¹ Anjing Tang,² and Zhoudao Lu¹

¹ College of Civil Engineering, Tongji University, Shanghai 200092, China

² College of Urban Construction and Administration, Yunnan University, Kunming 650091, China

Correspondence should be addressed to Anjing Tang; taj531@126.com

Received 5 October 2013; Revised 7 January 2014; Accepted 7 January 2014; Published 19 February 2014

Academic Editor: Filippo Berto

Copyright © 2014 Qingyang Chen et al. This is an open access article distributed under the Creative Commons Attribution License, which permits unrestricted use, distribution, and reproduction in any medium, provided the original work is properly cited.

Fracture tests of postfire normal concrete with ten temperatures up to 600°C are implemented. Residual fracture toughness using analytical method is determined. Two situations are divided at critical load when calculating the cohesive fracture toughness. The initial and critical fracture toughness could be calculated from the complete load-crack opening displacement curves. Finally, the validation of double-*K* fracture model to the postfire concrete specimens is proved.

1. Introduction

The fracture process of concrete structures underwent three main stages: (i) crack initiation, (ii) stable crack propagation, and (iii) unstable fracture. Accordingly, the double-*K* fracture criterion initially introduced by Xu and Reinhardt [1] showed the crack initiation, crack propagation, and failure during a fracture process until the maximum load is reached. And the two size-independent parameters, initial cracking toughness, K_I^{ini} , and unstable fracture toughness, K_I^{un} , can be used to study the crack propagation of concrete.

In order to determine the double-*K* fracture parameters analytically [2, 3] the value of cohesion toughness K_I^c due to cohesive stress distribution in the fictitious fracture zone was computed using method proposed by Jenq and Shah [4]. The influences of geometrical parameter [5–7] and size effect [2, 3, 8] on fracture toughness were studied by various researchers. It was found that the influence of a_0/D ratio and shape of test specimen on the values of fracture parameters were relatively less than the one of size effect.

The influence of temperature on the fracture parameters was also considered by several researchers, but mainly on the fracture energy and material brittleness [9–13] and relatively fewer discussions on the fracture toughness [14, 15]. In the present paper, the calculation of residual fracture toughness of concrete is carried out. Wedge-splitting experiments of totally ten temperatures varying from 20°C to 600°C are

implemented. The specimen sizes are of 230 × 200 × 200 mm with initial-notch depth ratios of 0.4. The validation of double-*K* fracture model to the postfire normal concrete is proved.

2. Analytical Determination of Cohesive Fracture Toughness

2.1. Effective Crack Extension Length and Residual Young's Modulus. The linear asymptotic superposition assumption was considered in the analytical method presented by Reinhardt et al. [2, 3] to introduce the concept of linear elastic fracture mechanics for calculating the double-*K* fracture parameters. Detailed explanation of the above assumption can be found elsewhere [2].

Based on this assumption, the value of the equivalent-elastic crack length for WS specimen is expressed as

$$a = (h + h_0) \left\{ 1 - \left(\frac{13.18}{E \cdot b \cdot c + 9.16} \right)^{1/2} \right\} - h_0, \quad (1)$$

where $c = \text{CMOD}/P$ is the compliance of specimens and b is specimens thickness; h is specimens height and h_0 is the thickness of the clip gauge holder. For calculation of critical value of equivalent-elastic crack length a_c , the value of crack mouth opening displacement (CMOD) and P is taken as CMOD_c and P_u , respectively.

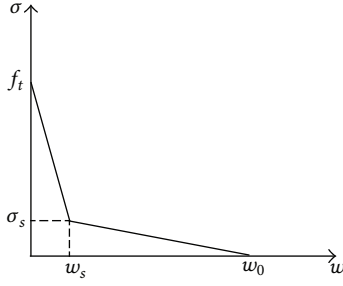


FIGURE 1: The bilinear softening traction-separation law.

The residual Young's modulus E is calculated using the P -CMOD curve as

$$E = \frac{1}{bc_i} [13.18 \times (1 - \alpha)^2 - 9.16], \quad (2)$$

where $c_i = \text{CMOD}_{\text{ini}}/P_{\text{ini}}$ is the initial compliance before cracking, $\alpha = (a_0 + h_0)/(h + h_0)$. The values of critical equivalent-elastic crack length a_c and residual Young's modulus E are listed in Table 1.

2.2. Crack Opening Displacement along the Fracture Process Zone. Since the cohesive stress distribution along the fracture process zone depends on the crack opening displacement and the specified softening law, it is important to know the value of crack opening displacement along the fracture line. It is difficult to measure directly the value of COD along the fracture process zone; for practical purposes the value of COD(x) at the crack length x is computed using the following expression [3]:

$$\begin{aligned} \text{COD}(x) &= \text{CMOD} \left\{ \left(1 - \frac{x}{a}\right)^2 + \left(1.018 - 1.149 \frac{a}{h}\right) \left[\frac{x}{a} - \left(\frac{x}{a}\right)^2 \right] \right\}^{1/2}. \end{aligned} \quad (3)$$

For calculation of critical value of crack tip opening displacement CTOD_c , the value of x and a (see Figure 3) in (3) is taken to be a_0 and a_c , respectively. The value of cohesive stress along the fictitious fracture zone to the corresponding crack opening displacement is evaluated using bilinear stress-displacement softening law as given in (6).

2.3. Softening Traction-Separation Law of Postfire Concrete. The softening traction-separation law is a prerequisite to determine the double- K fracture parameters, at room temperature; many expressions have been proposed based on direct tensile tests [16–20]. Based on numerical studies, simplified bilinear expressions for the softening traction-separation law (illustrated in Figure 1) were suggested by Petersson in 1981 [16], Hilsdorf and Brameshuber in 1991 [19], and Phillips and Zhang in 1993 [20]. The area under the softening curve was defined as the fracture energy G_F . Therefore, one could get the following equation:

$$G_F = \frac{1}{2} (f_t w_s + \sigma_s w_0), \quad (4)$$

where f_t is tensile strength of postfire specimens, w_s is the crack width at break point of softening curve, σ_s is the cohesive stress at the break point of softening curve, and w_0 is crack width at stress-free point.

As a consequence, a general form of the simplified bilinear expression of the softening traction-separation law is given as follows:

$$\begin{aligned} \sigma &= f_t - \frac{(f_t - \sigma_s)w}{w_0}, \quad 0 \leq w \leq w_s \\ \sigma &= \frac{\sigma_s (w_0 - w)}{(w_0 - w_s)}, \quad w_s \leq w \leq w_0 \\ \sigma &= 0, \quad w \geq w_0. \end{aligned} \quad (5)$$

Different values of the break point (σ_s, w_s) and the crack width w_0 at stress-free point were used for the expression proposed by different researchers. In the present work, the bilinear softening function of concrete proposed by Petersson is used for postfire specimens:

$$\begin{aligned} \sigma_s &= \frac{f_t}{3}, \\ w_s &= \frac{0.8G_F}{f_t}, \\ w_0 &= \frac{3.6G_F}{f_t}. \end{aligned} \quad (6)$$

2.4. Determination of Stress Intensity Factor Caused by Cohesive Force. The standard Green's function [21] for the edge cracks with finite width of plate subjected to a pair of normal forces is used to evaluate the value of cohesive toughness. The general expression for the crack extension resistance for complete fracture associated with cohesive stress distribution in the fictitious fracture zone for Mode I fracture is given as follows:

$$K_I^c = \int_{a_0}^a \frac{2\sigma(x) F(x/a, a/h)}{\sqrt{\pi a}} dx, \quad (7)$$

where

$$\begin{aligned} F\left(\frac{x}{a}, \frac{a}{h}\right) &= \frac{3.52(1-x/a)}{(1-a/h)^{3/2}} - \frac{4.35-5.28x/a}{(1-a/h)} \\ &+ \left\{ \frac{1.30-0.30(x/a)^{3/2}}{\sqrt{1-(x/a)^2}} + 0.83 - 1.76 \frac{x}{a} \right\} \\ &\times \left\{ 1 - \left(1 - \frac{x}{a}\right) \frac{a}{h} \right\} \end{aligned} \quad (8)$$

and $\sigma(x)$ is the cohesive force at crack length x , see Figure 3, and its expression is shown in (9) or (11).

At critical condition the value of a is taken to be a_c in (7) and (8). The integration of (8) is done by using Gauss-Chebyshev quadrature method because of existence of singularity at the integral boundary.

TABLE 1: The experimental results of fracture parameters.

Specimen	Temperature	P_{ini}/kN	P_{max}/kN	CMOD _c /mm	CTOD _c /mm	E GPa	G_F N/m	K_I^{ini} MPa·m ^{1/2}	$K_I^{\text{C-A}}$ MPa·m ^{1/2}	$K_I^{\text{un-E}}$ MPa·m ^{1/2}	$K_I^{\text{un-A}}$ MPa·m ^{1/2}
WS6		6.98	11.31	0.195	0.078	21.73	425.91	0.550	1.007	1.594	1.557
WS7		3.88	8.23	0.163	0.100	24.79	482.62	0.303	1.63	1.664	1.933
WS8	65°C	6.88	10.41	0.212	0.087	19.43	487.75	0.557	1.006	1.518	1.563
WS9		7.94	10.71	0.164	0.087	23.25	480.51	0.511	1.174	1.685	1.685
WS10		6.32	11.67	0.229	0.086	16.60	522.36	0.562	0.903	1.507	1.465
Average		6.42	10.47	0.193	0.088	21.16	479.83	0.480	1.161	1.594	1.641
WS16		—	—	—	—	—	—	—	—	—	—
WS17		4.22	6.60	0.317	0.143	11.58	282.51	0.211	0.803	1.206	1.014
WS18	200°C	3.97	6.15	0.213	0.138	6.98	215.14	0.353	0.485	0.863	0.838
WS19		2.41	5.33	0.213	0.138	9.17	235.91	0.215	0.72	0.924	0.935
WS20		3.32	5.24	0.458	0.211	7.00	368.94	0.245	0.796	1.022	1.041
Average		3.50	5.72	0.352	0.157	8.68	376.95	0.256	0.688	1.044	0.957
WS31		1.55	3.61	1.032	0.492	2.56	532.09	0.138	0.572	0.795	0.710
WS32		1.78	3.19	1.218	0.548	1.42	396.93	0.158	0.333	0.574	0.491
WS33	400°C	2.37	3.27	0.768	0.299	2.12	434.89	0.174	0.236	0.621	0.410
WS34		2.36	4.53	0.736	0.302	1.71	598.93	0.125	0.356	0.468	0.494
WS35		—	—	—	—	—	—	—	—	—	—
Average		2.01	3.78	0.901	0.410	1.95	490.71	0.152	0.374	0.615	0.526
WS46		0.76	1.13	1.482	0.684	0.47	228.23	0.067	0.174	0.221	0.231
WS47		0.53	1.48	2.082	0.684	0.48	395.06	0.063	0.209	0.277	0.284
WS48	600°C	0.81	1.65	1.908	0.813	1.14	539.22	0.072	0.478	0.550	0.550
WS49		0.58	1.14	1.687	0.973	0.38	331.99	0.052	0.188	0.225	0.225
WS50		0.62	1.48	2.082	0.727	0.38	273.07	0.068	0.155	0.213	0.213
Average		0.62	1.38	1.848	0.799	0.57	353.51	0.064	0.241	0.297	0.301

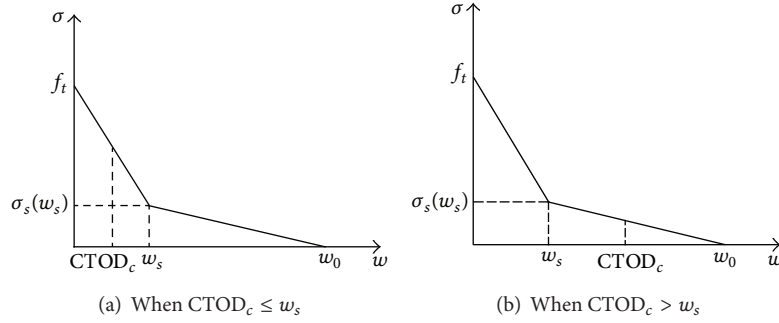
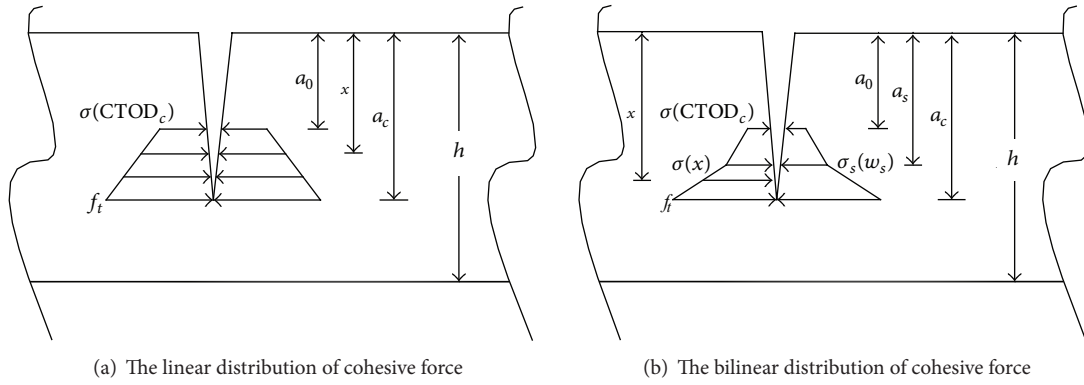
FIGURE 2: Two different situations for $CTOD_c$ and w_s .

FIGURE 3: Cohesive force distribution along the crack length at critical load.

As shown in Figure 2, two conditions at critical load, that is, $CTOD_c \leq w_s$ and $w_s \leq CTOD_c \leq w_c$, may arise at the notch tip while using bilinear softening function. For specimens subjected to temperatures less than 120°C , the critical $CTOD_c$ is less than w_s , whereas, for temperatures higher than 120°C , the critical $CTOD_c$ is wider than w_s .

(A) When the critical $CTOD_c$ corresponding to maximum load P_u is less than w_s as shown in Figure 2(a), the distribution of cohesive stress along the fictitious fracture zone is approximated to be linear as shown in Figure 3(a). The variation of cohesive stress along the fictitious fracture zone for this loading condition, that is, $a_0 \leq a \leq a_c$ or $0 \leq CTOD \leq CTOD_c$, is written as

$$\sigma(x) = \sigma(CTOD_c) + \frac{(f_t - \sigma(CTOD_c))(x - a_0)}{(a_c - a_0)}, \quad (9)$$

where, $\sigma(CTOD_c)$ is the critical values of cohesive stress being at the tip of initial notch. The value of $\sigma(CTOD_c)$ is determined by using bilinear softening function:

$$\sigma(CTOD_c) = \sigma_s(w_s) + \frac{w_s - CTOD_c}{w_s} (f_t - \sigma_s(w_s)). \quad (10)$$

(B) When the critical $CTOD_c$ corresponding to maximum load P_u is wider than w_s as shown in Figure 2(b), the distribution of cohesive stress along the fictitious

fracture zone is approximated to be bilinear as shown in Figure 3(b). The variation of cohesive stress along the fictitious fracture zone for this loading condition, also, $a_0 \leq a \leq a_c$ or $0 \leq CTOD \leq CTOD_c$, is written as

$$\begin{aligned} \sigma_1(x) &= \sigma(CTOD_c) \\ &+ (\sigma_s(w_s) - \sigma(w)) \frac{(x - a_0)}{(a_s - a_0)}, \quad a_s \leq x \leq a_0, \\ \sigma_2(x) &= \sigma_s(w_s) \\ &+ (f_t - \sigma_s(w_s)) \frac{(x - a_s)}{(a_c - a_s)}, \quad a_s \leq x \leq a_c. \end{aligned} \quad (11)$$

The value of $\sigma(CTOD_c)$ is determined by using bilinear softening function:

$$\sigma(CTOD_c) = \frac{w_0 - CTOD_c}{w_0 - w_s} \sigma_s(w_s). \quad (12)$$

The limits of integration of (7) should be taken in two steps: $a_0 \leq x \leq a_s$ for cohesive stress $\sigma_1(x)$ and $a_s \leq x \leq a_c$ for cohesive stress $\sigma_2(x)$, respectively. The same Green's function $F(x/a, a/h)$ for a given effective crack extension will

be determined using (8). The calculated formula is listed as follows:

$$K_I^c = \int_{a_0}^{a_s} \frac{2\sigma_1(x) F(x/a_c, a_c/h)}{\sqrt{\pi a_c}} dx + \int_{a_s}^{a_c} \frac{2\sigma_2(x) F(x/a_c, a_c/h)}{\sqrt{\pi a_c}} dx \quad (13)$$

The effective crack length at break point a_s (shown in Figure 3(b)) is computed from the following nonlinear expression [4] by substituting COD (a_s), CMOD, a_c and h :

$$\begin{aligned} \text{COD}(a_s) &= \text{CMOD} \left\{ \left(1 - \frac{a_s}{a_c} \right)^2 \right. \\ &\quad \left. + \left(1.018 - 1.149 \frac{a_c}{h} \right) \left[\frac{a_s}{a_c} - \left(\frac{a_s}{a_c} \right)^2 \right] \right\}^{1/2}, \end{aligned} \quad (14)$$

where COD (a_s) is the crack opening displacement at a_s , a_c is the effective crack length (according to (1)), and h is the specimen height.

3. Calculation of Double-K Fracture Parameters

The two parameters (K_I^{ini} and K_I^{un}) of double-K fracture criterion for wedge-splitting test are determined using linear elastic fracture mechanics formula given in XU [8]:

$$K(P, a) = \frac{P \times 10^{-3}}{\text{th}^{1/2}} f(\alpha), \quad (15)$$

$$f(\alpha) = \frac{3.675 \times [1 - 0.12(\alpha - 0.45)]}{(1 - \alpha)^{3/2}}, \quad \alpha = \frac{a}{h}. \quad (16)$$

The empirical expression (15) is valid within 2% accuracy for $0.2 \leq \alpha \leq 0.8$.

Equations (15) and (16) can be used in calculation of unstable fracture toughness, K_I^{un} at the tip of effective crack length a_c , in which $a = a_c$ and $P =$ maximum load, P_u for TPBT and CT test specimen geometries, respectively. The initiation toughness, K_I^{ini} , is calculated using (15) and (16) when the initial cracking load, P_{ini} , at initial crack tip is known. In the present paper, the P_{ini} is determined by graphical method using the starting point of nonlinearity in P -CMOD curve described in the following section.

Generally, for postfire concrete specimens the value of initial fracture toughness K_I^{ini} is far less than the value of critical fracture toughness, K_I^{un} , especially for higher temperatures. So much more consideration is put to the critical fracture toughness K_I^{un} . In double-K fracture model, the following relation can be employed:

$$K_I^{\text{un}} = K_I^{\text{ini}} + K_I^c. \quad (17)$$

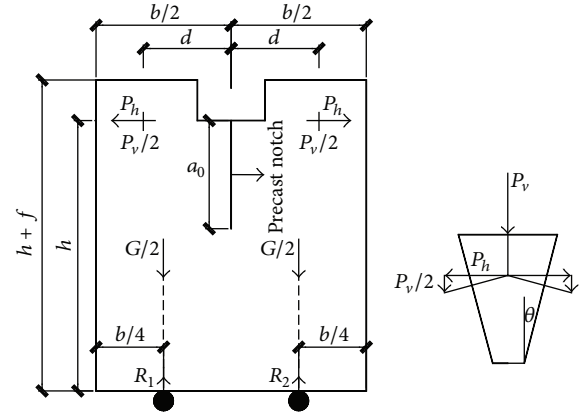


FIGURE 4: The geometry of specimens.

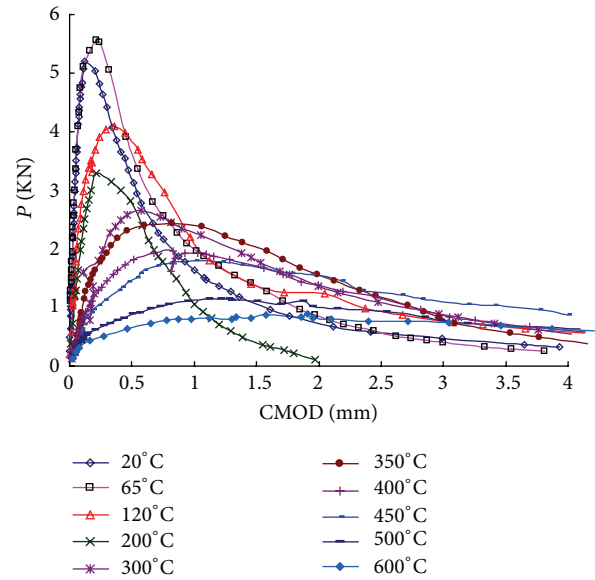
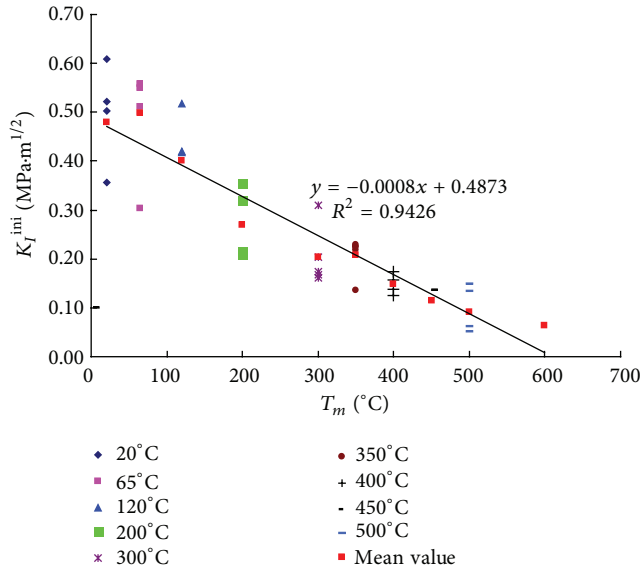
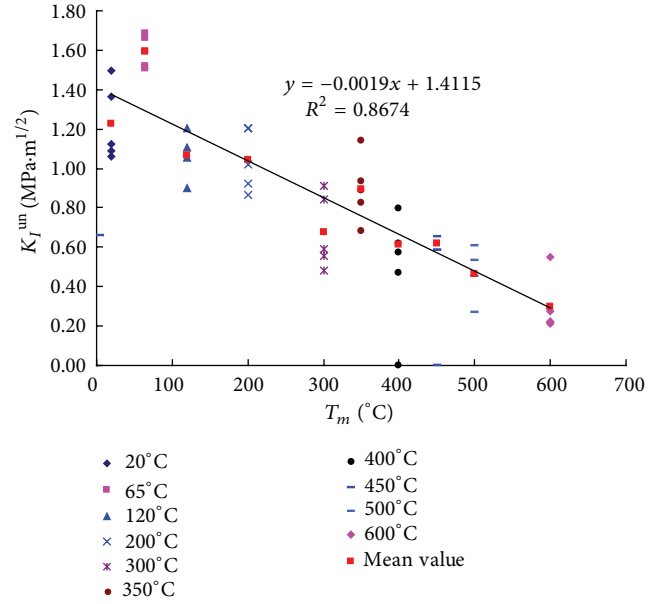
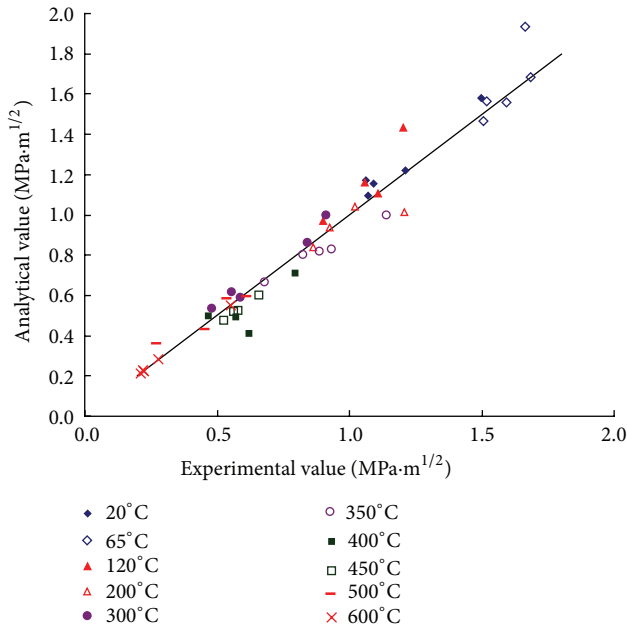


FIGURE 5: P versus CMOD curves of specimens with temperatures.

Here we denote the experimental value, analytical value of critical fracture toughness as $K_I^{\text{un-e}}$, $K_I^{\text{un-A}}$, respectively, and from which we would judge the validation of double-K fracture model to the postfire concrete.

4. Experimental Validation and Comparison of Results

4.1. Experimental Program and Experimental Phenomena. 50 concrete specimens with the same dimensions $230 \times 200 \times 200$ mm were prepared; the geometry of the specimens is shown in Figure 4 ($b = 200$ mm, $d = 65$ mm, $h = 200$ mm, $f = 30$ mm, $a_0 = 80$ mm, $\theta = 15^\circ$). The concrete mix ratios (by weight) were Cement: Sand: Coarse aggregate: Water = 1.00 : 3.44 : 4.39 : 0.80, with common Portland cement-mixed medium sand and 16 mm graded coarse aggregate. The compressive strength at 28 days is 34 MPa. Nine heating temperatures, ranging from 65°C to 600°C ($T_m = 65^\circ\text{C}$,

(a) The tendency of K_I^{ini} with T_m (b) The tendency of K_I^{un} with T_m FIGURE 6: The tendency of residual fracture toughness with heating temperatures T_m .FIGURE 7: Comparison between K_I^{un-A} and K_I^{un-E} .

120°C, 200°C, 300°C, 350°C, 400°C, 450°C, 500°C, 600°C), were adopted with the ambient temperature as a reference. Each wedge splitting specimen was embedded with a thermal couple in the center of specimen for temperature control. An electric furnace with net dimensions 300 × 300 × 900 mm was used for heating. When the designated T_m was reached, the furnace was shut down, and the specimens were naturally

cooled for 7 days prior to the test. It averagely took 50, 95, 135, 182, 218, 254, 294, 342, and 453 mins for the specimens to reach the final temperatures, respectively (from 65°C to 600°C). The detailed experimental information would be found elsewhere [22].

4.2. Experimental Results. Figure 5 shows typical complete load-displacement curves for different heating temperatures up to 600°C. The figure shows that the ultimate load P_u decreases significantly with increasing temperatures T_m , whereas the crack-mouth opening displacement (CMOD) increases with T_m . The initial slope of ascending branches decreases with heating temperatures, and the curves become gradually shorter and more extended.

The recorded maximum load P_u , the recorded crack mouth opening displacement $CMOD_c$ at P_u , the calculated crack tip opening displacement $CTOD_c$ based on (14), the initial cracking load P_{ini} determined by graphical method, the calculated residual Young's modulus E based on (2), the double- K fracture parameters, that is, K_I^{ini} and K_I^{un-E} , and the residual fracture energy G_F are summarized in Table 1. Here we only list part of the statistics.

4.3. Discussion. In order to express the influence on the residual fracture toughness in detail, Figure 6 plots the tendency of initial fracture toughness K_I^{ini} and the unstable fracture toughness K_I^{un} with heating temperatures T_m . It is concluded that the toughness of the two fractures decreases monotonously with T_m because of the thermal damage induced by the heating temperatures.

The initial fracture toughness continuously decreases from 0.498 MPa·m^{1/2} at room temperature to 0.269 MPa·m^{1/2}

at 200°C, 0.115 MPa·m^{1/2} at 450°C, and finally 0.064 MPa·m^{1/2} at 600°C, with a significant loss of 0.434 MPa·m^{1/2} or 96%. The unstable fracture toughness decreases from 1.186 MPa·m^{1/2} at room temperature to 0.297 MPa·m^{1/2} at 600°C, with a significant loss of 0.889 MPa·m^{1/2} or 75%.

Comparing the results shown in Table 1, it can be known that the value of $K_I^{\text{un-A}}$ evaluated by (17) has good coincidence with the one calculated by inserting the values of P_{max} and $a_c = h$ into (15), that is, the critical fracture toughness from analytical and experimental method. Figure 7 shows the relationship between the two parameters. In totally 45 effective specimens, the deviation between $K_I^{\text{un-A}}$ and $K_I^{\text{un-E}}$ of 22 specimens is below 5% and of 40 specimens is below 15%, which accounts for 89% of total specimens.

5. Conclusion

The determination of residual fracture parameter using analytical method is carried out in present research. In calculating the cohesive fracture toughness, two conditions are divided at critical load: for specimens subjected to temperatures less than 120°C, the critical CTOD_c is less than w_s , whereas, for temperatures higher than 120°C, the critical CTOD_c corresponding to maximum load P_u is wider than w_s . This part of work would be a useful supplement to the existed analysis.

Wedge-splitting tests with ten temperatures varying from 20°C to 600°C are implemented. The complete load-crack opening displacement curves are obtained and the initial and critical fracture toughness could be calculated experimentally.

The validation of double- K fracture model to the postfire concrete specimens is proved. In totally 45 effective specimens, the deviation between analytical value $K_I^{\text{un-A}}$ and experimental $K_I^{\text{un-E}}$ of 22 specimens is below 5% and of 40 specimens is below 15%, which accounts for 89% of total specimens.

Conflict of Interests

The authors declare that there is no conflict of interests regarding the publication of this paper.

Acknowledgment

The State Laboratory of Disaster Reduction in Civil Engineering (SLDRCE09-D-02) has supported this research.

References

- [1] S. Xu and H. W. Reinhardt, "Determination of double-K criterion for crack propagation in quasi-brittle fracture—part I: experimental investigation of crack propagation," *International Journal of Fracture*, vol. 98, no. 2, pp. 111–149, 1999.
- [2] X. U. Shilang and H. W. Reinhardt, "Determination of double-K criterion for crack propagation in quasi-brittle fracture—part II: analytical evaluating and practical measuring methods for three-point bending notched beams," *International Journal of Fracture*, vol. 98, no. 2, pp. 151–177, 1999.
- [3] S. Xu and H. W. Reinhardt, "Determination of double-K criterion for crack propagation in quasi-brittle fracture—part III: compact tension specimens and wedge splitting specimens," *International Journal of Fracture*, vol. 98, no. 2, pp. 179–193, 1999.
- [4] Y. S. Jenq and S. P. Shah, "A Fracture toughness criterion for concrete," *Engineering Fracture Mechanics*, vol. 21, no. 5, pp. 1055–1069, 1985.
- [5] Y. Murakami, *Stress Intensity Factors Handbook*, Pergamon Press, London, 1987.
- [6] S. Kumar and S. V. Barai, "Influence of specimen geometry and size-effect on the KR-curve based on the cohesive stress in concrete," *International Journal of Fracture*, vol. 152, no. 2, pp. 127–148, 2008.
- [7] S. Kumar and S. V. Barai, "Influence of specimen geometry on determination of double-K fracture parameters of concrete: a comparative study," *International Journal of Fracture*, vol. 149, no. 1, pp. 47–66, 2008.
- [8] B. L. Karihaloo and P. Nallathambi, "Size-effect prediction from effective crack model for plain concrete," *Materials and Structures*, vol. 23, no. 3, pp. 178–185, 1990.
- [9] Z. P. Bazand and P. C. Prat, "Effect of temperature and humidity on fracture energy of concrete," *ACI Materials Journal*, vol. 85, no. 4, pp. 262–271, 1988.
- [10] G. Baker, "The effect of exposure to elevated temperatures on the fracture energy of plain concrete," *Materials and Structures*, vol. 29, no. 6, pp. 383–388, 1996.
- [11] B. Zhang, N. Bicanic, C. J. Pearce, and G. Balabanic, "Residual fracture properties of normal- and high-strength concrete subject to elevated temperatures," *Magazine of Concrete Research*, vol. 52, no. 2, pp. 123–136, 2000.
- [12] C. V. Nielsen and N. Bicanic, "Residual fracture energy of high-performance and normal concrete subject to high temperatures," *Materials and Structures*, vol. 36, no. 8, pp. 515–521, 2003.
- [13] B. Zhang and N. Bicanic, "Fracture energy of high-performance concrete at high temperatures up to 450°C: the effects of heating temperatures and testing conditions (hot and cold)," *Magazine of Concrete Research*, vol. 58, no. 5, pp. 277–288, 2006.
- [14] G. Prokopski, "Fracture toughness of concretes at high temperature," *Journal of Materials Science*, vol. 30, no. 6, pp. 1609–1612, 1995.
- [15] H. Abdel-Fattah and S. A. Hamoush, "Variation of the fracture toughness of concrete with temperature," *Construction and Building Materials*, vol. 11, no. 2, pp. 105–108, 1997.
- [16] P. E. Petersson, "Crack growth and development of fracture zones in plain concrete and similar materials," Report TVBM-1006, Division of Building Materials, Lund Institute of Technology, Lund, Sweden, 1981.
- [17] V. S. Gopalaratnam and S. P. Shah, "Softening response of plain concrete in direct tension," *Journal of the American Concrete Institute*, vol. 82, no. 3, pp. 310–323, 1985.
- [18] H. W. Reinhardt, H. A. W. Cornelissen, and D. A. Hordijk, "Tensile tests and failure analysis of concrete," *Journal of Structural Engineering*, vol. 112, no. 11, pp. 2462–2477, 1986.
- [19] H. K. Hilsdorf and W. Brameshuber, "Code-type formulation of fracture mechanics concepts for concrete," *International Journal of Fracture*, vol. 51, no. 1, pp. 61–72, 1991.
- [20] D. V. Phillips and Z. Zhang, "Direct tension tests on notched and un-notched plain concrete specimens," *Magazine of Concrete Research*, vol. 45, no. 162, pp. 25–35, 1993.

- [21] H. Tada, P. C. Paris, and G. Irwin, *The Stress Analysis of Cracks Handbook*, Paris Productions Inc., St. Louis, Mo, USA, 1985.
- [22] J. T. Yu, K. Q. Yu, and Z. D. Lu, "Residual fracture properties of concrete subjected to elevated temperatures," *Materials and Structures*, vol. 45, no. 8, pp. 1155–1165, 2012.

Research Article

An Analytical Model for Predicting the Stress Distributions within Single-Lap Adhesively Bonded Beams

Xiaocong He and Yuqi Wang

Innovative Manufacturing Research Centre, Kunming University of Science and Technology, Kunming 650500, China

Correspondence should be addressed to Xiaocong He; hxxcc@yahoo.co.uk

Received 13 November 2013; Accepted 23 December 2013; Published 11 February 2014

Academic Editor: Filippo Berto

Copyright © 2014 X. He and Y. Wang. This is an open access article distributed under the Creative Commons Attribution License, which permits unrestricted use, distribution, and reproduction in any medium, provided the original work is properly cited.

An analytical model for predicting the stress distributions within single-lap adhesively bonded beams under tension is presented in this paper. By combining the governing equations of each adherend with the joint kinematics, the overall system of governing equations can be obtained. Both the adherends and the adhesive are assumed to be under plane strain condition. With suitable boundary conditions, the stress distribution of the adhesive in the longitudinal direction is determined.

1. Introduction

The use of adhesively bonded joint, which uses metallic, composite, and ceramic materials, is of great interest to many industrial sectors including aerospace, automotive, marine, machine tools, package, and appliance industries. This widespread use of adhesive joints is due to ease of application, time and cost savings, high corrosion and fatigue resistance, crack retardance, and good damping characteristics [1–3].

Any joint occurring in practice is designed to carry a given set of loads. Most of the adherends are loaded in tension. The subsequent loads on the adhesive are then a function of the geometry of the joint. Under most operating loads and environmental conditions, the adherends behave in a linearly elastic manner. However, the adhesive may exhibit viscoelastic or nonlinear behaviour. The exact analytical solution to the problem of stress distributions in the bonded area is complex. The existing analytical studies are, therefore, based on certain simplifying assumptions with regard to the modelling of the adhesive and adherends.

In Volkersen's shear-lag analysis, it was assumed that the adhesive deforms only in shear, while the adherend deformed only in tension [4]. The consequences of the rotation of the adherends were first taken into account by Goland and Reissner [5]. The authors derived equations to evaluate the

shearing and normal stresses in the bond layer as well as those in the jointed plates, assuming that the peel and shear stresses were constants across the adhesive thickness. In Cornell's work [6], a variation and extension of Goland and Reissner's method were presented for determining the stresses in adhesive lap joints. The author assumed that the two lap joint plates act like simple beam and the more elastic adhesive layer is an infinite number of shear and tension springs. Differential equations were set up which describe the transfer of the load in one beam through the springs to the other beam. From the solution of these differential equations a fairly complete analysis of the stresses in the lap joint was obtained.

Ojalvo and Eidinoff [7] presented results of an analytical investigation on the influence of bond thickness upon the stress distribution in single adhesive lap joints. The work extended the basic approach for bonded joints, originally introduced by Goland and Reissner, through the use of a more complete shear-strain/displacement equation for the adhesive layer. The work uncovers several interesting phenomena without adding any significant complication to the analysis. Delale et al. [8] analyzed a general plane strain problem of adhesively bonded structures which consist of two different orthotropic adherends. Both the transverse shear stress effects in the adherends and the in-plane normal strain in the adhesive were taken into account. The solution was

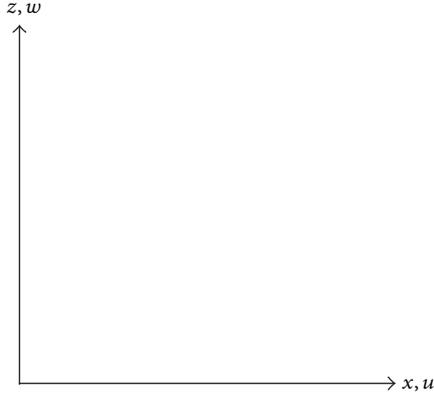


FIGURE 1: Coordinate system.

obtained by assuming linear stress-strain relations for the adhesive. The peak values of the shear as well as those of the normal stress in the adhesive were found to be at the edges of the overlap region. Rossettos et al. [9] established the governing equations for a step lap joint with a void using a modified shear-lag model, where the adhesive can have extensional as well as shear deformations. The model considers quadratic axial deformation across the adhesive thickness.

The objective of this work is to present an analytical model for predicting the stress distributions within a single-lap adhesively bonded beam under tension. This model is a development of the shear-lag analysis model of Volkersen [4]. The derivations are similar to those of Goland and Reissner [5] but the geometry employed is different. By combining the governing equations of each adherend with the joint kinematics, the overall system of governing equations can be obtained. Both the adherends and the adhesive are assumed to be under plane strain condition, and the adhesive stresses are assumed to be uniform across the thickness. With suitable boundary conditions, the stress distribution of the adhesive in the longitudinal direction is determined.

2. Formulation of the Problem

Figure 1 shows the coordinate system used in this study; x and z are coordinates, while u and w represent displacements. A single-lap-jointed beam is shown in Figure 2. The joint length is $2c$. The two adherends are considered to be of equal thickness t and equal length $(l + 2c)$. Two points a and b are the points at the centre of two free edge of the single-lap-jointed beam. The adhesive thickness is η . The joint width is assumed to be large compared with the adherend thickness. If the system is now loaded by tensile forces T per unit of adherend width at the points a and b , the line of action of the forces will be aob .

For studying the system deformation, two coordinate systems (x_1, z_1) and (x_2, z_2) are introduced in Figure 2. The first system is used to analyze the behavior of the left-hand adherend under load. The coordinate x_1 has its origin at the point a , extends along the longitudinal axis of the

adherend, and is positive to the right. w_1 represents transverse deformation of the adherend from the unloaded condition and is positive upwards. A similar definition is taken for (x_2, z_2) with reference to the joint.

If M_1 is equal to the bending moment in the adherend at station x_1 and M_2 is equal to the moment in the joint at station x_2 , each per unit of width, then

$$M_1 = T [\tan \alpha_n x_1 - w_1] \quad (0 \leq x_1 \leq l),$$

$$M_2 = T \left[\tan \alpha_n (l + x_2) - w_2 - \frac{t + \eta}{2} \right] \quad (0 \leq x_2 \leq c), \quad (1)$$

where

$$\tan \alpha_n = \frac{(t + \eta)/2}{l + c}. \quad (2)$$

As $\eta \ll t$ and $t \ll l$, (1) then reduce to the simplified forms by using Taylor series:

$$M_1 = T [\alpha_n x_1 - w_1] \quad (0 \leq x_1 \leq l),$$

$$M_2 = T \left[\alpha_n (l + x_2) - w_2 - \frac{t}{2} \right] \quad (0 \leq x_2 \leq c). \quad (3)$$

As for deformations w_1 and w_2 , we have

$$\frac{d^2 w_1}{dx_1^2} = -\frac{M_1}{D_1}, \quad (4)$$

$$\frac{d^2 w_2}{dx_2^2} = -\frac{M_2}{D_2},$$

where D_1 and D_2 are the flexural rigidities of the adherend and joint, respectively.

From (3) and (4), we have

$$\frac{d^2 w_1}{dx_1^2} = -\frac{T}{D_1} [\alpha_n x_1 - w_1] \quad (0 \leq x_1 \leq l), \quad (5)$$

$$\frac{d^2 w_2}{dx_2^2} = -\frac{T}{D_2} \left[\alpha_n (l + x_2) - w_2 - \frac{t}{2} \right] \quad (0 \leq x_2 \leq c). \quad (6)$$

From the four boundary conditions

$$\begin{aligned} & \text{at } x_1 = 0, & w_1 &= 0, \\ & \text{at } x_1 = l, & x_2 = 0, & w_1 = w_2, \\ & \text{at } x_1 = l, & x_2 = 0, & \frac{dw_1}{dx_1} = \frac{dw_2}{dx_2}, \\ & & \text{at } x_2 = c, & w_2 = 0. \end{aligned} \quad (7)$$

The two preceding equations (5) and (6) have solutions of the form

$$\begin{aligned} w_1 &= A_1 \cosh b_1 x_1 + B_1 \sinh b_1 x_1 + \alpha_n x_1 \quad (0 \leq x_1 \leq l), \\ w_2 &= A_2 \cosh b_2 x_2 + B_2 \sinh b_2 x_2 + \alpha_n \left(l + x_2 - \frac{t}{2} \right) \\ & \quad (0 \leq x_2 \leq c), \end{aligned} \quad (8)$$

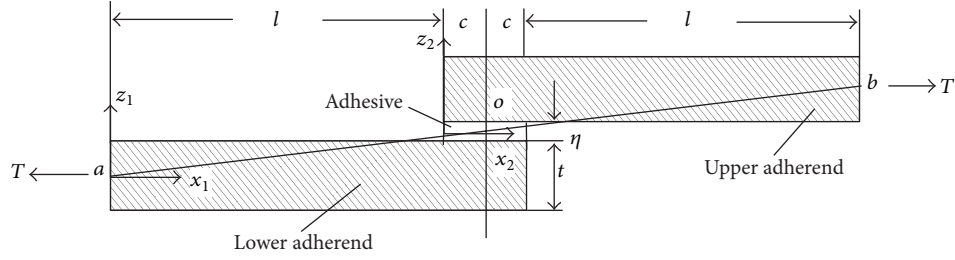


FIGURE 2: A single-lap-jointed beam.

where [5]

$$\begin{aligned}
 A_1 &= \frac{-(t/2) \sinh(b_2 c)}{\sinh(b_1 l) \cosh(b_2 c) + (b_2/b_1) \sinh(b_1 l) \cosh(b_2 c)}, \\
 A_2 &= \frac{(t/2) (b_2/b_1) \cosh(b_1 l) \sinh(b_2 c)}{\sinh(b_1 l) \cosh(b_2 c) + (b_2/b_1) \sinh(b_1 l) \cosh(b_2 c)}, \\
 B_1 &= \frac{-(t/2) \cosh(b_2 c)}{\sinh(b_1 l) \cosh(b_2 c) + (b_2/b_1) \sinh(b_1 l) \cosh(b_2 c)}, \\
 B_2 &= \frac{(t/2) (b_2/b_1) \cosh(b_1 l) \cosh(b_2 c)}{\sinh(b_1 l) \cosh(b_2 c) + (b_2/b_1) \sinh(b_1 l) \cosh(b_2 c)}, \\
 b_1^2 &= \frac{T}{D_1}, \\
 b_2^2 &= \frac{T}{D_2}.
 \end{aligned} \tag{9}$$

3. Stress Distributions in the Adhesive Layer

Figure 3 shows elements of the upper and lower adherends. M , V , and T are the bending moments, vertical shear, and axial tension in the adherends. The subscripts u and l designate quantities pertaining to the upper and lower adherend, respectively. σ_0 and τ_0 are the transverse normal stress and the shear stress, respectively.

The conditions of moment equilibrium for the elements of the adherends are

$$\begin{aligned}
 \frac{dM_u}{dx} - V_u + \tau_0 \frac{t}{2} &= 0, \\
 \frac{dM_l}{dx} - V_l + \tau_0 \frac{t}{2} &= 0.
 \end{aligned} \tag{10}$$

The conditions of horizontal force equilibrium are

$$\begin{aligned}
 \frac{dT_u}{dx} - \tau_0 &= 0, \\
 \frac{dT_l}{dx} + \tau_0 &= 0.
 \end{aligned} \tag{11}$$

The conditions of vertical force equilibrium for the elements of the adherends are

$$\begin{aligned}
 \frac{dV_u}{dx} - \sigma_0 &= 0, \\
 \frac{dV_l}{dx} + \sigma_0 &= 0.
 \end{aligned} \tag{12}$$

The transverse deflections of the upper and lower adherends are denoted by v_u and v_l , respectively, both measured positively upward. Then the thin plate theory gives

$$\begin{aligned}
 \frac{d^2 v_u}{dx^2} &= -\frac{M_u}{D_1}, \\
 \frac{d^2 v_l}{dx^2} &= -\frac{M_l}{D_1},
 \end{aligned} \tag{13}$$

$$\text{with } D_1 = \frac{Et^3}{12(1-\nu^2)},$$

where E and ν are Young's modulus and Poisson's ratio of adherends, respectively. D_1 refers to the flexural rigidity of the adherends.

The longitudinal displacements of the adherend at the adherend boundaries adjacent to the adhesive are denoted by u_u and u_l . Then from the stress-strain relations

$$\begin{aligned}
 \frac{du_u}{dx} &= \frac{1}{E} \left(\frac{T_u}{t} - 6 \frac{M_u}{t^2} \right), \\
 \frac{du_l}{dx} &= \frac{1}{E} \left(\frac{T_l}{t} + 6 \frac{M_l}{t^2} \right).
 \end{aligned} \tag{14}$$

Let E_{ad} and G_{ad} refer to Young's and shear moduli, respectively, of the adhesive material; then

$$\begin{aligned}
 \frac{\tau_0}{G_{ad}} &= \frac{u_u - u_l}{\eta}, \\
 \frac{\sigma_0}{E_{ad}} &= \frac{v_u - v_l}{\eta}.
 \end{aligned} \tag{15}$$

Combining equations from (10) to (14) and differentiating equation (15) we have

$$\frac{d^3 \tau_0}{dx^3} - \frac{8G_{ad}}{Et\eta} \frac{d\tau_0}{dx} = 0, \tag{16}$$

$$\frac{d^4 \sigma_0}{dx^4} + \frac{24(1-\nu^2)E_{ad}}{Et^3\eta} \sigma_0 = 0. \tag{17}$$

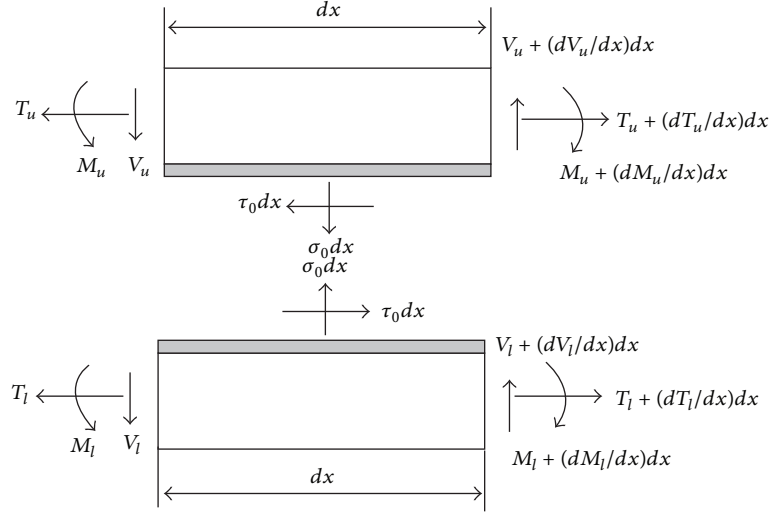


FIGURE 3: Free body diagram of joint with adhesive layer.

The boundary conditions can be written as

$$\begin{aligned}
 &\text{at } x = c, & M_u = T_u = V_u = 0, \\
 &M_l = M_0, & V_l = V_0, & T_l = T, \\
 &\text{at } x = -c, & M_l = T_l = V_l = 0, \\
 &M_u = -M_0, & V_u = V_0, & T_u = T.
 \end{aligned} \tag{18}$$

From (8) and (9) we have

$$\begin{aligned}
 M_0 &= (M_1)_{x_1=l} = -D_1 \left(\frac{d^2 w_1}{dx_1^2} \right)_{x_1=l} = k \frac{Tt}{2}, \\
 V_0 &= \left(\frac{dM_1}{dx_1} \right)_{x_1=l} = kT \left[3(1-\nu^2) \frac{T}{Et} \right]^{1/2}, \\
 k &= \frac{\sinh(b_1 l) \cosh(b_2 c)}{\sinh(b_1 l) \cosh(b_2 c) + (b_1/b_2) \cosh(b_1 l) \sinh(b_2 c)}.
 \end{aligned} \tag{19}$$

On the basis of the differential equations (16) and (17) and the boundary conditions, the distributions of σ_0 and τ_0 in the adhesive are obtained in the form

$$\begin{aligned}
 \sigma_0 &= \frac{pt^2}{\Delta c^2} \left[\left(R_2 \lambda^2 \frac{k}{2} + \lambda k' \cosh \lambda \cos \lambda \right) \cosh \lambda \frac{x}{c} \cos \lambda \frac{x}{c} \right. \\
 &\quad \left. + \left(R_1 \lambda^2 \frac{k}{2} + \lambda k' \sinh \lambda \sin \lambda \right) \sinh \lambda \frac{x}{c} \sin \lambda \frac{x}{c} \right] \\
 \tau_0 &= -\frac{pt}{8c} \left[\frac{\beta c}{t} (1+3k) \frac{\cosh(\beta x/t)}{\sinh(\beta c/t)} + 3(1-k) \right],
 \end{aligned} \tag{20}$$

where

$$\begin{aligned}
 \lambda &= \gamma \frac{c}{t}, & \gamma^4 &= 6 \frac{E_{ad} t}{E \eta}, & \beta^2 &= 8 \frac{G_{ad} t}{E \eta}, \\
 R_1 &= \cosh \lambda \sin \lambda + \sinh \lambda \cos \lambda, \\
 R_2 &= \sinh \lambda \cos \lambda - \cosh \lambda \sin \lambda, \\
 \Delta &= \frac{1}{2} (\sinh 2\lambda + \sin 2\lambda), & k &= \frac{2M_0}{pt^2}, & k' &= \frac{V_0 c}{pt^2}, \\
 b_1 &= 2 \left[\frac{3p(1-\nu^2)}{Et^2} \right]^{1/2}, & b_2 &= \frac{b_1}{2\sqrt{2}}.
 \end{aligned} \tag{21}$$

If the materials and the thickness of the adherends are different, then (17) may become a 7th order differential equation. It is obvious that the analytical model is very complex and only the stress distributions of the adhesive in the longitudinal direction are determined. In addition, the adhesive stresses actually are not uniform across the thickness. In other words, the simplifications have restricted the results. Usually, when we consider different boundary conditions by a closed-form analysis, the limitation is how tractable a realistic mathematical model is within an algebraic solution. To overcome this limitation, the finite element analysis (FEA) technique can be employed.

4. Summary

An analytical model was presented for predicting the stress distributions within a single-lap adhesively bonded beam under tension. By combining the governing equations of each adherend with the joint kinematics, the overall system of governing equations can be obtained. Both the adherends and the adhesive are assumed to be under plane strain condition, and the adhesive stresses are assumed to be uniform across the thickness. With suitable boundary conditions, the stress

distribution of the adhesive in the longitudinal direction is determined.

Conflict of Interests

The authors declare that there is no conflict of interests regarding the publication of this paper.

Acknowledgment

This study is partially supported by the Special Program of the Ministry of Science and Technology, China (Grant no. 2012ZX04012-031).

References

- [1] X. He, "A review of finite element analysis of adhesively bonded joints," *International Journal of Adhesion and Adhesives*, vol. 31, no. 4, pp. 248–264, 2011.
- [2] X. He, F. Gu, and A. Ball, "Fatigue behaviour of fastening joints of sheet materials and finite element analysis," *Advances in Mechanical Engineering*, vol. 2013, Article ID 658219, 9 pages, 2013.
- [3] X. He, "Finite element analysis of torsional free vibration of adhesively bonded single-lap joints," *International Journal of Adhesion and Adhesives*, vol. 48, pp. 59–66, 2014.
- [4] O. Volkersen, "Die Nietkraftverteilung in Zugbeanspruchten Nietverbindungen mit Konstanten Laschenquerschnitten," *Luftfahrtforschung*, vol. 15, pp. 41–47, 1938.
- [5] M. Goland and E. Reissner, "Stresses in cemented joints," *Journal of Applied Mechanics*, vol. 11, pp. A17–A27, 1944.
- [6] R. W. Cornell, "Determination of stresses in cemented lap joints," *Journal of Applied Mechanics*, vol. 20, pp. 355–364, 1953.
- [7] I. U. Ojalvo and H. L. Eidinoff, "Bond thickness effects upon stresses in single-lap adhesive joints," *AIAA Journal*, vol. 16, no. 3, pp. 204–211, 1978.
- [8] F. Delale, F. Erdogan, and M. N. Aydinoglu, "Stress in adhesively bonded joints: a closed-form solution," *Journal of Composite Materials*, vol. 15, no. 3, pp. 249–271, 1981.
- [9] J. N. Rossettos, P. Lin, and H. Nayeb-Hashemi, "Comparison of the effects of debonds and voids in adhesive joints," *Journal of Engineering Materials and Technology*, vol. 116, no. 4, pp. 533–538, 1994.

Research Article

Study on Strength and Ultrasonic Velocity of Air-Entrained Concrete and Plain Concrete in Cold Environment

Huai-shuai Shang,^{1,2} Ting-hua Yi,³ and Xing-xing Guo¹

¹ School of Civil Engineering, Qingdao Technological University, Qingdao 266033, China

² State Key Laboratory of Water Resources and Hydropower Engineering Science, Wuhan University, Wuhan 430072, China

³ School of Civil Engineering, Dalian University of Technology, Dalian 116023, China

Correspondence should be addressed to Huai-shuai Shang; shanghuashuai@yahoo.com.cn

Received 11 November 2013; Accepted 2 January 2014; Published 10 February 2014

Academic Editor: Konstantinos I. Tserpes

Copyright © 2014 Huai-shuai Shang et al. This is an open access article distributed under the Creative Commons Attribution License, which permits unrestricted use, distribution, and reproduction in any medium, provided the original work is properly cited.

Nondestructive testing technology is essential in the quality inspection of repair, alteration, and renovation of the existing engineering, especially for concrete structure in severe environment. The objective of this work is to deal with the behavior of ultrasonic velocity and mechanical properties of plain concrete and air-entrained concrete subjected to freeze-thaw cycles (F-T-C). The ultrasonic velocity and mechanical properties (tensile strength, compressive strength, cubic compressive strength, and splitting strength) of C30 air-entrained concrete and plain concrete with different water-cement ratio (water-cement ratio was 0.55, 0.45, and 0.50, resp.) after F-T cycles were measured. The influences of F-T cycles on ultrasonic velocity and mechanical properties of C30 air-entrained concrete and plain concrete were analyzed. And the relationship between mechanical properties and ultrasonic velocity was established. The experimental results can be useful for the design of new concrete structure, maintenance and life prediction of existing concrete structure such as offshore platform and concrete dock wall.

1. Introduction

For concrete structures during their service life, rapid decay may be caused by chemical, physical, and biological agents; then the service life will be shortened and more maintenance and repair costs will be used [1]. Such as concrete dams and hydraulic structures and so forth in cold environments. As one of the most important behavior of concrete materials, the durability [2–7] of concrete involves resistance to frost, carbonation, permeation, chemical attack, stress corrosion, and so forth. The durability is defined as follows: “as a durable structure, serviceability, strength, and stability should meet the requirements throughout its working life.” For preventing the deterioration of concrete [8] in cold climates, freeze-thaw action should be taken into consideration in the design of concrete structures.

As the most important technical measure to improve the frost resistance of concrete, air-entraining agents [9–11] have been widely used in concrete engineering, especially in cold zone (such as the northern of China and Europe,

arctic zone, etc.). Gokce et al. [12] discussed the freeze-thaw resistance when recycled coarse aggregate (the aggregate was produced from air-entrained concrete (A-E-C) and non-air-entrained concrete (N-A-E-C), resp.) was added into A-E-C. The conclusion that freeze-thaw resistance was poor when recycled coarse aggregate made with N-A-E-C was used even when air entrainment proper in the new system was got. The freeze-thaw resistance of high performance self-compacting concrete made with non-air-entrained admixtures was investigated in [13].

For concrete structures in service life, the deterioration was caused due to the chemical attack, environmental action (such as freeze-thaw action), and service loads. So it is important to accurately assess the service condition of concrete structures. The deterioration of concrete structures can be assessed by destructive testing technology and nondestructive testing technology (such as measurement of ultrasonic velocity and resonance frequency) [14–16], but reduction in load bearing area will be caused when destructive testing

methods were used. So the nondestructive testing methods were recommended to use when the service condition of concrete structure needs to be evaluated. Experimental study on the concrete samples containing artificial cracks with different depths and lengths was carried out the analytical studies based on the experimental results were compared by Shah and Ribakov [17]. The nonlinear ultrasonic testing of concrete in undamaged and damaged states was carried out by Shah and Ribakov [18]. The conclusion that nonlinear ultrasound was found to be very helpful in assessing degree of deterioration in concrete was got in [19].

Mechanical behavior, microstructure, ultrasonic velocity of A-E-C, and plain concrete after F-T cycles according to GB/TJ50082-2009 [20] were investigated in this paper. Based on the experimental results of F-T cycle tests, F-T damage mechanics models of A-E-C and plain concrete were established through the methods of mathematic simulation and damage mechanics.

2. Experimental Procedures

2.1. Materials and Mix Proportions. In this investigation, (1) the cementitious materials 32.5[#] and 42.5[#] ordinary Portland Cement [21] were used; (2) the coarse aggregate used was a crushed granite (specific gravity: 2.62 g/cm³, diameter: 5 mm to 10 mm); (3) the fine aggregate was natural river sand (fineness modulus: 2.6).

The mix proportions of A-E-C in per cubic meter is are follows: cement (412.68 kg/m³), sand (586.83 kg/m³), coarse aggregate (1186.00 kg/m³), water (164.30 kg/m³), and air-entraining agent (1.03 kg/m³). The major parameters and mix proportions of plain concrete with water-to-cementitious materials ratio of 0.45, 0.50, and 0.55 are given in Table 1.

The concrete mixtures were prepared in a mixer. After putting cementitious materials, fine aggregate and coarse aggregate, into the mixture, mixed the ingredients for about 1 min, and then added the water in 1 minute. After all water was added, the mixing continued for about 2 min.

2.2. Test Specimens and Testing Programs. The size of concrete cube is 100 mm × 100 mm × 100 mm (study for tensile strength, splitting strength, and compressive strength). The size of concrete prism is 100 mm × 100 mm × 400 mm (study for ultrasonic velocity and cubic compressive strength (cutting the specimen from the middle)). The samples were all casted in steel molds and removed from steel molds after 24 h. The samples were cured in a condition of 95 percent RH (relative humidity) and 20 ± 3°C until the age of 24 days. And then some of the samples were immersed into water for 4 days for experiment of F-T cycles, while others were cured until the age of 28 days.

In this experimental study, the F-T test apparatus [22] meeting the GB/T 50082-2009 requirement was used. The F-T cycle consisted of alternately lowering temperature of concrete samples from 6°C to -15°C and raising temperature of concrete samples from -15°C to 6°C, while lowering the temperature of antifreeze from 8 ± 2°C to -17 ± 2°C and warming from -17 ± 2°C to 8 ± 2°C all within 2.5~3 hours.

Specimens were removed for experiment study at 25-, 50-, 75-cycle intervals for plain concrete and at 50-, 100-, 150-, 200-, 300-, 350-, and 400-cycle intervals for A-E-C.

Stringent requirements on the stiffness of the servo hydraulic testing system or the control of the specimen deformation rate was required in the direct tension experiment because of the intrinsic brittleness of concrete. So the tensile tests were carried out in a triaxial testing machine [23]. The loading mode of direct tensile test in reference [23] was used. The loading mode of splitting test meeting JTJ 270-98 [24] was used. The compressive strength, cubic compressive strength, tensile strength and splitting strength of the specimens were monitored and recorded. At least, three samples for each batch should be tested.

3. Results and Discussions

3.1. Microstructure. The scanning electron SEM microphotographs of plain concrete and A-E-C prior to F-T cycles and subjected to different cycles of F-T were given in Figures 1 and 2, respectively. As shown in Figures 1(a) and 2(a), no crack between cement slurry and coarse aggregates as well as in cement slurry was found; the coarse aggregates did not split and the cement slurry is intact both for plain concrete and A-E-C (just as shown in rectangle in Figures 1(a) and 2(a)), and for A-E-C, the air bubble in the cement slurry is well proportioned and intact (just as shown in polygon in Figure 2(a)). For A-E-C after 400 cycles of F-T, the cement slurry becomes loosen, the crack in the cement slurry is caused, the crack between cement slurry and coarse aggregates expands greatly (just as shown in ellipse in Figure 2(b)), and the coarse aggregates and cement slurry are separated. While for plain concrete, only after 50 cycles, the crack in the cement slurry and between cement slurry and coarse aggregates is caused and even expands greatly (just as shown in ellipse in Figure 1(b)).

3.2. The Compressive Strength and Cubic Compressive Strength. The compressive stresses can be got by sharing the uniaxial compression load by the loading section area (0.01 m²).

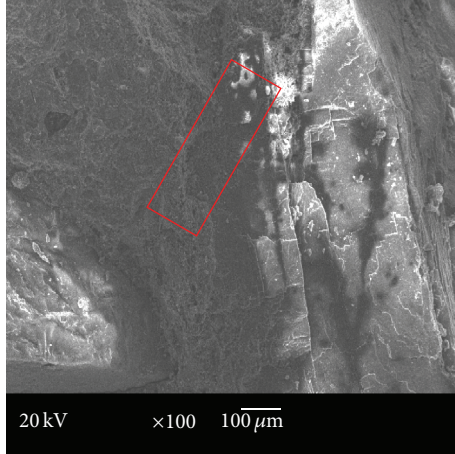
Table 2 listed the data of the compression tests for C30 A-E-C after different cycles of F-T, respectively. Table 3 listed the data of the compression tests for plain concrete (W/C was 0.55, 0.50, and 0.45) after different cycles of F-T, respectively.

As seen from Table 2, the cubic compressive strength and compressive strength decreased as F-T cycles increased. After the same cycles of F-T, the decreased percentage of the cubic compressive strength is larger than that of compressive strength for C30 A-E-C samples. After the action of 350 cycles of F-T, the cubic compressive strength of C30 A-E-C decreased to 55.9 percent of the initial cubic compressive strength, while the compressive strength decreased to 66.5 percent of the initial value prior to F-T cycles.

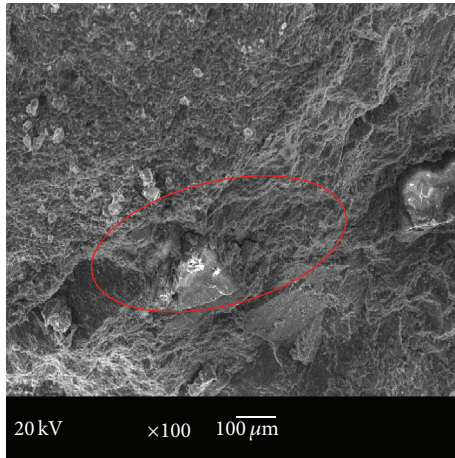
Besides, as shown in Table 3, the cubic compressive strength and the compressive strength of plain concrete decreased with the number of F-T cycles increasing. Unlike A-E-C, the decreased percentage of the cubic compressive

TABLE 1: The mix proportion of plain concrete per cubic metre.

W/C	Strength of cement (MPa)	Cement (kg/m ³)	Sand (kg/m ³)	Coarse aggregate (kg/m ³)	Water (kg/m ³)	Air content (%)
0.45	42.5	427	499	1284	192	0.9
0.50	42.5	383	663	1154	193	1.7
0.55	32.5	360	611	1241	198	1.9



(a) Prior to F-T cycle

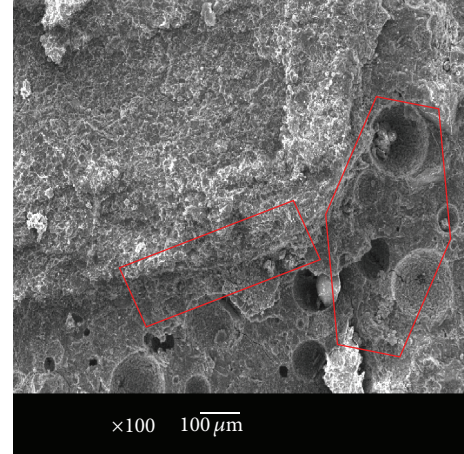


(b) 50 cycles of F-T

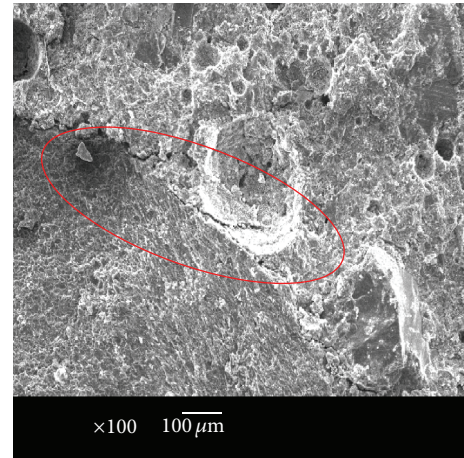
FIGURE 1: Scanning electron SEM microphoto graphs of plain concrete after F-T cycles.

strength is smaller than that of compressive strength for plain concrete after the same cycles of F-T. For plain concrete of water-cement ratio 0.55, the cubic compressive strength after 50 F-T cycles decreased to 66.0 percent of the initial cubic compressive strength, while the compressive strength after 50 F-T cycles decreased to 50.6 percent of the initial compressive strength.

The effect of F-T cycles on the C30 plain concrete was studied in [25]. According to the experimental results in [25], after 100 cycles of F-T, the compressive strength reduced to 63.7% of the initial compressive strength.



(a) Prior to F-T cycle



(b) 400 cycles of F-T

FIGURE 2: Scanning electron SEM microphoto graphs of A-E-C after F-T cycles.

3.3. The Tensile Strength, Splitting Strength of A-E-C, and Plain Concrete. The cracking behavior of concrete is controlled by its tensile properties, while this property was always ignored or treated only in the design and analysis of concrete structure. An accurate analysis for concrete of the crack width and load-deflection characteristics depended on the performance of postcracking response. Therefore, the experiment study of concrete in the area of tensile property was carried out.

Table 4 gives the experimental results of splitting and tensile strength of C30 A-E-C after F-T cycles on basis of the experimental results. As shown in Table 4, the present

test results indicated that for A-E-C after 400 cycles of F-T, the direct tensile strength was only 36.7 percent of the initial value, and the splitting strength decreased to only 55.16% of the splitting strength prior to F-T cycles. The loss rate of splitting strength is notably lower than the loss rate of tensile strength for A-E-C with the F-T cycles increasing.

The direct tensile strength of A-E-C was 10.1% and 6.9% of the compressive strength prior to F-T cycles and after 400 cycles of F-T, respectively. It means that, comparing to the compressive strength, the direct tensile strength dropped sharply as the F-T cycles increased. Reference [26] investigated the influence of F-T cycles on the mechanical behavior of high-strength concrete with air-entrained agent. The experiment results of the tensile strength were only 4.2 percent and 3.4 percent of the compressive strength prior to F-T cycles and after 700 cycles of F-T, respectively.

Table 5 gives the splitting strength and tensile strength of plain concrete samples with water-cement ratio 0.55, 0.50, and 0.45 after F-T cycles on basis of the experimental results. According to the experimental data in Table 5, after 75 cycles of F-T, the splitting and direct tensile strength of plain concrete with water-cement ratio 0.55 were only 59.2% and 29.0% of the initial value, while, for plain concrete with water-cement ratio being 0.45, the splitting and direct tensile strength were only 61.3% and 32.7% of the initial value.

According to the experimental results of plain concrete in [27], during the initial 25 F-T cycles, the tensile strength dropped sharply and the tensile strength after 25 F-T cycles decreased to about 58% of the initial value prior to F-T cycles. However, in subsequent F-T cycles, the phenomenon of continuing deterioration was observed, but the decreasing rate becomes smaller from 25 to 100 F-T cycles. And after 100 cycles of F-T, the tensile strength decreased to about 25% of the initial strength prior to F-T cycles. Namely, after the action of the first 25 cycles, the rate of reduction is lower with freeze-thaw cycles increasing. Reference [25] investigated the effect of F-T cycles on the splitting strength of C30 plain concrete. The experimental conclusion showed that splitting strength after 100 cycles of F-T decreased to 67.2% of the initial strength value prior to F-T cycles.

3.4. The Ultrasonic Velocity. Table 6 provides the reduced percentage of ultrasonic velocity measured on 100 mm cubic plain concrete samples with water-cement ratio being 0.55, 0.50, and 0.45 after F-T cycles.

As seen in Table 6, the ultrasonic velocity reduced with F-T cycles being increased. For plain concrete with water-cement ratio 0.45 and 0.55 after the action of 100 cycles of F-T, the ultrasonic velocity decreased to 30.8% and 61.65% of the initial value. There is a sudden descent stage for the plain concrete of water-cement ratio 0.45. After 100 cycles of F-T, the ultrasonic velocity decreased to 30.8% of the original value prior to F-T cycles. The diagram of the ultrasonic velocity loss versus number of F-T cycles was given in Figure 3.

Table 7 provides the reduced percentage of ultrasonic velocity measured on 100 mm cubic A-E-C samples after different cycles of F-T. According to the experimental results

in Table 7, the ultrasonic velocity of A-E-C after 100 cycles of F-T decreased to 97.68% of the initial value. It can be observed through comparing the results in Table 6 with those in Table 7 that, after the action of the same cycles of F-T, the reduced percentage of ultrasonic velocity of A-E-C was less than that of plain concrete. So it can be said that the F-T durability of plain concrete is poor than that of A-E-C.

3.5. Strength Loss. The strength (tensile strength, cubic compressive strength, compressive strength, and splitting strength) loss and ultrasonic velocity loss of plain concrete with water-cement ratio 0.55 after different F-T cycles were shown in Figure 3. The loss of tensile strength, splitting strength and cubic compressive strength compressive strength were 29.5%, 13.1%, 18.4% after 25 F-T cycles (the loss of compressive strength was 22.9% after 25 F-T cycles) and 71.0%, 40.8%, 40.0% after 75 F-T cycles, respectively. The loss of tensile strength was the largest compared to loss of other strength after the same cycles of F-T and the loss of splitting strength was the smallest. What is more, it can be realized from Figure 3 that the strength loss of plain concrete is synchronous with the loss of ultrasonic velocity after the action of freeze-thaw cycles. The strength loss and ultrasonic velocity loss of C30 A-E-C subjected to F-T cycles were given in Figure 4.

The loss of tensile strength, splitting strength, cubic compressive strength, and compressive strength for A-E-C was 14.5%, 9.6%, 7.4%, and 1.5% after 100 F-T cycles and 42.4%, 23.5%, 38.3%, and 14.0% after 300 F-T cycles, respectively. Compared to the loss of tensile strength and cubic compressive strength, the loss of compressive strength was smaller, especially after the action of first 300 cycles of F-T. What is more, the conclusion that the loss of ultrasonic velocity for plain concrete is much more than that of A-E-C after the same cycles of F-T can be drawn according to Figures 3 and 4.

It can be drawn that the effect of F-T cycles on tension behavior and compression behavior of A-E-C is different. But the reduction of compressive strength of concrete can be associated with the cycles of F-T, while the reduction of tensile strength of concrete should be associated with the occurrence of crack caused by F-T cycles.

For concrete material under the action of tensile loading, the initiation of new microcracks and growth of inherent micro-cracks will be caused. And this will result in the reduction of the load-carrying area and the increment of stress concentration at critical crack tips. The final result is the cracks to propagate further. If these cracks are not effectively prevented, failure of the concrete will occur.

As the basic representative value of mechanical behavior of concrete, the compressive strength is of vital importance to the application. Based on this, the relationship between the cubic compressive and ultrasonic velocity of plain concrete and C30 A-E-C can be established as follows:

$$\frac{f_c^D}{f_c} = a * P^2 + b * P + c, \quad (1)$$

TABLE 2: Compressive strength of A-E-C after different cycles of F-T (MPa).

Number of F-T cycles	0	50	100	150	200	300	350	400
Cubic compressive strength	34.20	33.40	31.67	27.60	26.38	21.10	19.13	16.22
Compressive strength	26.30	25.90	25.90	24.80	23.33	22.63	17.50	14.25

TABLE 3: Compressive strength of plain concrete after different cycles of F-T (MPa).

W/C	Number of F-T cycles	0	25	50	75
0.55	Cubic compressive strength	27.41	22.36	18.09	16.45
	Compressive strength	19.66	15.15	9.95	/
0.50	Cubic compressive strength	45.85	38.00	35.71	28.92
	Compressive strength	34.20	30.01	24.10	21.67
0.45	Cubic compressive strength	50.65	45.23	37.45	32.23
	Compressive strength	38.90	34.4	29.43	25.67

TABLE 4: The splitting and tensile strength of A-E-C after F-T cycles (MPa).

Number of F-T cycles	0	100	200	300	400
Tensile strength	2.67	2.28	2.06	1.54	0.98
Splitting strength	2.81	2.54	2.35	2.15	1.55

TABLE 5: The splitting and tensile strength of plain concrete after F-T cycles (MPa).

W/C	Number of F-T cycles	0	25	50	75	100
0.55	Tensile strength	1.93	1.36	0.84	0.56	/
	Splitting strength	2.13	1.85	1.62	1.26	1.18
0.5	Tensile strength	3.14	1.32	1.15	0.98	/
	Splitting strength	2.73	2.04	1.64	1.49	1.33
0.45	Tensile strength	3.61	1.99	1.36	1.18	/
	Splitting strength	3.31	2.93	2.62	2.03	1.53

TABLE 6: Reduced percentage of ultrasonic velocity of plain concrete subjected to F-T cycles.

W/C	Number of F-T cycles				
	0	25	50	75	100
0.45	100	92.86	86.19	69.64	30.80
0.50	100	85.23	67.53	59.43	—
0.55	100	92.08	85.45	72.69	61.65

TABLE 7: Reduced percentage of ultrasonic velocity of A-E-C subjected to F-T cycles.

Number of F-T cycles	0	100	200	300	400
Reduced percentage of ultrasonic velocity	100.00	97.68	97.63	91.02	84.70

where f_c^D is the cubic compressive strength of A-E-C and plain concrete after different cycles of F-T. P is the decreasing percentage of ultrasonic velocity for A-E-C and plain concrete after different F-T cycles. a , b , and c are the regress parameters.

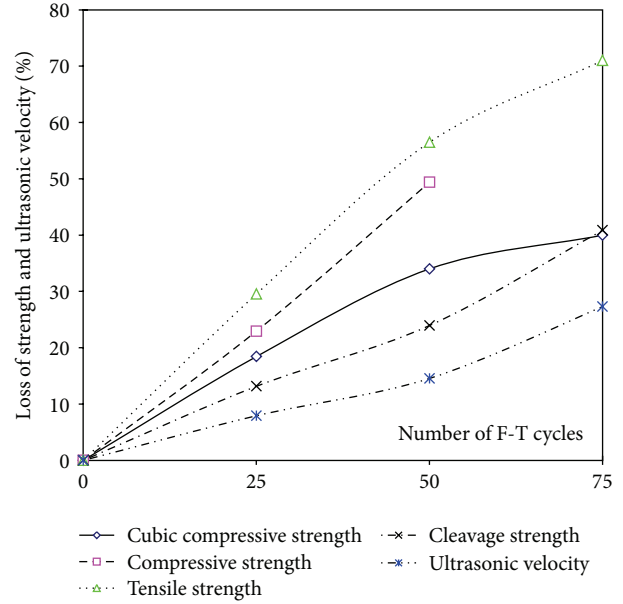


FIGURE 3: The loss of strength and ultrasonic velocity of plain concrete versus number of F-T cycles.

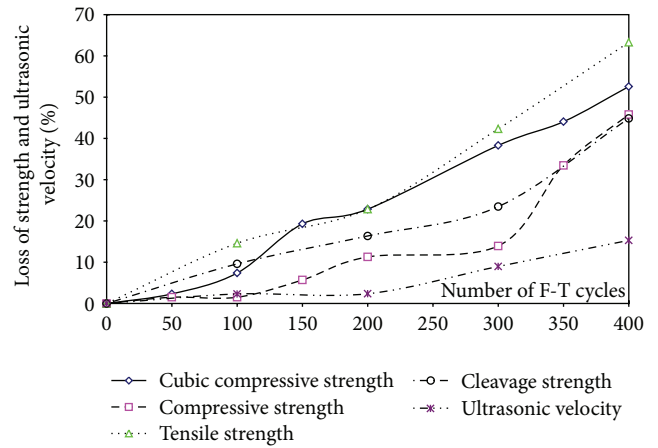


FIGURE 4: The loss of strength and ultrasonic velocity of A-E-C versus number of F-T cycles.

The regression coefficient such as R^2 , SSE, RM, and M used to judge the measure of accuracy was given in this study:

$$R^2 = 1 - \left\{ \frac{\left[\sum_{i=1}^n \left(f_{ci}^D(\text{tested}) - f_{ci}^D(\text{computed}) \right)^2 \right]}{\left[\sum_{i=1}^n \left(f_{ci}^D(\text{tested}) - f_{ci}^D(\text{mean}) \right)^2 \right]} \right\},$$

$$RM = \sqrt{\frac{1}{n} \sum_{i=1}^n \left(f_{ci}^D(\text{tested}) - f_{ci}^D(\text{computed}) \right)^2},$$

TABLE 8: Value of a, b, c, R^2 , SSE, RM, and M .

	a	b	c	R^2	RMSE	SSE	MAPE
A-E-C	14.979	-24.359	10.365	0.934	2.896	14.480	1.885%
Plain concrete with 0.55	6.013	-8.885	3.878	0.992	0.014	0.0007	-0.002%
Plain concrete with 0.50	0.049	0.727	0.212	0.922	0.037	0.005	-0.256%
Plain concrete with 0.45	3.459	-4.626	2.178	0.983	0.018	0.001	-0.046%

$$SSE = \sum_{i=1}^n \left(f_{ci}^D(\text{tested}) - f_{ci}^D(\text{computed}) \right)^2,$$

$$M = \frac{\sum_{i=1}^n \left(f_{ci}^D(\text{tested}) - f_{ci}^D(\text{computed}) \right) / \left(f_{ci}^D(\text{tested}) \right)}{n} \times 100\%, \quad (2)$$

where R^2 was the determination coefficient, SSE was the sum value of squared error RM was the root mean value of square error, and M was the mean absolute percentage error.

By computation, the results of R^2 , SSE, RM, and M are given in Table 8.

3.6. Discussion. From the microscale, concrete is a three-phase composite structure (aggregate, a cement matrix, and the interface or transition zone between above two materials). The distribution and direction of microcracks caused by F-T cycles are stochastic. Under the action of continuing F-T cycles, more serious damage will be caused by microcrack accumulation (mainly manifested as: the number of microcosmic cracks increase and the width of microcosmic cracks become broad) due to water pressure caused by F-T cycles. In another way, the initiation of new crack and growth of existing cracks under the action of tensile load, compressive load, and splitting load will reduce the load-carrying area. And the reduction of load-carrying area will lead the stress concentration at crack tips. At last, the deterioration of concrete (such as strength reduction, spalling) will be caused as F-T cycles were repeated.

On the other hand, billions of microscopic air cells were contained in A-E-C. The existence of microscopic air cells can relieve internal compressive pressure caused by F-T cycles through providing tiny chambers. So after the same cycles of F-T, the decreased percentage of strength of A-E-C is lower than that of plain concrete.

According to the experimental results in this paper and the experimental results obtained from other authors, the conclusion that the deterioration rate of durability of A-E-C is slower than deterioration rate of plain concrete can be got.

4. Conclusions

In the range of experimental works of plain concrete and A-E-C and discussion of the experimental results, the conclusion was stated as follows.

- (1) The mechanical behavior of A-E-C and plain concrete decreased as the F-T cycles increased. After the action of the same cycles of F-T, the decreased percentage of

the strength for C30 A-E-C specimens is larger than plain concrete specimens.

- (2) For F-T durability deterioration, the first reason is the cracks caused by freezing of water, and the second reason is the action of thermal stress caused by repeated F-T cycles. The failure of A-E-C specimens should be attributed to the cracking of the paste.
- (3) The F-T durability of plain concrete sample was poor (after 75 cycles of F-T cycles, the compressive strength loss of plain concrete ($W/C = 0.45$) exceeded 30 percent) according to experimental results, but the F-T durability of plain concrete can be improved greatly through adding air-entraining agent. It means that plain concrete can have higher F-T durability.
- (4) According to the results, the F-T durability of concrete should be taken into consideration in design and maintenance of concrete structure.

Conflict of Interests

The authors declare that there is no conflict of interests regarding the publication of this paper.

Acknowledgments

This work was supported by the “National Natural Science Foundation of China” (Grant nos. 51208273, 51121005, and 51222806), “Project of Shandong Province Higher Educational Science and Technology Program” (Grant no. J12LG07), “the Open Research Fund of State Key Laboratory of Simulation and Regulation of Water Cycle in River Basin (China Institute of Water Resources and Hydropower Research)” (Grant no. IWHR-SKL-201305), and “Open Research Fund Program of State Key Laboratory of Water Resources and Hydropower Engineering Science” (Grant no. 2013B113). The authors gratefully acknowledge the financial support.

References

- [1] M. Kosior-Kazberuk and W. Jezierski, “Surface scaling resistance of concrete modified with bituminous addition,” *Journal of Civil Engineering and Management*, vol. 10, no. 1, pp. 25–30, 2004.
- [2] European Committee for Standardization, “Tests for mechanical and physical properties of aggregates—part 2: methods for the determination of resistance to fragmentation,” EN 1097-2, p. 38, 2010.

- [3] H.-S. Shang and T.-H. Yi, "Freeze-thaw durability of air-entrained concrete," *The Scientific World Journal*, vol. 2013, Article ID 650791, 6 pages, 2013.
- [4] D. Jozwiak-Niedzwiedzka, "Scaling resistance of high performance concretes containing a small portion of pre-wetted lightweight fine aggregate," *Cement and Concrete Composites*, vol. 27, no. 6, pp. 709–715, 2005.
- [5] M. Marks, D. Józwiak-Niedzwiedzka, M. A. Glinicki et al., "Assessment of scaling durability of concrete with CFBC ash by automatic classification rules," *Journal of Materials Civil Engineering*, vol. 24, no. 7, pp. 860–867, 2012.
- [6] H.-S. Shang, T.-H. Yi, and Y.-P. Song, "Behavior of plain concrete of a high water-cement ratio after freeze-thaw cycles," *Materials*, vol. 5, pp. 1698–1707, 2012.
- [7] H. Binici, T. Shah, O. Aksogan, and H. Kaplan, "Durability of concrete made with granite and marble as recycle aggregates," *Journal of Materials Processing Technology*, vol. 208, no. 1–3, pp. 299–308, 2008.
- [8] L. Liu, G. Ye, E. Schlangen et al., "Modeling of the internal damage of saturated cement paste due to ice crystallization pressure during freezing," *Cement and Concrete Composites*, vol. 33, no. 5, pp. 562–571, 2011.
- [9] L. Du and K. J. Folliard, "Mechanisms of air entrainment in concrete," *Cement and Concrete Research*, vol. 35, no. 8, pp. 1463–1471, 2005.
- [10] S. Chatterji, "Freezing of air-entrained cement-based materials and specific actions of air-entraining agents," *Cement and Concrete Composites*, vol. 25, no. 7, pp. 759–765, 2003.
- [11] K. H. Khayat and J. Assaad, "Air-void stability in self-consolidating concrete," *ACI Materials Journal*, vol. 99, no. 4, pp. 408–416, 2002.
- [12] A. Gokce, S. Nagataki, T. Saeki, and M. Hisada, "Freezing and thawing resistance of air-entrained concrete incorporating recycled coarse aggregate: the role of air content in demolished concrete," *Cement and Concrete Research*, vol. 34, no. 5, pp. 799–806, 2004.
- [13] B. Łązniewska-Piekarczyk, "The frost resistance versus air voids parameters of high performance self compacting concrete modified by non-air-entrained admixtures," *Construction and Building Materials*, vol. 48, pp. 1209–1220, 2013.
- [14] M. I. Khan, "Evaluation of non-destructive testing of high strength concrete incorporating supplementary cementitious composites," *Resources, Conservation and Recycling*, vol. 61, pp. 125–129, 2012.
- [15] A. Ana Ivanović and R. D. Neilson, "Non-destructive testing of rock bolts for estimating total bolt length," *International Journal of Rock Mechanics & Mining Sciences*, vol. 64, pp. 36–43, 2013.
- [16] E. H. Saenger, G. K. Kocur, R. Jud, and M. Torrilhon, "Application of time reverse modeling on ultrasonic non-destructive testing of concrete," *Applied Mathematical Modelling*, vol. 35, no. 2, pp. 807–816, 2011.
- [17] A. A. Shah and Y. Ribakov, "Non-destructive measurements of crack assessment and defect detection in concrete structures," *Materials & Design*, vol. 29, no. 1, pp. 61–69, 2008.
- [18] A. A. Shah and Y. Ribakov, "Non-destructive evaluation of concrete in damaged and undamaged states," *Materials & Design*, vol. 30, no. 9, pp. 3504–3511, 2009.
- [19] J. D. Stauffer, C. B. Woodward, and K. R. White, "Nonlinear ultrasonic testing with resonant and pulse velocity parameters for early damage in concrete," *ACI Materials Journal*, vol. 102, no. 2, pp. 118–121, 2005.
- [20] National Standard of the People's Republic of China, "The test method of long-term and durability on ordinary concrete," Tech. Rep. GB/T50082-2009, National Standard of the People's Republic of China, Beijing, China, 2009.
- [21] National Standard of the People's Republic of China, "Portland cement and ordinary portland cement," Tech. Rep. GB175-99, National Standard of the People's Republic of China, Beijing, China, 1999.
- [22] L.-K. Qin, Y.-P. Song, Y.-J. Wang, C.-J. Yu, and Z. Zhang, "Influence of Cycles of Freezing and Thawing on the Compressive Property of Concrete in Seawater," *Concrete*, pp. 16–18, 2004.
- [23] H.-S. Shang, Y.-P. Song, and J.-P. Ou, "Mechanical behaviour of air-entrained concrete," *Magazine of Concrete Research*, vol. 61, no. 2, pp. 87–94, 2009.
- [24] National Standard of the People's Republic of China, "Testing code of concrete for port and waterwog engineering," Tech. Rep. JTJ 270-98, National Standard of the People's Republic of China, Beijing, China, 1998.
- [25] H.-Q. Cheng, L.-S. Zhang, and P.-X. Li, "The influence of freeze-thaw to concrete strength," *Henan Science*, vol. 61, no. 2, pp. 214–216, 2003.
- [26] H. Marzouk and D. Jiang, "Effects of freezing and thawing on the tension properties of high-strength concrete," *ACI Materials Journal*, vol. 91, no. 6, pp. 577–586, 1994.
- [27] L.-K. Qin, *Study on the strength and deformation of concrete under multiaxial stress after high-temperature of freeze-thaw cycling [Ph.D. thesis]*, Dalian University of Technology, Liaoning, China, 2003.

Research Article

Preparation, Microstructure, and Mechanical Properties of Spinel-Corundum-Sialon Composite Materials from Waste Fly Ash and Aluminum Dross

Juntong Huang,¹ Minghao Fang,¹ Zhaohui Huang,¹ Yan'gai Liu,¹ Jingzhou Yang,¹ Saifang Huang,¹ Youguo Xu,¹ Kai Chen,¹ Shuai Yi,¹ and Shaowei Zhang²

¹ School of Materials Science and Technology, China University of Geosciences, Beijing 100083, China

² College of Engineering, Mathematics and Physical Sciences, University of Exeter, Exeter EX4 4QE, UK

Correspondence should be addressed to Zhaohui Huang; huang118@cugb.edu.cn and Shaowei Zhang; s.zhang@exeter.ac.uk

Received 27 November 2013; Accepted 5 December 2013; Published 30 January 2014

Academic Editor: Filippo Berto

Copyright © 2014 Juntong Huang et al. This is an open access article distributed under the Creative Commons Attribution License, which permits unrestricted use, distribution, and reproduction in any medium, provided the original work is properly cited.

The solid wastes fly ash and aluminum dross were used to prepare the low cost, high added-value product spinel-corundum-Sialon with an *in situ* aluminothermic reduction-nitridation reaction. The effects of varying raw material components and heating temperatures on the phase compositions, microstructure, bulk density, apparent porosity, and bending strength of products were investigated. The presence of hazardous or impure elements in the products was also evaluated. The sintered materials mainly consisted of micro-/nanosized plate corundum, octahedral spinel, and hexagonal columnar β -Sialon. The bulk density and bending strength of product samples initially increased and then decreased as Al content increased. Product samples with an Al content exceeding 10 mass% that were sintered at 1450°C exhibited the highest bending strength (288 MPa), the lowest apparent porosity (1.24%), and extremely low linear shrinkage (0.67%). The main impurity present was Fe₃Si₃ with hazardous elements P, Cr, Mn, and Ni doping. This work could provide a new method to reduce environmental pollution and manufacture low cost high performance refractory materials using the abundant waste materials fly ash and aluminum dross.

1. Introduction

The recycling of industrial solid wastes is gaining importance as the need for environmental protection increases. Fly ash is a product of the high temperature combustion of coal at fired power stations. It is captured from the exhaust of the boiler [1, 2]. Most fly ashes are primarily composed of aluminosilicates with a small amount of impurity elements, such as Fe, Ca, Mg, Na, K, and S [3], as well as a trace amount of toxic heavy metal elements, including Pb, Zn, Hg, Cd, Ni, and Cr [4]. Aluminum dross is a residual waste material formed on the surface of molten Al in the furnace during primary and secondary Al fusion. Apart from aluminum metal, aluminum dross normally contains other compounds (e.g., Al₂O₃, MgO, AlN, NaCl, and KCl) and impure or noxious elements (e.g., Fe, Ca, Ti, Cr, P, Cu, and Mn) [5, 6]. Worldwide, coal-fired power stations annually produce approximately 600 million tons of fly ash [7] and the aluminum industry over 4.5 million

tons of aluminum dross [6]. The majority of fly ash and aluminum dross are disposed of in landfills, resulting in leaching of toxic metal ions into soils, surface water, and even groundwater [8, 9].

Fly ash and aluminum dross are utilized as recycled materials in engineering and agriculture in order to reduce the environmental burden and enhance the economic benefit. They are used in industry as a raw material to prepare nonaerated concrete, concrete bricks, and filler in asphalt. In agriculture, they are employed to produce soil amendments, fertilizer, cattle feeders, and agricultural pipes [10–12]. However, the dominant waste management option employs direct land filling, especially in China. It is necessary and urgent to increase the use of fly ash and aluminum dross in high value-added products with an easy, effective, and economically affordable method.

Up to now, many valuable products have been synthesized using fly ash or aluminum dross, including mullite [13],

TABLE 1: Chemical compositions of fly ash and aluminum dross as determined by XRF analysis (mass%).

Component	Al ₂ O ₃	SiO ₂	MgO	Fe ₂ O ₃	CaO	TiO ₂	Na ₂ O	K ₂ O	SO ₃	Cr ₂ O ₃	MnO	CuO	Others	LOI
Fly ash	40.37	52.45	0.54	2.36	0.75	1.52	0.12	0.21	0.13	—	—	—	—	1.56
Aluminum dross	69.60	5.90	7.10	4.00	2.80	1.60	2.60	0.56	0.50	0.23	0.50	0.86	3.43	0.32

cordierite [14], zeolite [15], and (Mg, Si)Al₂O₄ [5]. β -Sialon (Si_{6-z}Al_zO_zN_{8-z} with $0 < z \leq 4.2$) is the solid solution formed by equivalent substitution of Si and N in β -Si₃N₄ by Al and O, respectively [16]. Sialon-based materials have excellent mechanical, chemical, and thermal properties and are used as high temperature engineering materials, cutting tools, and abrasive materials [17, 18]. Their application, however, has always been limited by the high cost of high purity raw materials. To overcome this drawback, many researches were devoted to synthesize Sialon using low cost sources of aluminosilicates, including clay [19], zeolite [20], and slag [21], as well as fly ash [22] and aluminum dross [23] via the carbothermal reduction and nitridation (CRN) method. The CRN method, however, has many disadvantages. It is difficult to precisely regulate the phase compositions of the product, due to variations in the partial pressure of the formed gas CO. The shape and dimension of the product are hard to control due to the large linear shrinkage. The product is very fragile and the strength is very low. The CRN method is associated with the emission of the toxic gas CO and the greenhouse gas CO₂.

Aluminum dross contains a large amount of metallic Al, which can be used as a reducing agent. Herein, we advance the concept of the collaborative use of waste resources. Since fly ash contains highly reactive SiO₂ and Al₂O₃ and aluminum dross contains Al₂O₃, AlN, and MgO, it is possible to design and tailor the spinel-corundum-Sialon composite refractories only using fly ash and aluminum dross as raw materials without introducing carbon. The spinel could be synthesized via the solid-state reaction of MgO and Al₂O₃ and Sialon by *in situ* aluminothermic reduction-nitridation (ARN) reaction of SiO₂, Al₂O₃, and AlN in a nitrogen atmosphere at high temperature. To date, there has been little study of the hazardous or impure elements in the final products although impurity is an important obstacle for the utilization of industrial wastes.

The purpose of the study was to efficiently utilize the solid wastes fly ash and aluminum dross in the preparation of highly value-added spinel-corundum-Sialon composites. The manufacturing process was optimized by investigating the phase composition, microstructure, physicomechanical properties, and the presence of hazardous or impure elements in the final product. The spinel-corundum-Sialon composite product can be used as structural refractory materials. It is a very low cost and environmentally friendly method for manufacturing high performance refractories products from waste materials.

2. Materials and Methods

The fly ash used in this work was provided by the Shuozhou Electric Power Development Co., Ltd. in Shanxi Province,

China. The aluminum dross was obtained from the aluminum recycling company, Shanghai Sigma Metals Inc. The chemical composition of fly ash and aluminum dross was determined using X-ray fluorescence (XRF, Magix PW2403, Panalytical, Holland) (Table 1). The main crystalline phase of fly ash was mullite. Some amorphous glass phase was also present. The aluminum dross consisted of Al, Al₂O₃, AlN, quartz, NaCl, KCl, and a small amount of glass phase. The particle size of the fly ash and aluminum dross was less than 74 μ m. The principle of stoichiometric ingredient is that according to the contents of the metallic Al in aluminum dross, SiO₂ in fly ash and aluminum dross is reduced by the metallic Al and totally transformed to Si₃N₄, which subsequently reacted with Al₂O₃ and AlN to form Sialon. Herein, this work performed the stoichiometric composition of 41.23 mass% fly ash (FA) and 58.77 mass% aluminum dross (AD), and other series with exceeding 10 mass% (38.94 mass% FA, 61.06 mass% AD), 50 mass% (31.87 mass% FA, 68.13 mass% AD), and 100 mass% (25.97 mass% FA, 74.03 mass% AD) of the metallic Al in the aluminum dross were also investigated.

Fly ash and aluminum dross powders were ball-milled together for 2 h and passed through a 200-mesh sieve. The mixture was pressed into compact bars (45 mm \times 6 mm \times 6 mm) with 8 wt.% polyvinyl alcohol (PVA) under a pressure of 50 MPa for 30 s. The green bodies were compressed using an isostatic pressure of 200 MPa for 60 s. The bars were dried at 80°C for 6 h in a drying oven and then placed in a graphite crucible and heated in flow nitrogen (purity 99.99%) in a graphite furnace at 1350, 1450, and 1550°C for 3 h, respectively. The corresponding raw material powders were chosen as the packing powders in order to prevent deformation of the product bars. All the samples were cooled down naturally.

The crystalline phases were examined via X-ray diffractometer (XRD, XD-3, China), using Cu K α 1 radiation ($\lambda = 1.5406 \text{ \AA}$) with a step of 0.02° (2θ) and a scanning rate of 4° min^{-1} . Semiquantitative analysis of the crystalline phase content was based on calibration curves determined from the relative intensity of the diffraction peaks of (311) spinel, (113) Al₂O₃, and (020) β -Sialon [24, 25]. The shrinkage percent in the width direction of the sintered samples was measured using a vernier caliper. The bulk density and apparent porosity were measured in water using a conventional method, according to Archimedes' principle. The bending strength was determined using a conventional three-point bending method. The microstructure and morphology of products were observed using a scanning electron microscope (SEM, JSM-6460, Japan, XL30 ESEM-TMP) equipped with an energy dispersive spectroscopy detector (EDS, Philips-FEI) and a high-resolution transmission electron microscope (HRTEM, JEOL JEM-2100, Phillips) with EDS (Oxford INCA). Product samples were held with a copper grid and

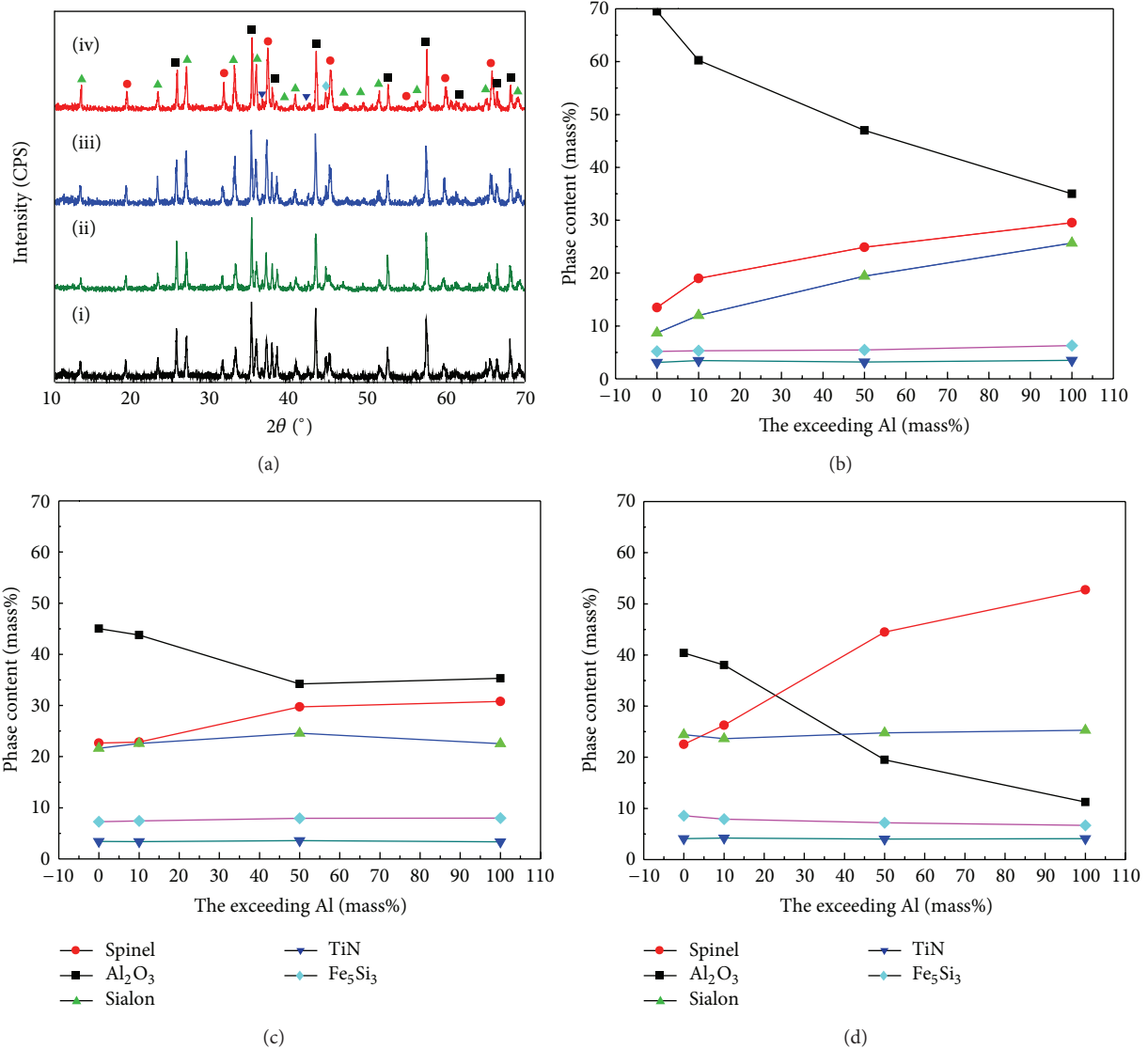


FIGURE 1: Phase assemblages of products. (a) XRD patterns of samples sintered at 1450°C with the exceeding metallic Al of (i) 0 mass%, (ii) 10 mass%, (iii) 50 mass%, and (iv) 100 mass%. Dependence of product phase content on content of the exceeding Al in aluminum dross sintered at different temperatures (b) 1350°C, (c) 1450°C, and (d) 1550°C.

coated with carbon to improve the electrical conductivity prior to TEM observation.

3. Results

3.1. Characterization of Phase Assemblages and Product Microstructures. The crystalline phases of the product samples sintered at different temperatures were determined with XRD. They were mainly comprised of the same kinds of phase assemblages, that is, corundum, spinel, and Sialon, along with some minor phases such as TiN and Fe_5Si_3 . The typical pattern of samples sintered at 1450°C with various exceeding metallic Al is shown in Figure 1(a). The phase content of products sintered at different temperatures was calculated and plotted in Figures 1(b)–1(d). At 1350°C (Figure 1(b)),

with a stoichiometric addition of Al, the final products were mainly corundum (69.5 mass%) with a small amount of spinel (MgAl_2O_4 , 13.5 mass%) and Sialon ($\text{Si}_3\text{Al}_3\text{O}_3\text{N}_5$, 8.7 mass%). As the amount of Al was increased, the amount of spinel and β -Sialon increased and corundum dramatically decreased. At 1450°C (Figure 1(c)), the products from a stoichiometric feed ratio of Al consisted of 45.1 mass% corundum, 22.7 mass% spinel, and 21.6 mass% Sialon. As the amount of Al was increased, the trend of phase content was similar to that at 1350°C. At 1550°C (Figure 1(d)), an Al-rich spinel was obtained in the products (XRD not shown here) and its amount increased as Al content increased. There was a yield of 52.7 mass% Al-rich spinel and 11.2 mass% corundum in the product with the exceeding 100 mass% Al. Herein, XRD analysis defined formula for spinel as $\text{Mg}_{0.388}\text{Al}_{2.408}\text{O}_4$. The z -value of β -Sialon increased from 3 to 4.

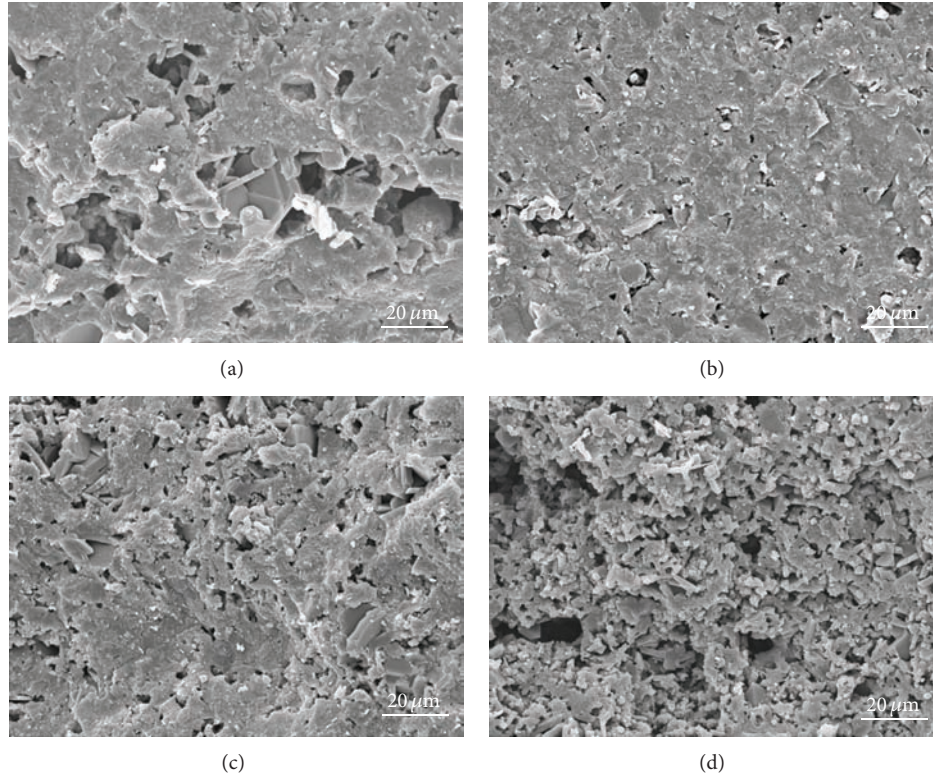


FIGURE 2: Product microstructure. SEM images of samples sintered at 1450°C with exceeding Al of (a) 0 mass%, (b) 10 mass%, (c) 50 mass%, and (d) 100 mass%.

The microstructure of product samples was recorded using SEM (JSM-6460, Japan). Typical images of product sintered at 1450°C are shown in Figure 2. The sample with a stoichiometric amount of Al consisted of a large quantity of glassy phase with a certain amount of porosity, which provided sufficient space to grow plate corundum. Spinel and β -Sialon phases were not seen. As Al content exceeded 10 mass%, the porosity decreased and the product was well sintered. With higher Al content, the plate Al_2O_3 and other crystal grains became apparent, the number of small micropores increased, and the amount of glassy phase (mainly consisting of Al, Si, and O) decreased (further TEM and EDS evidences on this will be given below). The decreased amount of the glass phase in the product was due to the reduction of SiO_2 in the starting composition of the sample. The morphology of the crystalline phases was further observed by SEM (XL30 ESEM-TMP) (Figure 3). The micrographs visualized many randomly dispersed plate corundum grains of about 5–10 μm diameter, some octahedral spinel crystals of 3–5 μm diameter, and columnar β -Sialon crystals with typical widths of 0.8–1.2 μm and aspect ratios of 3–6 (Figure 3(a)). Occasionally, some Al_2O_3 grains were observed with a step-like fracture (Figure 3(c)). The impurities in the starting materials, Fe, Cu, Mn, and Cr, were alloyed into spherical particles (Figure 4(c)) which were apparent by their bright contrast (see more details in the TEM images and EDS patterns later). Prismatic β -Sialon crystals were well crystallized and intensively distributed in some regions of the sample, and

a few grew in an epitaxial direction on the plate corundum (Figure 3(e)). EDS analysis (Figure 3(f)) demonstrated both Ca and Mg in β -Sialon. It is believed that β -Sialon has the capacity to incorporate a variety of metallic ions into its interstices, making multiphase materials with much lower glass content.

The morphology and microstructure of the products were further characterized by TEM and HRTEM (Figure 4). Microsized spinel, Al_2O_3 , and β -Sialon grains were observed by SEM. Contiguous nanosized grains in the glassy matrix were visualized with TEM (Figures 4(a) and 4(b)). Typical TEM images, HRTEM images, and the selected area electron diffraction (SAED) pattern of β -Sialon nanograins are displayed in Figures 4(c), 4(d), and 4(e). The EDX pattern was compatible with a β -Sialon nanograin consisting of Si, Al, O and N, with a small amount of Mg and Ca (Figure 4(f)). HRTEM lattice fringe image (Figure 4(d)) revealed β -Sialon nanograins with a hexagonal structure. The measured d spacings of 0.67 nm and 0.38 nm corresponded well to the (01 $\bar{1}$ 0) and (11 $\bar{2}$ 0) planes of β -Sialon.

3.2. The Physicomechanical Properties of Spinel-Corundum-Sialon Composite Materials. The apparent porosity and bulk density of product samples as a function of the exceeding Al content are shown in Figure 5. The bulk density initially increased and then decreased as Al content increased. The opposite trend was observed for the apparent porosity. The highest bulk density of product sample, 3.15 $\text{g}\cdot\text{cm}^{-3}$, was seen

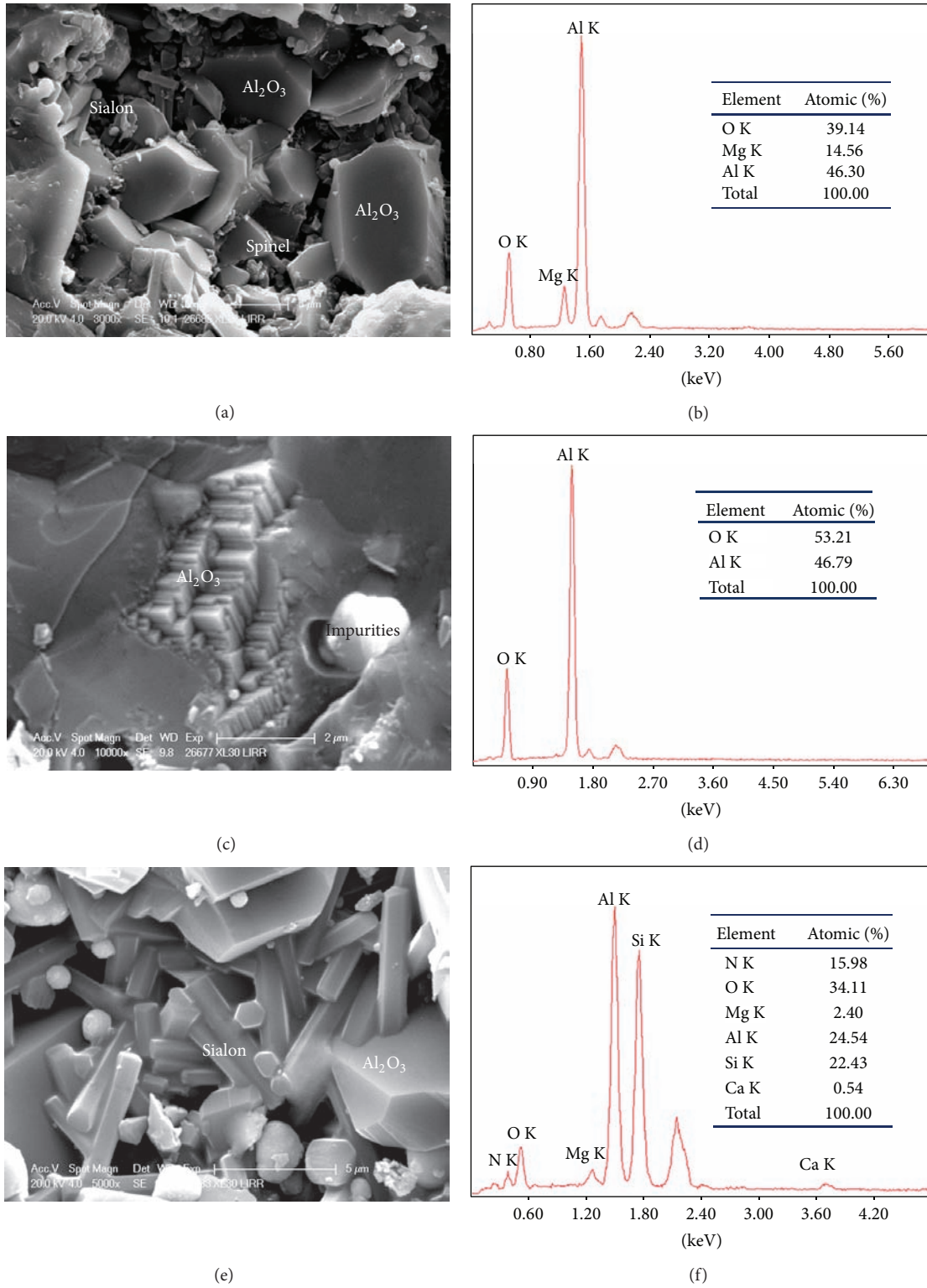


FIGURE 3: Typical SEM images and EDS results of the products sample with the exceeding metallic Al of 10 mass% sintered at 1450°C. (a) SEM image of product, showing plate corundum, octahedral spinel, and columnar β -Sialon. (b) The EDS pattern of spinel. ((c), (d)) SEM image and EDS pattern of step-like corundum. ((e), (f)) SEM image and EDS pattern of columnar β -Sialon.

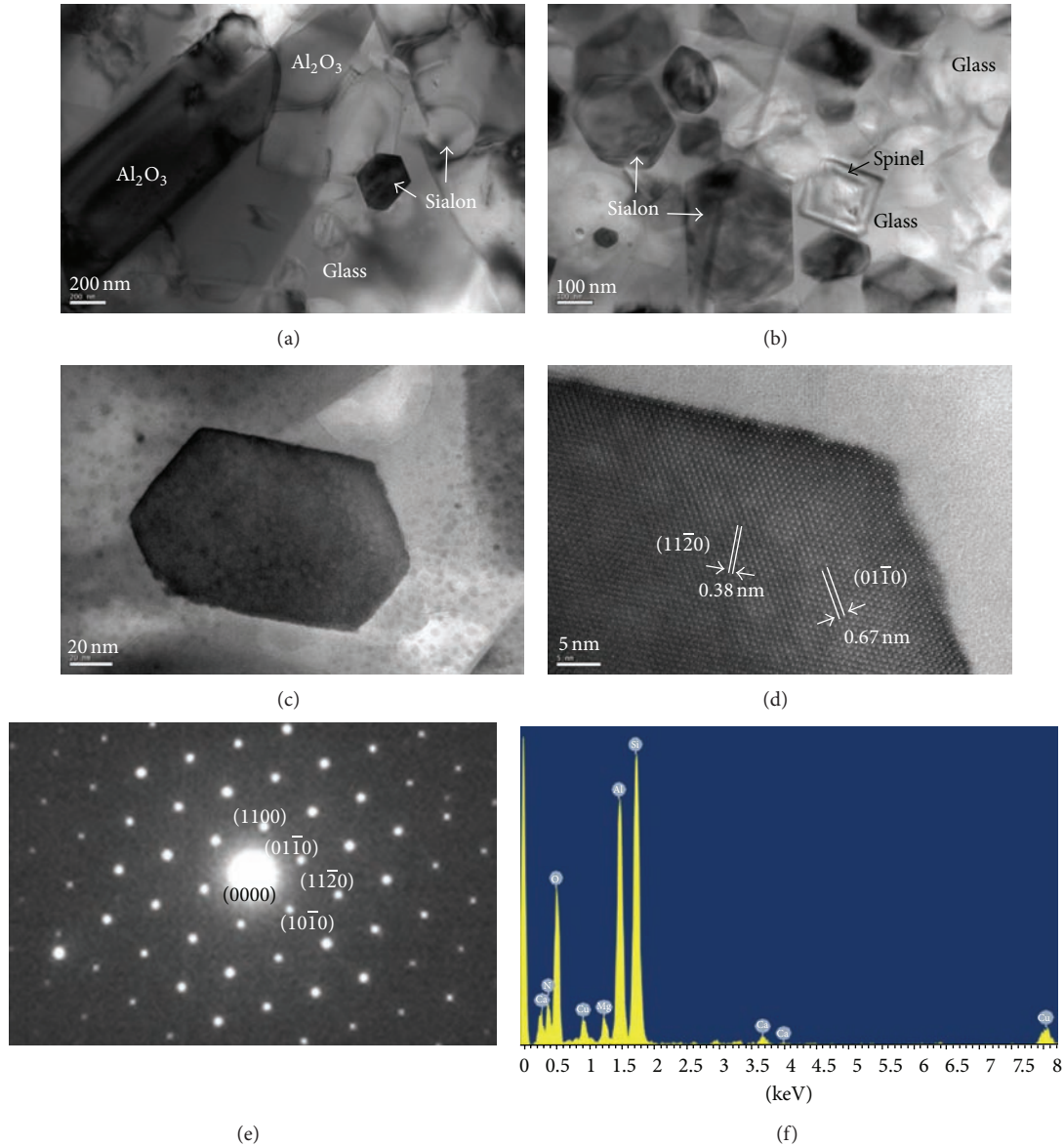


FIGURE 4: Microstructure of products. ((a), (b)) TEM images of product samples with the exceeding metallic Al of 10 mass% sintered at 1450°C. ((c)–(f)) Typical TEM, HRTEM, and SAED images and EDS patterns of Sialon nanograins in the products.

with the exceeding 10 mass% Al content at 1450°C. Therefore, the appropriately exceeding Al contributed to the increased density of the sample. As expected, an increase in temperature was associated with an increase in bulk density. The apparent porosity decreased and the bulk density increased as sintering temperatures increased from 1350°C to 1550°C. The diffusion coefficient was related to temperature according to the formula $D = D_0 \exp(-Q/RT)$ [26]. At low temperatures, surface diffusion governed the sintering process while body diffusion dominated it at high temperatures. However, the densification of final products only depended on body diffusion. Temperature was the primary factor affecting final product density. The amount of spinel and Sialon increased with the Al increasing (Figures 1(b)–1(d)). The porosity also increased distinctly with the increase of Al (Figure 5(a)). This increase in Al could be attributed to the increased use of

aluminum dross (or less fly ash) in the raw materials and resulted in a decrease in the glass phase consisting of Si, Al, and O (Figure 2). This revealed that the appropriate liquid phase promoted the sintering process as well as densification at high firing temperatures.

The plot of bending strength versus the amount of the exceeding Al at different sintering temperatures is illustrated in Figure 6. The bending strength initially increased and subsequently decreased as Al content increased, at temperatures from 1350 to 1550°C. The highest bending strength (288 MPa) was achieved in product with the exceeding 10 mass% Al sintered at 1450°C. The product sintered at 1450°C had high bending strength and extremely low linear shrinkage (0.67%). The inset in Figure 6 is a digital photo of samples sintered at 1450°C. The samples did not bend after sintering in packing powders. Sintering in the corresponding packing powders

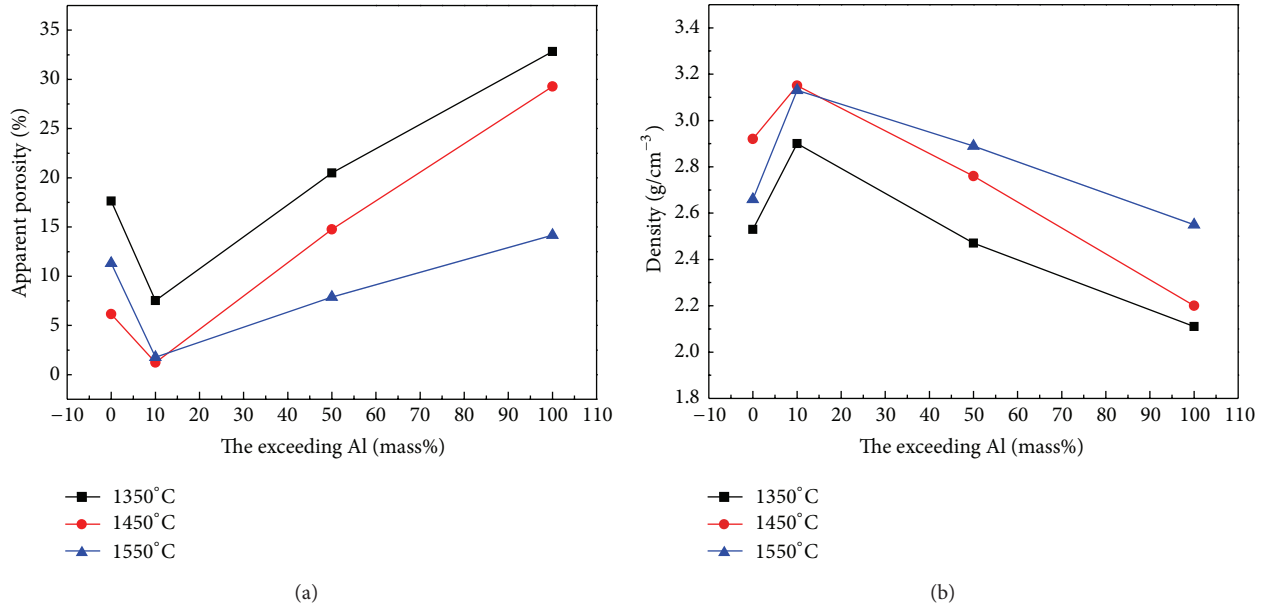


FIGURE 5: The physical properties of spinel-corundum-Sialon composite materials. (a) The apparent porosity and (b) bulk density of samples sintered at different temperatures as a function of the exceeding Al content.

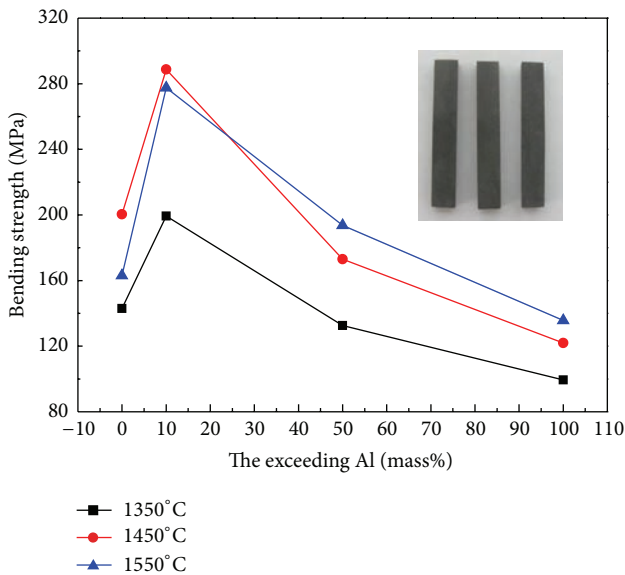


FIGURE 6: Bending strength of spinel-corundum-Sialon composite materials. The bending strength of product sintered at different temperatures as a function of the exceeding Al content. The inset is the digital image of product sintered at 1450°C.

was associated with the same shrinkage rate during heating. Hence, the *in situ* aluminothermic reduction-nitridation of fly ash and aluminum dross with appropriate packing powders resulted in spinel-corundum-Sialon composite materials that maintained their shape during processing.

3.3. Analysis of Hazardous Impurities. Many kinds of hazardous or impure elements are present in fly ash and

aluminum dross. They are another obstacle to the use of these waste materials. An analysis of these elements in the product samples was performed. Most of Ca cations were incorporated into β -Sialon crystals (Figures 3(f) and 4(f)). Fewer Ca cations were present in the glassy phase (Figures 7(a) and 7(d)), playing a key role in reducing the sintering temperature.

Figures 3(c) and 3(d) show that some aggregate impurities (shiny spheres) were embedded in the products. Their structures were further characterized by TEM, SAED, and EDS (Figure 7). Impurities were clearly seen as particles with a different (brighter) contrast. The TEM image, SAED images, and EDS patterns demonstrated that the impurities contained 35.20 at.% Si and 56.76 at.% Fe and that the crystalline phase was Fe_5Si_3 , a hard alloy. The EDS pattern identified trace elements (P, Cr, Mn, and Ni) in the Fe_5Si_3 particle. The effect these aggregates had on the spinel- Al_2O_3 -Sialon composites properties was examined. Cracks were seen along the grain boundary of impurity-rich Fe_5Si_3 spheres (TEM image, Figure 7(b)). These cracks could absorb fracture energy, resulting in improved fracture strength and toughness of the spinel- Al_2O_3 -Sialon composites.

Chemical and foregoing EDS analysis did not identify the trace element Ti. The product samples were carefully examined with TEM and the column-like nanograins characteristics of Ti and N were found (Figures 7(c) and 7(f)). XRD (Figure 1(a)), SAED, and EDS patterns (Figures 7(c) and 7(f)) revealed these nanograins to be TiN crystals.

4. Discussion

Using only the solid wastes of fly ash and aluminum dross as raw materials and a facile *in situ* aluminothermic

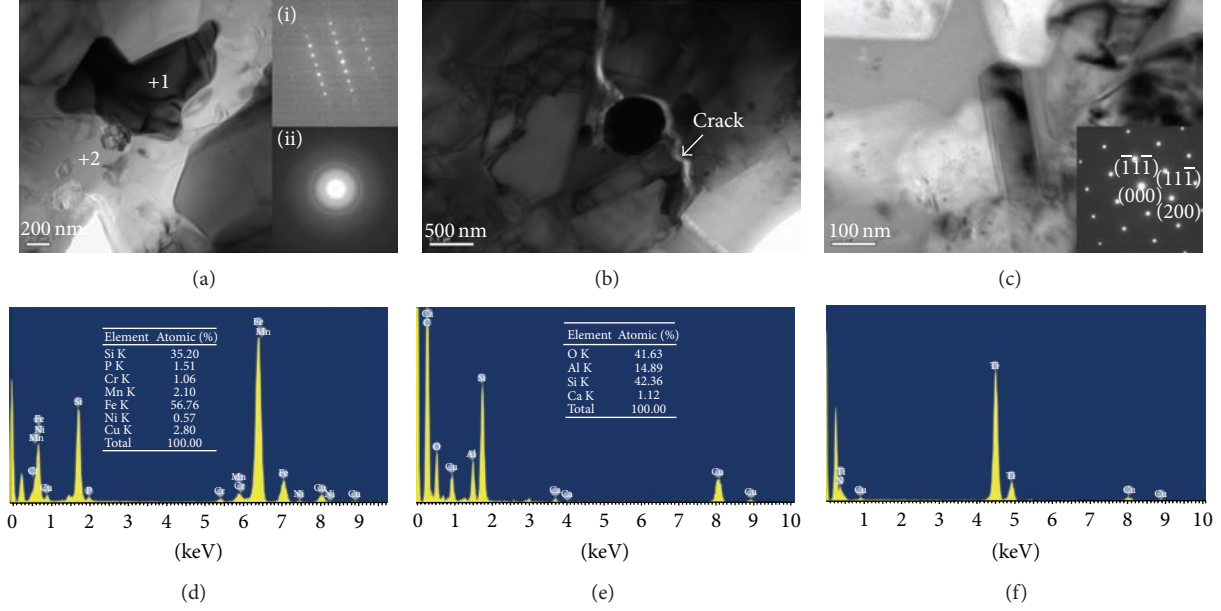


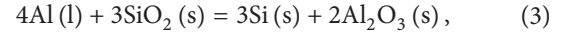
FIGURE 7: Typical TEM images, SAED images, and EDS patterns of impurities and glassy phase in the products. ((a), (b)) TEM images and ((d), (e)) the EDS results of impurities and the glassy phase in zone 1 and zone 2, respectively. (i) and (ii) show the SAED patterns of impurities and glass, respectively. ((c), (f)) Typical TEM, SAED, and EDS patterns of TiN in the products.

reduction-nitridation method, we prepared valuable spinel-corundum-Sialon composite materials, confirmed by XRD results (Figure 1(a)), along with EDS (Figure 3). The metallic Al in the aluminum dross enhanced the formation of spinel and Sialon at low temperatures. This finding was confirmed by the phase content analysis of the products sintered at different temperatures (Figures 1(b)–1(d)). The amount of spinel was increased due to the increase of MgO and Al₂O₃, while for Sialon it was produced due to the increased Al content. The aluminothermic reduction-nitridation reaction was exothermic [27], and the increased Al content resulted in the resultant increase in temperature. This increase in temperature also facilitated the formation of Sialon. Increasing the reaction temperature increased the production of spinel and Sialon and formed Al-rich spinel with a higher z-value Sialon. SEM (Figures 2 and 3) and TEM (Figure 4) images revealed that spinel-corundum-Sialon composite materials were composed of not only micro-sized, but also nano-sized spinel, Al₂O₃, and β -Sialon grains. The *in situ* grown nanograins would increase the fracture strength of the β -Sialon multiphase materials. In addition, as a hard and wear-resistant material [28, 29], TiN, the content of which basically had no variation in the product samples, can serve to improve the strength and wear resistance of the spinel-Al₂O₃-Sialon composites.

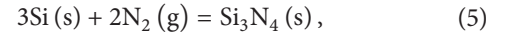
Only two nitrides, Sialon and TiN, were produced during the aluminothermic reduction-nitridation reaction. Their possible reaction mechanisms are proposed below, along with the underlying thermodynamic calculations [30]:



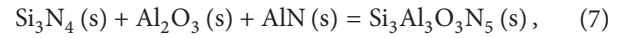
$$\Delta_r G_1 = -652.954 + 0.2328T - 0.0191T \lg \left(\frac{P_{N_2}}{P^\theta} \right), \quad (2)$$



$$\Delta_r G_2 = -675.922 + 0.1591T, \quad (4)$$

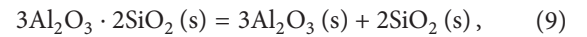


$$\Delta_r G_3 = -722.836 + 0.3150T - 0.0382T \lg \left(\frac{P_{N_2}}{P^\theta} \right), \quad (6)$$



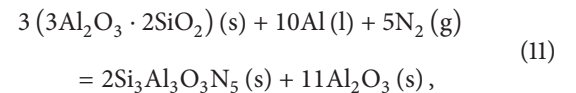
$$\Delta_r G_4 = -83.887 + 0.018T. \quad (8)$$

Mullite is a crystalline phase found in the fly ash. Its decomposition reaction and Gibbs free energy ($\Delta_r G$) are



$$\Delta_r G_5 = -8.6 + 0.0174T. \quad (10)$$

When the temperature was higher than 494.0 K, $\Delta_r G_5$ was greater than 0, and mullite did not easily decompose to Al₂O₃ and SiO₂. The mullite reacted directly with Al and N₂ to form Sialon as



$$\Delta_r G_6 = -3648.940 + 1.2382T - 0.0955T \lg \left(\frac{P_{N_2}}{P^\theta} \right). \quad (12)$$

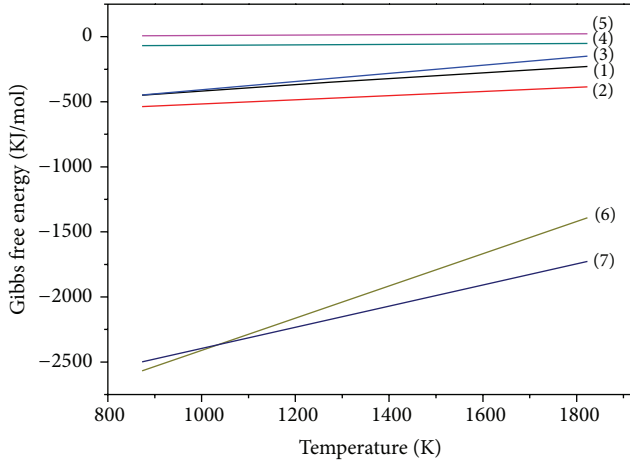
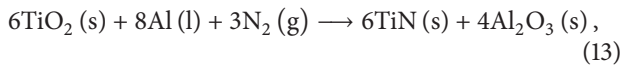


FIGURE 8: Gibbs free energy of reaction ($\Delta_r G$) versus temperature (T) for reactions (1) through (13). Under the experimental conditions of this study, all the above reaction equations could occur except (9).

The formation of TiN could be explained by reaction (13) through the aluminothermic reduction-nitridation process:



$$\Delta_r G_7 = -3209.88 + 0.8137T - 0.0573T \lg \left(\frac{P_{\text{N}_2}}{P^\theta} \right). \quad (14)$$

High purity nitrogen gas ($\geq 99.999\%$) at a pressure of 0.1 MPa was used during synthesis. The pressure of N_2 was $P_{\text{N}_2}/P^\theta \approx 1$. The Gibbs free energy of reaction ($\Delta_r G$) for (1) through (13) at different temperatures (T) was calculated (Figure 8). Under the experimental conditions of this study, all the above reactions could occur except (9). The reaction pathway for the formation of Sialon could be through route 1, that is, ((1) + (3) + (5) + (7)), and/or route 2, that is, (11). The β -Sialon product was surrounded by glassy phase (Figure 4(c)), and its formation might occur in a liquid phase via solution-diffusion-nucleation-precipitation, as previously reported by Cai et al. [31].

The bending strength of the spinel-corundum-Sialon composite materials was dependent on the composition of the raw materials and the testing temperature. These two factors had a remarkable effect on the content of the liquid phase, microstructure, apparent porosity, and bending strength of the products. The relationship between the bending strength and apparent porosity of the spinel-corundum-Sialon composites was absolutely in agreement with the exponential equation of the strength-porosity dependence [32], $\sigma = \sigma_0 \exp(-np)$, where the mechanical strength of inorganic nonmetallic materials usually decreases with an increase in porosity. An interesting result of this study was that the highest bending strength (288 MPa) of the spinel-corundum-Sialon composites was achieved at the exceeding 10 mass% Al after being sintered at 1450°C rather than 1550°C . This may be attributed to more liquid phase formed at the lower temperature, which resulted in a larger amount of spinel and

Sialon (Figures 1(c) and 1(d)). Although the liquid phase itself did not enhance the mechanical strength of the products, it did facilitate bulk sintering [27]. These findings suggest that the mechanical properties depend on a combination of the sintering temperature and amount of liquid phase.

Most of the hazardous or impure elements found in the fly ash and aluminum dross were found in the products. A few impurities such as NaCl and KCl from aluminum dross and Na_2O and K_2O from fly ash were not present in the products. The boiling point of these salts is about 1450°C and the sublimation point of these oxides is less than 1300°C [33], so these impurities would evaporate during sintering. The volatiles that leave the reaction furnace during sintering can be collected in order to minimize environmental pollution.

5. Conclusions

Low cost spinel-corundum-Sialon composite materials were prepared from fly ash and aluminum dross by *in situ* aluminothermic reduction-nitridation (ARN) at relatively low sintering temperatures. The product composites mainly consisted of micro-/nanosized plate corundum, octahedral spinel, and hexagonal columnar β -Sialon. As Al content increased (i.e., use of the aluminum dross), the bending strength and bulk density of sintered products initially increased and subsequently decreased. The apparent porosity exhibited an opposite trend. Samples with an exceeding 10 mass% Al (i.e., 38.94 mass% fly ash, 61.06 mass% aluminum dross) that were sintered at 1450°C exhibited the highest bending strength of 288 MPa and bulk density ($3.15 \text{ g}\cdot\text{cm}^{-3}$) and owned extremely low linear shrinkage (0.67%). The presence of hazardous or impure elements was also investigated. The main impurity phase was Fe_5Si_3 containing P, Cr, Mn, and Ni. Ca element was mostly incorporated into β -Sialon and less so into the glassy phase. Ti element was converted into TiN, which can improve the strength and wear resistance of the produced spinel- Al_2O_3 -Sialon composites. This research may provide a new environmentally friendly approach to use the vast waste resources of fly ash and aluminum dross to produce low cost structural refractories.

Conflict of Interests

The authors have declared that no conflict of interests exists.

Acknowledgments

This work was financially supported by the National Natural Science Foundation of China (Grant no. 51032007) and the Fundamental Research Funds for Central Universities (Grant no. 2010ZD12).

References

- [1] R. S. Iyer and J. A. Scott, "Power station fly ash—a review of value-added utilization outside of the construction industry," *Resources, Conservation & Recycling*, vol. 31, no. 3, pp. 217–228, 2001.

- [2] O. M. Dunens, K. J. Mackenzie, and A. T. Harris, "Synthesis of multiwalled carbon nanotubes on fly ash derived catalysts," *Environmental Science & Technology*, vol. 43, no. 20, pp. 7889–7894, 2009.
- [3] F.-F. Zhu, M. Takaoka, K. Shiota, K. Oshita, and Y. Kitajima, "Chloride chemical form in various types of fly ash," *Environmental Science & Technology*, vol. 42, no. 11, pp. 3932–3937, 2008.
- [4] L. D. Hulett Jr., A. J. Weinberger, K. J. Northcutt, and M. Ferguson, "Chemical species in fly ash from coal-burning power plants," *Science*, vol. 210, no. 4476, pp. 1356–1358, 1980.
- [5] T. Hashishin, Y. Kodera, T. Yamamoto, M. Ohyanagi, and Z. A. Munir, "Synthesis of (Mg,Si)Al₂O₄ spinel from aluminum dross," *Journal of the American Ceramic Society*, vol. 87, no. 3, pp. 496–499, 2004.
- [6] E. David and J. Kopac, "Hydrolysis of aluminum dross material to achieve zero hazardous waste," *Journal of Hazardous Materials*, vol. 209–210, pp. 501–509, 2012.
- [7] J. Johnson, "The foul side of 'clean coal,'" *Chemical & Engineering News*, vol. 87, no. 8, pp. 44–47, 2009.
- [8] A. Baba and A. Kaya, "Leaching characteristics of solid wastes from thermal power plants of western Turkey and comparison of toxicity methodologies," *Journal of Environmental Management*, vol. 73, no. 3, pp. 199–207, 2004.
- [9] J. A. Borchering, H. Chen, J. C. Caraballo et al., "Coal fly ash impairs airway antimicrobial peptides and increases bacterial growth," *PLoS ONE*, vol. 8, no. 2, Article ID e57673, 2013.
- [10] S. B. Wang and H. W. Wu, "Environmental-benign utilisation of fly ash as low-cost adsorbents," *Journal of Hazardous Materials*, vol. 136, no. 3, pp. 482–501, 2006.
- [11] J. Y. Hwang, X. Huang, and Z. Xu, "Recovery of metals from aluminum dross and saltcake," *Journal of Minerals & Materials Characterization & Engineering*, vol. 5, no. 1, pp. 47–62, 2006.
- [12] M. C. Yusta, I. Mármol, J. Morales, and L. Sánchez, "Use of olive biomass fly ash in the preparation of environmentally friendly mortars," *Environmental Science & Technology*, vol. 45, no. 16, pp. 6991–6996, 2011.
- [13] J.-H. Li, H.-W. Ma, and W.-H. Huang, "Effect of V₂O₅ on the properties of mullite ceramics synthesized from high-aluminum fly ash and bauxite," *Journal of Hazardous Materials*, vol. 166, no. 2–3, pp. 1535–1539, 2009.
- [14] N. N. Sampathkumar, A. M. Umarji, and B. K. Chandrasekhar, "Synthesis of α -cordierite (indialite) from flyash," *Materials Research Bulletin*, vol. 30, no. 9, pp. 1107–1114, 1995.
- [15] M. Miyake, C. Tamura, and M. Matsuda, "Resource recovery of waste incineration fly ash: synthesis of zeolites A and P," *Journal of the American Ceramic Society*, vol. 85, no. 7, pp. 1873–1875, 2002.
- [16] J.-T. Huang, Y.-G. Liu, Z.-H. Huang et al., "Ni(NO₃)₂-assisted catalytic synthesis and photoluminescence property of ultra-long single crystal Sialon nanobelts," *Crystal Growth & Design*, vol. 13, no. 1, pp. 10–14, 2013.
- [17] F. L. Riley, "Silicon nitride and related materials," *Journal of the American Ceramic Society*, vol. 83, no. 2, pp. 245–265, 2000.
- [18] Z.-H. Huang, J.-Z. Yang, Y.-G. Liu et al., "Novel sialon-based ceramics toughened by ferro-molybdenum alloy," *Journal of the American Ceramic Society*, vol. 95, no. 3, pp. 859–861, 2012.
- [19] L.-H. Xu, F. Lian, H. Zhang, Y.-B. Bi, K. Cheng, and Y.-B. Qian, "Optimal design and preparation of beta-SiAlON multiphase materials from natural clay," *Materials & Design*, vol. 27, no. 7, pp. 595–600, 2006.
- [20] F. J. Li, T. Wakihara, J. Tatami, K. Komeya, T. Meguro, and K. J. D. MacKenzie, "Elucidation of the formation mechanism of β -SiAlON from a zeolite," *Journal of the American Ceramic Society*, vol. 90, no. 5, pp. 1541–1544, 2007.
- [21] W.-W. Chen, P.-L. Wang, D.-Y. Chen et al., "Synthesis of (Ca,Mg)- α -sialon from slag by self-propagating high-temperature synthesis," *Journal of Materials Chemistry*, vol. 12, no. 4, pp. 1199–1202, 2002.
- [22] J. E. Gilbert and A. Mosset, "Preparation of β -SiAlON from fly ashes," *Materials Research Bulletin*, vol. 33, no. 1, pp. 117–123, 1998.
- [23] Y. Miyamoto, S. Kanehira, and M. Radwan, "Recycling of industrial and natural wastes to SiAlONs," *Refractories Applications and News*, vol. 9, no. 1, pp. 15–16, 2004.
- [24] O. Yamamoto, M. Ishida, Y. Saitoh, T. Sasamoto, and S. Shimada, "Influence of Mg²⁺ on the formation of β -SiAlON by the carbothermal reduction-nitridation of homogeneous gel," *International Journal of Inorganic Materials*, vol. 3, no. 7, pp. 715–719, 2001.
- [25] G. H. Liu, K. X. Chen, H. P. Zhou, X. S. Ning, and J. M. F. Ferreira, "Effect of diluents and NH₄F additive on the combustion synthesis of Yb α -SiAlON," *Journal of the European Ceramic Society*, vol. 25, no. 14, pp. 3361–3366, 2005.
- [26] K. Matsui, T. Yamakawa, M. Uehara, N. Enomoto, and J. Hojo, "Mechanism of alumina-enhanced sintering of fine zirconia powder: influence of alumina concentration on the initial stage sintering," *Journal of the American Ceramic Society*, vol. 91, no. 6, pp. 1888–1897, 2008.
- [27] X. M. Feng, X. Q. Lian, M. X. Jiang, and Y. E. He, "The influences of TiN content on the properties of the in situ Al₂O₃-TiN composites," *Advanced Materials Research*, vol. 311–313, pp. 1906–1910, 2011.
- [28] R. A. Janes, M. Aldissi, and R. B. Kaner, "Controlling surface area of titanium nitride using metathesis reactions," *Chemistry of Materials*, vol. 15, no. 23, pp. 4431–4435, 2003.
- [29] Z. J. Peng, H. Z. Miao, L. H. Qi, S. Z. Yang, and C. Z. Liu, "Hard and wear-resistant titanium nitride coatings for cemented carbide cutting tools by pulsed high energy density plasma," *Acta Materialia*, vol. 51, no. 11, pp. 3085–3094, 2003.
- [30] D. L. Ye and J. H. Hu, *Practical Thermodynamics Data Handbook of Inorganic Substances*, Metallurgical Industry Press, Beijing, China, 2002.
- [31] Y. B. Cai, Z. J. Shen, J. Grins, and S. Esmaeilzadeh, "Sialon ceramics prepared by using CaH₂ as a sintering additive," *Journal of the American Ceramic Society*, vol. 91, no. 9, pp. 2997–3004, 2008.
- [32] K. Shizaki, S. Komarneni, and M. Nanko, *Porous Materials: Process Technology and Applications*, vol. 4 of *Materials Technology Series*, Kluwer Academic, Dordrecht, The Netherlands, 1998.
- [33] D. L. Perry, *Handbook of Inorganic Compounds*, CRC Press, Boca Raton, Fla, USA, 2nd edition, 2011.

Research Article

Effect of Silicon Addition on High-Temperature Solid Particle Erosion-Wear Behaviour of Mullite-SiC Composite Refractories Prepared by Nitriding Reactive

Xiaochao Li,¹ Shusen Chen,¹ Zhaohui Huang,¹ Minghao Fang,¹
Yan'gai Liu,¹ Xiaowen Wu,¹ Juntong Huang,¹ and Baolin Liu²

¹ School of Materials Science and Technology, National Laboratory of Mineral Materials, China University of Geosciences (Beijing), Beijing 100083, China

² Key Laboratory on Deep Geodrilling Technology of the Ministry of Land and Resources, China University of Geosciences (Beijing), Beijing 100083, China

Correspondence should be addressed to Zhaohui Huang; huang118@cugb.edu.cn and Baolin Liu; lbaolin@cugb.edu.cn

Received 6 November 2013; Accepted 11 December 2013; Published 16 January 2014

Academic Editor: Majid R. Ayatollahi

Copyright © 2014 Xiaochao Li et al. This is an open access article distributed under the Creative Commons Attribution License, which permits unrestricted use, distribution, and reproduction in any medium, provided the original work is properly cited.

Solid particle erosion-wear experiments on as-prepared mullite-SiC composite refractories by nitriding reactive sintering were performed at elevated temperatures, using sharp black SiC abrasive particles at an impact speed of 50 m/s and the impact angle of 90° in the air atmosphere. The effects of silicon powder addition and erosion temperature on the erosion-wear resistance of mullite-SiC composite refractories were studied. The test results reveal that Si powders caused nitriding reaction to form β -sialon whiskers in the matrix of mullite-SiC composite refractories. The erosion-wear resistance of mullite-SiC composite refractories was improved with the increase of silicon powder addition and erosion temperature, and the minimum volume erosion rate was under the condition of 12% silicon added and a temperature of 1400°C. The major erosion-wear mechanisms of mullite-SiC composite refractories were brittle erosion at the erosion temperature from room temperature to 1000°C and then plastic deformation from 1200°C to 1400°C.

1. Introduction

With the development of technology of circulating fluidized bed boiler, garbage incineration boiler, and coke dry quench there is a growing demand for high-temperature erosion-wear-resistant materials with better performances whereas the conventional wear-resistant materials cannot fully meet these requirements anymore. For instance, the refractory linings materials for circulating fluidized bed boiler are commonly eroded between 850°C and 1100°C by the coal powders, high-melting mineral impurity particles, and limestone grits for desulfurizing; their services can be severely shortened by such high-temperature erosion-wear [1, 2]. At present, the commonly used wear-resistant refractories mainly include the traditional mullite-SiC [3], SiC bricks, and Si₃N₄/sialon bonded SiC [4]. The traditional mullite-SiC bricks cannot

meet the serve in high temperature due to their low erosion-wear resistance. SiC bricks and Si₃N₄/sialon bonded SiC bricks cannot be used on a large scale because of their high cost. Therefore, it is essential to devise a new sort of promising candidate erosion resistant material with high performance, low cost, and long service life.

β -sialon is a kind of solid solutions with the formula Si_{6-z}Al_zO_zN_{8-z} (0 < z ≤ 4.2) where Si⁴⁺ and N³⁻ are partially replaced by Al³⁺ and O²⁻, respectively. Such replacements without changing the crystal structure only increase the crystal unit sizes [5, 6]. Sialon-based materials are regarded as a promising candidate for erosion resistant materials, because of their excellent properties such as high strength, high toughness, chemical inertness, good wear resistance, corrosion resistance, and outstanding thermal shock resistance. For example, these sialon-based materials

TABLE I: Compositions of the samples.

Sample	Mullite with different grain size			SiC with different grain size		Si	Al ₂ O ₃	Binder
	1~0.5 mm	0.5~0 mm	≤45 μm	0.2~0 mm	≤45 μm			
M1	23	14	14	23	23	0	3	3
M2	23	14	10	23	23	4	3	3
M3	23	14	6	23	23	8	3	3
M4	23	14	2	23	23	12	3	3

Content, wt.%.

are widely used in valve seats, cutting tools, engines, cylinder liners, and other mechanical systems, which all requiring wear resistance at elevated temperatures [7–10]. Recently, the work on the wear properties of α/β -sialon composites ceramics revealed that under mild wear conditions, the single phase α -sialon materials showed better resistant under mild wear conditions. However, under more severe conditions, composites with higher β -sialon content showed better wear properties [11–13]. Chen et al. [14–17] have proposed that β -sialon could be easily prepared by high-temperature combustion syntheses, which were suitable for use as reinforcing agent in composites. It was found that with increasing β -sialon content in the composites, there was a monotonic increase in both bending strength and fracture toughness. Also, the wear resistance and fracture toughness of the material increased with increasing the size of elongated β -sialon grains. Therefore, introducing sialon phase into the mullite-SiC composite matrixes would be a useful approach for enhancing their erosion resistant.

Refractories consisting of aggregate and binder phases are regarded as representative brittle materials. The fracture toughness of material plays an important role in erosion-wear resistance. We can predict the erosion-wear resistance to conduct the experiment on fracture toughness of materials. It is noted that a lot of research works have been done on the fracture toughness experiments for ceramics. In the present research work, fracture toughness was usually evaluated in three different stress states (which include pure mode I, pure mode II, and combined mode I and mode II) using the asymmetric in the four-point bending method by a centrally cracked Brazilian disk specimen for ceramics [18–33]. At present, we have not conducted the research on fracture toughness of materials in this paper, and we will emphasize and discuss the relationship between fracture toughness and the erosion-wear resistance in the next work.

In this paper, we employed silicon and Al₂O₃ powders as raw materials to *in-situ* nitride to generate sialon, which surrounded mullite and SiC particles to form sialon bonded mullite-SiC composite refractories. Mullite-SiC composite refractories with high performance and low cost were prepared by nitriding reaction sintered. The work on their preparation and mechanical properties, heated at different temperatures by carbonization reaction sintering, has been reported recently [3]. The as-prepared sialon bonded mullite-SiC composite refractories could be developed as the linings materials of circulating fluidized bed boiler, garbage incineration boiler, and coke dry quench, which are usually suffered

solid particles erosion. Up to now, the study on the erosion-wear resistance of mullite-SiC composites refractories has not been reported previously. Therefore, in this paper, we investigated the solid particles erosion-wear behavior of the as-prepared mullite-SiC composite refractories by nitriding reactive sintering at high temperature. This work may provide theoretical basis for the development of wear-resistant refractory materials.

2. Experimental Details

The main starting materials used in the experiment were as follows: mullite ((Al₂O₃ + SiO₂) content > 98 wt.%, grain sizes (0.5~0 mm, 1~0.5 mm, ≤45 μm), Shanxi Xixiaoping Refractories, Ltd., China); α -SiC (98 wt.% pure, grain sizes (0.2~0 mm, ≤45 μm), Luoyang Refractory Research and Industry Trade Co., Ltd., China); silicon powder (98 wt.% pure, grain size ≤ 45 μm, Luoyang Refractory Research and Industry Trade Co., Ltd., China); α -Al₂O₃ powder (99.9 wt.% pure, grain size ≤ 0.5 μm, Aluminum Corporation of China, Ltd.); nitrogen (purity ≥ 99.99 wt.%); some sintering additives. Compositions of the samples are tabulated in Table I, showing different addition amounts of silicon powder.

The starting materials according to the mixture ratio designed in Table 1 were mixed in the mixer and the right water into the mixture during the mixing process was added. After the mixing uniformity, the materials mixture was pressed at 40 MPa for 30 s to get cylindrical samples of Φ 50 mm × 10 mm. Subsequently, the cylindrical samples were further compacted by cold isostatic pressing at 120 MPa for 90 s. Then these green bodies were dried at 110°C for 12 h. Finally, the green bodies were sintered at the temperature of 1300°C and 1400°C for 90 minutes, then rose to 1500°C for 3 h in a nitrogen atmosphere. When the sintering process was finished, the fired samples were furnace-cooled to room temperature.

The erosion-wear experiments were performed by self-designed high-temperature solid particle erosion-wear equipment, according to ASTM G76-04. The schematic diagram of erosion-wear experiment is presented in [2, 34]. Angular black SiC particles (the particles size of 325–830 μm is more than 97%) were used as abrasive particles. The pressure of compressed air was 0.45 MPa. The flux rate of impact particles was 60 g/min. The impingement angle of impact particles stream on the target was 90° and impacted at different temperatures (25°C, 200°C, 400°C, 600°C, 800°C, 1000°C, 1200°C, and 1400°C) with 100 g of black SiC particles.

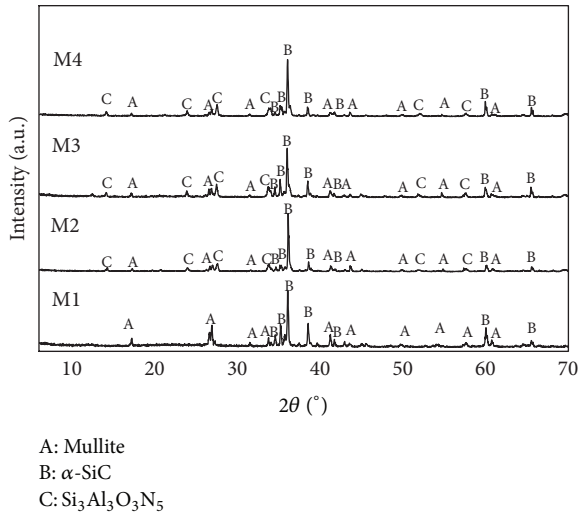


FIGURE 1: XRD patterns of samples with different silicon powder addition nitridation sintered at 1500°C for 3 h.

Solid particle erosion-wear resistance was characterized using volume erosion rate, which could be calculated with the following expression [2]:

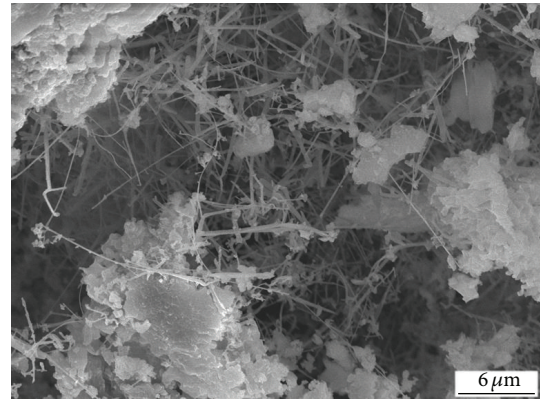
$$\text{volume erosion rate (mm}^3\text{/g)} = \frac{\text{average mass loss}}{\text{specimen density} \times \text{the mass of impact particles}} \quad (1)$$

Archimedes water immersion method was used in the determination of bulk density and apparent porosity. According to the ASTM C1421-01b (R2007), the bending strength was determined via conventional three-point bending method with a support roller span of 20 mm and a crosshead speed of 0.05 mm/min at room temperature, and the bend samples (6 mm × 6 mm × 40 mm) were tested more than three times. The crystalline phase was monitored via X-ray diffraction (XRD, XD-3, Cu K α_1 radiation, $\lambda = 1.5406$, Purkinje General Instrument Co., Ltd.). And the scanning electron microscopy (SEM, JEM-6460LV, Japan) was used to observe the microstructure of the samples eroded by SiC abrasive particles.

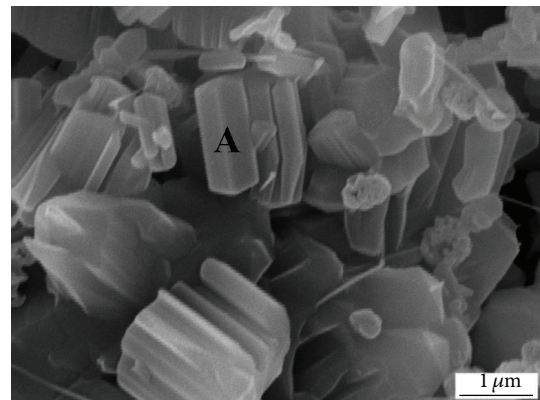
3. Results and Discussion

3.1. Effect of Silicon Addition on Phase, Microstructure, and Performance of Samples. Mullite-SiC composites were prepared using β -SiC, mullite, Si and Al $_2$ O $_3$ as raw materials by nitriding reaction sintering at 1500°C for 3 h. Figure 1 shows the phase compositions of samples. As this figure shows, the phase compositions consist of mullite, α -SiC, and Si $_3$ Al $_3$ O $_3$ N $_5$, which were formed in samples only when silicon powder has been added. The appearance of Si $_3$ Al $_3$ O $_3$ N $_5$ was due to the nitriding reaction of silicon powder and Al $_2$ O $_3$.

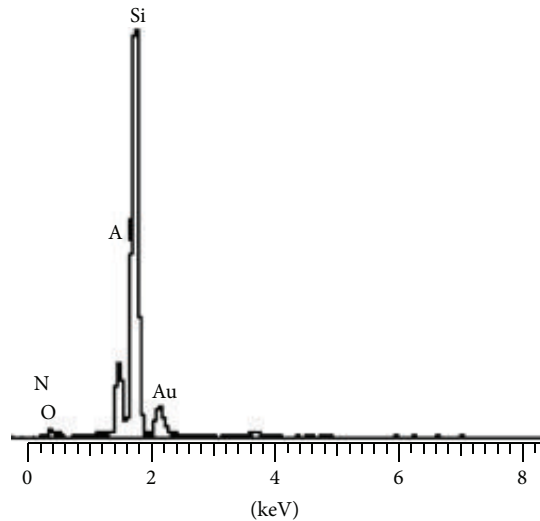
Figure 2 shows SEM photographs and EDS spectrum of samples. There are large amounts of whiskers structure to



(a)



(b)



(c)

FIGURE 2: SEM photographs and EDS spectrum of samples: (a) surface fracture microstructure of sample M4; (b) surface microstructure of sample M4; (c) EDS spectrum of point A in (b).

form in the fracture surface of sample M4 (shown in Figure 2(a)). Moreover, the columnar-like structure is formed in the surface of sample M4 (shown in Figure 2(b)). It is believed that the columnar-like and whiskers consisted mainly of Si $_3$ Al $_3$ O $_3$ N $_5$ by XRD, SEM, and EDS analyses. The fundamental properties of samples are listed in Table 2. The properties of

TABLE 2: Properties of mullite-SiC composite refractories prepared by nitriding reactive.

Property	Samples			
	M1	M2	M3	M4
Bulk density (g/cm ³)	2.12	2.15	2.19	2.27
Apparent porosity (%)	28.4	27.2	26.1	23.6
Cold compression strength (MPa), \geq	40	60	80	120
Cold bending strength (MPa)	17.30	24.58	29.96	40.08
Vickers hardness of binder phase (GPa)	8.7	9.5	10.4	11.9

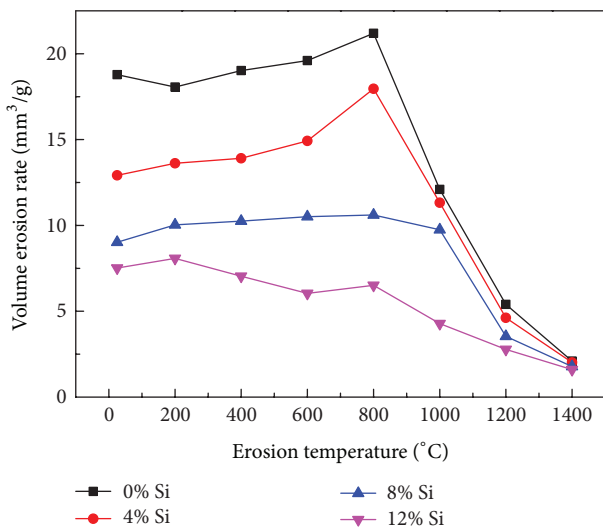


FIGURE 3: The volume erosion rates of the samples with respect to the test temperature and silicon powder addition.

sample M4 (12% silicon powder added) are better than other samples.

3.2. Effect of Silicon Addition and Erosion Temperature on the Volume Erosion Rates of Samples. Figure 3 shows the effect of erosion temperature and silicon powder addition on the volume erosion rates of the samples. As Figure 3 reveals, the volume erosion rate tends to slightly change with increasing the *erosion* temperature from 25°C to 800°C, then sharply decreases from 800°C to 1400°C. The result reveals that mullite-SiC composites refractories had excellent high temperature erosion-wear resistance. The reasons can be explained as follows. The binder phase was softer and can show more plastic deformation at elevated temperatures. So it can consume and absorb more impact energy made by SiC erosion particles. Also at high temperature, the volume of aggregates would expand to a certain extent and make a higher bonding strength with the binder phase, which could improve the erosion-wear and spalling resistance of refractories.

As Figure 3 further reveals, the volume erosion rates of samples decreased sharply with the increasing of silicon powder addition at the erosion temperature from 25°C to 1000°C the reason could be due to the apparent porosity decrease and the mechanical properties improved with the increasing of silicon powder addition. Furthermore, the content of β -sialon increased with the increasing of silicon powder addition, which can improve the erosion-wear resistance at the experiment temperature from 25°C to 800°C. The refractory linings materials of circulating fluidized bed boiler, garbage incineration boiler, and coke dry quench are commonly used at the temperature between 850°C and 1100°C. The volume erosion rate of sample M4 (12% silicon added) tends to slightly change and reach the lowest value about 5 mm³/g under the use of temperature between 850°C and 1100°C. Therefore, sample M4 (12% silicon added) can meet the use as the lining wear-resisting refractories.

3.3. Erosion-Wear Mechanisms Analysis. Refractories are regarded as brittle materials, which consist of coarse aggregate and binder phase. So the material removal of refractories is the main brittle erosion mechanism. Figure 4 shows erosion morphologies of the binder phase in the samples. As Figure 4 reveals, the structure of sample M1 (no silicon added) was loosened (shown in Figure 4(a)), and the bonding strength was weak in both aggregate and binder phases. Therefore, the aggregate was easier to be dropped due to impact of the 36 SiC erosion particles, which caused the high volume of erosion rate. While the structure of sample M4 (12% silicon added) was denser, the bonding strength of the aggregate and binder phases of sample M4 was improved. So the erosion mechanism of binder phase was mainly started from the defects on the edge of pores (shown in Figures 4(b) and 4(c)) at low temperature in sample M4. Pores of the binder phase were enlarged gradually because of impact of the 36 SiC erosion particles, which caused the loss of binder phase. The erosion damage for the sample M1 is more serious than the sample M4, which shows that the overall strength and erosion resistance of samples were improved with the increasing of silicon addition.

Figure 5 shows the typical brittle erosion mechanism of aggregate in sample M4 (12% silicon added). As can be seen from Figure 5, the cracks and brittle fractures have occurred in the aggregate during the impact of the SiC erosion particles. Then the material was removed as the brittle fracture of the aggregate, which causes the high erosion rates at low temperature. Given the above, we can know that the erosion-wear resistance of samples was improved with the silicon addition. Also, the brittle erosion mechanism is a dominant model for the refractories removal at low temperature.

Figure 6 displays SEM images and EDS patterns of sample M4 (12% Silicon added) eroded at 1400°C. It can be seen from Figures 6(a) and 6(b) that α -SiC on the surface of samples was oxidized at high temperature to form a thin dense SiO₂ glassy film which can blunt the surface cracks and improve the high-temperature erosion resistant materials [35]. Figure 7 shows the representative plastic deformation mechanism of samples at high temperature. When erosion occurred at high temperature, the binder phase started to soften because of

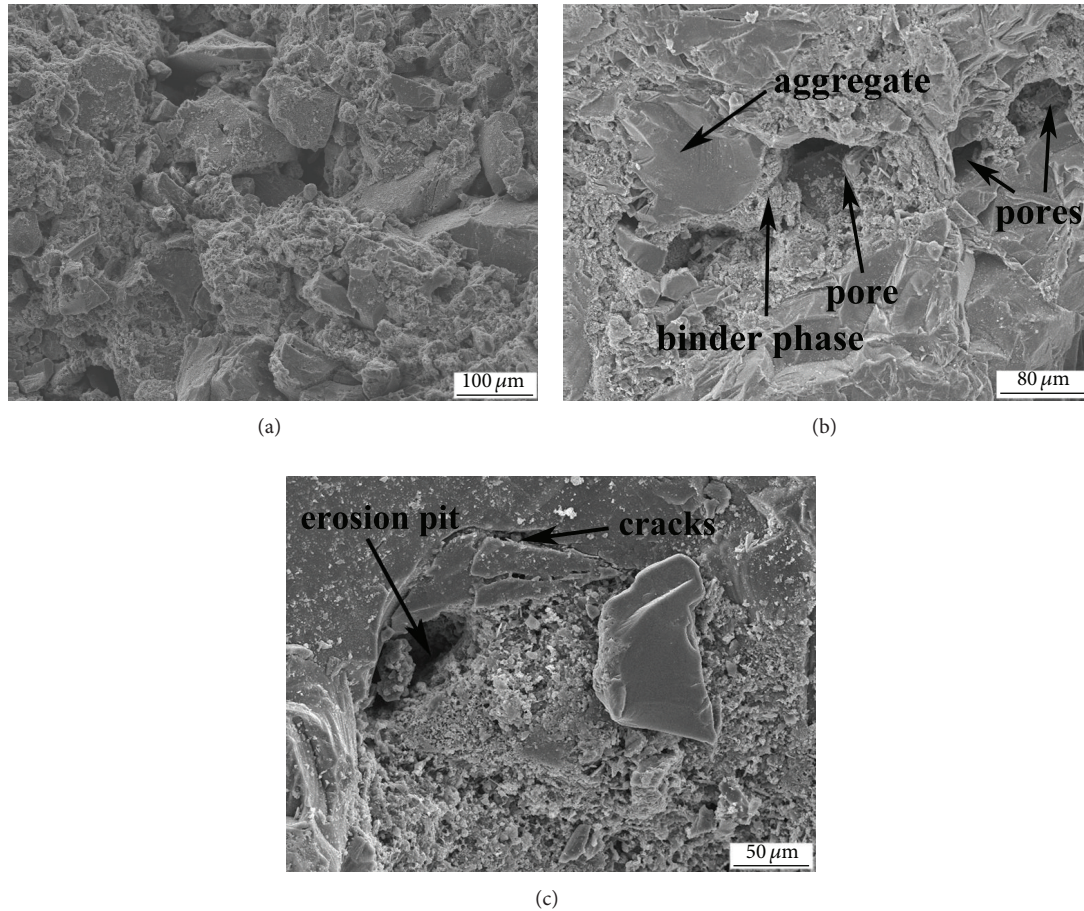


FIGURE 4: Erosion morphologies of the aggregate and binder phases in the samples: (a) sample M1 (no silicon added) eroded at 25°C; (b) sample M4 (12% silicon added) eroded at 25°C; (c) sample M4 (12% silicon added) eroded at 800°C.

the oxidation and formed a layer of glass-like substance on the surface of samples, which can accommodate more plastic deformation. The plastic deformation can reduce sharply the volume erosion rate of material. However, there is still some brittle erosion at 1200°C in sample M1 (no silicon added), which caused the higher volume erosion rate than the sample M1.

We can conclude from the above study about phase, performance and microstructure of materials that the mechanical properties and erosion-wear resistance of samples increased with silicon powder addition. The results can be explained that the addition of silicon powder is helpful to form β -sialon whiskers (depicted in Figure 2), which can fill the void and enhance the toughness of the material. Some studies indicate that *in situ* formed whiskers in the material are without pollution and spread evenly, and the formation of whiskers can prevent grain slip and improve the toughness of material through the bridge and pull-out mechanism [36, 37]. Furthermore, silicon powders had melted when sintered in 1500°C because of the low melting point 1410°C of silicon [3]. The liquid silicon may fill the space between particles and make particles combine more closely by the surface tension, which can decrease the porosity and increase volume density

[38]. Therefore, the mechanical properties and erosion-wear resistance of samples were improved with silicon powder addition.

4. Conclusions

The main phase of mullite-SiC composite refractories by nitriding reaction sintering is mullite, α -SiC and β -Sialon, and *in-situ* form β -Sialon whiskers in the matrix of mullite-SiC composite refractories can enhance the mechanical properties and erosion-wear resistance. The erosion resistance of mullite-SiC composite refractories increased with the increase of silicon powder addition and test temperature, and the minimum erosion rate was at 12% silicon added and 1400°C. The major erosion mechanism of mullite-SiC composite refractories is brittle erosion at the temperature from room temperature to 1000°C. The material removal is mainly due to the brittle fracture of aggregates and pores expansion of the binder phase causing the aggregates pull-outs. From 1000°C to 1400°C, the major erosion mechanism of mullite-SiC composite refractories is plastic deformation, which mainly resulted from oxidation and softening of the material.

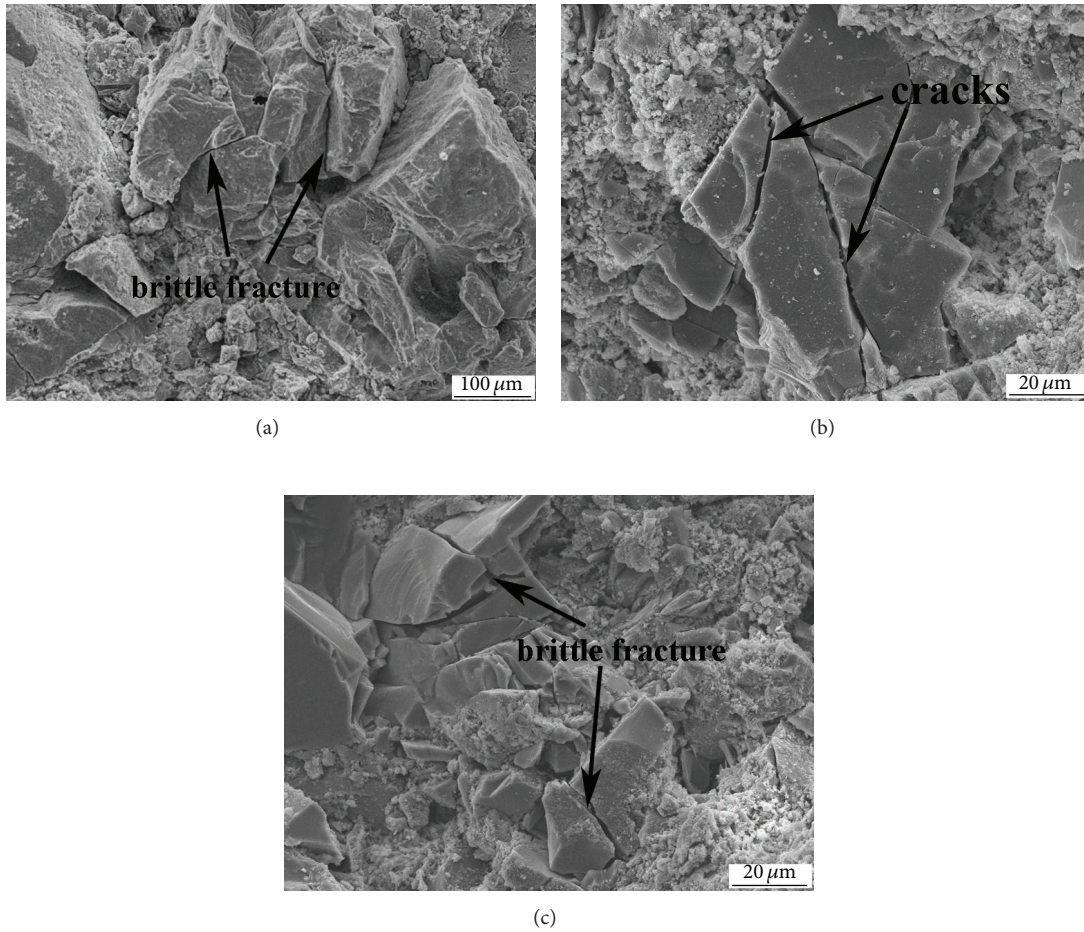


FIGURE 5: Typical brittle erosion morphologies of aggregate in sample M4 (12% silicon added): (a) eroded at 25°C; (b) eroded at 800°C; (c) eroded at 1000°C.

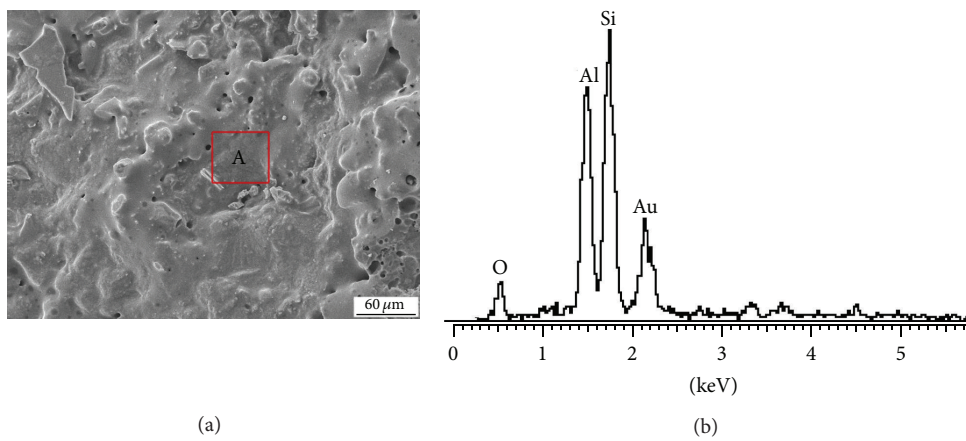
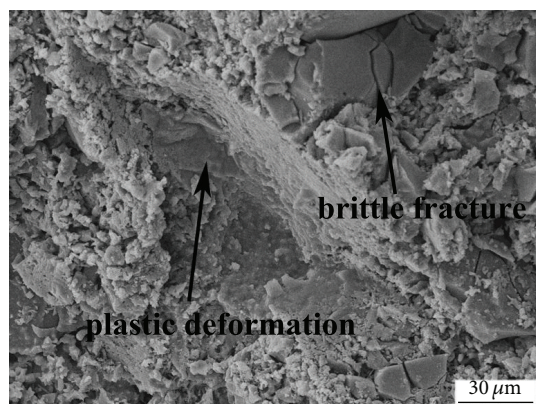


FIGURE 6: SEM images and EDS patterns of sample M4 (12% silicon added) eroded at 1200°C: (a) SEM micrographs of the surface of sample and (b) EDS result of area A.



(a)



(b)

FIGURE 7: Representative SEM photography shows plastic deformation of samples: (a) sample M1 (no silicon added) eroded at 1200°C and (b) sample M4 (12% silicon added) eroded at 1200°C.

Conflict of Interests

The authors declare that there is no conflict of interests regarding the publication of this paper.

Acknowledgments

This work was financially supported by National Natural Science Foundation of China (Grant no. 51032007 and no. 51272241) and Research Fund for the Doctoral Program of Higher Education of China (Grant no. 20130022110006).

References

- [1] J. P. Bennett and K. S. Kwong, "Refractory liner materials used in slagging gasifiers," *Refractories Application and News*, vol. 9, pp. 21–25, 2004.
- [2] J.-Z. Yang, M.-H. Fang, Z.-H. Huang et al., "Solid particle impact erosion of alumina-based refractories at elevated temperatures," *Journal of the European Ceramic Society*, vol. 32, no. 2, pp. 283–289, 2012.
- [3] X. C. Li, Z. H. Huang, Y. G. Liu et al., "Effect of silicon addition on mechanical properties of mullite-SiC composite refractories," *Journal of the Ceramic Society of Japan*, vol. 120, pp. 574–578, 2012.
- [4] D.-S. Park, B.-D. Han, D.-S. Lim, and I.-W. Yeo, "A study on wear and erosion of sialon-Si₃N₄ whisker ceramic composites," *Wear*, vol. 203–204, pp. 284–290, 1997.
- [5] J. T. Huang, Y. G. Liu, Z. H. Huang et al., "Ni(NO₃)₂-assisted catalytic synthesis and photoluminescence property of ultralong single crystal Sialon nanobelts," *Crystal Growth & Design*, vol. 13, pp. 10–14, 2013.
- [6] V. A. Izhevskiy, L. A. Genova, J. C. Bressiani, and F. Aldinger, "Progress in SiAlON ceramics," *Journal of the European Ceramic Society*, vol. 20, no. 13, pp. 2275–2295, 2000.
- [7] T. Ekström and M. Nygren, "SiAlON ceramics," *Journal of the American Ceramic Society*, vol. 75, pp. 259–276, 1992.
- [8] S. Kurama, M. Herrmann, and H. Mandal, "The effect of processing conditions, amount of additives and composition on the microstructures and mechanical properties of α-SiAlON ceramics," *Journal of the European Ceramic Society*, vol. 22, no. 1, pp. 109–119, 2002.
- [9] J. Huang, M. Fang, Y. Liu, and Z. Huang, "Preparation of β-Sialon from fly ash by carbothermal reduction-nitridation reaction," *Key Engineering Materials*, vol. 368, pp. 910–912, 2008.
- [10] Z.-H. Huang, J.-Z. Yang, Y.-G. Liu et al., "Novel sialon-based ceramics toughened by ferro-molybdenum alloy," *Journal of the American Ceramic Society*, vol. 95, no. 3, pp. 859–861, 2012.
- [11] J. M. Ferreira and K. X. Chen, "Toughening Y α-sialon ceramics by using new-developed rod-like Y α-sialon crystals as reinforcing agents," *Key Engineering Materials*, vol. 224, pp. 269–274, 2002.
- [12] M. I. Jones, K. Hirao, H. Hyuga, Y. Yamauchi, and S. Kanzaki, "Wear properties of Y-α/β composite sialon ceramics," *Journal of the European Ceramic Society*, vol. 23, no. 10, pp. 1743–1750, 2003.
- [13] M. I. Jones, H. Hyuga, K. Hirao, and Y. Yamauchi, "Wear behaviour of single phase and composite sialon ceramics stabilized with Y₂O₃ and Lu₂O₃," *Journal of the European Ceramic Society*, vol. 24, no. 10–11, pp. 3271–3277, 2004.
- [14] V. X. Lima Filho, J. P. Davim, C. A. Cairo, and J. M. F. Ferreira, "Preparation and characterization of SiAlON matrix composites reinforced with combustion synthesis rod-like SiAlON particles," *International Journal of Refractory Metals and Hard Materials*, vol. 27, no. 3, pp. 647–652, 2009.
- [15] K. X. Chen, J. Haibo, H. Zhou, and J. M. Ferreira, "Microstructure and formation mechanism of combustion-synthesized rod-like Ca α-sialon crystals," *Journal of Materials Research*, vol. 16, no. 7, pp. 1928–1934, 2001.
- [16] K. Chen, M. E. F. L. Costa, H. Zhou, and J. M. F. Ferreira, "Novel rod-like yttrium α-sialon crystalline powders prepared by combustion synthesis," *Materials Chemistry and Physics*, vol. 75, no. 1–3, pp. 252–255, 2002.
- [17] R. Fu, K. Chen, X. Xu, and J. M. F. Ferreira, "Combustion synthesis of rod-like α-SiAlON seed crystals," *Materials Letters*, vol. 58, no. 12–13, pp. 1956–1958, 2004.
- [18] D. K. Shetty, A. R. Rosenfield, and W. H. Duckworth, "Mixed-mode fracture in biaxial stress state: application of the diametral-compression (Brazilian disk) test," *Engineering Fracture Mechanics*, vol. 26, no. 6, pp. 825–840, 1987.
- [19] S. Dileep and D. K. Shetty, "Fracture toughness of polycrystalline ceramics in combined mode I and mode II loading," *Journal of the American Ceramic Society*, vol. 72, no. 1, pp. 78–84, 1989.
- [20] D. Singh and D. K. Shetty, "Microstructural effects on fracture toughness of polycrystalline ceramics in combined mode I and

- mode II loading,” *Journal of Engineering for Gas Turbines and Power*, vol. 111, pp. 174–180, 1989.
- [21] D. Singh and D. K. Shetty, “Subcritical crack growth in soda-lime glass in combined mode I and mode II loading,” *Journal of the American Ceramic Society*, vol. 7, pp. 3597–3606, 1990.
- [22] S. Y. Yarema, G. S. Ivanitskaya, A. L. Maistrenko, and A. I. Zboromirskii, “Crack development in a sintered carbide in combined deformation of types I and II,” *Strength of Materials*, vol. 16, no. 8, pp. 1121–1128, 1984.
- [23] S. Suresh, C. F. Shih, A. Morrone, and N. P. O’Dowd, “Mixed-mode fracture toughness of ceramic materials,” *Journal of the American Ceramic Society*, vol. 73, no. 5, pp. 1257–1267, 1990.
- [24] H. Awaji and T. Kato, “Griffith criterion for mode II fracture of ceramics,” in *Proceedings of the 11th International Conference on Experimental Mechanics*, pp. 1199–1204, Oxford, UK, 1998.
- [25] M. R. Ayatollahi and M. R. M. Aliha, “Mixed mode fracture analysis of polycrystalline graphite—a modified MTS criterion,” *Carbon*, vol. 46, no. 10, pp. 1302–1308, 2008.
- [26] M. R. M. Aliha and M. R. Ayatollahi, “On mixed-mode I/II crack growth in dental resin materials,” *Scripta Materialia*, vol. 59, no. 2, pp. 258–261, 2008.
- [27] T. Machida and N. Isobe, “Evaluation of mixed-mode fracture toughness using cracked Brazilian disk,” *Transactions of the Japan Society of Mechanical Engineers A*, vol. 61, no. 592, pp. 2552–2559, 1995.
- [28] A. R. Rosenfield, “Fracture of brittle materials under a simulated wear stress system,” *Journal of the American Ceramic Society*, vol. 72, no. 11, pp. 2117–2120, 1989.
- [29] M. R. Ayatollahi and M. R. M. Aliha, “Mixed mode fracture in soda lime glass analyzed by using the generalized MTS criterion,” *International Journal of Solids and Structures*, vol. 46, no. 2, pp. 311–321, 2009.
- [30] M. R. Ayatollahi and M. R. M. Aliha, “Fracture analysis of some ceramics under mixed mode loading,” *Journal of the American Ceramic Society*, vol. 94, no. 2, pp. 561–569, 2011.
- [31] M. R. M. Aliha and M. R. Ayatollahi, “Analysis of fracture initiation angle in some cracked ceramics using the generalized maximum tangential stress criterion,” *International Journal of Solids and Structures*, vol. 49, pp. 1877–1883, 2012.
- [32] V. Tikare and S. R. Choi, “Combined mode I-mode II fracture of 12-mol%-ceria-doped tetragonal zirconia polycrystalline ceramic,” *Journal of the American Ceramic Society*, vol. 80, no. 6, pp. 1624–1626, 1997.
- [33] M. Li and M. Sakai, “Mixed-mode fracture of ceramics in asymmetric four-point bending: effect of crack-face grain interlocking/bridging,” *Journal of the American Ceramic Society*, vol. 79, no. 10, pp. 2718–2726, 1996.
- [34] F. Liu, M. Fang, X. Wang, Y. Liu, and Z. Huang, “Solid particle erosion behavior of 3YSZ ceramics at elevated temperatures,” *Key Engineering Materials*, vol. 492, pp. 85–88, 2012.
- [35] Z. H. Huang, J. L. Sun, J. X. Wang, and Y. R. Hong, “ β -sialon- Al_2O_3 -SiC composite refractories,” *Key Engineering Materials*, vol. 224, pp. 275–280, 2002.
- [36] J. B. Wachtman, W. R. Cannon, and M. J. Matthewson, *Mechanical Properties of Ceramics*, John Wiley & Sons, New York, NY, USA, 2009.
- [37] E. Karamian and A. Monshi, “Influence of additives on nano-SiC whisker formation in alumina silicate-SiC-C monolithic refractories,” *Ceramics International*, vol. 36, no. 2, pp. 811–816, 2010.
- [38] M. W. Barsoum and B. Houng, “Transient plastic phase processing of titanium-boron-carbon composites,” *Journal of the American Ceramic Society*, vol. 76, pp. 1445–1451, 1993.

Research Article

Average Fracture Energy for Crack Propagation in Postfire Concrete

Kequan Yu, Jiangtao Yu, and Zhoudao Lu

College of Civil Engineering, Tongji University, Shanghai 200092, China

Correspondence should be addressed to Jiangtao Yu; yujiangtao@tongji.edu.cn

Received 20 September 2013; Accepted 20 October 2013

Academic Editor: Filippo Berto

Copyright © 2013 Kequan Yu et al. This is an open access article distributed under the Creative Commons Attribution License, which permits unrestricted use, distribution, and reproduction in any medium, provided the original work is properly cited.

Wedge-splitting tests of postfire concrete specimens were carried out in the present research to obtain the load-displacement curves. Ten temperatures varying from room temperature to 600°C were employed. In order to calculate the accurate fracture energy, the tails of load-displacement curves were best fitted using exponential and power functions. Three fracture energy quantities (fracture energy G_F , stable fracture energy G_{FS} , and unstable fracture energy G_{FU}) with their variation tendency and their mutual relationship were determined to predict energy consumption for the complete fracture propagation. Additionally, the stable fracture work W_{FS} was also calculated. All these fracture parameters sustain an increase-decrease tendency which means that the fracture property of postfire concrete shares the same tendency.

1. Introduction

Since the application of fracture mechanics to concrete, the energy consumption for crack propagation in concrete has been a popular topic. For concrete, the specific fracture energy G_F has been proven to be a useful parameter in the structure design and fracture behavior modeling. The specific fracture energy of concrete was defined based on a tensile test as the energy absorbed per unit crack area in widening the crack from zero to or beyond the critical value above which no stress can transmit [1]. Based on the work-of-fracture principle, three-point bending test [2], compact tension [3], and wedge-splitting method [4] were proposed as alternative methods to determine the specific fracture energy G_F . It is computed as the area under the entire imposed load P and load-line displacement curve divided by the projected area of uncracked ligament, so the fracture energy G_F represents the average or nominal energy consumption of concrete for an entire crack propagation process.

The existence of fracture process zone FPZ ahead of a crack is now well accepted. Since the 1970s, it has been known that the evolution of the FPZ undergoes two distinct periods—precritical stable crack growth and unstable fracture process [5]. There is no doubt that crack propagation is accompanied by energy dissipation, and the motive for

crack propagation comes from either work provided by the imposed load or released strain energy. Fracture energy is one appropriate consideration to describe the amount of energy consumed during crack propagation process.

It is worth noting that the fracture energy can only represent the amount of average energy dissipation for entire crack propagation from crack initiation to complete failure without characterizing crack stable propagation and unstable fracture periods. So even with G_F , it is still not clear how much energy is dissipated during those two crack extension periods. Xu et al. [6] proposed two new concepts the stable fracture energy G_{FS} and unstable fracture energy G_{FU} to describe fracture responses for different crack propagation periods. It is found that G_{FS} kept constant for different ligament lengths, whereas G_F and G_{FU} showed the apparent size effect. But the accurate calculation of fracture surface remains unsolved. It is known that the true path of crack extension is tortuous, not straight as expected. The projected area underestimates the true fracture area. Hence, these parameters are actually nominal values.

The fracture energy of postfire concrete has been studied by several researchers [7–12]. It is found that the residual fracture energy sustained an increase-decrease tendency with the turning point at approximately 450°C. The increase tendency is due to the energy dissipation of microcracks distributing in

the concrete, whereas the thermal damage induced by high temperatures reduces the residual fracture energy. However, in these researches, the influence of loading-displacement tail was unknown or not considered.

In present paper, wedge-splitting experiments of under ten temperatures levels varying from 20°C to 600°C and the specimens size of 230 mm × 200 mm × 200 mm with initial-notch depth ratios 0.4 are implemented [12]. Based on the work-of-fracture idea, the residual fracture energy G_F is calculated considering the influence of load-displacement tail. Furthermore, the fracture energy consumption for crack stable extension and unstable extension, that is, G_{FS} , G_{FU} , is investigated. However, the true fracture surface remains undetermined and extremely difficult for specimens subjected to high temperatures, so these three fracture energy parameters are still nominal values. Hence, corresponding to G_{FS} and G_{FU} , the stable and unstable fracture work which neglect the fracture surface and their variation about temperatures are thus determined. From these parameters the fracture properties of postfire concrete could be described.

2. Fracture Energies for an Entire Crack Propagation Period

Based on the global energy balance principle, the work performed by a generalized force P on its displacement will be transformed into energy: one part of energy is stored in the body in the form of strain energy and the other part is used for crack propagation. It can be mathematically written as [6]:

$$G_{Fi}A_i = W_i - \Delta U_i = \int_0^{\delta_i} Pd\delta - \Delta U_i, \quad (1)$$

where G_{Fi} = average energy needed for unit crack propagation during period from crack initiation to any instant of time i ; A_i = newly formed fracture area for this period; the product of these two quantities represents the energy absorbed for crack propagation during this period; W_i = work performed by the external force P during the same period; U_i = increase of elastic strain energy of the body until time i ; δ_i = crack opening displacement corresponding to P . If time i is approaching the failure terminal point $i = 1$, where the load drops to zero, then G_{Fi} in (1) will reduce to

$$G_F = \frac{W}{A_{lig}} = \frac{\int_0^{\delta_1} Pd\delta}{b(h-a_0)}, \quad (2)$$

where G_F = RILEM fracture energy; W = total energy provided by the external force P for crack propagation; A_{lig} = projected fracture area perpendicular to the tensile stress direction; b = specimen thickness; h = specimen height; a_0 = initial crack length.

During the stable crack propagation period, the load will increase up to its peak value P_{max} with its corresponding displacement reaching COD_c ; see Figure 1. So, based

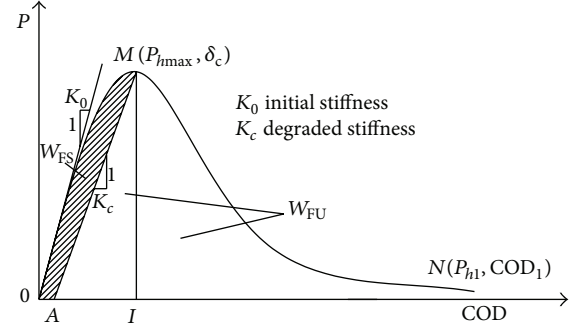


FIGURE 1: Energy consumption for an entire crack propagation period.

on (1), the average energy absorbed during this period can be evaluated by

$$\begin{aligned} G_{FS} &= \frac{W_{FS}}{A_S} = \frac{W_P - \Delta U_S}{A_S} = \frac{W_{OAMO}}{A_S} \\ &= \frac{W_{OIMO} - W_{AIMA}}{A_S} = \frac{\int_0^{COD_c} PdCOD_c - \Delta U_S}{A_S}, \end{aligned} \quad (3)$$

where G_{FS} by naming the stable fracture energy = average energy needed for the crack to grow unit area during the crack stable propagation; A_S = change in fracture area; W_{FS} = W_{OAMO} = energy provided for stable crack propagation as shown in Figure 1 by the shaded area; W_P = W_{OIMO} = work performed by the external force P for crack increases its area A_S ; ΔU_S = W_{AIMA} = increased elastic strain energy of the body; and COD_c = critical crack opening displacement.

From the definition of the stable fracture energy G_{FS} , it is implied that the work from the imposed load P is expended in two forms during the crack stable propagation: one part is stored in the body in the form of the elastic strain energy (ΔU_S) and the other part is the energy absorbed by the fracture zone mainly to counteract the resistance caused by the cohesive forces along the FPZ. In the same way, the unstable fracture energy, denoted by G_{FU} , is defined based on energy equilibrium as

$$G_{FU} = \frac{W_U}{A_U} = \frac{W - W_S}{A_U}, \quad (4)$$

where W_U = energy needed for the crack unstable propagation period and A_U = change in fracture area. During this period, the stored energy is completely released until the deformation reaches its maximum value COD_1 when the load closes to zero. Similar to the RILEM fracture energy G_F , the establishment of the stable fracture energy G_{FS} and unstable fracture energy G_{FU} rests upon the implicit assumption that no other energy consumption occurs outside the fracture zone.

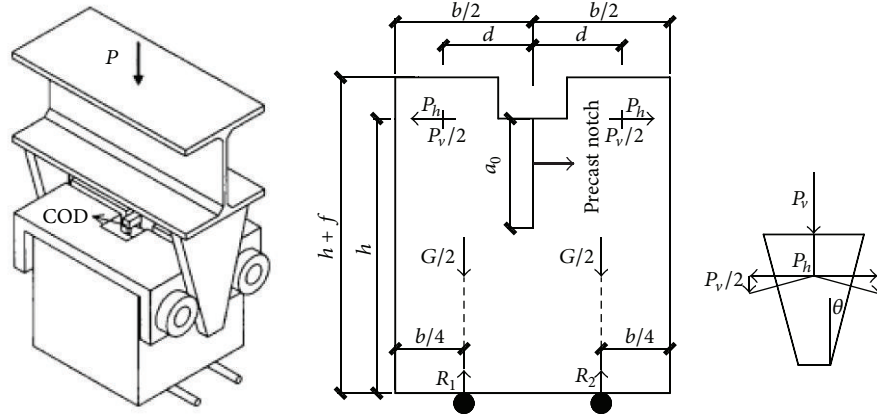


FIGURE 2: Test setup and geometry of specimens.

3. Experimental Program and Experimental Phenomena

In this test, concrete specimens were prepared using an ordinary silicate cement PO. 42.5 produced conforming to the Chinese standard. Coarse aggregate was calcareous crushed stone with a maximum size of 16 mm, and river sand was used as the fine aggregates and its maximum diameter was 5 mm. Details of the mix proportioning (by weight) used for concrete and some mechanical properties are Cement : Sand : Limestone Coarse aggregate : Water : fly ash = 1.00 : 3.44 : 4.39 : 0.80 : 0.26.

Fracture properties of concrete were determined by means of the wedge splitting test [4]. The test setup and geometry of the specimen are schematically represented in Figure 2. Compared to three-point bending notched beams, the wedge-splitting test has following advantages. For the three-point bending beams, inaccurate measurement of load-point displacement and the self-weight of the specimen could influence the real value of the fracture energy. During the test, beams should be carefully handled due to their heavy weight. However, using the WS specimens, the recorded COD in a horizontal plane is not affected by the crushing of the specimen at the supports or some other factors. Besides, the WS specimens are simple and easily prepared in laboratories or on site.

A total of 50 concrete specimens with the same dimensions $230 \times 200 \times 200$ mm were prepared; the geometry of the specimens and the test setup are shown in Figure 2 ($b = 200$ mm, $d = 65$ mm, $h = 200$ mm, $f = 30$ mm, $a_0 = 80$ mm, and $\theta = 15^\circ$). All the specimens had a precast notch of 80 mm height and 3 mm thickness, achieved by placing a piece of steel plate into the molds prior to casting. Each wedge splitting specimen was embedded with a thermal couple in the center of specimen for temperature control.

Nine heating temperatures, ranging from 65°C to 600°C ($T_m = 65^\circ\text{C}$, 120°C , 200°C , 300°C , 350°C , 400°C , 450°C , 500°C , and 600°C), were adopted with the ambient temperature as a reference. Because it was recognized that the fracture behavior measurements were generally associated

with significant scatter, five repetitions were performed for each temperature.

An electric furnace with net dimensions $300 \times 300 \times 900$ mm was used for heating. When the designated T_m was reached, the furnace was shut down, and the specimens were naturally cooled for 7 days prior to the test. It averagely took 50, 95, 135, 182, 218, 254, 294, 342, and 453 minutes for the specimens to reach the final temperatures, respectively (from 65°C to 600°C). Figure 3 shows the typical temperature history for several cases with different maximum temperatures. After heating, microcracks disperse on the specimen surface, especially for temperatures higher than 200°C (see in Figure 4).

The fracture surfaces at different temperature intervals (20°C , 200°C , 350°C , 450°C , and 600°C) are shown in Figure 5, which became lighter but more tortuous with increasing temperatures.

A universal machine with a maximum capacity of 1000 kN was used to conduct the wedge splitting tests. During the test, the vertically applied load P_v and the crack opening displacement COD along the horizontal load line were simultaneously recorded through a data acquisition system. Referring to Figure 2, the splitting force P_h is actually the horizontal component of the force acting on the bearing. Taking the wedge angle into consideration, its relation with the recorded applied load P_v can be developed based on force equilibrium ignoring the small influence from the friction for different roller bearings:

$$P_h = \frac{P_v}{2 \tan \theta}. \quad (5)$$

To obtain the complete P -COD curves (shown in Figure 6), the test rate was fixed at 0.4 mm/min, such that it took approximately 20 minutes to complete a single test of specimens subjected to less than 300°C and 30 minutes for beyond 300°C .

The fracture of specimen is essentially due to the bending moment caused by the horizontal splitting force P_h , vertical component $1/2 P_v$, and self-weight of the specimen. Two

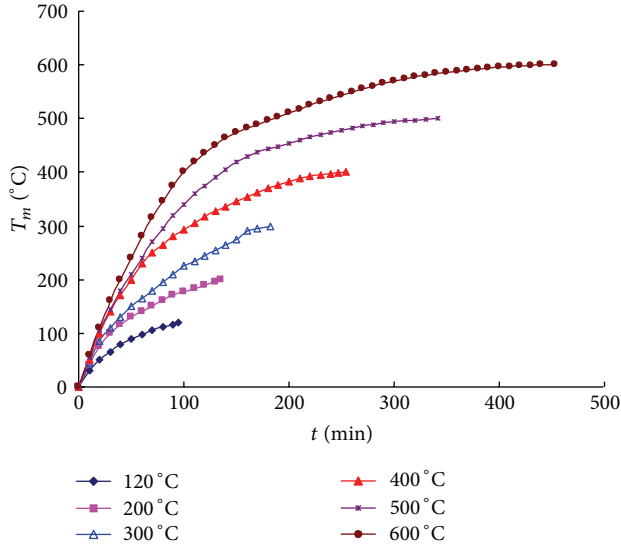


FIGURE 3: Typical temperature history of specimens.



FIGURE 4: Microcracks on specimen surface (600°C).

symmetrical supports are placed below the center of gravity of each half of the specimen. In doing so, the influence of the dead weight of the specimen and part of the vertical component force on the calculation of the fracture energies could be counteracted. Each roll axis is fixed at the same horizon as the lower plane of the groove and is very close to the center of gravity of each half of the specimen in the vertical position (shown in Figure 2). Due to the carefulness in the choice of the specimen geometry, the roll axis location, and the placement of the supports, the horizontal force P_h contributes most to fracturing the specimen. Therefore, P_h -COD curves were directly used in the calculation of the RILEM fracture energy G_F , stable fracture energy G_{FS} , and unstable fracture energy G_{FU} .

For our test results, the P_h -COD curves could be easily obtained from the monitored P_v -COD curves and (5). Figure 6 contains the plots of P_h -COD curves for several temperatures and typical P_v -COD curves for all temperatures.

From Figure 6(a) to 6(c), it is found that with the increasing of temperature (20°C–600°C), the divergence between the curves for the same temperature is more significant. In particular 600°C, the ultimate load P_u of specimen WS50 is one time higher than the one of specimen WS47. Additionally, the whole loading process is not stable for specimens WS49 (a sudden snap-back) due to the thermal damage induced by high temperature. Figure 6(d) shows the typical P -COD curves of all temperatures. The ultimate load P_u decreases significantly with increasing temperatures T_m , whereas the crack mouth opening displacement (COD) increases with T_m . The initial slope of ascending branches decreases with heating temperatures, and the curves become gradually shorter and more extended.

It is found that the ultimate load $P_{h,max}$ decreases with the increasing temperatures, whereas the COD_c increases with T_m (Figure 8). The average value of P_u decreases from 9.17 kN at ambient temperature to 7.92 kN at 120°C, 4.29 kN at 300°C, 3.16 kN at 450°C, and finally 1.38 kN at 600°C, with a final drop of 85%. The value of COD_c increases from 0.178 mm at ambient temperature to 0.352 mm at 200°C, 0.901 mm at 400°C, and 1.848 mm at 600°C, nearly 10 times as the ambient value.

4. Experimental Results and Analysis

4.1. Determination of Residual Fracture Energy G_F . In the calculation of RILEM fracture energy G_F , two things should be carefully considered. One thing is that the work done by the self-weight of loading device should be taken into account. In present experiments, the loading device is attached to the testing machine and the P_h -COD curve includes the self-weight; hence the work should not be calculated again. The other concern pertains to the tail part of the P_h -COD curve: the recorded point (P_{h1}, COD_1) is just one point when the experiment stops, not the actual point of when the load drops to zero. Therefore, cutting the load-deflection tail may lead to noticeable inaccuracy in the true value of fracture energy. Thus, to account for these two factors, the actual RILEM fracture energy G_F based on the work-of-fracture method becomes (see Figure 9)

$$G_F = \frac{W}{A_{lig}} = \frac{W_1 + W_2}{t(h - a_0)}, \quad (6)$$

where W_1 = measured work enclosed by the P_h -COD curve until $COD = COD_1$; A_{lig} = fresh fracture area; W_2 is the work caused by tail effect part. For W_2 , curve fitting technology based on Excel software was used to get its approximate value. In previous research from the test results at ambient temperature [13], it was found out that the descending branch of the P_h -COD curve after one-third of the peak load could be well described by power function (the coefficient of determination R^2 for each curve is close to 1). This study indicates that for specimens subject to no more than 120°C, the power function is more accurate; however, for specimens subject to higher temperatures, exponential function is more suitable (see Figure 9).



FIGURE 5: Fracture surfaces of postfire specimens.

For power function $P_h = \beta \times \text{COD}^{-\lambda}$, $\lambda > 0$, where $\beta, \lambda = \text{constants}$ for fitting curves. And then the unrecorded work W owing to cutting load-deflection tail can be written as

$$W_2 = \int_{\text{COD}_1}^{\infty} \beta \times \text{COD}^{-\lambda} d\text{COD} = \frac{\beta}{(\lambda - 1) \times \text{COD}_1^{\lambda-1}}. \quad (7)$$

For exponential function $P_h = m \times e^{-n \times \text{COD}}$, $m, n > 0$, where $m, n = \text{constants}$ for fitting curves. And then the unrecorded work W owing to cutting load-deflection tail can be written as

$$W_2 = \int_{\text{COD}_1}^{\infty} m \times e^{-n \times \text{COD}} d\delta = \frac{m}{ne^{n \times \text{COD}_1}}. \quad (8)$$

The parameters of β, λ for 20°C~120°C and m, n for 200°C~600°C, and the value of w_1, w_2 is listed in Table 1.

Some necessary test results are tabulated in Table 1, including the maximum value of the horizontal load $P_{h\text{max}}$ and its corresponding crack opening displacement COD_c , the

endpoint where P_{h1} approaches zero and the crack opening displacement arrives at COD_1 , the initial slope of P_h -COD, that is, the initial stiffness K_0 , and the modulus of elasticity E .

Hence, the residual fracture energy described by (1) could be calculated. The values are listed in Table 2 and are shown in Figure 10.

Though the residual fracture energy at each temperature has significant scatter, Figure 10 shows that the average values sustain an increase-decrease tendency with T_m . From 20°C to 450°C, average G_F increases from 339.3 Nm^{-1} to 609 Nm^{-1} , while the temperature reaches 600°C and the fracture energy falls back to 307.8 Nm^{-1} . The detailed explanation would be seen elsewhere [12].

4.2. Determination of Stable Fracture Energy G_{FS} and Unstable Fracture Energy G_{FU} . As an extension of fracture energy G_F , two other energy-based fracture characteristics, the stable fracture energy G_{FS} and unstable fracture energy G_{FU} , are proposed to describe fracture responses for different crack propagation periods. The analysis shows that fracture energy G_F is actually the weighed average of G_{FS} and G_{FU} , and G_{FS}

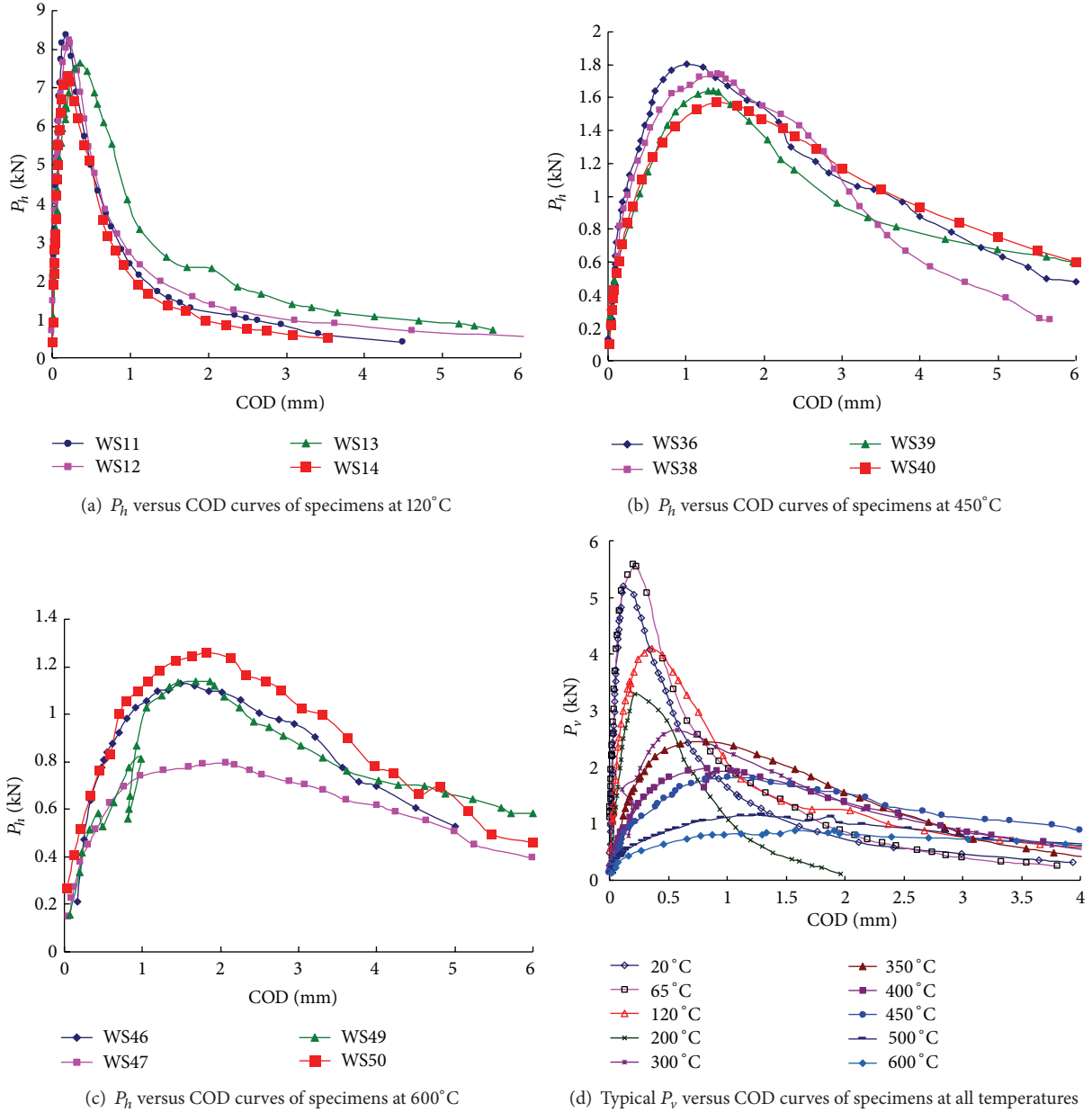


FIGURE 6: P versus CMOD curves of specimens with temperatures.

and G_{FU} could be regarded as two components of G_F . This is very helpful in understanding the whole crack propagation process from the aspect of energy consumption.

To obtain the values of G_{FS} and G_{FU} , the critical effective crack length a_c should first be determined for the calculation of the fracture areas A_S and A_U . Herein, the value a_c was computed based on the double- K fracture model [14]:

$$a = (h + h_0) \left\{ 1 - \left(\frac{13.18}{E \cdot b \cdot c + 9.16} \right)^{1/2} \right\} - h_0, \quad (9)$$

where $c = COD/P$ is the compliance of specimens, E is modulus of elasticity, b is specimen thickness, h is specimen

height, and h_0 is the thickness of the clip gauge holder. For calculation of critical value of equivalent elastic crack length a_c , the value of crack mouth opening displacement (COD) and P are taken as COD_c and $P_{h,max}$, respectively. Equation (9) is valid for 0.2–0.8 within 2% accuracy. The value of a_c is reported in Table 1.

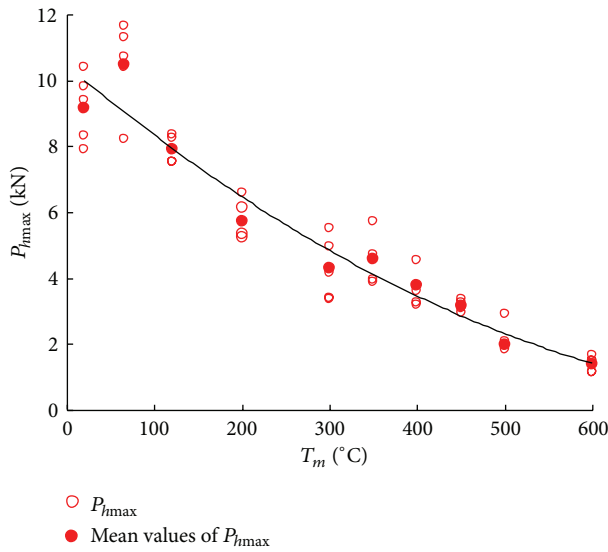
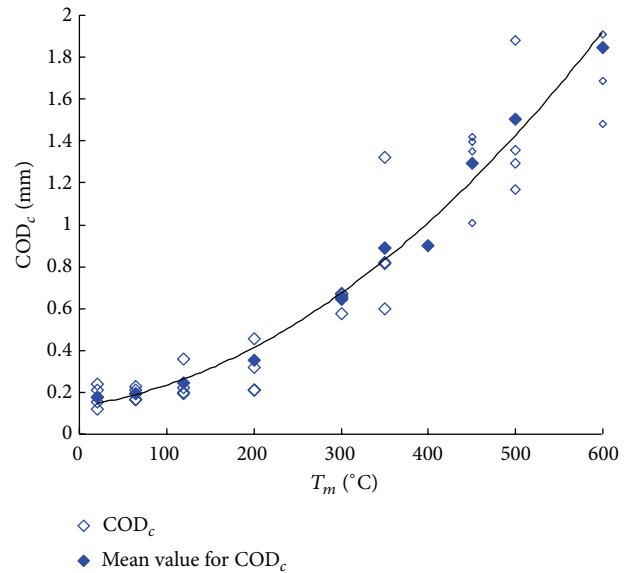
In a typical load-displacement curve shown in Figure 1, K_0 is the initial stiffness of the load-displacement curve before the start of the fracture process. At critical state when the load arrives at its peak value P_{max} and its corresponding displacement reaches COD_c , the stiffness K_c may not be the same as the initial K_0 . The degradation of stiffness is the result of crack propagation. To make it simple, here, the value

TABLE I: Parameters calculated from wedge-splitting test.

Specimen	Temperature	$P_{h\max}$ (kN)	E (GPa)	a_c (mm)	β/m	λ/n	R^2	W_1	W_2	COD_c (mm)	COD_1 (mm)	K_0 (kN/mm)	K_c (kN/mm)
WS1	20°C	8.304	15.30	0.107	1.484	2.273	0.970	5.231	0.389	0.174	1.926	87.081	79.219
WS2		9.407	20.51	0.097	3.131	1.206	0.998	10.468	1.140	0.205	4.914	116.710	113.648
WS3		10.379	20.66	0.114	2.464	1.117	0.991	8.699	1.818	0.195	3.280	117.610	110.633
WS4		7.884	18.88	0.112	1.599	3.224	0.964	5.128	0.137	0.152	1.903	107.480	98.911
WS5		9.364	15.45	0.107	2.048	1.683	0.991	6.970	0.735	0.199	2.657	87.940	80.103
Average		9.068	18.16	0.107	—	—	0.983	7.299	0.844	0.185	2.936	103.364	96.503
WS6	65°C	11.282	21.73	0.113	2.781	1.506	0.996	9.238	0.984	0.195	3.205	123.690	116.172
WS7		8.151	24.79	0.132	2.739	0.987	0.999	10.320	1.263	0.215	6.072	141.100	136.109
WS8		10.379	19.43	0.115	6.114	1.992	0.954	11.004	0.702	0.212	4.549	110.560	105.418
WS9		10.681	23.25	0.119	2.658	1.030	0.993	9.283	2.250	0.164	3.535	132.330	124.685
WS10		11.610	16.60	0.107	3.185	1.252	0.983	11.466	1.071	0.190	5.324	94.490	90.418
Average		10.421	21.16	0.117	—	—	0.985	10.262	1.254	0.195	4.537	120.434	114.560
WS11	120°C	8.353	10.65	0.095	2.477	1.085	0.990	8.423	1.094	0.191	3.418	60.638	57.254
WS12		8.226	11.87	0.107	2.667	0.890	0.999	10.624	1.803	0.224	6.443	67.564	65.212
WS13		7.631	9.48	0.119	4.340	0.998	0.980	13.227	2.487	0.357	5.641	53.926	50.511
WS14		7.302	15.42	0.117	2.139	1.153	0.998	6.934	1.357	0.198	3.534	87.758	82.839
WS15		—	—	—	—	—	—	—	—	—	—	—	—
Average		7.878	11.85	0.109	—	—	0.992	9.802	1.685	0.243	4.759	67.472	63.954
WS16	200°C	—	—	—	—	—	—	—	—	—	—	—	—
WS17		6.466	11.58	0.127	2.266	1.526	0.952	6.260	0.520	0.284	2.558	65.913	57.759
WS18		5.884	6.98	0.115	2.268	2.982	0.995	5.035	0.129	0.335	1.968	39.732	32.967
WS19		5.071	9.17	0.127	2.770	2.087	0.969	5.397	0.265	0.306	2.786	52.178	46.456
WS20		5.228	7.00	0.130	2.530	0.366	0.903	7.605	1.250	0.458	4.447	39.866	35.765
Average		5.662	8.68	0.125	—	—	0.955	6.074	0.541	0.346	2.940	49.422	43.237
WS21	300°C	3.341	2.45	0.121	4.023	0.361	0.981	10.019	0.491	0.792	3.101	13.939	11.004
WS22		5.513	3.49	0.117	4.090	0.300	0.987	13.570	1.105	0.667	5.065	19.869	17.251
WS23		3.371	1.91	0.113	6.985	0.610	0.982	7.727	0.475	0.672	4.957	10.854	9.384
WS24		4.761	1.99	0.105	4.285	0.345	0.990	12.552	0.987	0.728	6.816	11.350	10.138
WS25		4.076	4.03	0.137	2.172	0.206	0.963	11.532	1.667	0.869	6.874	22.960	20.438
Average		4.213	2.78	0.119	—	—	0.981	11.080	0.945	0.746	5.363	15.794	13.643
WS26	350°C	5.701	6.05	0.131	5.702	0.447	0.995	12.290	1.475	0.599	4.549	34.409	29.878
WS27		3.840	2.03	0.125	6.245	0.335	0.958	14.150	1.490	1.003	6.768	11.538	9.829
WS28		4.718	3.60	0.131	5.553	0.454	0.997	11.312	1.107	0.815	4.053	13.490	16.360
WS29		4.554	3.38	0.130	9.025	0.608	0.995	11.635	0.355	0.821	5.940	19.240	16.582
WS30		3.931	3.21	0.134	7.135	0.532	0.990	10.251	0.654	0.832	5.335	18.279	15.427
Average		4.549	3.65	0.130	—	—	0.987	11.927	1.016	0.814	5.329	19.391	17.615
WS31	400°C	3.584	2.56	0.136	3.934	0.307	0.999	11.737	1.033	0.921	6.937	14.557	12.391
WS32		3.039	1.42	0.126	21.138	0.828	0.992	9.300	0.226	0.904	5.614	8.084	6.331
WS33		3.228	2.12	0.114	2.100	0.224	0.995	8.533	1.575	0.842	5.819	7.348	6.419
WS34		4.476	1.71	0.111	4.208	0.322	0.929	13.388	0.986	0.985	5.940	12.035	8.463
WS35		—	—	—	—	—	—	—	—	—	—	—	—
Average		3.582	1.95	0.122	—	—	0.979	10.740	0.955	0.913	6.078	10.506	8.401

TABLE I: Continued.

Specimen	Temperature	$P_{h\max}$ (kN)	E (GPa)	a_c (mm)	β/m	λ/n	R^2	W_1	W_2	COD _c (mm)	COD ₁ (mm)	K_0 (kN/mm)	K_c (kN/mm)
WS36	450°C	3.336	1.41	0.125	5.280	0.299	0.977	13.124	1.553	1.224	5.625	8.037	6.289
WS37		—	—	—	—	—	—	—	—	—	—	—	—
WS38		3.118	1.46	0.123	10.235	0.543	0.981	10.601	0.978	1.057	5.672	8.291	6.216
WS39		3.056	1.34	0.127	2.518	0.137	0.995	11.955	3.960	1.281	6.784	7.611	6.099
WS40		2.935	1.58	0.137	4.328	0.226	0.998	13.896	2.395	1.394	6.000	8.988	6.900
Average		3.111	1.45	0.128	—	—	0.988	12.394	1.663	1.239	6.020	8.232	6.376
WS41	500°C	—	—	—	—	—	—	—	—	—	—	—	—
WS42		2.153	1.76	0.146	3.056	0.245	0.976	7.762	3.054	1.284	5.153	7.251	7.506
WS43		2.857	1.09	0.119	3.648	0.306	0.979	10.092	1.342	1.174	6.533	6.179	5.069
WS44		1.929	0.75	0.109	2.234	0.153	0.968	8.758	4.119	1.225	6.591	4.243	3.651
WS45		1.838	1.48	0.147	2.300	0.186	0.996	7.826	3.012	1.354	6.225	6.078	6.591
Average		2.194	1.27	0.130	—	—	0.977	8.002	2.494	1.259	6.125	5.938	5.704
WS46	600°C	1.129	0.47	0.130	2.102	0.278	0.931	4.197	1.280	1.482	7.000	2.656	2.094
WS47		1.474	0.48	0.128	3.018	0.238	0.954	7.245	2.236	1.784	10.000	2.718	2.233
WS48		1.649	1.14	0.152	1.992	0.132	0.979	8.390	4.551	1.908	7.100	3.909	2.858
WS49		1.138	0.38	0.131	1.183	0.120	0.971	5.018	2.950	1.865	10.000	1.165	1.761
WS50		1.243	0.38	0.124	2.507	0.285	0.943	5.273	1.280	1.644	8.000	1.174	1.727
Average		1.326	0.57	0.133	—	—	0.956	6.025	2.460	1.737	8.420	2.324	2.135

FIGURE 7: Variation tendency of $P_{h\max}$ with T_m .FIGURE 8: Variation tendency of COD_c with T_m .

of K at any value of displacement is assumed to be linear with increased deformation [15].

$$K = \frac{K_0 (\text{COD}_1 - \text{COD})}{(\text{COD}_1 - \text{COD}_0)}, \quad (10)$$

where COD_1 = final deformation when the load P approaches zero and COD_0 = displacement before which the stiffness is still kept at K_0 . At the origin of P -COD curve, the initial tangent stiffness is K_0 . The stiffness becomes degraded beyond the origin point; hence COD_0 is presumed to be zero. It is clear from (10) that $K = K_0$ when $\text{COD} = 0$ and

$K = 0$ when $\text{COD} = \text{COD}_1$, and K is assumed to be a linear function with respect to the displacement. With the crack opening displacement $\text{COD} = \text{COD}_c$, the stiffness K_c at this point could approximately be obtained through (10). Note that P -COD is a general term for load-displacement; in our case, the load is the horizontal force P_h and its corresponding displacement is the COD. Therefore, with K_0 , COD_1 , and COD_c , the approximate degraded stiffness K_c can be gained from (10) and the result is shown in Table 1. Figure 11 shows that the values of stiffness K_c decrease monotonously with temperature due to the thermal damage induced by high temperatures.

TABLE 2: Fracture energies for crack propagation.

Specimen	Temperature	W_0 (Nm)	A_{lig} (m ²)	G_F (Nm ⁻¹)	W_{OIMA} (Nm)	W_{AIMA} (Nm)	W_{FS} (Nm)	A_{FS} (m ²)	G_{FS} (Nm ⁻¹)	W_{FU} (Nm)	A_{FU} (m ²)	G_{FU} (Nm ⁻¹)
WS1	20°C	5.620	0.024	234.147	1.217	0.407	0.810	0.005	152.502	4.809	0.019	257.361
WS2		11.608		483.664	1.575	0.388	1.187	0.003	350.795	10.421	0.021	504.972
WS3		10.517		438.217	2.124	0.470	1.654	0.007	242.557	8.863	0.017	515.877
WS4		5.265		219.394	0.994	0.314	0.680	0.006	107.537	4.586	0.018	259.384
WS5		7.705		321.055	1.693	0.525	1.169	0.005	212.824	6.536	0.019	353.175
Average		8.143		339.295	1.521	0.421	1.100	0.005	213.243	7.043	0.019	378.154
WS6	65°C	7.666	0.024	425.907	1.791	0.535	1.255	0.007	281.835	6.411	0.017	480.239
WS7		8.687		482.619	1.076	0.241	0.835	0.010	113.926	7.852	0.014	768.132
WS8		8.779		487.745	1.475	0.509	0.966	0.007	208.612	7.813	0.017	602.385
WS9		8.649		480.507	1.027	0.440	0.587	0.008	118.113	8.062	0.016	656.640
WS10		9.402		522.360	1.419	0.733	0.686	0.005	210.596	8.716	0.019	614.693
Average		8.637		479.828	1.357	0.492	0.866	0.007	186.616	7.771	0.017	624.418
WS11	120°C	7.137	0.024	396.516	1.335	0.588	0.746	0.003	251.423	6.391	0.021	416.985
WS12		9.321		517.822	1.475	0.511	0.964	0.005	178.684	8.357	0.019	616.201
WS13		11.785		654.732	2.079	0.560	1.520	0.008	193.937	10.266	0.016	878.097
WS14		6.218		345.463	1.044	0.312	0.732	0.007	98.944	5.486	0.017	455.357
WS15		—		—	—	—	—	—	—	—	—	—
Average		8.615		478.633	1.483	0.493	0.991	0.006	180.747	7.625	0.018	591.660
WS16	200°C	—	0.024	—	—	—	—	—	—	—	—	—
WS17		6.780		282.509	1.522	0.345	1.176	0.009	123.021	5.604	0.015	385.812
WS18		5.163		215.135	1.556	0.525	1.031	0.007	146.955	4.132	0.017	243.300
WS19		5.662		235.913	1.252	0.270	0.982	0.009	104.764	4.680	0.015	320.014
WS20		8.854		368.937	1.828	0.365	1.463	0.010	145.364	7.391	0.014	530.467
Average		6.615		275.624	1.540	0.376	1.163	0.009	130.026	5.452	0.015	369.898
WS21	300°C	10.510	0.024	437.920	2.005	0.439	1.566	0.008	188.640	8.944	0.016	568.895
WS22		14.675		611.467	3.546	0.820	2.726	0.007	364.621	11.949	0.017	723.160
WS23		8.202		341.770	2.048	0.579	1.469	0.007	220.394	6.733	0.017	388.453
WS24		13.539		564.120	3.065	1.081	1.984	0.005	404.514	11.555	0.019	605.107
WS25		13.200		549.990	2.552	0.389	2.163	0.011	190.295	11.037	0.013	870.055
Average		12.025		501.053	2.643	0.662	1.982	0.008	273.693	10.044	0.016	631.134
WS26	350°C	13.765	0.024	573.540	2.689	0.511	2.179	0.010	211.652	11.586	0.014	845.346
WS27		15.639		651.638	2.589	0.703	1.887	0.009	207.566	13.753	0.015	922.314
WS28		12.420		517.489	3.827	0.919	2.908	0.010	317.145	9.512	0.014	664.527
WS29		11.990		499.602	2.900	0.611	2.289	0.010	228.349	9.701	0.014	694.230
WS30		10.905		454.375	2.796	0.475	2.320	0.011	216.312	8.585	0.013	646.739
Average		12.944		539.329	2.960	0.644	2.317	0.010	236.205	10.627	0.014	754.631
WS31	400°C	12.770	0.024	532.090	2.240	0.484	1.756	0.011	156.074	11.014	0.013	860.665
WS32		9.526		396.932	2.678	0.656	2.022	0.009	207.133	7.504	0.015	516.314
WS33		10.109		421.188	2.411	0.760	1.651	0.007	242.302	8.457	0.017	491.692
WS34		14.374		598.926	3.638	0.918	2.720	0.006	401.879	11.654	0.018	668.062
WS35		—		—	—	—	—	—	—	—	—	—
Average		11.695		487.284	2.742	0.705	2.037	0.008	251.847	9.658	0.016	634.184

TABLE 2: Continued.

Specimen Temperature	W_0 (Nm)	A_{lig} (m ²)	G_F (Nm ⁻¹)	W_{OIMA} (Nm)	W_{AIMA} (Nm)	W_{FS} (Nm)	A_{FS} (m ²)	G_{FS} (Nm ⁻¹)	W_{FU} (Nm)	A_{FU} (m ²)	G_{FU} (Nm ⁻¹)
WS36	14.677	—	611.530	3.255	0.779	2.477	0.009	277.088	12.200	0.015	809.983
WS37	—	—	—	—	—	—	—	—	—	—	—
WS38	450°C	0.024	482.451	3.284	0.669	2.615	0.009	303.750	8.964	0.015	582.382
WS39	—	—	663.097	3.281	0.704	2.578	0.009	272.015	13.337	0.015	918.284
WS40	—	—	678.790	3.847	0.532	3.315	0.011	292.743	12.976	0.013	1023.630
Average	14.057	—	608.967	3.417	0.671	2.746	0.010	286.399	11.869	0.014	833.570
WS41	—	—	—	—	—	—	—	—	—	—	—
WS42	500°C	0.024	450.668	2.080	0.355	1.725	0.013	138.244	9.091	0.011	831.501
WS43	—	—	476.413	2.890	0.743	2.146	0.008	272.496	9.288	0.016	576.031
WS44	—	—	536.544	1.495	0.475	1.021	0.006	170.514	11.856	0.018	652.188
WS45	—	—	451.571	2.720	0.308	2.412	0.013	186.562	8.426	0.011	785.892
Average	10.496	—	478.799	2.296	0.470	1.826	0.010	191.954	9.665	0.014	711.403
WS46	600°C	0.024	228.226	1.404	0.287	1.117	0.010	110.974	4.361	0.014	312.890
WS47	—	—	395.057	2.526	0.460	2.066	0.010	213.423	7.415	0.014	517.849
WS48	—	—	539.225	2.621	0.389	2.232	0.014	155.808	10.709	0.010	1107.140
WS49	—	—	331.988	1.514	0.635	0.879	0.010	115.238	7.088	0.014	491.494
WS50	—	—	273.074	1.749	0.773	0.976	0.009	151.878	5.578	0.015	342.831
Average	8.484	—	353.514	1.963	0.509	1.454	0.011	149.464	7.030	0.013	632.922

The stable fracture energy G_{FS} and unstable fracture energy G_{FU} can be derived by following (11)~(13). The specific values of G_{FS} and G_{FU} are compiled in Table 2:

$$G_{FS} = \frac{W_{FS}}{A_S} = \frac{W_{OAMO}}{A_S} = \frac{W_{OIMO} - W_{AIMA}}{A_S}, \quad (11)$$

$$G_{FU} = \frac{W_U}{A_U} = \frac{W - W_{FS}}{A_U},$$

$$A_S = B(a_c - a_0), \quad A_U = B(h - a_c), \quad (12)$$

$$W_{AIMA} = \frac{0.5P_{hmax}^2}{K_c}. \quad (13)$$

Figure 12 shows the variation of stable fracture energy G_{FS} with temperatures. Similar to the residual fracture energy G_F , it also keeps an increase-decrease tendency with temperatures. Temperatures less than 120°C appear not to induce much thermal damage to concrete, so the cracking resistance almost keeps constant. The values of stable fracture energy G_{FS} at these temperatures are 213 Nm⁻¹, 186 Nm⁻¹, and 180 Nm⁻¹, respectively. The fracture surfaces tend to be more tortuous between 200°C and 450°C than those observed at lower temperatures (see Figure 4) and there exist several cracks competing to form the final fracture, so more energy was dissipated in these specimens. Additionally, the opening of microcracks on the surface and inside the specimens also dissipates energy (see Figure 3). Finally, higher heating temperatures would cause more micro cracks, dehydration, and decomposition and would degrade the resistance. After 450°C, cracking resistance continuously decreases with T_m .

Table 2 shows that the unstable fracture G_{FU} also sustains an increase-decrease tendency with T_m , and its value is much larger than stable fracture energy. Two reasons for larger values of G_{FU} are provided [5]. First, energy consumption besides the main fracture zone takes places for the whole fracture process. During the unstable fracture process, the energy consumption for plasticity or other nonlinear deformation beyond the main FPZ would be much higher, especially for specimens subjected to high temperatures. The other possible reason lies in the calculation of true fracture area. It is known that the interface (transition zone) between cement and aggregate is the weak link in microstructure for normal concrete, and crack propagation would proceed in the path where the energy needs are least. So the true path of crack extension is tortuous and the higher the temperature is, the more tortuous the fracture surface is (see Figure 4), not straight as expected. The projected area is used in the calculation of fracturing surface A_S or A_U , which underestimates the true fracture area. Since the crack experiences much longer distance for the unstable extension, which leads to a greater underestimation of the calculation of the newly fractured area A_U , the calculated G_{FU} is overestimated.

Moreover, in view of (11) and (12), another expression for the fracture energy G_F with respect to G_{FS} and G_{FU} can be followed:

$$G_F = \frac{W}{A} = \frac{G_{FS}A_S + G_{FU}A_U}{A} = G_{FS} \cdot \frac{A_S}{A} + G_{FU} \cdot \frac{A_U}{A}. \quad (14)$$

Since $A_S + A_U = A$, the fracture energy G_F is the weighed average of G_{FS} and G_{FU} . However, for engineering application, the stable crack propagation is considered to be more

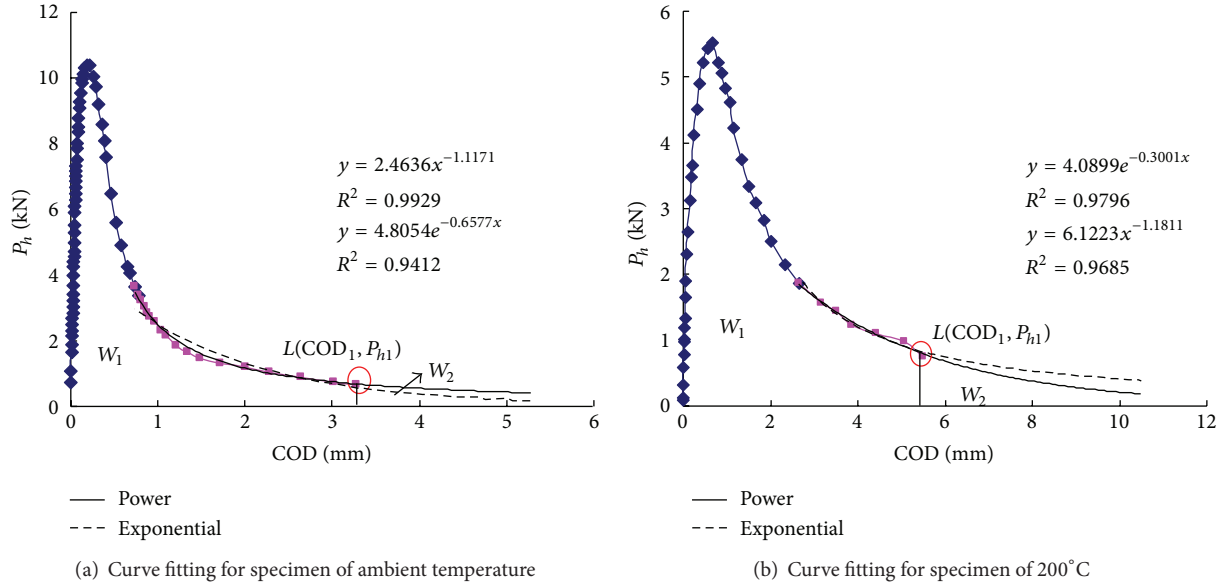


FIGURE 9: P -CMOD tail curve fitting of specimens.

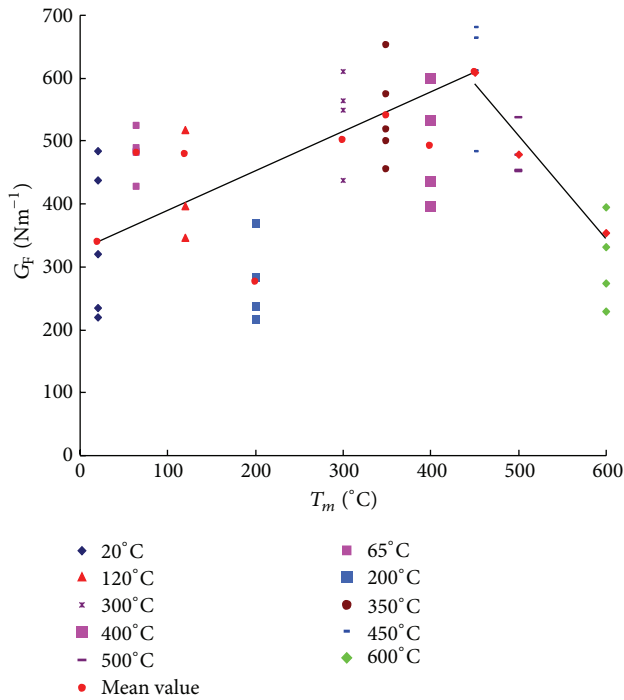


FIGURE 10: Residual fracture energy with T_m .

important, because when the load exceeds the maximum value the whole structure would be in an unstable situation. Hence from Figures 7 and 9, it is concluded that the fracture property of postfire concrete sustains an increase-decrease tendency to 600°C, with a turning point at 450°C.

Furthermore, as mentioned above, the fracture surfaces of A , A_S , A_U are project areas, so G_F , G_{FS} , G_{FU} are nominal fracture energies. To avoid the violence of fracture surface, the variation tendency of stable fracture work W_{FS} is determined

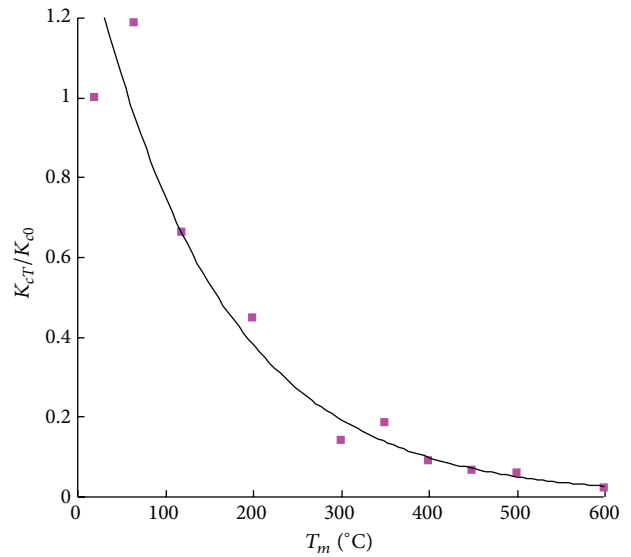


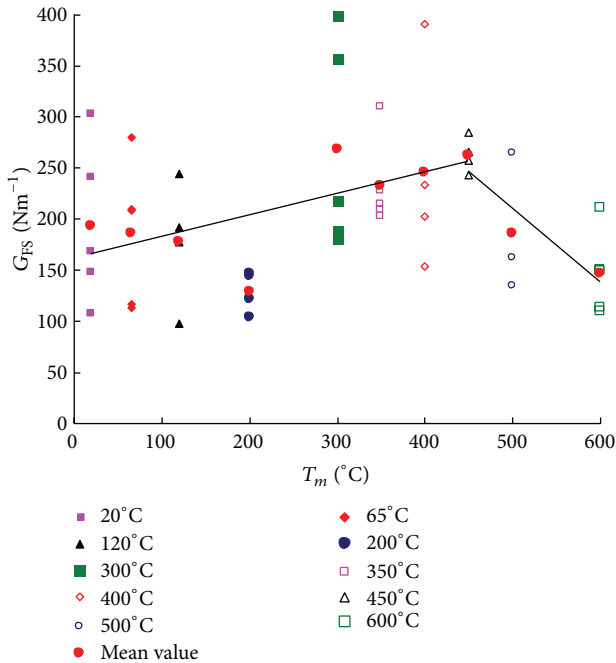
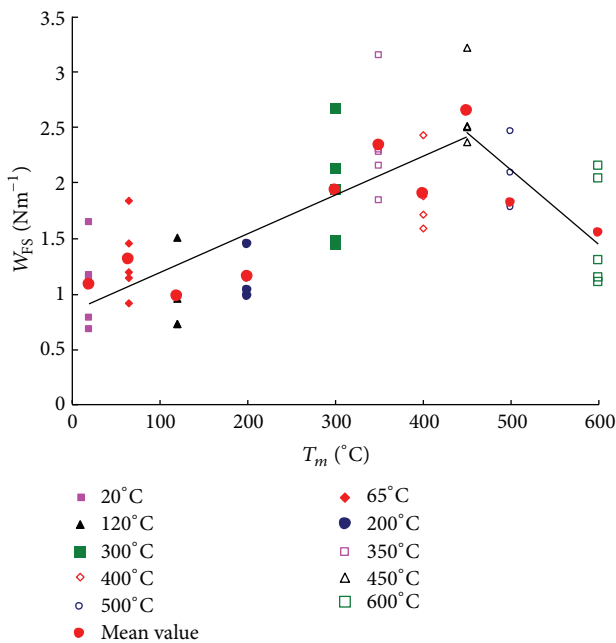
FIGURE 11: Stiffness K_c with T_m .

(see Figure 10). Similarly, W_{FS} also keeps an increase-decrease tendency at the same turning temperature of 450°C.

5. Conclusions

Energy consumption during an entire crack propagation period has been investigated, including the fracture energy G_F , stable fracture energy G_{FS} , unstable fracture energy G_{FU} , and stable fracture work W_{FS} . The conclusions are as follows.

- (1) Wedge-splitting tests of ten temperatures levels varying from room temperature to 600°C and the specimen size of 230 mm × 200 mm × 200 mm with initial-notch depth ratios 0.4 have been presented. Complete P -COD curves and the curve tails are obtained using

FIGURE 12: Stable fracture energy with T_m .FIGURE 13: Stable fracture work with T_m .

exponential and power functions. For specimens subject to no more than 120°C, the power function is more accurate; for higher temperatures, exponential function is more suitable.

- (2) Three fracture energy quantities corresponding to different aspects of fracture are proposed. The fracture energy G_F in a general case only represents the average energy dissipation for an entire crack propagation process. G_{FS} , the stable fracture energy, denotes the

average energy absorption during crack stable propagation, and G_{FU} is used to characterize the average energy consumption for crack unstable propagation and a higher value of G_{FU} than G_{FS} is observed. G_F is actually the weighed average of G_{FS} and G_{FU} .

- (3) However, for engineering applications, the stable crack propagation is considered to be more important. From the wedge-splitting tests of different temperatures, it is concluded that G_F , G_{FS} sustain an increase-decrease tendency to 600°C, with a turning point at 450°C. Furthermore, the variation of stable fracture work W_{FS} is determined and shares the same tendency with G_F and G_{FS} (Figure 13). All these three parameters mean that the fracture property of postfire concrete sustains an increase-decrease tendency.

Acknowledgments

The State Key Laboratory of Disaster Reduction in Civil Engineering (SLDRCE09-D-02) and Young Scientist Project of Natural Science Foundation of China (NSFC) have supported this research.

References

- [1] A. Hillerborg, "The theoretical basis of a method to determine the fracture energy G_F of concrete," *Materials and Structures*, vol. 18, no. 4, pp. 291–296, 1985.
- [2] RILEM-Draft-Recommendation (50-FCM) (RILEM), "Determination of the fracture energy of mortar and concrete by means of three-point bend tests on notched beams," *RILEM Materials and Structures*, vol. 18, no. 4, pp. 285–290, 1985.
- [3] ASTM International Standard E399-06, "Standard test method for linear-elastic method plane-strain fracture toughness K_{IC} of Metallic Materials," 2006.
- [4] E. Brühwiler and F. H. Wittmann, "The wedge splitting test, a new method of performing stable fracture mechanics tests," *Engineering Fracture Mechanics*, vol. 35, no. 1–3, pp. 117–125, 1990.
- [5] S. Xu and H. W. Reinhardt, "Determination of double-K criterion for crack propagation in quasi-brittle fracture, Part I: experimental investigation of crack propagation," *International Journal of Fracture*, vol. 98, no. 2, pp. 111–149, 1999.
- [6] S. Xu, Y. Zhao, and Z. Wu, "Study on the average fracture energy for crack propagation in concrete," *Journal of Materials in Civil Engineering*, vol. 18, no. 6, pp. 817–824, 2006.
- [7] Z. P. Bazand and P. C. Prat, "Effect of temperatures and humidity on fracture energy of concrete," *ACI Materials Journal*, vol. 85, no. 4, pp. 262–271, 1988.
- [8] G. Baker, "The effect of exposure to elevated temperatures on the fracture energy of plain concrete," *Materials and Structures*, vol. 29, no. 190, pp. 383–388, 1996.
- [9] B. Zhang, N. Bicanic, C. J. Pearce, and G. Balabanic, "Residual fracture properties of normal- and high-strength concrete subject to elevated temperatures," *Magazine of Concrete Research*, vol. 52, no. 2, pp. 123–136, 2000.
- [10] C. V. Nielsen and N. Bičanić, "Residual fracture energy of high-performance and normal concrete subject to high temperatures," *Materials and Structures*, vol. 36, no. 262, pp. 515–521, 2003.

- [11] B. Zhang and N. Bicanic, "Fracture energy of high-performance concrete at high temperatures up to 450°C: the effects of heating temperatures and testing conditions (hot and cold)," *Magazine of Concrete Research*, vol. 58, no. 5, pp. 277–288, 2006.
- [12] J. Yu, K. Yu, and Z. Lu, "Residual fracture properties of concrete subjected to elevated temperatures," *Materials and Structures*, vol. 45, no. 8, pp. 1155–1165, 2012.
- [13] Y. H. Zhao, *The analytical study on the energy in the fracture process of concrete [Ph.D. thesis]*, Dalian University of Technology, Dalian, China, 2002.
- [14] S. Xu and H. W. Reinhardt, "Crack extension resistance and fracture properties of quasi-brittle softening materials like concrete based on the complete process of fracture," *International Journal of Fracture*, vol. 92, no. 1, pp. 71–99, 1998.
- [15] R. K. Navalurkar, C. T. Hsu, S. K. Kim, and M. Wecharatana, "True fracture energy of concrete," *ACI Materials Journal*, vol. 96, no. 2, pp. 213–225, 1999.

Research Article

Al and Si Influences on Hydrogen Embrittlement of Carbide-Free Bainitic Steel

Yanguo Li, Cheng Chen, and Fucheng Zhang

State Key Laboratory of Metastable Materials Science and Technology, Yanshan University, Qinhuangdao 066004, China

Correspondence should be addressed to Fucheng Zhang; zfc@ysu.edu.cn

Received 14 September 2013; Accepted 17 October 2013

Academic Editor: Filippo Berto

Copyright © 2013 Yanguo Li et al. This is an open access article distributed under the Creative Commons Attribution License, which permits unrestricted use, distribution, and reproduction in any medium, provided the original work is properly cited.

A first-principle method based on the density functional theory was applied to investigate the Al and Si influences on the hydrogen embrittlement of carbide-free bainitic steel. The hydrogen preference site, binding energy, diffusion behaviour, and electronic structure were calculated. The results showed that hydrogen preferred to be at the tetrahedral site. The binding energy of the cell with Si was the highest and it was decreased to be the worst by adding hydrogen. The diffusion barrier of hydrogen in the cell containing Al was the highest, so it was difficult for hydrogen to diffuse. Thus, hydrogen embrittlement can be reduced by Al rather than Si.

1. Introduction

Carbide-free bainitic steel (CFBS) is considered to be one of the most promising candidates for heavy-duty railway crossings due to its excellent and compressive properties, such as high strength and toughness. However, some report indicated that brittle spalling and fracture occurred in the CFBS during the service and it was very sensitive to hydrogen embrittlement (HE) [1]. Hydrogen can greatly change the mechanical properties of alloys and steels and therefore can bring about material failure. It has been well proved that the probability of HE increases with the increase in strength. There was an appropriate silicon concentration (about 2 wt%) in CFBS, which suppressed the precipitation of cementite from austenite during the process of bainite transformation [2]. Previous studies proved that aluminium played a similar role to Si, and partial replacement of Si by Al had been studied in transformation-induced plasticity (TRIP) steels [3–6]. Besides, experimental results showed that the sensitivity of HE to CFBS was reduced due to the partial replacement of Si by Al [7]. However, its exact mechanisms are still only partly understood.

Nowadays, the first-principle study on HE of body-centred cubic (bcc) iron (α -Fe) is well known [8, 9]. A number of different mechanisms on HE had been proposed including decohesion [10, 11], hydrogen-enhanced localised plasticity

[12, 13], and high mobility of hydrogen [14]. In the work, the behaviours of interstitial H atoms inside the pure iron steel and the steel containing aluminium or silicon were investigated using a first-principle approach. The preference site of H in each cell, the binding energies of H atom for different interstitial sites, the diffusion barriers of H between neighbouring sites, and the electronic structure were calculated and discussed. The work provides the micromechanism that the partial replacement of Si by Al reduces the HE in CFBS.

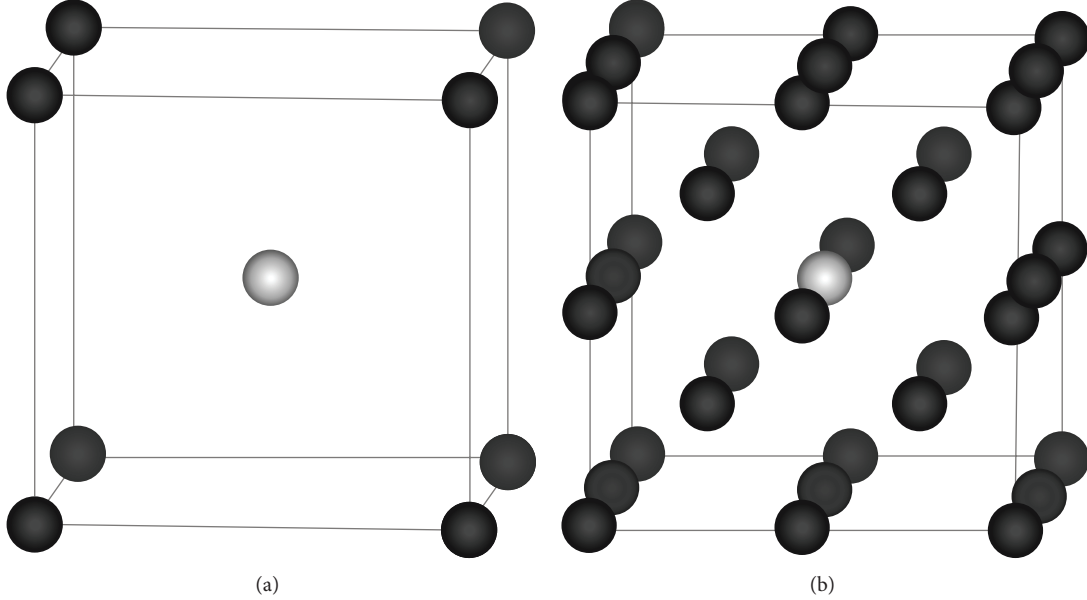
2. Methodology

The chemical composition of the bainitic steels is shown in Table 1. The steel ingots obtained by vacuum melting are forged into round bars of $\Phi 20$ mm. The standard smooth cylindrical tensile samples which have a diameter of 5 mm and a length of 25 mm are machined from the bainitic steels. At the same time, the smooth cylindrical specimens for testing hydrogen content are with a diameter of 5 mm and a length of 50 mm.

In order to determine the hydrogen embrittlement characteristics of the bainitic steels, we have prepared the steels which have a range of different hydrogen contents. The smooth cylindrical tensile specimens are used for cathodic hydrogen charging by the YJ83/2 type DC stabilized power supply. The times of hydrogen charging are 5 min, 20 min,

TABLE I: Chemical composition of the bainitic steels (wt.%).

	C	Si	Mn	Cr	Ni	Mo	Al	P	S
1#	0.30	1.80	1.76	1.71	0.39	0.35	0	0.010	0.011
2#	0.30	1.55	1.78	1.73	0.41	0.35	0.19	0.010	0.011
3#	0.30	1.02	1.83	1.75	0.40	0.34	0.75	0.010	0.010
4#	0.32	0.48	1.82	1.77	0.40	0.35	1.31	0.010	0.010

FIGURE 1: Schematic diagram of FeX (a) and Fe₁₅X (b) (Fe black and X grey, X represents Al or Si).

100 min, and 180 min, respectively. The electrolyte is a mixed solution of 0.5 mol/L H₂SO₄ + 200 mg/L Na₃AsO₃. The current density of hydrogen charging is 10 mA/cm². According to the hydrogen charging time, the samples can be obtained with different hydrogen content. The samples can be protected by bright cadmium plating to prevent the hydrogen escaping from the samples. Then the hydrogen of the samples can be uniformly distributed by the homogenization heat treatment at 200°C for 10 h. The method of electroplating can be referred to [15]. Moreover, the analysis of the content of hydrogen in the bainitic steels is carried out by a CQY-2 type hydrogen content analyzer.

The hydrogen embrittlement sensitivity to the bainitic steels used in this study is investigated by SSRT. The experimental equipment is the DDL-100 electronic universal testing machine. A slow strain rate, that is, $5.6 \times 10^{-5} \text{ s}^{-1}$ (stretching rate is 0.1 mm/min), is employed in full reflecting the hydrogen embrittlement sensitivity of the bainitic steels.

The calculations presented in this paper were performed using the Cambridge Serial Total-Energy Package (CASTEP), which was based on density-functional theory (DFT), using a plane-wave basis set for the expansion of the electronic wave-function [16]. In the work, the ultrasoft pseudopotential (USPP) [17] was used to describe the computationally expensive core-valence interaction, and the generalised gradient approximation (GGA) of Perdew-Burke-Ernzerhof (PBE)

[18] was employed for the exchange-correlation energy. Brillouin zone sampling was performed using a Monkhorst-Pack grid [19] of special k-points. The electronic occupancies were determined according to a Methfessel-Paxton scheme [20] with an energy smearing of 0.1 eV. A plane-wave cutoff energy of 400 eV was used for all calculations. All calculations were employed spin-polarisation to account for the ferromagnetic state of bainitic steel. Unless otherwise stated, the DFT calculations were relaxed respective to supercell shape and volume, as well as all atomic positions, in order to find the minimum energy. During geometry optimisation, convergence criteria were chosen as the energy changes on each atom of less than $5 \times 10^{-6} \text{ eV}$ and the force on each atom of less than $0.01 \text{ eV}/\text{\AA}$.

Two different bcc iron cells were used: $1 \times 1 \times 1$ (2 atoms) and $2 \times 2 \times 2$ (16 atoms) conventional bcc cells, corresponding to a k-point sampling of $12 \times 12 \times 12$ and $6 \times 6 \times 6$. One of the iron atoms in each cell was substituted by a Si or an Al atom, which was in the minimum energy state as shown in Figure 1.

In the bcc lattice there are two high-symmetry interstitial sites available for the hydrogen atom, that is, the octahedral (O) site and the tetrahedral (T) site. Total energy and lattice distortion of each cell were calculated to estimate the preference site of hydrogen. Binding energy was investigated to characterize the bonding strength of each cell. The diffusion barrier of H was calculated by a transition state (TS)

TABLE 2: Calculated results of total energy (E_{total}), the energy difference ($\Delta E = E_{\text{O}} - E_{\text{T}}$) between H in the O-site and T-site, and lattice distortion (a/c) in unit cells, eV.

	Fe ₂ H		FeSiH		FeAlH	
	T	O	T	O	T	O
E_{total}	-1746.321	-1746.378	-988.081	-987.884	-938.034	-937.767
ΔE		-0.057		0.197		0.267
a/c	1.00	1.49	1.05	1.37	1.05	1.41

TABLE 3: Calculated results of total energy (E_{total}), the energy difference ($\Delta E = E_{\text{O}} - E_{\text{T}}$) between H in the O-site and T-site, and lattice distortion (a/c) in supercells, eV.

	Fe ₁₆ H		Fe ₁₅ SiH		Fe ₁₅ AlH	
	T	O	T	O	T	O
E_{total}	-13860.979	-13860.859	-13104.230	-13103.649	-13052.927	-13052.410
ΔE		0.120		0.581		0.517
a/c	1.00	1.04	1.00	1.05	0.99	1.06

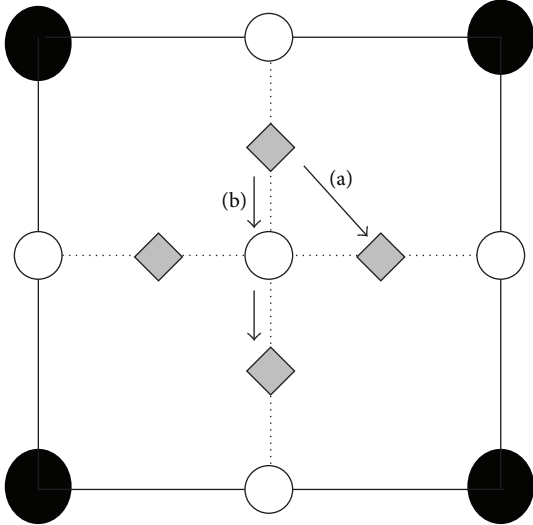


FIGURE 2: O-sites and T-sites from a (001) view of the bcc lattice, open circles, and diamonds, respectively. Full circles represent Fe atoms.

search via the complete linear/quadratic synchronous transit method (LST/QST) [21]. Since hydrogen atom prefers to occupy the tetrahedral sites [22], here the diffusion between two tetrahedral interstitial sites was only considered. There were two possible paths between the adjacent tetrahedral sites: path (a) between the nearest neighbouring tetrahedral sites (T-T) and path (b) between the tetrahedral sites via the O-site in the middle of the path (T-O-T), as shown in Figure 2. The electron density and the state density were computed at their equilibrium lattice constants and optimise structures.

3. Results and Discussion

The HE characteristics of CFBS with different sets of aluminium content (0 wt%, 0.19 wt%, 0.75 wt%, and 1.31 wt%) have been investigated, as shown in Figure 3.

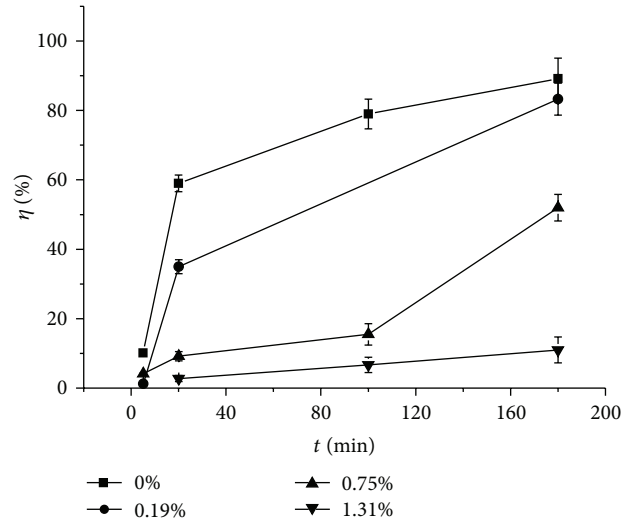


FIGURE 3: Relationships between the embrittlement index and hydrogen charging time of the four different aluminium contents of bainitic steels at a strain rate of $5.6 \times 10^{-5} \text{ s}^{-1}$.

The total content of aluminium and silicon is about 1.8 wt%, so the content of silicon is 1.8 wt%, 1.55 wt%, 1.02 wt%, and 0.48 wt%, respectively. It can be seen that the embrittlement index increases as hydrogen content increases; however, it decreases as aluminium content increase. We consider that aluminium can refine bainite, tendency to increase M_s and M_f , which is found to be the most sensitive to hydrogen by a metallographic microscope and an X-ray diffraction analysis. In this work, the influences of Al and Si on HE were further studied using first-principle.

3.1. Hydrogen Site Preference in Each Cell. In the bcc lattice, two high-symmetry sites (O and T) competed to locate the interstitial atoms as mentioned earlier. Both sites were investigated for H atoms in order to find the optimal site. The calculation results of unit cells and supercells are summarised in Tables 2 and 3.

TABLE 4: Calculated binding energy of unit cells, eV.

	Fe ₂	Fe ₂ H		FeSi	FeSiH		FeAl	FeAlH	
		T	O		T	O		T	O
E_b (eV)	5.44	4.693	4.712	6.06	4.604	4.538	4.95	4.312	4.223
$\Delta\%$ ^a	—	13.75%	13.40%	—	24.01%	25.09%	—	12.83%	14.63%

$$^a \Delta\% = [E(\text{Fe}_n\text{XH}) - E(\text{Fe}_n\text{X})]/E(\text{Fe}_n\text{X}) \times 100\%.$$

TABLE 5: Calculated binding energy of supercells, eV.

	Fe ₁₆	Fe ₁₆ H		Fe ₁₅ Si	Fe ₁₅ SiH		Fe ₁₅ Al	Fe ₁₅ AlH	
		T	O		T	O		T	O
E_b (eV)	5.44	5.314	5.307	5.52	5.386	5.352	5.38	5.262	5.230
$\Delta\%$	—	2.38%	2.51%	—	2.52%	3.14%	—	2.28%	2.87%

Even if on average the density of hydrogen absorbed in iron is expected to be small, it can be accumulated locally in some regions where the density is high. It is at the O-site that the total energy is the lowest for high concentrations (Fe₂H). Generally speaking, the lowest energy corresponds to the most stable site. However, it induces a large deformation ($a/c = 1.49$) on the bcc lattice where H is at the O-site. There is no distortion of lattice for H at the T-site and the total energy is slightly higher (0.056 eV). For FeSiH and FeAlH cells, H at the T-site corresponds to the lowest energy and the least distortion. Table 2 shows that it induces a slight deformation where H is at both the T-site and O-site in supercells. However, H prefers a T-site over an O-site by 0.581 eV and 0.517 eV for Fe₁₅SiH and Fe₁₅AlH. Therefore, we are more inclined towards hydrogen at T-sites than at O-site.

3.2. Binding Energy. The binding energy of the crystal can be used to characterize the bonding strength of crystal, which can be expressed as follows:

$$E_b = \frac{1}{(n+2)[n \times E(\text{Fe}) + E(\text{X}) + E(\text{H}) - E(\text{Fe}_n\text{XH})]}, \quad (1)$$

where $E(\text{Fe})$, $E(\text{X})$, and $E(\text{H})$ are the energy of the isolated Fe, X (Si or Al), and H atom, respectively. $E(\text{Fe}_n\text{XH})$ is the total energy of Fe_nXH cell, which has been optimized, and n is the number of atoms. The higher the binding energy is, the higher the strength is. All results of binding energy are listed in the Tables 4 and 5. The binding energy of the cell with hydrogen is less than that without hydrogen. It indicates that the introduction of hydrogen reduces the binding energy. Besides, the degree of reduction increases with the increase of hydrogen content. The decohesion theory indicates that, when the hydrogen electron enters the unfillable 3d electronic shell in the pure iron cell, the repulsive force increases; however, the binding energy decreases.

For the cells containing silicon or aluminium, the binding energy increases when an iron atom is substituted by a silicon atom. However, the degree of reduction is the highest when a hydrogen atom is added, which corresponds to the macroscopic phenomenon that the higher it strength is, the more sensitive to HE is. The binding energy decreases a little

TABLE 6: Diffusion barrier of hydrogen in pure iron, eV.

	Fe ₂ H	Fe ₁₆ H
T-T	0.159	0.111
T-O-T	0.448	0.179

TABLE 7: Diffusion barrier of hydrogen in the system with silicon or aluminium, eV.

	FeSiH	FeAlH	Fe ₁₅ SiH	Fe ₁₅ AlH
T-T	0.404	0.514	0.056	0.117

when an iron atom is substituted by an aluminium atom, and the degree of reduction is the lowest when a hydrogen atom is added. It can be concluded that the aluminium replacing silicon can reduce the HE of CFBS.

3.3. Diffusion Behaviour of Hydrogen. Hydrogen as a temporary alloying element in steel has high diffusivity and mobility, which is a major reason for HE. The diffusion barriers of hydrogen along the two paths in pure α -Fe cell are calculated and compared with experimental values. The calculated values are reported in [14, 23, 24], which are also listed in the Table 6.

In the first direction of the T-T path, the calculated energy barriers of Fe₂H and Fe₁₆H are 0.159 eV and 0.111 eV. The former result is slightly larger than the experimental value, but the latter one is in good agreement with the experimental value is 0.035~0.142 [23], and the calculated values are 0.088, 0.106 [14, 24] However, the results of the second T-O-T path are much higher than the experimental value. In other words, the hydrogen atom prefers energetically to diffuse between the nearest neighbouring sites. Thus the energy barriers of systems containing a silicon or are aluminium atom are calculated according to the path (a), which are listed in Table 7.

It can be clearly seen that the energy barriers of hydrogen in the Fe-Al system are much higher than those in the Fe-Si system. In supercells especially, the calculated value of 0.117 eV of Fe₁₅AlH is double that of 0.056 eV of Fe₁₅SiH. It indicates that hydrogen diffuses more difficultly if silicon is substituted by aluminium. It further proves that HE can be reduced by the partial replacement of Si by Al.

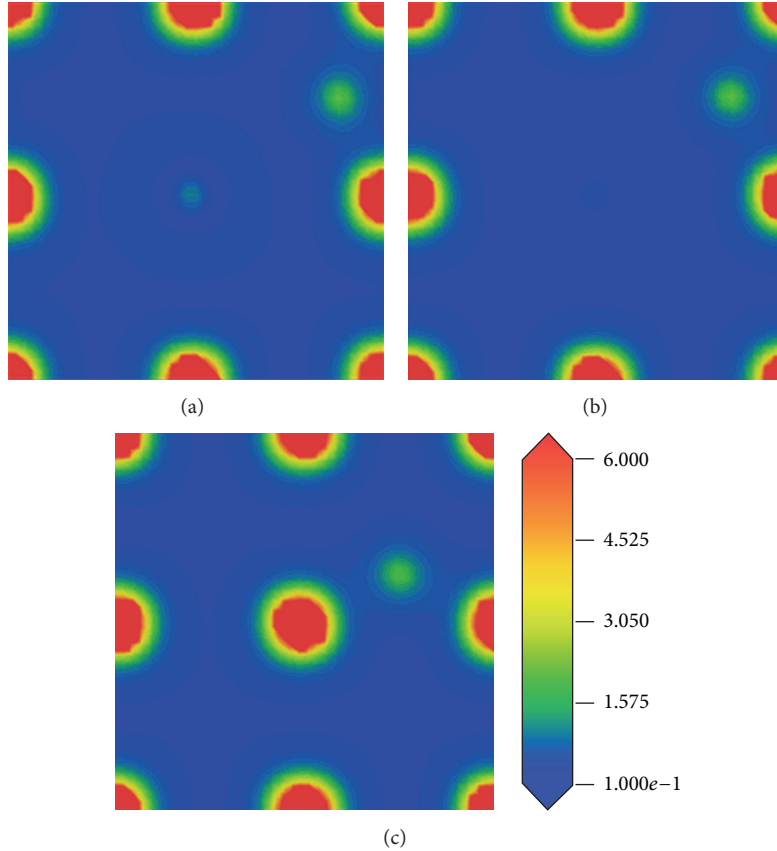


FIGURE 4: Electron density distribution map of supercells on the (200) plane. (a) Fe₁₆H, (b) Fe₁₅SiH, and (c) Fe₁₅AlH.

3.4. Electronic Structure. Valence charge density distribution reveals the features of the atomic bonds [25]. Figure 4 illustrates the charge density distribution map of a Fe₁₅XH (X for Fe, Si, or Al) supercell on the (200) plane.

It can be seen that the valence charge is mainly concentrated around the Fe atoms; the charge density around the Si atom is smaller and that around the Al atom is the lowest. It can be considered that there are more valence electrons for the Fe atom and less for Si or Al atoms. Besides, both Si and Al atoms have clear repulsion to hydrogen, which can also be seen in Figure 4. There is no significant difference between Fe₁₅SiH and Fe₁₅AlH in charge density distribution. However, it is very different in the density of states, as shown in Figure 5.

Figure 5(a) shows the calculated total density of states (TDOS) and partial density of states (PDOS) of the Fe-Si system. One can see that the TDOS at the Fermi level (E_F) is not zero, and band gap does not occur in the vicinity of E_F , which corresponds to be metallic. There are three peaks in the valence band: one at about -10 eV that is mainly contributed by the s states of the Si atom. The other two peaks from -8 to 0 eV are dominated by the d states of the Fe atom. There is a band gap in which DOS is zero from -9 to -8 eV. The TDOS in E_F is not zero and still reflects a metallic character after the addition of a hydrogen atom, as shown in Figure 5(b). However, a new peak appears from -9 to -8 eV, which is mainly caused by hybridisation between s states of H and p

states of Si. The band gap from -9 to -8 eV in the Fe-Si system has a right offset and the width is decreased when hydrogen is added. The TDOS of the Fe-Al system (Figure 5(c)) in E_F is not zero, either. There is no band gap in the valence band. However, one appears at about -8 eV after the addition of hydrogen (Figure 5(d)). It can be considered that the electron densities of Al and Fe atoms are redistributed by hydrogen. In addition, it is at -9 eV that the density of states is the highest for hydrogen atoms in the Fe-Al-H system, which is different from the Fe-Si-H system. There is a new peak from -10 to -8 eV, which is also because hydrogen has an effect on the interaction between Al and Fe atoms and thus makes a new peak occur from -10 to -8 eV.

4. Conclusions

- (1) In pure α -Fe, hydrogen in the octahedral site is more stable for high concentrations (Fe₂H), but it induces a large deformation on the bcc lattice. Hydrogen prefers tetrahedral sites for low concentrations. In cells with Si or Al, hydrogen is eager to enter tetrahedral sites.
- (2) The binding energy of the cell with Si is the highest, and it is severely reduced by the addition of hydrogen, which demonstrates that HE increases with the increase strength; HE can be reduced by the partial replacement of Si by Al.

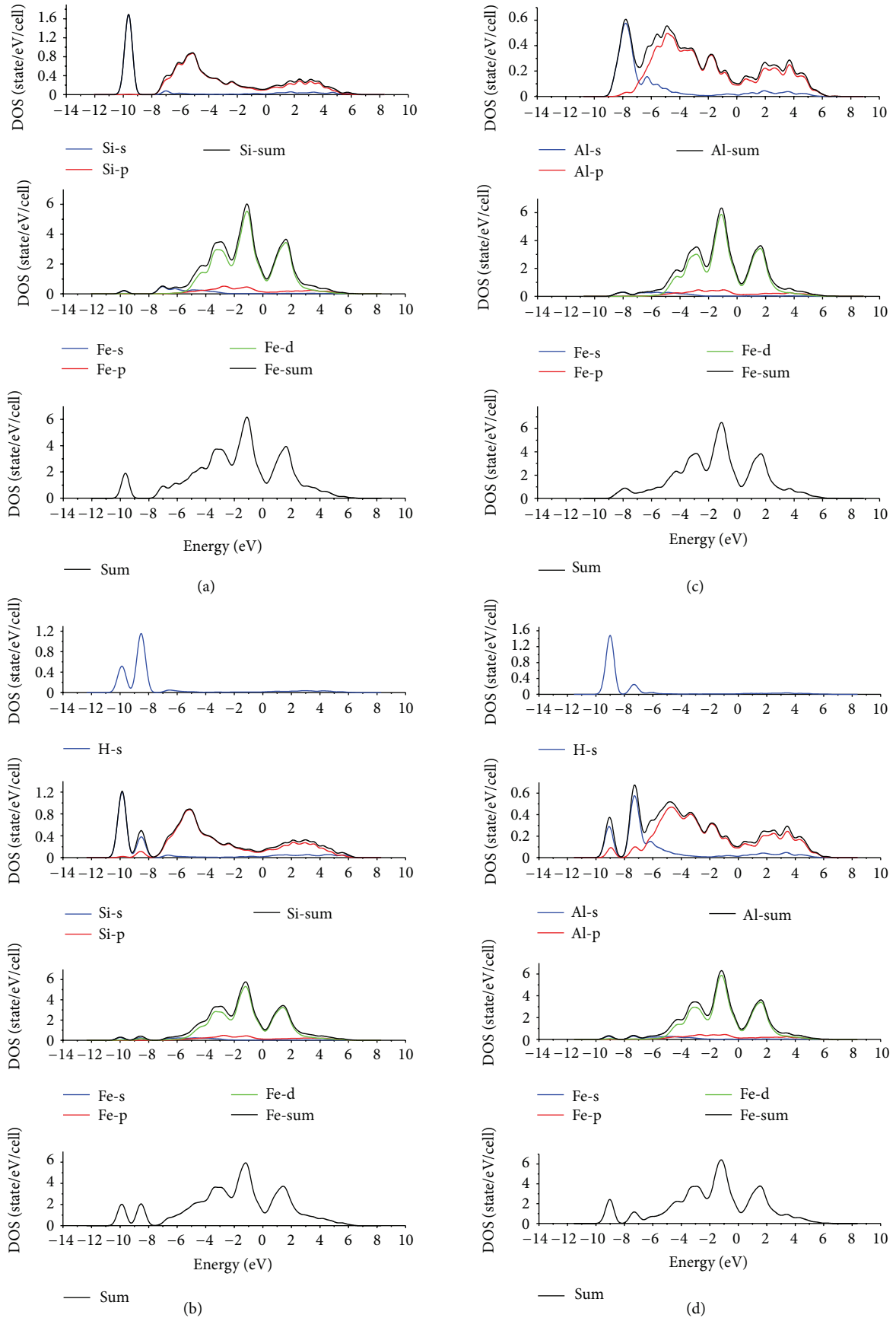


FIGURE 5: Partial and total density of states. (a) Fe-Si system, (b) Fe-Si-H system, (c) Fe-Al system, and (d) Fe-Al-H system.

- (3) Hydrogen atoms energetically prefer to diffuse between the nearest neighbouring sites. The diffusion barrier of hydrogen in the cell containing Al is the highest and it is difficult for hydrogen to diffuse, which is another reason that HE can be reduced by the replacement of Si by Al.

Acknowledgments

The paper Sponsored by National Science Foundation for Distinguished Young Scholars (no. 50925522) and the National Natural Science Foundation of China (no. 50871094).

References

- [1] F. C. Zhang, C. L. Zheng, B. Lv, T. S. Wang, M. Li, and M. Zhang, "Effects of hydrogen on the properties of bainitic steel crossing," *Engineering Failure Analysis*, vol. 16, no. 5, pp. 1461–1467, 2009.
- [2] F. G. Caballero, H. K. D. H. Bhadeshia, K. J. A. Mawella, D. G. Jones, and P. Brown, "Very strong low temperature bainite," *Materials Science and Technology*, vol. 18, no. 3, pp. 279–284, 2002.
- [3] C. Garcia-Mateo, F. G. Caballero, and H. K. D. H. Bhadeshia, "Acceleration of low-temperature bainite," *ISIJ International*, vol. 43, no. 11, pp. 1821–1825, 2003.
- [4] T. Hojo, K. Sugimoto, Y. Mukai, and S. Ikeda, "Effects of aluminum on delayed fracture properties of ultra high strength low alloy TRIP-aided steels," *ISIJ International*, vol. 48, no. 6, pp. 824–829, 2008.
- [5] E. Jimenez-Melero, N. H. van Dijk, L. Zhao et al., "Characterization of individual retained austenite grains and their stability in low-alloyed TRIP steels," *Acta Materialia*, vol. 55, no. 20, pp. 6713–6723, 2007.
- [6] M. Gomez, C. I. Garcia, D. M. Haezebrouck, and A. J. Deardo, "Design of composition in (Al/Si)-alloyed TRIP steels," *ISIJ International*, vol. 49, no. 2, pp. 302–311, 2009.
- [7] C. L. Zheng, B. Lv, C. Chen, Z. Yan, F. Zhang, and L. Qian, "Hydrogen embrittlement of a manganese-aluminum high-strength bainitic steel for railway crossings," *ISIJ International*, vol. 51, no. 10, pp. 1749–1753, 2011.
- [8] R. Matsumoto, Y. Inoue, S. Taketomi, and N. Miyazaki, "Influence of shear strain on the hydrogen trapped in bcc-Fe: a first-principles-based study," *Scripta Materialia*, vol. 60, no. 7, pp. 555–558, 2009.
- [9] D. Psiachos, T. Hammerschmidt, and R. Drautz, "Ab initio study of the interaction of H with substitutional solute atoms in α -Fe: trends across the transition-metal series," *Computational Materials Science*, vol. 65, pp. 235–238, 2012.
- [10] A. R. Troiano, "The role of hydrogen and other interstitials in the mechanical behaviour of metals," *Transactions of ASM*, vol. 52, pp. 54–80, 1960.
- [11] R. A. Oriani and P. H. Josephic, "Equilibrium aspects of hydrogen-induced cracking of steels," *Acta Metallurgica*, vol. 22, no. 9, pp. 1065–1074, 1974.
- [12] C. D. Beachem, "A new model for hydrogen-assisted cracking (hydrogen "embrittlement")," *Metallurgical Transactions*, vol. 3, no. 2, pp. 441–455, 1972.
- [13] H. K. Birnbaum and P. Sofronis, "Hydrogen-enhanced localized plasticity—a mechanism for hydrogen-related fracture," *Materials Science and Engineering A*, vol. 176, no. 1-2, pp. 191–202, 1994.
- [14] D. E. Jiang and E. A. Carter, "Diffusion of interstitial hydrogen into and through bcc Fe from first principles," *Physical Review B*, vol. 70, no. 6, Article ID 064102, 9 pages, 2004.
- [15] C. L. Zheng, B. Lv, F. C. Zhang, Z. G. Yan, R. Dan, and L. H. Qian, "Effect of secondary cracks on hydrogen embrittlement of bainitic steels," *Materials Science and Engineering A*, vol. 547, pp. 99–103, 2012.
- [16] M. D. Segall, P. J. D. Lindan, M. J. Probert et al., "First-principles simulation: ideas, illustrations and the CASTEP code," *Journal of Physics Condensed Matter*, vol. 14, no. 11, pp. 2717–2744, 2002.
- [17] D. Vanderbilt, "Soft self-consistent pseudopotentials in a generalized eigenvalue formalism," *Physical Review B*, vol. 41, no. 11, pp. 7892–7895, 1990.
- [18] J. P. Perdew, K. Burke, and M. Ernzerhof, "Generalized gradient approximation made simple," *Physical Review Letters*, vol. 77, no. 18, pp. 3865–3868, 1996.
- [19] H. J. Monkhorst and J. D. Pack, "Special points for Brillouin-zone integrations," *Physical Review B*, vol. 13, no. 12, pp. 5188–5192, 1976.
- [20] M. Methfessel and A. T. Paxton, "High-precision sampling for Brillouin-zone integration in metals," *Physical Review B*, vol. 40, no. 6, pp. 3616–3621, 1989.
- [21] T. A. Halgren and W. N. Lipscomb, "The synchronous-transit method for determining reaction pathways and locating molecular transition states," *Chemical Physics Letters*, vol. 49, no. 2, pp. 225–232, 1977.
- [22] P. Khowash, S. Gowtham, and R. Pandey, "Electronic structure calculations of substitutional and interstitial hydrogen in Nb," *Solid State Communications*, vol. 152, no. 9, pp. 788–790, 2012.
- [23] Y. Hayashi and W. M. Shu, "Iron (ruthenium and osmium)-hydrogen systems," *Solid State Phenomena*, vol. 73–75, pp. 65–114, 2000.
- [24] D. C. Sorescu, "First principles calculations of the adsorption and diffusion of hydrogen on Fe(1 0 0) surface and in the bulk," *Catalysis Today*, vol. 105, no. 1, pp. 44–65, 2005.
- [25] G. H. Lu, S. H. Deng, and T. M. Wang, "Theoretical tensile strength of an Al grain boundary," *Physical Review B*, vol. 69, no. 13, Article ID 134106, 9 pages, 2004.